

DISS. ETH NO. 29135

Driven-dissipative phenomena in quantum many-body systems

A thesis submitted to attain the degree of
DOCTOR OF SCIENCES of ETH ZÜRICH
(Dr. sc. ETH Zürich)

presented by

Rui Lin

MSc ETH Physics, ETH Zürich
born on 18.05.1994
citizen of China

accepted on the recommendation of

Prof. Dr. Manfred Sgrist
Dr. Chitra Ramasubramanian
Univ.-Prof. Dr. Helmut Ritsch

2023

Abstract

Quantum simulation provides an arena for investigating complex quantum many-body phenomena, which are otherwise inaccessible through conventional techniques like analytical calculations and numerical simulations. One intriguing platform is ultracold atomic gases driven by external lasers and coupled to lossy optical cavities. Its ease of controllability and tunability endowed by tremendous technology advances has led to its great success in simulating a large variety of quantum many-body Hamiltonians and associated phenomenology not easily implemented in traditional condensed matter systems. Specifically, cavity-boson systems have also provided the first experimental realisation of the renowned Dicke model and related models, whose simplicity and tractability offer the opportunity for a more profound insight into driven-dissipative processes.

Nevertheless, a fundamental distinction between quantum gases subject to driving and dissipation as simulators and condensed matter systems as simulatees is that the former is inherently out of equilibrium. Recently, an increasing number of studies manifest unique and exotic behaviours in out-of-equilibrium systems, which potentially obscures the role of quantum gases as faithful quantum simulators.

This doctoral thesis addresses the interplay between drive and dissipation, as well as their impact on the physics of quantum many-body systems through two perspectives. On the one hand, using cavity-boson systems as examples, this thesis thoroughly investigates a plethora of many-body phenomena of inherently driven-dissipative nature, and demonstrates the emergence of many peculiar phenomena, including limit cycles and chaotic behaviours, a continuous family of multistable steady states, and a uni-directional atomic current on synthetic momentum lattice. On the other hand, a framework is sought for a better clarification of quantum driven-dissipative dynamics, which captures and categorises the underlying mechanisms leading to the aforementioned phenomena in ultracold atomic systems. The acquired understandings, as reformulated in the Floquet and Keldysh formalisms, are finally harnessed and applied to condensed matter systems. Specifically, it reveals an unexploited mechanism where the interplay between drive and dissipation is shown to generate a substantial enhancement of superconductivity at finite temperatures.

In summary, this thesis elucidates the role of quantum-optical ultracold-atomic systems as quantum simulators. They go far beyond the simulators of static

systems via effective stroboscopic Hamiltonians, and are intrinsically capable of emulating thermal environmental effects ubiquitous to quantum many-body systems of both quantum gases and condensed matter. This thesis thus sheds light on a novel paradigm for driven-dissipative engineering of quantum many-body systems, which potentially has broad applications in the realms of, e.g., quantum critical phenomena, quantum many-body phase preparation, and quantum information processing.

Kurzfassung

Die Quantensimulation bietet einen Schauplatz für die Untersuchung komplexer Quanten-Vielteilchenphänomene, die ansonsten durch herkömmliche Techniken wie analytische Berechnungen und numerische Simulationen nicht zugänglich sind. Eine faszinierende Plattform sind ultrakalte atomare Gase, die von externen Lasern getrieben und an verlustbehaftete optische Resonatoren gekoppelt werden. Ihre einfache Kontrollier- und Abstimbarkeit dank enormer technologischer Fortschritte haben zu ihrem bedeutenden Erfolg bei der Simulation einer grossen Vielfalt von Quanten-Vielteilchen-Hamiltonian-Operatoren und der damit verbundenen Phänomenologie geführt, die in herkömmlichen Systemen mit kondensierter Materie anspruchsvoll auszuführen sind. Insbesondere haben Resonator-Boson-Systeme auch die erste experimentelle Realisierung des wohlbekannten Dicke-Modells und verwandter Modelle geliefert, deren Einfachheit und Handhabbarkeit die Möglichkeit für einen tieferen Einblick in getrieben-dissipative Prozesse bieten.

Dennoch besteht ein grundlegender Unterschied zwischen Quantengasen als Simulatoren und kondensierter Materie als zu simulierenden Systemen, dass Erstere die Antrieb und Dissipation unterliegen und daher von Natur aus nicht im Gleichgewicht sind. In letzter Zeit zeigen immer mehr Studien einzigartige und fremdartige Verhaltensweisen in Systemen ausserhalb des Gleichgewichts, was eventuell die Rolle von Quantengasen als wahrheitsgetreue Quantensimulatoren undeutlich macht.

Diese Doktorarbeit befasst sich aus zwei Perspektiven mit dem Zusammenspiel von Antrieb und Dissipation sowie deren Auswirkungen auf die Physik von Quanten-Vielteilchensystemen. Einerseits untersucht diese Dissertation am Beispiel von Resonator-Boson-Systemen eine Auswahl an Vielteilchenphänomenen von inhärent getrieben-dissipativer Natur und zeigt die Entstehung mehrerer eigenartiger Phänomene, einschliesslich Grenzzyklus- und chaotisches Verhalten, eine kontinuierliche Familie multistabiler stationärer Zustände und ein unidirektionaler atomarer Strom in einem synthetischen Impulsgitter. Andererseits wird zur besseren Erklärung der getrieben-dissipativen Quantendynamik ein Rahmen gesucht, der die zugrunde liegenden Mechanismen, die zu den oben genannten Phänomenen führen, erfasst und einstuft. Die erworbenen Erkenntnisse, die durch die Formalismen von Floquet und Keldysh umformuliert werden können, werden schliesslich auf Systeme der kondensierten Materie angewendet. Insbesondere offenbart es einen bisher

noch unerschlossenen Mechanismus, bei dem das Zusammenspiel zwischen Antrieb und Dissipation eine wesentliche Verstärkung der Supraleitfähigkeit bei endlichen Temperaturen hervorruft.

Zusammenfassend klärt diese Dissertation die Rolle von quantenoptischen ultrakalten atomaren Systemen als Quantensimulatoren auf. Sie gehen weit über die Simulatoren statischer Systeme mit effektiven stroboskopischen Hamiltonian-Operatoren hinaus. Intrinsisch sind sie selbst in der Lage, die in allen Arten von Quanten-Vielteilchensystemen allgegenwärtigen thermischen Umgebungseffekte nachzubilden. Diese Arbeit beleuchtet somit ein neuartiges Paradigma für getrieben-dissipatives Engineering von Quanten-Vielteilchensystemen, das potenziell breite Anwendungen in den Bereichen von z.B. quantenkritischen Phänomenen, Quanten-Vielteilchen-Phasenpräparation und Quanteninformationsverarbeitung hat.

摘要

量子模拟逐渐成为继解析计算、数值仿真等成熟方法後，新一代研究复杂量子多体现象的良好平台。受外部激光激励、并与有损光学谐振腔相耦合的超冷原子气就是其中一种备受瞩目的系统。近年的技术进步赋予了这类系统更精准的可控性和可调节性，并使之成功地模拟了一系列在传统凝聚态系统中难以实现的量子多体哈密顿量与相关的多体现象。不仅如此，谐振腔—波色子系统更首次在实验中实现了简洁、易处理且有丰富内涵的迪克模型及其相关模型，促进了对驱动—耗散过程的深入理解。

诚然，作为量子模拟器的量子气体必然是受驱动的且有耗散的，因此也就必然处于非平衡态。这使得它们与作为被模拟对象的凝聚态系统有着本质上的区别。的确，近年来的研究愈发地揭示了在这些非平衡系统中所表现出的许多独特的、尤其是在平衡系统中无法复刻的特性。这最终将导致人们对量子气体作为量子模拟器的可靠性产生了疑虑。

故此，本博士论文就驱动和耗散在量子多体系统中的地位和作用，从两方面展开针对性的研究。一方面，以谐振腔—波色子系统为主要研究对象，本论文详尽地研究了一系列与驱动—耗散本质密切相关的多体现象，并展示了其中的一些新奇又独特的现象，譬如极限环与混沌行为、双参数连续性的多稳态以及合成动量晶格中的单向原子流。另一方面，本论文尝试以弗洛凯理论和克尔德什理论为基础，探寻构建一个系统性地解释驱动—耗散动力学现象的理论框架。该框架不仅在超冷原子系统中为上述现象生成机制的描述和分类提供了清晰的图像，更在凝聚态系统中预测出一种崭新的在有限温度下显著增强超导性能的机制。

综上，本论文阐述了量子光学—超冷原子系统作为量子模拟器的内涵。这一类系统远不止能够通过其等效闪烁哈密顿量来模拟静态系统，更能从根本上兼顾环境因素对量子多体系统所产生的热力学效应。而这些影响均天然且普遍地存在于量子气体和凝聚态系统中。望本论文可启发量子多体工程中运用驱动—耗散效应的新范式得以形成，并藉此促成其在诸如量子临界效应、量子多体相制备及量子信息处理等领域中更广泛的应用。

琴瑟弦皆有應聲宮弦則應少宮商弦即應少商
其餘皆隔四相應今曲中有聲者須依此用之
欲知其應者先調諸弦令聲和乃剪紙人加弦
上鼓其應弦則紙人躍他弦即不動聲律高下
苟同雖在他琴鼓之應弦亦震此之謂正聲

“String instruments all manifest response of sound. A string of *middle C* sound responds to a *treble C* sound; a string of *middle D* sound responds to a *treble D* sound, and so do other strings and sounds which are an octave apart. To explore such response of sound, one can put a small piece of paper on each string of a harmonically tuned instrument. When a string is played, only the piece of paper on its responding string dances, while pieces on other strings remain still. The responding string produces a sound at the same pitch. This phenomenon can be observed even if the responding string is on a different instrument. This is the proper sound of a note.”

Excerpted from
Dream Pool Essays
by SHEN Kuo

Record in the 12th century of *harmonic resonance* on string instruments, a driven-dissipative effect in classical systems.

Contents

Abstract	i
Kurzfassung	iii
摘要	v
1 Introduction	1
1.1 Introduction	1
1.1.1 Drive and dissipation in few-body classical and quantum mechanical systems	1
1.1.2 Quantum driven-dissipative many-body systems	3
1.2 Outline of thesis and Contributions	5
1.3 MCTDH-X	7
1.3.1 Methodology	8
1.3.2 Observables	9
1.3.3 Extraction of experimental data via machine learning	10
I Cavity-boson systems as effectively static systems in a rotating frame	13
2 Floquet theory and Lindblad form	15
2.1 Floquet theory for periodically driven quantum systems	15
2.1.1 The Shirley-Floquet formalism	15
2.1.2 Application: Rotating wave approximation in quantum optical systems	18
2.2 Lindblad form for dissipation	20
2.3 Conclusions	21
3 Introduction to the cavity-BEC system	23
3.1 Introduction to the Dicke model	23
3.2 The experimental setup and its Hamiltonian	25
3.3 Mapping to the driven-dissipative Dicke model	28
4 Superradiant transition and Mott transition in a cavity-BEC system	33
4.1 Introduction	33
4.2 Experimental setup and measurement protocol	34

4.2.1	Cavity-BEC system and superfluid–Mott-insulator transition	34
4.2.2	Measurement protocol	39
4.3	Simulation methodology	41
4.3.1	Numerical method	41
4.3.2	Reduction of system dimensionality and rescaling of the contact interaction strength	41
4.3.3	Four-well model	43
4.4	Results	47
4.4.1	The Mott transition	47
4.4.2	Comparison to Wannier-based Bose-Hubbard approaches	51
4.5	Conclusions	53
 II Driven-dissipative cavity-boson systems with inherent system-bath rotation		55
5	Keldysh formalism	57
5.1	The Keldysh formalism	57
5.2	Combining Keldysh and Floquet formalisms in bosonic Nambu space	60
5.3	From formalism to practical methodology: Hamiltonian and Lindbladian	64
6	Mechanisms of driven-dissipative stabilities and instabilities	67
6.1	The Dicke model and the cavity-boson system	68
6.1.1	Stability of the normal phase in the Dicke model – Exceptional point instability	68
6.1.2	Cavity fluctuations in the normal phase of the Dicke model	70
6.1.3	Cavity fluctuations in a cavity-boson system with effective long-range interaction	72
6.2	The Tavis-Cummings model	74
6.3	Stabilisation and destabilisation mechanisms in driven-dissipative systems	76
6.4	Conclusions	79
7	Quasi-periodic dynamics and chaos in a cavity-boson system	81
7.1	Introduction	81
7.2	Mean-field features: Dynamical behaviours and dimerisation	84
7.3	Correlated many-body phases	89
7.4	Conclusions	91
8	Dissipation-engineered family of nearly-dark many-body	

states in a cavity-boson system	93
8.1 Introduction	93
8.2 The underlying SU(3) atomic system	95
8.2.1 Conserved quantities in the atomic systems	97
8.2.2 Three-level SU(2) spin-1 systems	97
8.3 Open system phase diagram	98
8.3.1 Introduction to inverted states	98
8.3.2 Excitation spectra and stabilities	99
8.4 Dynamics: Cavity-mediated atomic transfer	104
8.5 Instability in the superradiant phase	105
8.6 Conclusions	107
9 Uni-directional atomic current in a momentum lattice synthesised in a cavity-boson system	109
9.1 Introduction to the experimental setup	109
9.2 Mapping to Dicke-like model and uni-directional atomic current in the momentum lattice	111
9.3 Gross-Pitaevskii simulations	114
9.3.1 Equations of motion	114
9.3.2 Numerical solution of the dynamics	115
9.3.3 Dynamics due to harmonic confinement and contact interactions	116
9.4 Conclusions	121
III Driven-dissipative enhancement of superconductivity	123
10 Keldysh-Floquet formalism on superconductors	125
10.1 System description	125
10.2 The self-consistency equation for order parameter	126
10.2.1 The coupling to the bath	126
10.2.2 Hubbard-Stratonovich transformation	128
10.2.3 Invariance of order parameter in different frames	132
11 Non-thermal driven effects in superconductors	133
11.1 Spectral and response functions	133
11.2 Enhancement of superconductivity at finite temperature	138
11.3 Conclusions	140
Conclusions and Outlook	143

Appendices	146
A Shirley-Floquet formalism	149
A.1 Shirley-Floquet Hamiltonian	149
A.2 Shirley-Floquet Green function	151
A.3 Useful formulae for the Shirley-Floquet matrices	153
A.4 Solution of Rabi driving in Shirley-Floquet formalism	153
A.4.1 Standard method	153
A.4.2 Alternative method	154
A.4.3 Geometric interpretation of the two transformations	156
B Methodologies and techniques used in solving driven-dissipative quantum optical systems	157
B.1 Collective behaviours 1: Dynamical evolutions	157
B.2 Collective behaviours 2: Steady state	158
B.3 Microscopic behaviours 1: Holstein-Primakoff transformation	159
B.4 Microscopic behaviours 2: Third quantisation	162
B.5 Microscopic behaviours 3: Cavity fluctuations	163
B.6 Bosonic Bogolyubov transformation	163
B.7 Third quantisation from perspective of Keldysh formalism	166
C Calculations pertaining to Part III	169
C.1 Retarded Green function for commuting drive	169
C.2 Oscillating components of the order parameter	171
C.3 Dispersive superconductor in the weak coupling limit	173
References	177
List of publications	197
Curriculum vitae	201
Acronyms	203
Acknowledgments	205

1 | Introduction

1.1 Introduction

1.1.1 Drive and dissipation in few-body classical and quantum mechanical systems

DRIVING and dissipation, manifesting themselves as enforced temporal periodicity and loss of energy respectively, are universal phenomena which have been extensively investigated in classical systems. In the recent past, they have become a prevalent research theme in quantum many-body systems.

Drive and dissipation in classical systems have since centuries ago been studied systematically, with the most representative example being a harmonic oscillator subject to external time-periodic driving and dissipation [1, 2]. For classical systems, the external driving governs the long-term steady state behaviours whereas the dissipation introduces damping and makes the initial condition obsolete. When the frequency of the external driving matches the intrinsic frequency of the oscillator better and better, the in-phase oscillations of the system with respect to the drive leads to accumulation of energy manifesting as a growing oscillation amplitude. This phenomenon known as resonance manifests itself in all realms of classical-world engineering, and is often harnessed for technological applications.

The more intriguing cousins of external driving and resonance are the parametric ones [3, 4], where the parameters of the system, like the harmonic oscillator's intrinsic frequency, vary periodically in time. The most well-known examples of parametric resonance are the Mathieu oscillator [5–7] and the Kapitza pendulum [8] as paradigmatic models, as well as varicap diode [9], mechanical degenerate parametric amplifier [10], and particle production in the universe [11, 12] as actual applications. Compared to external driving, these systems are able to achieve resonance without an exact agreement between the frequencies, but rather in a relatively wide range of parameter regimes. More importantly, any finite dissipation cannot completely wipe out parametric resonance.

For classical systems, drive and dissipation are usually related to thermalisation and cooling via magnification and depletion of oscillation amplitude, respectively. However, for quantum systems, they are involved in a much larger collec-

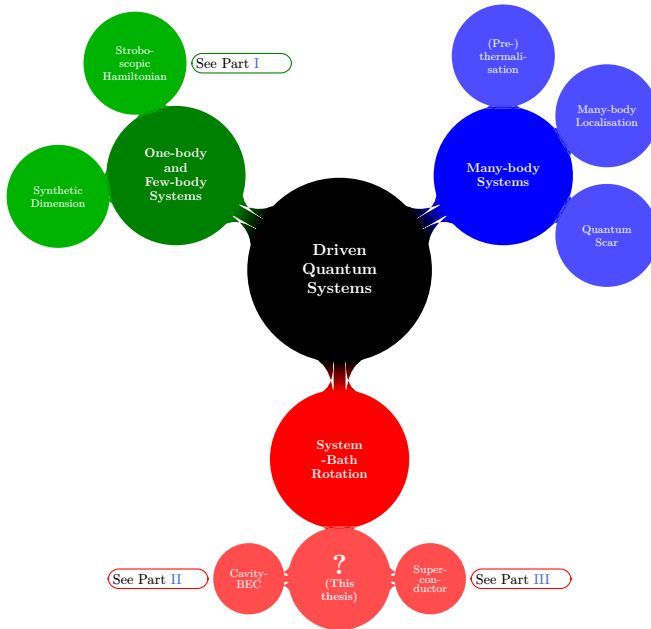


Figure 1.1: Illustration describing the three different aspects of driven quantum systems, and the situation of this thesis.

tion of effects, essentially due to the non-commutativity of quantum mechanical operators. In quantum mechanics, one of the most established methodologies for solving time-periodic systems is the Floquet theory [13], which provides two different perspectives for viewing time-periodically driven quantum systems, both of them commonly being referred to as Floquet engineering [14, 15].

From one point of view, the Floquet theory, as improved by Shirley [16, 17], views the time-periodic systems as tight-binding models in the frequency space, where each lattice site hosts a replica of the static system, and the hopping between them is mediated by the drive. This interpretation immediately allows us to synthesise, or more precisely, make practical use of the time/frequency dimension [18]. The apparent advantage of such dimension synthesis is two-fold: It allows access to phenomena intrinsic to four dimensions [19], and spatially more compact devices. It provides a platform for achieving a variety of many-body phenomena, including synthetic gauge fields [20–22], synthetic topological states [23–26], and optical isolator [27].

From another point of view, Floquet theory provides an effective stroboscopic

Hamiltonian for the system, which is usually achieved in the high driving frequency limit via Magnus expansion [17, 28]. In the lowest order, the Floquet theory approximates the time periodic Hamiltonian by its time average, which usually indicates a reduction and potentially a switching of sign in the corresponding system parameter. The most famous examples of these effects concern the tunnelling strength of a tight-binding model, where the former effect induces the coherent destruction of tunnelling [29–31], also known as dynamical localisation, while the latter effect entails an effective BCS-BEC crossover in the presence of two-body interaction [32, 33]. Taking first order effects beyond time average into account, the non-commutativity between the driving term and the static Hamiltonian can introduce new effective terms into the Hamiltonian otherwise not achievable by conventional engineering of material properties. This notably includes the realisation of topological states in the context of superconductor [34–38] and insulator [39–42], which further leads to the application of Floquet topological pump [43, 44].

These two perspectives of driven quantum systems are in fact highly related. Specifically, the stroboscopic Hamiltonian is obtained by diagonalising along the Floquet frequency dimension while keeping the remaining dimensions untouched. This understanding also captures the parametric resonance seen in classical systems, which occurs in quantum systems as well. Specifically, it manifests itself as spreading of the system’s eigenstate across an infinite number of Floquet lattice sites.

1.1.2 Quantum driven-dissipative many-body systems

The promising aspects of Floquet engineering discussed above concern primarily one-body or few-body systems, and tend to fail inevitably in the thermodynamic limit due to heating effects [45–47]. In most many-body systems, the Floquet-Magnus expansion is generally not convergent and thereby prohibits the existence of an effective stroboscopic Hamiltonian. As a result, the Floquet eigenstates of such many-body systems are characterised by an effective infinite temperature and the loss of any internal structure [48, 49], similar to the case of parametric resonance discussed above. Moreover, the eigenstate thermalisation hypothesis [50], which is in fact recently on its way to becoming formulated as a theory [51], stipulates that these completely thermalised eigenstates are in the majority of cases guaranteed to be reached eventually. Nevertheless, the dynamics of quantum systems towards thermalisation contribute to yet another intriguing focus of recent research. This includes particularly the transient pre-thermalisation plateaux at intermediate time scales, and the onset of thermalisation [46, 47, 52]. These features of driven quantum many-body systems can be characterised within the generalised periodic Gibbs ensemble [49, 53, 54].

Thermalisation is the most common eventual fate of a driven many-body sys-

tem, be it classical or quantum, but there are a few exemptions. These include integrable systems [50] where a convergent stroboscopic Hamiltonian exists thanks to their maximal symmetry, many-body localisation [55, 56] where the system retains the memory of its initial condition for a long time due to emergent integrability [57, 58], and quantum many-body scarred states [59, 60] which are specific states with unusually low entropies surviving in an otherwise thermalising system. Moreover, even in a system which eventually thermalises, interesting physical processes remain as transient behaviours at a long-lasting intermediate time scale despite the eventual loss of system structure, which is referred to as the pre-thermalisation plateau where effective stroboscopic description remains valid [46, 47]. All these topics constitute enthralling themes of recent research.

The experimental realisation of quantum driven-dissipative systems is predominantly achieved in two categories of systems, quantum optical and condensed matter. Quantum optical systems are naturally driven because of the pumping lasers, and dissipative because of the radiation of photons. The high frequency driving and Markovian dissipation in these systems can together be described succinctly by a Liouvillian super-operator composed of a rotating-wave approximated Hamiltonian and a Lindbladian [61–63]. Quantum optical systems consisting of ultracold atoms possess the favourable feature of easy tunability and controllability of parameters, making them a paradigmatic platform for quantum simulating a wide variety of quantum many-body phenomena [64–67]. Among them, driven-dissipative cavity-BEC systems can be mapped to a family of Dicke-like models [66] generally characterised by a transition to the superradiant phase, which, unlike conventional quantum phase transitions, is driven by an exceptional point instability common to non-Hermitian systems [68]. More intriguingly, the complex many-body effects manifested in these models can be easily accessed by a collection of theoretical techniques like Holstein-Primakoff transformation [69, 70] and third quantisation [71, 72]. They thus provide an ideal platform for our investigation, helping us identify and categorise the different driven-dissipative mechanisms.

Meanwhile, drive and dissipation on condensed matter systems are optional yet versatile. This complexity allows for a larger degree of freedom in manipulation, but also limits the extent of investigation into the different driven-dissipative effects, making them a platform yet to be fully explored. As we discussed above, the main focus of contemporary research on driven condensed matter systems is on Floquet engineering the effective stroboscopic Hamiltonian, which constitutes but one aspect of the full quantum driven-dissipative picture. In this thesis, the condensed matter system of superconductor thus provides us with a novel platform to validate, verify and extend our results developed from the quantum optical-ultracold gaseous systems.

Dissipation in quantum systems is usually modelled as a weak coupling of the system to a large ensemble of harmonic oscillators called the bath, whose behaviours are barely influenced by the system [73]. Similar to classical systems, dissipation usually introduces a channel for reducing perturbation, energy, and coherence, thereby providing a way to escape thermalisation in the context of quantum many-body systems. Moreover, dissipation channel can be engineered to be orthogonal to a specific mode in a quantum many-body system [74], thereby rendering this mode dominant. Such engineering can lead to, e.g. η -pairing superconductor in a Fermi-Hubbard system [75]. Other applications of dissipation in quantum many-body systems include quantum synchronisation [76] and dissipative freezing [77]. In the last decade, more and more unexpected traits of non-trivial quantum dissipative effects have been observed. For instance, introduction of dissipation can yield a qualitative impact on the quantum fluctuations [78], or stabilise a quantum state with relatively high energy [79, 80]. Not immediately clear is the existence of either a direct connection between these pieces of a puzzle, or a relation between them and the underlying driving. The obscure understanding of these effects thus motivates this thesis, where we try to gain a systematic understanding of these effects under a unified approach based on Floquet and Keldysh formalisms [81, 82]. After validating the formalism by a few examples in quantum optical and gaseous systems, we will finally apply it tentatively to the under-explored driven-dissipative effects in the condensed matter system of superconductors.

Before presenting the outline of the thesis, we comment on the terminology used in this thesis. Throughout the thesis, we will contrast between driven and static systems, as well as dissipative and non-dissipative systems. However, to avoid further confusion, we will refrain from using the terminologies of “closed” and “open” systems, despite their wide usage in literature.

1.2 Outline of thesis and Contributions

We provide here a synopsis for the thesis. It consists of three parts which progressively provide a more and more profound view into the driven-dissipative effects of quantum many-body systems. Part I investigates driven-dissipative cavity-boson systems seen as static systems described by the rotating-wave approximated Hamiltonians, whereas Part II reveals their intrinsically driven-dissipative features and discuss the mechanism behind them. Such understanding goes beyond the effective stroboscopic Hamiltonians, and culminates in its application to a superconductor in Part III, where a new mechanism for enhancement of superconductivity is proposed. During all projects, my supervisor R. Chitra and various collaborators supported me with their ideas, insights, and expertise.

Part I begins with a brief review to the Floquet theory and the Lindblad form in Chapter 2, which lay the most important building blocks for the theoretical tools used throughout this thesis. In Chapter 3, we review the cavity-boson system which serves as the paradigm for a major part of this thesis, as well as its mapping onto the Dicke model. Focusing on features which are fully consistent with the rotating-wave approximated Hamiltonian, we proceed to investigate the Mott transition in cavity-boson systems in Chapter 4. With the help of the numerical tool MCTDH-X, we are able to explore a numerically exact solution for searching for the superfluid–Mott-insulator phase boundary, and compare it quantitatively to experimental results. This numerical work opens a new possibility for investigating similar many-body correlated ultracold-atom systems, besides the conventional mapping to the Hubbard model. This work is supported from the numerical side by P. Mognini, A.U.J. Lode, and M. Büttner, and from the experimental side by H. Keßler’s group.

Part II is then dedicated to the intrinsic driven-dissipative phenomena seen in cavity-boson systems. Chapter 5 provides a brief review to the Keldysh formalism in the context of Dicke model, which helps develop the understanding of different driven-dissipative mechanisms in Chapter 6 leading to dissipative (in)stability and qualitatively different quantum fluctuation behaviours. These mechanisms as confirmed by the spectrum from third quantisation lay the foundation for the three following inter-related works, which focus on the dissipative dynamics of cavity-boson systems.

Chapter 7 focuses on a special parameter regime of the cavity-boson system, where the cavity is blue detuned from the driving laser. In this regime, system manifests time periodicity which is not simply defined by harmonic multiples of underlying energy scales. This phenomenon is also referred to as a “time crystal”, and has been shown to be prohibited in a static system. This work also provides the first example confirming our previous analysis that driven-dissipative systems do not necessarily always explore the low-energy sector of the system. Our results are supported by an analytical mapping of the continuum system to a dynamical system on a two-parameter phase space, and confirmed by a numerical study by MCTDH-X. This work has been a collaboration with P. Mognini and A.U.J. Lode.

Chapters 8 and 9 then investigate a more complex cavity-boson system composed by spinor bosons and driven by two laser pumps. With a collaboration with T. Esslinger’s group, we show from theoretical and experimental perspectives, respectively, that drive and dissipation are able to stabilise collective states with thermodynamically high energy. Specifically, in Chapter 8, through a mapping of the bosonic system to a V-shaped three-level system, we explore a family of dissipatively stabilised continuously multistable states featured by dark-state behaviours. In Chapter 9, we show that this same mechanism

observed in the theoretical model should eventually lead to a cascade to non-Hermitian hopping dynamics in the continuum system. Our results based on MCTDH-X simulations are again quantitatively consistent with experimental results.

Thereafter, Part III investigates the strongly-correlated electronic system of superconductor using the same lens of Keldysh and Floquet formalisms developed in Part II. We will first derive the corresponding gap equation in Chapter 10 using a mean-field Hubbard-Stratonovich transformation. In comparison to conventional results, our gap equation is particularly able to capture the relative rotation between the superconductor and the thermal bath providing temperature. With a more thorough investigation into the spectral function and response function under driving in Chapter 11, we are able to propose a new scheme for enhancing superconductivity at finite temperature comparable to the critical temperature of the static superconductor. This work involves a collaboration with A. Ramirez.

Finally, in [Conclusions and Outlook](#), we discuss how the findings and understandings of quantum driven-dissipative effects gained from this thesis can potentially be applied in a wider realm of the quantum many-body world.

1.3 MCTDH-X

The multiconfigurational time-dependent Hartree method for indistinguishable particles [83–85] implemented by the program [MCTDH-X](#) [RL6, RL11] is a numerical tool designed for solving a bosonic or fermionic many-body Schrödinger equation. It is used throughout the thesis for investigating the cavity-boson systems in the continuum. During the course of my doctoral research, I participated in the development of different models and functionalities of the program, promoted it by composing a tutorial [Quantum Sci. Technol.](#) **5**, 024004 (2020) [RL6] together with my collaborators for guiding potential users of the package, and finally proposed a scheme for improving experimental data extraction and classification by applying it with artificial neural network [Phys. Rev. A](#) **104**, L041301 (2021) [RL7] (repository see Ref. [RL12]). Before we dive into the main body of the thesis, we first briefly review the methodology and functionalities of MCTDH-X with a focus on bosonic systems.

1.3.1 Methodology

We consider a bosonic Hamiltonian consisting of one-body potential V and two-body interaction W , both of which can in principle be time-dependent ¹

$$\begin{aligned}
 H = & \int d\vec{x} \Psi^\dagger(\vec{x}) \left(-\frac{\nabla^2}{2m} + V(\vec{x}) \right) \Psi(\vec{x}) \\
 & + \int d\vec{x} W(\vec{x}, \vec{x}') \Psi^\dagger(\vec{x}) \Psi^\dagger(\vec{x}') \Psi(\vec{x}) \Psi(\vec{x}')
 \end{aligned} \tag{1.1}$$

MCTDH-X is able to solve the ground state of the Hamiltonian or propagate a quantum state under the Hamiltonian using a variational approach. Specifically, it uses an ansatz for the many-body state

$$\begin{aligned}
 |\Psi(t)\rangle &= \sum_{\vec{n}} C_{\vec{n}}(t) |\vec{n}, t\rangle \\
 |\vec{n}, t\rangle &= \prod_{k=1}^M \left[\frac{(b_k^\dagger(t))^{n_k}}{\sqrt{n_k!}} \right] |\text{vac}\rangle,
 \end{aligned} \tag{1.2}$$

where N is the number of particles, M is the number of single-particle wavefunctions (called “orbitals”) and $\vec{n} = (n_1, n_2, \dots, n_M)$ gives the number of atoms in each orbital with constraint $\sum_{k=1}^M n_k = N$. The creation operators b_k correspond to the orthonormal basis wavefunctions represented in the real space $\psi_k(\vec{x}; t)$, and are thus related to the many-body field operator as

$$\Psi^\dagger(\vec{x}; t) = \sum_{k=1}^M b_k^\dagger \psi_k^*(\vec{x}; t). \tag{1.3}$$

We emphasise that the time dependence lies in both the coefficients $C_{\vec{n}}(t)$ and the orbitals $\psi_k(\vec{x}; t)$, allowing a much larger degree of freedom during the variational propagation process. This is particularly true in comparison to the conventional Hartree method where only the orbitals are variationally evolved, and full configuration interaction method where only the coefficients are variationally evolved. In MCTDH-X, the evolution of the coefficients and the orbitals follow the MCTDH-X equations of motion, which are linear partial differential equations obtained from Euler-Lagrange equations of the system, and are described in detail in Refs. [83–85].

The most important parameter controlling the numerical accuracy and complexity of MCTDH-X simulations is the number of orbitals M [84–86]. The macroscopic occupation of more than one orbital is called fragmentation [87], and it is fundamentally related to many-body effects like correlations and

¹Throughout this thesis, the reduced Planck constant \hbar and the Boltzmann constant k_B are generally suppressed, except in the experimentally relevant Chapters 4 and 9.

fluctuations. With a single orbital $M = 1$, the Gross-Pitaevskii mean-field limit is reproduced, where all many-body effects are lost. On the contrary limit $M \rightarrow \infty$, MCTDH-X produces numerically exact results for the many-body Schrödinger equation. However, this limit cannot be reached in practice because the computational complexity scale as $\binom{M+N+1}{M}$. It is thus important to choose the correct M for simulations, which can be achieved for example by gradually increasing M until convergence. Furthermore, M can also be chosen empirically according to the understanding of the system. For instance, Mott insulation can be satisfactorily captured when there are at least as many orbitals as lattice sites [RL1, RL2, 88], whereas a fermionic gas intrinsically requires $M \geq N$ due to its statistical property. There are even systems inherently requiring an infinite number of orbitals. This includes the vicinity of a critical point (cf. Fig. 6.3(b)) and Tonks-Girardeau gas [89].

We finally comment on the capability of MCTDH-X capturing out-of-equilibrium behaviours of the driven-dissipative system. Inherently, MCTDH-X solves the Schrödinger equation of a static, non-dissipative system, which are not necessarily valid for driven-dissipative systems as to be discussed in Section 6.1.3. Nevertheless, it is feasible to implement the cavity dissipation as a Lindbladian in the cavity equation of motion, which provides us with access to a large subset of crucial driven-dissipative dynamics in cavity-BEC systems.

1.3.2 Observables

After solving the many-body wavefunction of the system, features of the quantum state can be analysed by extracting a collection of observables. We briefly summarise the main observables which are discussed throughout the thesis.

The most basic observables are the density distributions in the real and momentum spaces,

$$\begin{aligned}\rho(\vec{x}) &= \frac{1}{N} \langle \Psi^\dagger(\vec{x}) \Psi(\vec{x}) \rangle \\ \rho(\vec{k}) &= \frac{1}{N} \langle \Psi^\dagger(\vec{k}) \Psi(\vec{k}) \rangle.\end{aligned}\tag{1.4}$$

We remark that $\rho(\vec{x})$ is in most cases, but not always, insensitive to many-body effects and can be correctly captured by using $M = 1$ orbital in the Gross-Pitaevskii mean-field limit. On the contrary, $\rho(\vec{k})$ is highly sensitive to many-body effects. When $M = 1$ orbital is used, $\rho(\vec{k})$ is trivially the Fourier transform of $\rho(\vec{x})$. However, when a sufficient number of M is used, it will greatly reveal the many-body atomic correlations and fluctuations.

Besides the density distributions, the Glauber correlations functions can also be obtained [90]. Most importantly for this thesis are the one-body and two-body

Glauber correlation functions in the position space,

$$\begin{aligned} g^{(1)}(\vec{x}, \vec{x}') &= \frac{\rho^{(1)}(\vec{x}, \vec{x}')}{\sqrt{\rho^{(1)}(\vec{x}, \vec{x})\rho^{(1)}(\vec{x}', \vec{x}')}} \\ g^{(2)}(\vec{x}, \vec{x}') &= \frac{\rho^{(2)}(\vec{x}, \vec{x}')}{\rho^{(1)}(\vec{x}, \vec{x})\rho^{(1)}(\vec{x}', \vec{x}')} \end{aligned} \quad (1.5)$$

where

$$\begin{aligned} \rho^{(1)}(\vec{x}, \vec{x}') &= \frac{1}{N} \langle \Psi^\dagger(\vec{x}) \Psi(\vec{x}') \rangle \\ \rho^{(2)}(\vec{x}, \vec{x}') &= \frac{1}{N} \langle \Psi^\dagger(\vec{x}) \Psi^\dagger(\vec{x}') \Psi(\vec{x}) \Psi(\vec{x}') \rangle. \end{aligned} \quad (1.6)$$

These functions are useful for characterising many-body effects like Mott insulation. Particularly, coherence in the quantum state is signalled by $g^{(1)} = 1$, indicating that the density distribution can provide all information regarding to the quantum state.

Finally, the deviation of the quantum state from a Gross-Pitaevskii mean-field description, i.e. coherence, is called fragmentation. It can be described by the occupancy ρ_i of different natural orbitals ϕ_i , which are the eigenvalues and eigenvectors of the one-body reduced density matrix, respectively:

$$\rho^{(1)}(\vec{x}, \vec{x}') = \sum_{k=1}^M \rho_k \phi_k^*(\vec{x}') \phi_k(\vec{x}), \quad (1.7)$$

with the order $\rho_1 \geq \rho_2 \geq \dots \geq \rho_M$. A complementary index for measuring fragmentation is

$$\Delta_{\text{frag}} = \sum_{k=1}^N \rho_k^2. \quad (1.8)$$

Interestingly, Δ_{frag} can serve as an order parameter of numerical origin for physical phase transitions [91, 92]. A pure quantum state is coherent (fragmented) when $\rho_1 = 1$ and $\Delta_{\text{frag}} = 1$ ($\rho_1 < 1$ and $\Delta_{\text{frag}} < 1$).

1.3.3 Extraction of experimental data via machine learning

For completeness of the introduction to MCTDH-X, we also briefly introduce our toolkit: the Universal Neural-network Interface for Quantum Observable Readout from N -body wavefunctions (UNIQUORN) [RL7, RL12]. As a proof of concept, it trains an artificial neural network using data sets obtained from MCTDH-X simulations, and in principle can be used for improved extraction of experimental data.

As an example, we use it on many-body quantum phases of interacting bosons in a double-well potential. Depending on the shape of the double well, the boson can undergo a transition from a coherent state to a fragmented state, where bosons in the two wells are Mott insulating from each other. Using MCTDH-X, we are able to generate single-shot images, each of which is a single instantaneous “screenshot” of the many-body state. Numerically, it is a sample

$$s(\vec{x}) = \sum_{k=1}^N \delta(\vec{x} - \vec{x}_k), \quad (1.9)$$

where the collection of coordinates $(\vec{x}_1, \vec{x}_2, \dots, \vec{x}_N)$ is drawn randomly according to the distribution [93, 94]

$$P(\vec{x}_1, \vec{x}_2, \dots, \vec{x}_N) = |\Psi(\vec{x}_1, \vec{x}_2, \dots, \vec{x}_N)|^2. \quad (1.10)$$

These single-shot images naturally mimic the raw experimental data in ultracold-atom experiments obtained from, e.g. time-of-flight measurements, and thus serves as the input data of our neural network. On the other hand, MCTDH-X can also extract the density distributions, one-body and two-body correlation functions described above in a numerically exact way, which can then be used as labels of our neural network. For the current system of double wells, these observables can well distinguish between the coherent and fragmented phases.

We then feed our MCTDH-X generated data into a convolutional neural network of standard architecture, which consists of a sequence of convolutions and max-pooling filters for condensing our input data into the desired labels. Thereafter, we test our trained neural network using a new set of validation data, whose result is briefly summarised below. We find that the advantage of our MCTDH-X-based neural network method is twofold in comparison to conventional methods. On the one hand, conventionally density distributions and correlation functions can also be calculated from single-shot images using averaging method, e.g.

$$\begin{aligned} \rho(\vec{x}) &\approx \frac{1}{N_s} \sum_{k=1}^{N_s} s_k(\vec{x}), \\ \rho^{(2)}(\vec{x}, \vec{x}') &\approx \frac{1}{N_s} \sum_{k=1}^{N_s} s_k(\vec{x}) [s_k(\vec{x}) - \delta(\vec{x}, \vec{x}')], \end{aligned} \quad (1.11)$$

where N_s is the total number of single-shot images being used. This averaging method is feasible as long as the single-shot images and the desired observables lie in the same space, e.g. the real space or the momentum space. Notably,

1

in this case, the neural network is found to be able to reduce a loss function measuring deviation between the predicted results and the true label by a factor of 5, when, for example, $N_s = 100$ single-shot images are used. On the other hand, when the single-shot images and the desired observables are not lying in the same space, for example when predicting momentum-space density distributions from real-space single-shot images, an empirical formula does not exist. Strikingly, we also find that the neural network works reliably in this case, and indeed is able to fully capture the many-body effects in the quantum system.

In summary, neural-network-based observable extraction can be a highly promising method for improving the performance of standard measurements in ultracold-atom-based experiments. Importantly, it can drastically reduce the number of single-shot images and thereby the runtime of a costly experimental setup, in comparison to using the conventional averaging approach. Moreover, it can extract momentum-space observables from real-space single-shot images and vice versa without any tedious reconfiguration of the imaging setup and at a very high degree of accuracy. Our results thus herald the potential of neural networks to reliably and rapidly obtain even more information from ultracold-atom-based quantum simulators.

PART I

Cavity-boson systems as effectively static systems in a rotating frame

OUT-of-equilibrium systems subject to external driving is a versatile platform for achieving a large variety of quantum few-body and many-body phenomena. These include in particular quantum optical systems, which are subject to laser pumps at extremely high frequencies. To solve the dynamics of these driven systems with time-dependent Hamiltonian, the most straightforward and widely applied method is to look for a rotating frame where the system, more specifically its Hamiltonian, appears to be static. This yields the so-called effective stroboscopic Hamiltonian in the Floquet theory, which can be solved using conventional techniques for static systems.

Particularly in the case of quantum optical systems, the driving frequency is comparable to the atomic fine structure. Consequently, the co-rotating dynamics at a much lower energy scale becomes dominating. In the presence of dissipation, such dynamics can be systematically captured by the rotating wave approximated Hamiltonian in conjunction with the Lindblad form. This is conventionally implemented for practical calculations and fully captures the essential physics. These methods are conveniently used for investigating many-body phases of a cavity-boson system, where the use of Floquet theory overcomplicates the problem without bringing more profound insights. In this Part, we focus on a wide range of phenomena qualitatively similar to their counterparts in static systems. They seem to suggest the full equivalence, up to a few caveats, between driven systems and their static counterparts described by the stroboscopic Hamiltonian.

2 | Floquet theory and Lindblad form

Originality declaration: This Chapter is a review on established results in literature on the Floquet theory [13, 16, 17] and the Lindblad form [61–63]. It sets the background for a later discussion on the mechanism of driven-dissipative effects in Chapters 5 and 6.

2.1 Floquet theory for periodically driven quantum systems

Recently, time periodicity in quantum many-body systems becomes a focus of research, both naturally in quantum optical systems and also in condensed matter systems. Quantum systems with periodic driving can be solved using the Floquet theory [13], which is the counterpart, in fact the predecessor, of the much-better-known Bloch theory in the time domain. The Floquet theory provides a systematic way for searching for an effective stroboscopic Hamiltonian, particularly for single-particle systems without many-body interaction. This Hamiltonian removes all explicit time dependence of the problem, and can thus be solved as a regular static Hamiltonian. This methodology is later re-expressed by Shirley as a temporal tight-binding model, gaining a mathematically succinct form useful for more complex calculations for many-body systems.

We will first briefly review the Shirley-Floquet formalism for periodically driven quantum systems in Section 2.1.1, and later apply it to quantum optical systems in Section 2.1.2, showing another perspective of the rotating wave approximation.

2.1.1 The Shirley-Floquet formalism

For a Schrödinger equation

$$[H(t) - i\partial_t]\Psi(t) = 0 \quad (2.1)$$

with time-periodic Hamiltonian

$$H(t) = \sum_{\ell \in \mathbb{Z}} H_\ell e^{i\ell\Omega t}, \quad (2.2)$$

2.1. Floquet theory for periodically driven quantum systems

the Floquet theory provides a general ansatz for the wavefunction [13],

$$\Psi(t) = \psi(t)e^{i\epsilon_n t} \quad (2.3)$$

where $\psi(t + 2\pi/\Omega) = \psi(t)$ is periodic in time, and ϵ_n is the quasi-energy. Similar to the Bloch theory for spatial periodicity, the temporal periodicity also manifests itself as a redundancy in energy shift: quasi-energies with a difference of multiples of Ω are physically equivalent, corresponding to the same quantum state.

This structure of the Floquet systems motivated Shirley to propose a matrix formalism which captures the time periodicity systematically [16, 17]. As illustrated in Fig. 2.1, the Floquet space acts as an infinitely long one-dimensional lattice chain, where replicas of the static system H_0 sit on each lattice site, and the drive $H_{\ell \neq 0}$ with frequency $\ell\Omega$ acts as a hopping term between two sites which are ℓ sites apart. Correspondingly, we can construct the Shirley-Floquet Hamiltonian (see Appendix. A for detailed derivation)

$$\mathbb{H} = H_0 \mathbb{F}_0 + \sum_{\ell \in \mathbb{Z} \setminus \{0\}} H_\ell \mathbb{F}_\ell - \Omega \mathbb{N} \quad (2.4)$$

with $(\mathbb{F}_\ell)_{m,n} = \delta_{m,n-\ell}$ and $\mathbb{N}_{m,n} = i\delta_{m,n}$ matrices in the Floquet space with infinite dimension. Examples of these matrices are as follows:

$$\mathbb{F}_1 = \begin{pmatrix} \vdots & \vdots & \vdots & \vdots & \vdots & \vdots \\ \dots & 0 & 1 & 0 & 0 & 0 & \dots \\ \dots & 0 & 0 & 1 & 0 & 0 & \dots \\ \dots & 0 & 0 & 0 & 1 & 0 & \dots \\ \dots & 0 & 0 & 0 & 0 & 1 & \dots \\ \dots & 0 & 0 & 0 & 0 & 0 & \dots \\ \vdots & \vdots & \vdots & \vdots & \vdots & \vdots & \vdots \end{pmatrix}, \quad \mathbb{F}_2 = \begin{pmatrix} \vdots & \vdots & \vdots & \vdots & \vdots \\ \dots & 0 & 0 & 1 & 0 & 0 & \dots \\ \dots & 0 & 0 & 0 & 1 & 0 & \dots \\ \dots & 0 & 0 & 0 & 0 & 1 & \dots \\ \dots & 0 & 0 & 0 & 0 & 0 & \dots \\ \dots & 0 & 0 & 0 & 0 & 0 & \dots \\ \vdots & \vdots & \vdots & \vdots & \vdots & \vdots & \vdots \end{pmatrix},$$

$$\mathbb{F}_{-1} = \begin{pmatrix} \vdots & \vdots & \vdots & \vdots & \vdots \\ \dots & 0 & 0 & 0 & 0 & 0 & \dots \\ \dots & 1 & 0 & 0 & 0 & 0 & \dots \\ \dots & 0 & 1 & 0 & 0 & 0 & \dots \\ \dots & 0 & 0 & 1 & 0 & 0 & \dots \\ \dots & 0 & 0 & 0 & 1 & 0 & \dots \\ \vdots & \vdots & \vdots & \vdots & \vdots & \vdots & \vdots \end{pmatrix}, \quad \mathbb{N} = \begin{pmatrix} \vdots & \vdots & \vdots & \vdots & \vdots \\ \dots & -2 & 0 & 0 & 0 & 0 & \dots \\ \dots & 0 & -1 & 0 & 0 & 0 & \dots \\ \dots & 0 & 0 & 0 & 0 & 0 & \dots \\ \dots & 0 & 0 & 0 & 1 & 0 & \dots \\ \dots & 0 & 0 & 0 & 0 & 2 & \dots \\ \vdots & \vdots & \vdots & \vdots & \vdots & \vdots & \vdots \end{pmatrix}. \quad (2.5)$$

The first two terms of \mathbb{H} correspond to $H(t)$ as $e^{i\ell\Omega t} \mapsto \mathbb{F}_\ell$, whereas the third term to the time derivative as $i\partial_t \mapsto \Omega \mathbb{N}$. Notably, this formalism eliminates the explicit time dependence of the problem, providing an effectively static Hamiltonian \mathbb{H} , whose solution can be found using standard diagonalisation techniques.

The temporally periodic systems share two important notions with the spatially periodic systems: the Wigner functions and the Brillouin zones, which are discussed in detail below.

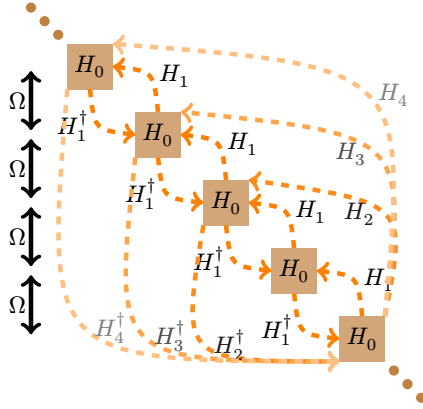


Figure 2.1: Illustration of the Floquet structure. Each brown square is a replica of the static system H_0 , whose energies are separated by the driving frequency Ω from each other. These replicas act like lattice sites in an infinite one-dimensional lattice. The driving at the n -multiple harmonics $n\Omega$, denoted by H_n , connects n -th neighbouring replicas, acting like hopping terms between them.

It can be immediately recognised that the Shirley-Floquet Hamiltonian constructed above contains repeated information. Each row of \mathbb{H} is essentially a complete replica for the driven system $H(t)$, containing the information from each and every H_ℓ . This redundancy in the construction indicates that every entry of the matrix with indices sharing the same $\ell = i - j$, e.g. the pair $\mathbb{H}_{0,0}$ and $\mathbb{H}_{2,2}$, as well as the pair $\mathbb{H}_{1,2}$ and $\mathbb{H}_{5,6}$, are physically equivalent. As a result, it allows to introduce the temporal Wigner representation [81, 95, 96]

$$\mathbb{A}_\ell(\omega) \equiv \mathbb{A}_{i,i+\ell}(\omega - (i + \ell/2)\Omega), \quad (2.6)$$

where \mathbb{A} represents any equal-time or two-time observable of the system, particularly including the Hamiltonian \mathbb{H} and the Green function \mathbb{G} . These families of matrix elements in \mathbb{H} and \mathbb{G} also referred to as the ℓ -th Wigner component will be useful later in Part III.

The eigenvalues of the Shirley-Floquet Hamiltonian \mathbb{H} are called the quasi-energies ϵ_n . Similar to their spatial counterparts, quasi-momenta, they repeat themselves in a periodicity of Ω . It is thus possible to restrict oneself to the quasi-energies in the first temporal Brillouin zone $\epsilon_n \in (-\Omega/2, \Omega/2]$ for a full spectrum of the system. For the Green function in Wigner representation $\mathbb{G}_\ell(\omega)$, this implies that the positions of its poles are periodic in ω , but notably

2.1. Floquet theory for periodically driven quantum systems

the function itself, i.e. its values at the poles, are not,

$$\begin{aligned} \mathbb{G}_\ell(\omega) &\neq \mathbb{G}_\ell(\omega + \Omega) \\ \forall \omega_0, n \in \mathbb{Z} \quad \mathbb{G}_\ell^{-1}(\omega_0) = 0 &\implies \mathbb{G}_\ell^{-1}(\omega_0 + n\Omega) = 0. \end{aligned} \quad (2.7)$$

In most scenarios, rich phenomena induced by the driving can already be captured by the stroboscopic Hamiltonian of the system, which is effective static, and can be obtained by block-diagonalising the Shirley-Floquet matrix in the Floquet space. This yields a Shirley-Floquet Hamiltonian describing an effectively static system $\mathbb{H}' = H'_0 \mathbb{F}_0 - \Omega \mathbb{N}$, where H'_0 is the stroboscopic Hamiltonian. This transformation of the time-dependent reference frame can generally be described using the van Vleck transformation [17, 97–99], with ansatz

$$\mathbb{P} = \exp \left(\sum_{\ell \in \mathbb{Z}} S_\ell \mathbb{F}_\ell \right), \quad (2.8)$$

where S_ℓ are matrices spanning in the space of H_ℓ . Nevertheless, the infinite dimensionality of the Floquet space prohibits a general algorithm for such diagonalisation. In fact, even the feasibility of such diagonalisation is often not guaranteed, leading to phenomena like heating. However, when the driving frequency constitutes the sole highest energy scale in the problem, there exists a standardised procedure based on the ansatz above, called the Magnus expansion. This facilitates driving systems as described by their stroboscopic Hamiltonians to be the main focus of the present-day investigations in quantum optical and condensed matter physics.

2.1.2 Application: Rotating wave approximation in quantum optical systems

In quantum optics, the system is usually driven by a laser pump which is monochromatic and linearly polarised. The interaction between such pumping laser and matter can usually be described using the dipole approximation. Considering the two energy levels of the matter $|e\rangle$ and $|g\rangle$ whose energy difference ω_0 is in close resonance with the driving frequency, we can write down the Hamiltonian of the system under the basis $(|e\rangle, |g\rangle)^T$ as

$$H(t) = \frac{\omega_0}{2} \sigma_z + \lambda \cos(\Omega_p t) \sigma_x, \quad (2.9)$$

with energy scales $\omega_0 \approx \Omega_p \gg \lambda \approx \omega_0 - \Omega_p \equiv \Delta_0$, which can be expressed using Shirley-Floquet matrices as

$$\mathbb{H} = \frac{\omega_0}{2} \sigma_z \mathbb{F}_0 + \frac{\lambda}{2} \sigma_x (\mathbb{F}_1 + \mathbb{F}_{-1}) - \Omega_p \mathbb{N}. \quad (2.10)$$

For our narrative, we split the second term into two,

$$\mathbb{H} = \frac{\omega_0}{2} \sigma_z \mathbb{F}_0 + \frac{\lambda_1}{2} (\sigma_+ \mathbb{F}_1 + \sigma_- \mathbb{F}_{-1}) + \frac{\lambda_2}{2} (\sigma_- \mathbb{F}_1 + \sigma_+ \mathbb{F}_{-1}) - \Omega_p \mathbb{N}, \quad (2.11)$$

where $\sigma_{\pm} = (\sigma_x \pm i\sigma_y)/2$, and we later set $\lambda_1 = \lambda_2$.

This model cannot be solved exactly and requires an approximated solution. The two driving terms λ_1 and λ_2 connects neighbouring ‘‘Floquet lattice sites’’. Interestingly, once the Hamiltonian is written down in matrix form as

$$\mathbb{H} = \begin{pmatrix} \ddots & & & & & & & & & & \\ \cdots & \frac{1}{2}\omega_0 + \Omega_p & 0 & 0 & \frac{1}{2}\lambda_2 & 0 & 0 & 0 & \cdots & & \\ \cdots & 0 & -\frac{1}{2}\omega_0 + \Omega_p & \frac{1}{2}\lambda_1 & 0 & 0 & 0 & 0 & \cdots & & \\ \cdots & 0 & \frac{1}{2}\lambda_1 & \frac{1}{2}\omega_0 & 0 & 0 & 0 & \frac{1}{2}\lambda_2 & \cdots & & \\ \cdots & \frac{1}{2}\lambda_2 & 0 & 0 & -\frac{1}{2}\omega_0 & \frac{1}{2}\lambda_1 & 0 & 0 & \cdots & & \\ \cdots & 0 & 0 & 0 & \frac{1}{2}\lambda_1 & \frac{1}{2}\omega_0 - \Omega_p & 0 & 0 & \cdots & & \\ \cdots & 0 & 0 & \frac{1}{2}\lambda_2 & 0 & 0 & 0 & -\frac{1}{2}\omega_0 - \Omega_p & \cdots & & \\ \vdots & \vdots & \vdots & \vdots & \vdots & \vdots & \vdots & \vdots & \ddots & & \end{pmatrix}, \quad (2.12)$$

where the dashed lines separate different Floquet sectors, it is easy to observe that λ_1 (λ_2) couples two energy levels from two different ‘‘Floquet lattice sites’’, but with a relatively small (large) energy difference $\omega_0 - \Omega_p$ ($\omega_0 + \Omega_p$). In the energy scale of λ , this allows us to truncate the infinite-dimensional Shirley matrix into the local 2×2 matrices, which are illustrated in the formula above by the green and red blocks. We have thus found an effective static system for the driven system,

$$H_{\text{eff}} = \frac{\omega_0 - \Omega_p}{2} \sigma_z + \frac{\lambda}{2} \sigma_x. \quad (2.13)$$

Our approximation above is essentially the *rotating wave approximation* commonly used in quantum optics. The two terms, λ_1 and λ_2 are the so-called co-rotating and counter-rotating terms, which are kept and discarded in the approximation, respectively. Such an approximation leads to a *Rabi model*, whose dynamical evolution can be solved exactly, i.e., there exists an exactly solvable rotating frame where the Rabi model appears static. An analytical solution and discussion of the Rabi model using the Shirley-Floquet formalism can be found in Appendix A.4. Indeed, the Rabi model can be rotated into a static model by the rotation $P = e^{-i\Omega_p t \sigma_z/2} = \frac{1}{2} \sigma_0 (e^{i\Omega_p t/2} + e^{-i\Omega_p t/2}) - \frac{1}{2} \sigma_z (e^{i\Omega_p t/2} - e^{-i\Omega_p t/2})$, which in the Shirley-Floquet formalism corresponds to

$$\mathbb{P} = \frac{1}{2} \sigma_0 (\mathbb{F}_1 + \mathbb{F}_{-1}) - \frac{1}{2} \sigma_z (\mathbb{F}_1 - \mathbb{F}_{-1}). \quad (2.14)$$

2.2. Lindblad form for dissipation

In reality, the higher-energy $|e\rangle$ mode of the atoms is usually eliminated adiabatically, leaving all the dynamics of the system in the $|g\rangle$ mode. Thus, effectively for the ground mode, the rotation operator reads

$$\mathbb{P} = \mathbb{F}_1. \quad (2.15)$$

This discussion provides the essential background for the cavity-boson system discussed in this thesis.

2.2 Lindblad form for dissipation

The dissipation provides a channel for energy leakage. For instance, in cavity-boson systems, this naturally arises from the transmittance of the cavity mirrors. The dissipation channel is captured by coupling the system to a reservoir of harmonic oscillators called “bath”,

$$H = \underbrace{\sum_i \epsilon_i c_i^\dagger c_i}_{H_{\text{system}}} + \underbrace{\sum_j \xi_j b_j^\dagger b_j}_{H_{\text{bath}}} + \underbrace{\sum_i \gamma_{ij} (c_i^\dagger b_j + b_j^\dagger c_i)}_{H_{\text{coupling}}}. \quad (2.16)$$

In order to understand how the coupling to the bath affects the system, a straightforward method is using the Born-Markov approximation and rotating-wave approximation to obtain the Lindbladian.

The Born approximation assumes a weak coupling to the bath, such that not only the density matrix of the system-bath ensemble can be written as a product, but the bath also always remains thermal and unaffected by the system over time,

$$\rho_{\text{sys-bath}}(t) = \rho_{\text{system}}(t) \otimes \rho_{\text{bath}}, \quad (2.17)$$

with $\rho_{\text{bath}} \propto \exp(-\beta H_{\text{bath}})$. Meanwhile, Markov approximation assumes that the bath is Markovian, or has no memory. This can be described by a rapid decay of time correlations in the bath $\langle b_j^\dagger(t) b_j(t') \rangle = \delta(t-t')$, which corresponds to a constant spectral density of bath in frequency space

$$\Sigma(\omega) = \Sigma_0, \quad (2.18)$$

or in other words, it is equally possible to find a harmonic oscillator with any frequency. Finally, the bath is treated by rotating-wave approximation, because it is assumed to be rotating with a high frequency in comparison to its temperature $\Omega \gg T$ [100, 101].

With these three approximations, the coupling to the bath can be effectively treated by the Lindbladian with jump operator L_i . With this, the dynamical

evolutions of the system is governed in the Schrödinger picture by the master equation [61–63]¹

$$\partial_t \rho = -i[H, \rho] + \underbrace{\sum_i \kappa_i \left(L_i \rho L_i^\dagger - \frac{1}{2} L_i^\dagger L_i \rho - \frac{1}{2} \rho L_i^\dagger L_i \right)}_{=\mathcal{L}\rho, \text{ Liouvillian super-operator}}, \quad (2.19)$$

and in the Heisenberg picture by the equations of motion for observables

$$\partial_t O = -i[O, H] - \sum_i \kappa_i \left(L_i^\dagger O L_i - \frac{1}{2} L_i^\dagger L_i O - \frac{1}{2} O L_i^\dagger L_i \right). \quad (2.20)$$

In cavity-boson systems, the jump operator is usually given by the annihilation operator of the cavity field $L_1 = a$: The photons leak out of the cavity mirror without any means of returning.

2.3 Conclusions

In this Chapter, we have discussed two most important ingredients of a quantum optical system with high-frequency driving: the system and the dissipation. Specifically, the high driving frequency allows us to perform a rotating wave approximation which gives an effective static Hamiltonian for the system, as well as a simple description via Lindblad form for the dissipation. In the rest of Part I, this formalism will be implemented on the cavity-boson systems, capturing quantitative dissipative effects in the many-body systems. The brief review on the formalism in this Chapter also lays the first bricks for a thorough investigation of qualitative driven-dissipative effects and their mechanisms in Part II.

¹Throughout this thesis, we use the partial derivative of time ∂_t consistently instead of the full derivative d/dt for clarity of notation, even though in some cases the operators, e.g. ρ or O , are indeed purely functions of time.

3 | Introduction to the cavity-BEC system

Originality declaration: This Chapter is a review on established results in literature regarding the cavity-BEC system [102, 103] and its mapping to the Dicke model [104]. The narrative is chosen to with emphasis on features insensitive to the driven-dissipative nature of the system, setting the background and contrast for elaborating intrinsic driven-dissipative effects in Parts II and III.

3.1 Introduction to the Dicke model

After a general introduction to the driven systems and the dissipative systems, we proceed to introduce one of the most important quantum many-body systems in this thesis, the coupled systems of light and matter. Specifically, in Parts I and II, we mainly focus on various coupled systems of cavity and bosons, which can in general be mapped to a family of Dicke-like models. The simplicity and richness of the Dicke model, particularly in conjunction with the Lindblad form, enable us to investigate different aspects of many-body phases and transitions in the presence of drive and dissipation.

The Dicke model proposed in 1954 [105],

$$H = \omega_c a^\dagger a + \omega_0 \sum_{i=1}^N |1_i\rangle\langle 1_i| + \frac{\lambda}{\sqrt{N}} (a + a^\dagger) \sum_{i=1}^N (|0_i\rangle\langle 1_i| + |1_i\rangle\langle 0_i|), \quad (3.1)$$

describes the coupled system of an ensemble of N two-level atoms $|\mu_i\rangle\langle \nu_i|$ to a bosonic field a . The atomic ensemble can be viewed collectively as a pseudo-spin- $N/2$,

$$\sum_{i=1}^N |1_i\rangle\langle 1_i| \rightarrow J_z + 1, \quad \sum_{i=1}^N (|0_i\rangle\langle 1_i| + |1_i\rangle\langle 0_i|) \rightarrow 2J_x, \quad (3.2)$$

where J_i are the pseudo-spin operator, and the commutation relation is preserved by the mapping. Because spin- $N/2$ is one representation of the $\mathfrak{su}(2)$ Lie algebra, the atoms live in an underlying $SU(2)$ space.

One of the most attractive features of this model is its superradiant phase transition [106–108]. Fundamentally, this is related to the fact that the coupling

3.1. Introduction to the Dicke model

becomes comparable to the cavity and atomic energy scales. As a result, the counter-rotating dynamics described by $a|0_i\rangle\langle 1_i| + a^\dagger|1_i\rangle\langle 0_i|$ becomes as important as the co-rotating dynamics $a^\dagger|0_i\rangle\langle 1_i| + a|1_i\rangle\langle 0_i|$. This prohibits an omission of the counter-rotating terms, and a reduction of the model to the Rabi model. At the critical point of the Dicke model,

$$\lambda_c = \frac{1}{2}\sqrt{\omega_0\omega_c}, \quad (3.3)$$

the Z_2 symmetry of the system

$$a \mapsto -a, \quad J_x \mapsto -J_x, \quad (3.4)$$

is spontaneously broken. The system then enters the superradiant phase, where the number of excited bosonic field scales proportionally to N , i.e., $|\langle a \rangle|^2 \sim \mathcal{O}(N)$.

The potential access to superradiant phenomena intrigues a lasting attempt for experimental realisation of the Dicke model in the five decades after its proposal. As a straightforward generalisation of the Jaynes-Cummings model for a large number of atoms, it is thus conventionally expected that its experimental realisation can be implemented by coupling the atomic fine structure to light. However, despite the enduring interest, this model and particularly the superradiant phase can never be realised in experimentally relevant setups for a long time.

In fact, such experimental realisation is hindered by two obstacles. The first one is technical. The atomic fine structure usually corresponds to a large energy scale, which thus requires correspondingly a large coupling between the light and the atoms. The second one is more fundamental, and eventually leads to the no-go theorem of the Dicke model [109]. The coupling between atoms and light can be described using the minimal coupling, where the atomic momentum is coupled to the vector potential. This will always introduce an extra diamagnetic term which describes the magnetic field,

$$\begin{aligned} H_{\text{atom-light}} = & \omega_c a^\dagger a + \omega_0 \sum_{i=1}^N |1_i\rangle\langle 1_i| \\ & + \frac{\lambda}{\sqrt{N}} (a + a^\dagger) \sum_{i=1}^N (|0_i\rangle\langle 1_i| + |1_i\rangle\langle 0_i|) + \frac{D}{N} (a + a^\dagger)^2. \end{aligned} \quad (3.5)$$

Unfortunately, it can be shown that the coefficient of the diamagnetic term always dominates as $D \geq \lambda^2/\omega_0$ using a Thomas-Reiche-Kuhn sum rule. As a result, the diamagnetic term always counteracts the superradiant instability, and thus prohibits the system from transitioning into the superradiant phase.

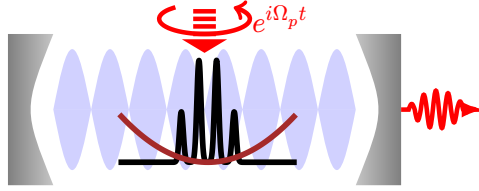


Figure 3.1: Schematics of the cavity-BEC system

In order to bypass the no-go theorem, it has been theoretically proposed to make use of the atomic motional degrees of freedom [104]. Specifically, a uniformly distributed atomic state and a standing-wave atomic state are used as the two atomic levels. With this construction, the diamagnetic term is no longer subject to the sum rule constraint detrimental to superradiance. From the perspective of this thesis, all these experimental realisations of the Dicke model are achieved with a rotating-wave approximated Hamiltonian in the rotating frame. They are thereby fundamentally driven-dissipative, and provide us with a versatile platform for investigating the relevant dynamics. In the following Sections, we will discuss in detail the cavity-BEC system and its mapping to the Dicke model, and give a first impression on the driven-dissipative effects in these systems.

3.2 The experimental setup and its Hamiltonian

The cavity-boson system, consisting of a Bose-Einstein condensate (BEC) whose motional degree of freedom is coupled to a high-finesse optical cavity (schematics see Fig. 3.1), serves as a versatile platform for quantum simulation due to its easy controllability in comparison to traditional condensed matter systems. It was the first experimental realisation of the Dicke model [102], manifesting the superradiant transition when the coupling between the atoms and the cavity becomes strong enough.

For the purpose of this thesis, it also serves as a platform to explore out-of-equilibrium phases of matter, both within and beyond the description of stroboscopic Hamiltonian. In this Section, we will focus on the original setup proposed in Ref. [104] and realised in Zürich [102] and Hamburg [103], which possesses a variety of features insensitive to the driven-dissipative nature. The many-body Hamiltonian of the effectively two-dimensional system can be writ-

3.2. The experimental setup and its Hamiltonian

ten as [110]

$$\begin{aligned}
 H = \int d\mathbf{x} \Psi^\dagger(\mathbf{x}) \left\{ -\frac{\nabla^2}{2m} + \frac{g}{2} \Psi^\dagger(\mathbf{x}) \Psi(\mathbf{x}) + V_{\text{trap}}(\mathbf{x}) + \underbrace{\eta^2/U_0}_{=E_p} \cos^2(k_c y) \right\} \Psi(\mathbf{x}) \\
 + U_0 a^\dagger a \int d\mathbf{x} \Psi^\dagger(\mathbf{x}) \Psi(\mathbf{x}) \cos^2(k_c x) \\
 + \eta(a + a^\dagger) \int d\mathbf{x} \Psi^\dagger(\mathbf{x}) \Psi(\mathbf{x}) \cos(k_c x) \cos(k_c y) \\
 - \Delta_c a^\dagger a, \tag{3.6}
 \end{aligned}$$

where $\Psi(\mathbf{x})$ is the many-body atomic operator.

To build the experimental system ¹, a BEC with repulsive contact interaction is prepared and trapped at the focus of the optical cavity. The preparation of the BEC is achieved using a series of cooling techniques, including a magneto-optical trap followed by a repumping, and a sub-Doppler cooling, which achieves temperatures of a few μK . During this procedure, it is loaded into a quadrupole-Ioffe trap, which is effectively the external harmonic trap $V_{\text{trap}} = \frac{m}{2}(\omega_x^2 x^2 + \omega_y^2 y^2)$. In the BEC, the bosons are almost all condensed into the same coherent state, which is localised in momentum space at zero momentum, while uniformly spread out in real space. The relatively weak repulsive interaction $g > 0$ between the bosons makes the BEC into a Thomas-Fermi cloud which is slightly fragmented, i.e., not entirely coherent. This is described by the first three terms in the first line of Eq. (3.6). Nevertheless, we note that experimentally the interaction strength cannot be easily tuned by Feshbach resonance for ⁸⁷Rb. The BEC is then pumped by an external laser along the y axis with strength E_p . In the rotating frame, this external laser is described by a standing wave $\cos^2(k_c y)$ in the last term of the first line. This effective description has taken into account that the dynamics between atomic fine structure ($\sim \text{GHz}$) is much faster than the atomic motional dynamics ($\sim \text{kHz}$), and can thus be adiabatically eliminated. The external laser provides photon which are virtually absorbed by the atoms and then emitted into the cavity. This Raman scattering process and its reverse process effectively mediates a coupling between the uniformly distributed BEC and a standing-wave atomic configuration through the cavity. It is described by the third line of the Hamiltonian, with $\cos(k_c x) \cos(k_c y)$ the interference pattern between the pumping field and the cavity field and η the effective coupling strength between the cavity and atomic fields. After the cavity gathers photons, it gains energy proportional to the number of photons as described by the fourth line of the Hamiltonian. Note that the energy gain per photon is given by the cavity

¹A detailed description of the experimental apparatus can be found in, e.g., Chapter 2 of the theses by Nishant Dogra [111] or Xiangliang Li [112].

detuning $\Delta_c \equiv \omega_c - \omega_p$ because we are working in the rotating frame defined by the driving frequency ω_p of the laser pump. More importantly, the cavity also induces an effective potential as described by the second line, where U_0 is the single atom light shift. The relation between the pump field, the cavity field, and their interference field is reflected in their amplitudes as $E_p = \eta^2/U_0$. Finally, we remind ourselves that Eq. (3.6) is a rotating-wave approximated Hamiltonian in the rotating frame. Therefore, the dissipation of the system can be captured by the equation of motion of the cavity field

$$\partial_t a = i[H, a] - \kappa a. \quad (3.7)$$

This corresponds to a jump operator of $L = \sqrt{\kappa}a$ in the Lindblad form, see Eq. (2.20).

As the cavity detuning Δ_c and cavity-atom coupling strength η vary, the system undergoes two phase transitions and thus goes through three different phases. These two phase transitions and the three accompanying steady state phases provide the first and most straightforward examples, where observables of the system are only quantitatively sensitive to the driven-dissipative nature, in the way that the dissipation renormalises the cavity-atom coupling by a factor of $(1 + \kappa^2/\omega_c^2)$ (see discussion in Section 3.3).

The system first experiences a superradiant transition to the self-organised phase, where the Z_2 symmetry of the system

$$x \mapsto x + \pi/k_c, \quad a \mapsto -a \quad (3.8)$$

is spontaneously broken, and the atoms self-organise into a checkerboard lattice whose lattice constant is defined by the cavity wavelength. The Z_2 symmetry spontaneously break into the even or odd configuration, where lattice sites at $(m\lambda_c/2, n\lambda_c/2)$ with even and odd values of $m + n$ are occupied, respectively. This spontaneous symmetry breaking has been confirmed by experimental observations [113]. As to be immediately discussed in details in the Section 3.3, this transition can be mapped to the superradiant transition of the Dicke model, which plays an essential role in this thesis.

The experimental realisation of the superradiant physics in the cavity-bosons system provides a precise yet versatile platform for the further realisation of more complex quantum many-body phenomena. Even with the first generation, a variety of intriguing physics are predicted and observed, including a roton mode softening consistent with the system's polariton excitation spectrum [114, 115], a driven-dissipative criticality fundamentally different from its quantum-phase-transition counterpart [116, 117], a hysteresis effects across the superradiant transition due to the intrinsic dissipative nature [118], a second phase transition within the self-organised phase from self-organised superfluid (SSF) phase to the self-organised Mott insulator (SMI) phase [119]. In this

3.3. Mapping to the driven-dissipative Dicke model

thesis, we will discuss many of these driven-dissipative in detail, and, step by step, appreciate their inherent non-triviality. For example, in the forthcoming Chapter, we will focus on the Mott transition, which unlike the superradiant transition, is intrinsically beyond the Gross-Pitaevskii mean-field description, and its phase boundary is hard to predict analytically.

Since then, more and more complex cavity-boson systems have also been proposed theoretically and realised experimentally, and they are able to simulate more many-body phenomena. When the spinor aspect of the bosons is explicitly exploited, various spin density wave states and spin texture states can be achieved [120–125]. Furthermore, the dissipative nature also leads to dynamics in time evolution, which are not achievable in non-driven systems. This includes in particular limit cycle behaviours [RL2, 126–129] and self-oscillating topological pumps as well [130, 131]. Finally, a combination of detuned laser pumps can synthesise a gauge field on top of the bosons, which will eventually lead to fractal structures like Hofstadter spectra [132, 133]. A more exhaustive list and discussion of these novel quantum many-body phenomena achieved by cavity-boson systems is reviewed in Ref. [66].

We conclude the Section by providing relevant parameters used in experiments. A typical setup uses rubidium-87 (^{87}Rb) atoms with mass $m = 1.44 \times 10^{-25}\text{kg}$ and a total number of roughly $N = 5 \times 10^4$. The cavity wavevector k_c is chosen with corresponding wavelength $\lambda_c = 795\text{nm}$, such that it is in close resonance with the fine structure of the ^{87}Rb , which is 780nm . This wavevector also corresponds to a recoil frequency of $\omega_R = \hbar k_c^2/2m = 2\pi \times 3.55\text{kHz}$. Other system parameters taken from the Hamburg experimental setup are typically given as follows: $U_0 = -2\pi \times 0.36\text{Hz}$, $0 > \Delta_c > -2\pi \times 40\text{kHz}$, $\kappa = 2\pi \times 4.45\text{kHz}$, $\omega_x = 202\text{Hz}$, $\eta^2/U_0 < 15\omega_R$.

3.3 Mapping to the driven-dissipative Dicke model

The phase transition to the superradiant, self-organised phase can also be understood from the perspective of the Dicke model [104]. The interference term of the cavity mediates a coupling between the zero momentum mode of the BEC $|0\rangle$ and the k_c momentum mode $|1\rangle$ of the BEC, which are given respectively as

$$\begin{aligned} |0\rangle &= |k_x = 0, k_y = 0\rangle \propto 1 \\ |1\rangle &= \frac{1}{2} (|k_c, k_c\rangle + |k_c, -k_c\rangle + |-k_c, k_c\rangle + |-k_c, -k_c\rangle) \\ &\propto \cos(k_c x) \cos(k_c y). \end{aligned} \quad (3.9)$$

The cavity-BEC system can indeed be mapped to the Dicke model Eq. (3.1), when it is projected into these two atomic modes. In the following, we compare

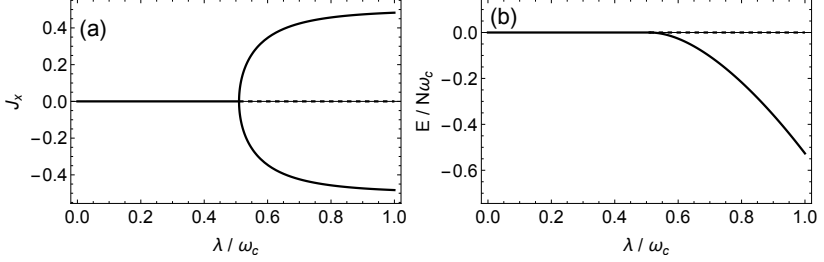


Figure 3.2: (a) The steady state solutions of the Dicke model, represented by the order parameter $\langle J_x \rangle$ as a function of λ . The solid lines are the stable steady states, while the dashed line is the unstable solution. (b) The energy E of the solutions as a function of λ . Parameters of the Dicke model are taken as $\omega_c = 1$, $\omega_0 = 1$, $\kappa = 0.2$.

the two Hamiltonians Eqs. (3.6) and (3.1) term by term.

In the first line of the cavity-boson Hamiltonian Eq. (3.6), the kinetic energy has expectation values of 0 and $D\omega_R = D\hbar k_c^2/2m$, respectively, in the $|0\rangle$ and $|1\rangle$ modes, while the external potential $\cos^2(k_c y)$ contributes no energy difference between the two states. When the contact interaction g and the external trap V_{trap} are neglected, it can be mapped to the $\omega_0 = D\omega_R$ term in Eq. (3.1). Here D is the dimensionality of the system. The second line of Eq. (3.6) is usually neglected, because usually the limit $N|U_0| \ll |\Delta_c|$ is considered. Nevertheless, this term can induce interesting dynamics in the regime $N|U_0| > |\Delta_c|$, which is studied in Ref. [134]. In the third line of the cavity-boson Hamiltonian, we observe that the atomic operator $\Theta = \int d\mathbf{x} \Psi^\dagger(\mathbf{x}) \Psi(\mathbf{x}) \cos(k_c x) \cos(k_c y)$ can be projected onto the $\{|0\rangle, |1\rangle\}$ representation as $\langle 0|\Theta|0\rangle = \langle 1|\Theta|1\rangle = 0$, $\langle 0|\Theta|1\rangle = 1$. Therefore, by identifying $\lambda = \eta\sqrt{N}$, we are able to map this line to the coupling term in the Dicke Hamiltonian. In contrast to the Rabi driving Eq. (2.9), the coupling term λ is now in the same scale as ω_c and ω_0 . This is considered as the ultra-strong coupling regime of quantum optics [135], where the omission of the counter-rotating term is invalidate, and enriched physics entails. It is also worth emphasizing that the cavity also mediates coupling between $|1\rangle$ and higher-momentum modes, which are not taken into account here only because of their relatively high energy. Not considering these modes should not bring fundamental differences to the physics of the system, particularly should not have quantitative influence on the superradiant/self-organisation phase boundary. Finally, the last line in Eq. (3.6) exactly describes the energy of the cavity field in Eq. (3.1), upon a sign change in the convention $\omega_c = -\Delta_c$.

The steady states of the driven-dissipative Dicke model can be found as the

3.3. Mapping to the driven-dissipative Dicke model

fixed points of the Liouvillian evolution according to Eq. (3.7). With a mean-field decoupling of the cavity and the atomic fields, this reads

$$\begin{aligned}
 0 &= \partial_t \langle a \rangle = -i[(\omega_c - i\kappa)\langle a \rangle + \frac{2\lambda}{\sqrt{N}}\langle J_x \rangle] \\
 0 &= \partial_t \langle J_x \rangle = -\omega_0 \langle J_y \rangle \\
 0 &= \partial_t \langle J_y \rangle = \omega_0 \langle J_x \rangle - \frac{4\lambda}{\sqrt{N}} \text{Re}\langle a \rangle \langle J_z \rangle \\
 0 &= \partial_t \langle J_z \rangle = \frac{4\lambda}{\sqrt{N}} \text{Re}\langle a \rangle \langle J_y \rangle.
 \end{aligned} \tag{3.10}$$

From the equations we can clearly see that $\langle J_y \rangle = 0$ and the cavity field $\langle a \rangle = \frac{2\lambda}{\sqrt{N}(-\omega_c + i\kappa)} \langle J_x \rangle$ is directly related to the atomic field. Further considering the constraint from the Casimir of the $\text{su}(2)$ algebra $\langle J_x \rangle^2 + \langle J_y \rangle^2 + \langle J_z \rangle^2 = N^2/4$, we can represent our solution solely by the atomic order parameter $\langle J_x \rangle$. This set of equations always has a trivial solution called the normal phase $\langle J_x \rangle = 0$, where the atoms are macroscopically occupying the ground mode $|0\rangle$, and the cavity field is not activated. Beyond the critical point $\lambda > \lambda_c$ where

$$\lambda_c = \frac{1}{2} \sqrt{\frac{\omega_0(\omega_c^2 + \kappa^2)}{\omega_c}}, \tag{3.11}$$

there is also a non-trivial solution called the superradiant phase $\langle J_x \rangle = \pm \frac{N}{2} \sqrt{1 - \lambda_c^4/\lambda^4}$, where the excited atomic mode $|1\rangle$ starts to become macroscopically occupied, and the cavity field is in a coherent state with $\langle a \rangle \neq 0$. The two superradiant solutions with opposite signs correspond to the spontaneously broken Z_2 symmetry. When compared to the normal solution, the superradiant solution always has a lower energy as long as it physically exists. Naively applying the energy minimisation argument, we obtain the correct conclusion that the superradiant phase is the steady state above the critical point, leading to the phase diagram of the driven-dissipative Dicke model as summarised in Fig. 3.2(a). Indeed, dissipation only quantitatively changes the phase boundary of the Dicke model.

We now elaborate on the energy minimisation argument. In static systems, the ground state can be found by minimisation of the system energy

$$E = \omega_c |\langle a \rangle|^2 - \omega_0 \sqrt{\frac{N^2}{4} - \langle J_x \rangle^2} + 4 \frac{\lambda}{\sqrt{N}} \text{Re}\langle a \rangle \langle J_x \rangle + \frac{1}{2} \omega_0 N. \tag{3.12}$$

It is tempting to apply a similar argument for the steady state of the driven-dissipative system. This seems promising at the first glance, since the superradiant solution indeed has lower energy in comparison to the normal solution

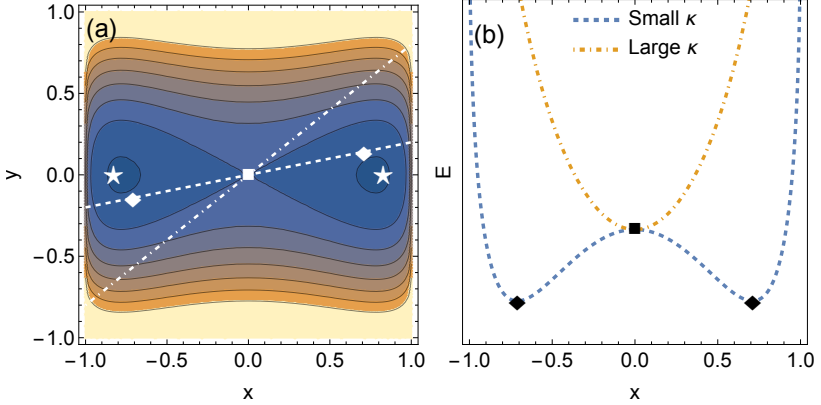


Figure 3.3: (a) The potential landscape $E(x, y)$ of a hypothetical Hamiltonian with a two-dimensional phase space of (x, y) , capturing the essence of the energy dependence of the steady states in the Dicke model. Darker colours indicate a deeper potential. The two stars are the ground states of the static system, or steady states of the non-dissipative $\kappa = 0$ driven system. The diamonds (square) are (is) the steady state(s) of a weakly (strongly) dissipative system, with the dashed (dash-dotted) line the sub-phase-space satisfying the corresponding bad-cavity constraint $\partial_t \langle a \rangle = 0$. (b) The energy landscape $E(x)$ within the aforementioned sub-phase-space for the weakly dissipative and strongly dissipative cases. The steady states indeed correspond to the minima of the respective potentials.

beyond the critical point, see Fig. 3.2(b). At a closer look, we remind ourselves that the introduction of dissipation κ changes neither the Hamiltonian, thus nor the potential landscape. However it does shift the steady state solution away from the static solution located at the minimum of the potential landscape, even eventually recovering the normal state solution for large enough dissipation. This implies that dissipation stabilises a state with high energy, as illustrated in the representative two-dimensional phase space in Fig. 3.3(a). It seems that the immediate invalidity of the energy minimisation scheme can be reconciled by further consideration. In the bad-cavity limit, the dissipation is the largest frequency scale in the system, and thus can be adiabatically eliminated by $\partial_t \langle a \rangle = 0$ [cf. Eq. (3.10)]. This extra constraint defines a subspace of the phase space schematically depicted by the dashed lines in Fig. 3.3(a), whose energy landscape is given by

$$E' = -\frac{4\lambda^2}{N} \frac{\omega_c}{\omega_c^2 + \kappa^2} \langle J_x \rangle^2 - \omega_0 \sqrt{\frac{N^2}{4} - \langle J_x \rangle^2} + \frac{1}{2} \omega_0 N, \quad (3.13)$$

and schematically depicted in Fig. 3.3(b). Within these subspaces, the steady

3.3. Mapping to the driven-dissipative Dicke model

3

state is indeed the one with the lowest energy. Particularly, if we start from a potential landscape in the superradiant phase with two symmetric minima [blue dashed line in Fig. 3.3(b)], and then increase the dissipation κ until Eq. (3.11) is satisfied, we will eventually go through a transition into the normal phase with only one minimum with vanishing cavity field [orange dash-dotted line in Fig. 3.3(b)].

Nevertheless, as we will clarify in Part II, this reconciliation does not generally work. In some cases, drive and dissipation even tends to stabilise the highest energy state. In fact, as we will argue later in Chapter 6, the superradiant phase transition is completely driven by exceptional point instability instead of energetic arguments, and the energy minimisation seen in the steady states of the Dicke model is purely a coincidence. The invalidity of this energy minimisation scheme is one of the main results of this thesis, highlighting the intrinsic differences between static and driven systems.

4 | Superradiant transition and Mott transition in a cavity-BEC system

As the first work discussed in this thesis, we present here a numerical investigation into the superradiant transition and the Mott transition in a red-detuned cavity-BEC system. As discussed in Chapter 3, these transitions manifest in the quantum optical system are only quantitatively sensitive to the driven-dissipative nature of the system via a renormalisation of the cavity-atom coupling by the dissipation. Particularly, we use numerical simulations to obtain the Mott transition boundary, which does not have an analytical solution, and quantitatively comparing the simulated boundary with the experimental measurement from Hamburg.

Originality declaration: This Chapter is adapted from our work [SciPost Phys. 11, 030 \(2021\) \[RL1\]](#), with some experimental details suppressed. The work was completed with supervision by R. Chitra, and collaboration on the numerical side with Paolo Molignini, Miriam Büttner, Axel Lode, and on the experimental side with Christoph Georges, Jens Klinder, Andreas Hemmerich and Hans Keßler.

4.1 Introduction

During the past decade, experimental and theoretical progress using quantum gases to realise models of solid state physics has made it possible to study many-body effects in isolated and highly controllable scenarios [136–138]. In particular, the interplay between light and matter creates a unique platform for the exploration of a multitude of exotic behaviours in quantum systems [102, 113, 115, 118, 119, 122, 139–143]. One topic receiving enduring interest is the many-body effects in ultracold atomic systems, particularly the coherence between particles in the superfluid phase and its loss in the Mott-insulator phase of a lattice system. The transition between these two phases was first realised by controlling an optical lattice potential in cold-atom systems in three [144] and two dimensions [145, 146], respectively. A similar transition

4.2. Experimental setup and measurement protocol

between a self-organised superfluid (SSF) phase and a self-organised Mott-insulator (SMI) phase can also be realised through a competition between the short-range interaction due to s -wave scattering between the atoms and the infinite-range interaction mediated by an optical cavity. The cavity-Bose-Einstein condensates (BEC) system can thus reproduce a quantum-optical version of the Bose-Hubbard model.

The SSF–SMI transition has been observed experimentally [119, 147] and investigated theoretically [RL2, RL8, 87, 148, 149], but hitherto a direct quantitative comparison between experiment and theory has not been presented because of the enormous computational effort required. However, this comparison is crucial for future applications like machine learning techniques, which have recently been applied to various physical systems [150–154], including ultracold atomic systems [RL7, 155, 156]. Because of their exact control of system parameters and their shorter time scale in data collection, quantitative numerical simulations provide complementary access to data for the training of neural networks for experimental systems.

In this work, we perform quantitative numerical simulations of the SSF–SMI phase transition, in particular of the phase diagram by employing MCTDH-X [RL6, 83–85, RL11, 157, 158], and validate the simulated results with the experimental one. MCTDH-X captures many-body effects beyond the Gross-Pitaevskii mean-field limit, including but not limited to the coherence between the atoms. In order to keep the computational complexity within a tractable range, we construct a simplification scheme for the simulations by exploiting the nature of the cavity-BEC system and the superfluid–Mott-insulator transition. This simplification scheme nevertheless retains the many-body essence of the system to a satisfactory degree, and quantitatively reproduces the phase boundary in agreement with the experiments in a wide parameter range. The comparison is summarised in the phase diagram in Fig. 4.2.

4.2 Experimental setup and measurement protocol

4.2.1 Cavity-BEC system and superfluid–Mott-insulator transition

The experimental system, as sketched in Fig. 4.1, consists of a laser-driven Bose-Einstein condensate (BEC) of $N_{3D} = 5.5 \times 10^4$ rubidium-87 (^{87}Rb) atoms dispersively coupled to a high-finesse optical cavity with strength Ω_g . The atoms are magnetically trapped in a three-dimensional harmonic potential with trapping frequencies $(\omega_x, \omega_y, \omega_z) = 2\pi \times (25.2, 202.2, 215.6)$ Hz. In the absence of external drive, the ensemble forms a Thomas-Fermi cloud with measured radii $(r_x, r_y, r_z) = (26.8, 3.3, 3.1)$ μm [Fig. 4.1(a)]. The three-dimensional atomic cloud is overlapped with the fundamental mode of the high-finesse

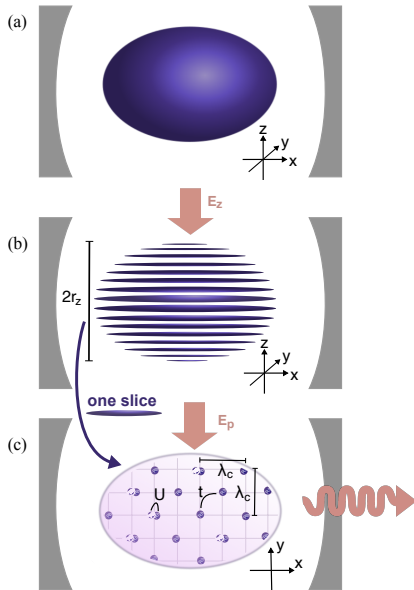


Figure 4.1: Sketch of the experimental system. The atoms are first prepared as (a) a three-dimensional BEC, and then cut into (b) two-dimensional slices by an external laser pump along z direction. (c) Due to the pumping laser along y direction and the interplay with the cavity, they finally self-organise into a checkerboard lattice with wavelength λ_c along both x and y directions. The onset of the self-organisation can be detected by the intracavity photons. After the checkerboard lattice is formed, the system can be mapped to a Bose-Hubbard model with tunnelling strength t and on-site interaction U .

optical cavity oriented along the x direction. The cavity resonance frequency ω_c and wave vector k_c correspond to a wavelength of $\lambda_c = 803$ nm and a recoil energy of $E_{\text{rec}} = \hbar^2 k_c^2 / 2m_{\text{Rb}} = \hbar \times 2\pi \times 3.55$ kHz. The cavity has a field decay rate of $\kappa = 2\pi \times 4.45$ kHz comparable to the recoil frequency, and therefore operates in the sub-recoil regime [159]. After the initial preparation, the atomic cloud is then loaded into an external optical lattice oriented along the z direction, which is given by $E_{\text{ext}}(z) = E_z \cos^2(2\pi z / \lambda_z)$ with wavelength $\lambda_z = 803$ nm and depth $E_z = 12.5 E_{\text{rec}}$. The strong external lattice suppresses tunnelling along the z direction and renders the system into effective two-dimensional slices spanned on the x - y plane, as illustrated in Fig. 4.1(b).

After preparing and loading the BEC into $E_{\text{ext}}(z)$, the ensemble is transversely pumped along the y direction by a laser with effective pump strength E_p and

4.2. Experimental setup and measurement protocol

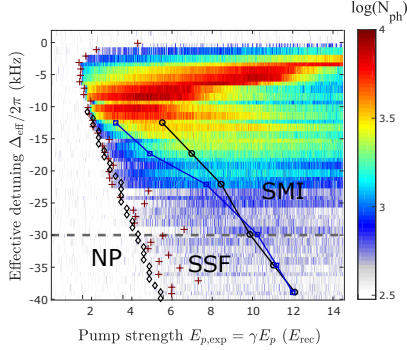


Figure 4.2: The steady-state phase diagram identifying the normal BEC phase (NP), the self-organised superfluid phase (SSF) and the self-organised Mott-insulator phase (SMI). It is plotted against effective cavity-pump detuning Δ_{eff} and pump strength $E_{p,\text{exp}} = \gamma E_p$ in units of the recoil energy E_{rec} , where $\gamma = 1.36$ is a calibration factor between the pump strength used in experiments and simulations. To determine the experimental NP–SSF boundary (dark red crosses), we use the slow ramping protocol with ramping time $T_r = 40$ ms and measure the intracavity photon number (background colour). The boundary is then defined by the rapid increase in the photon number. It is compared to the simulated NP–SSF boundary (black diamonds). To determine the experimental SSF–SMI boundary (black circles), we use the fast ramping protocol with $T_r = 20$ ms and measure the momentum space density. The boundary is then defined by the rapid increase in the central peak width. It is compared to the simulated SSF–SMI boundary (blue squares) which is obtained through our proposed simplification scheme. The simplification scheme induces systematic errors in the predicted boundary of roughly $\pm 0.5 E_{\text{rec}}$. The black and blue lines are guide to the eyes, and the grey dashed line marks the detuning Δ_{eff} used in Figs. 4.5 and 4.6.

frequency $\omega_p = 2\pi\lambda_p/c$, which forms an effective standing-wave optical lattice $E_y(y) = E_p \cos^2(2\pi y/\lambda_p)$. We work in the dispersive regime $\omega_p < \omega_a$ using pump light at a wavelength of $\lambda_p = 803$ nm. This is far detuned from the relevant atomic transition of ^{87}Rb at $\lambda_a = 795$ nm. We note that the atoms and the cavity are both red-detuned from the pump light $\Delta_a = \omega_p - \omega_a < 0$, $\Delta_c = \omega_p - \omega_c < 0$.

Combining all the aforementioned components of the setup, we can write down

the full many-body Hamiltonian of the cavity-BEC system [102, 160, 161],

$$\mathcal{H} = \int dx dy dz \Psi^\dagger \left(-\frac{\hbar^2 \nabla^2}{2m_{\text{Rb}}} + V_{\text{trap}} + V_{\text{opt}} \right) \Psi + \frac{g_{3\text{D}}}{2} \int dx dy dz \Psi^\dagger \Psi^\dagger \Psi \Psi \quad (4.1\text{a})$$

$$V_{\text{trap}} = \frac{m_{\text{Rb}}}{2} (\omega_x^2 x^2 + \omega_y^2 y^2 + \omega_z^2 z^2) \quad (4.1\text{b})$$

$$V_{\text{opt}} = -E_p \cos^2(k_c y) - E_z \cos^2(k_c z) + \hbar U_0 |\alpha|^2 \cos^2(k_c x) + \sqrt{\hbar E_p |U_0|} (\alpha + \alpha^*) \cos(k_c x) \cos(k_c y). \quad (4.1\text{c})$$

Here, $\Psi \equiv \Psi(x, y, z)$ is the atomic annihilation operator, $m_{\text{Rb}} = 1.44 \times 10^{-25}$ kg is the mass of the ^{87}Rb atoms, $g_{3\text{D}}$ is the atom-atom contact interaction strength, and $U_0 = \Omega_g^2 / \Delta_a = -2\pi \times 0.36$ Hz is the single-atom light shift. Importantly, in comparison to the Hamiltonian introduced in Eq. (3.6), we use the lattice depth $E_p = \hbar \eta^2 / |U_0|$ to represent η . The cavity field, pumping laser, and external lattice are near resonance $\lambda_c \approx \lambda_p \approx \lambda_z$, and for clarity we denote the wavelengths and wave vectors along all three directions as λ_c and k_c respectively in Eq. (4.1) and in the rest of this work. A summary of the experimental parameters is given in Table 4.1.

The cavity field is treated as coherent light and represented by its expectation value $\alpha = \langle a \rangle$, where a is the annihilation operator of the cavity field. The expectation value α follows the equations of motion [102, 160, 161]

$$\partial_t \alpha = [i(\Delta_c - N_{3\text{D}} U_0 B) - \kappa] \alpha - i \sqrt{\frac{E_p |U_0|}{\hbar}} N_{3\text{D}} \theta \quad (4.2\text{a})$$

$$\theta = \int dx dy dz \rho(x, y, z) \cos(k_c x) \cos(k_c y) \quad (4.2\text{b})$$

$$B = \int dx dy dz \rho(x, y, z) \cos^2(k_c x), \quad (4.2\text{c})$$

where $\rho(x, y, z) = \langle \Psi^\dagger \Psi \rangle / N_{3\text{D}}$ is the spatial density distribution. Under this treatment, the cavity field effectively imposes a one-body potential upon the atoms, as evident in the second line of Eq. (4.1c). This treatment of the cavity field is legitimate as long as the cavity fluctuations $\langle \delta a^2 \rangle = \langle a^\dagger a \rangle - |\alpha|^2$ are small, which is indeed the case except near the self-organisation boundary [RL8, 78, 116, 117], which will be introduced in detail below.

The atomic many-body wavefunction of the steady state of the cavity-BEC system can be obtained by solving Eqs. (4.1) and (4.2) self-consistently. While for small pump strengths the system remains in the normal phase, for pump strengths above a critical threshold, the atoms reduce the potential energy by

4.2. Experimental setup and measurement protocol

self-organising into a chequerboard lattice with lattice spacing λ_c along the x and y directions as depicted in Fig. 4.1(c), and constructively scatter photons from the pump into the cavity [78, 102, 113, 116, 118, 161]. In a steady state, the dominant part $[\cos(k_c x) \cos(k_c y)]$ of the cavity-induced potential has an effective depth

$$E_{\text{cb}} = \left| \frac{2E_p U_0 N_{3\text{D}} \theta (\Delta_c - N_{3\text{D}} U_0 B)}{(\Delta_c - N_{3\text{D}} U_0 B)^2 + \kappa^2} \right|. \quad (4.3)$$

This self-organisation transition can be mapped to the Hepp-Lieb normal-superradiant phase transition of the Dicke model [105–108], and is accompanied by the spontaneous breaking of the \mathbb{Z}_2 symmetry, which is reflected by the sign of θ . A positive (negative) θ corresponds to an even (odd) lattice configuration. In our experimental system this symmetry is well established, and the system spontaneously breaks into either configuration upon self-organisation [127].

Deep in the self-organised phase, the atoms progressively localise on the chequerboard lattice sites as the pump strength increases and the induced optical potential deepens. Coherence between atoms at different lattice sites gradually decays, leading to a second transition from the SSF phase to the SMI phase [RL2, RL8, 119]. During this transition, cavity fluctuations are indeed minimal [RL8, 78, 116, 117], validating our mean-field treatment of the cavity field. The SSF and SMI phases behave similar to the superfluid and Mott-insulator phases, respectively, of the usual Bose-Hubbard model

$$H_{\text{BH}} = -t \sum_{\langle i,j \rangle} (b_i^\dagger b_j + b_j^\dagger b_i) + \frac{U}{2} \sum_i b_i^\dagger b_i^\dagger b_i b_i, \quad (4.4)$$

where b_i is the annihilation operator for bosonic atoms at the i -th lattice site, t is the tunnelling strength, U is the on-site interaction, and $\langle i, j \rangle$ indicates the summation is over nearest neighbours. In this model, a superfluid is characterised by a fluctuating particle number per site and phase coherence of the whole ensemble due to large tunnelling between different lattice sites. On the contrary, in a Mott-insulator, phase coherence is lost, the particle fluctuations vanish and the number of atoms per lattice site is fixed due to the suppressed tunnelling. The differences between the two phases lead to distinct behaviours in various quantities, including the variance of on-site atom number $\text{Var} = \langle (b_i^\dagger b_i)^2 \rangle - \langle b_i^\dagger b_i \rangle^2$ [162–164] and the momentum space density distribution [RL2, RL8, 87, 91, 92, 119, 144–146, 165–167]

$$\tilde{\rho}(\mathbf{k}) = \langle \Psi^\dagger(\mathbf{k}) \Psi(\mathbf{k}) \rangle. \quad (4.5)$$

Since the former quantity is hard to measure experimentally [162], we choose $\tilde{\rho}(\mathbf{k})$ as our main quantity of interest for defining the phase boundary. As the system enters the Mott-insulator phase from the superfluid phase, a significant

increase in the full width at half maximum (FWHM) \mathcal{W} of the central peak in the momentum space density distribution can be observed [RL2, RL8, 119, 144–146, 165–167] accompanying the loss of phase coherence. The transition between the two phases is thus smooth and has only weak criticality.

In the cavity-BEC system, the total number of atoms enters the equation of motion Eq. (4.2) and effectively modifies the cavity detuning. Meanwhile, the number of atoms per site, equivalent to the filling factor in the Bose-Hubbard model, is an important ingredient in determining the SSF–SMI boundary [145, 165, 168–170]. Therefore, a quantitative comparison between experiment and theory necessitates an estimate to the number of atoms in each two-dimensional slice as well as at each lattice site near the centre of the harmonic trap. For simplicity, we assume a uniform distribution of the atoms in the central cuboid of the three-dimensional harmonic trap, such that x/r_x , y/r_y and z/r_z are all within the interval $[-1/2, 1/2]$. In this region, since the two-dimensional slices are $\lambda_c/2$ apart from each other along the z direction, there are $2r_z/\lambda_c \approx 8$ slices in total and each slice contains roughly $N_{2D} \approx 6,900$ atoms. Once the system enters the self-organised phase, the atoms in each slice will further form a lattice with two lattice sites per area of λ_c^2 . There are thus $2r_x r_y / \lambda_c^2 = 275$ lattice sites in the considered rectangle on each slice, and each of the lattices contains $\nu \approx 25$ atoms.

4.2.2 Measurement protocol

The comparison between the experimental and simulated phase diagrams involves both the NP–SSF and the SSF–SMI boundaries for the steady state. In experiments, we fix the effective detunings

$$\Delta_{\text{eff}} = \Delta_c - \frac{1}{2} N_{3D} U_0 \quad (4.6)$$

while ramping up the pump strength linearly from zero to $E_{p,\text{exp}} = 14.5E_{\text{rec}}$ within a time T_r . There is a trade-off when choosing an appropriate ramping time, and we choose two different ramping times for the measurements of different observables to best approximate the steady-state phase boundaries.

In the vicinity of the NP–SSF boundary, the photonic behaviour is dominating in the system due to significant cavity fluctuations. As the cavity decay rate is small in comparison to the effective detuning $\kappa < |\Delta_{\text{eff}}|$, the cavity field experiences a retardation effect when crossing the steady-state NP–SSF boundary [118]. As a result, the dynamical NP–SSF boundary shifts towards higher pump strength for shorter ramping time T_r , and converges to the steady-state boundary with long T_r . With a ramping time of $T_r = 40$ ms, the hysteresis area is negligibly small and the steady-state boundary can be well approximated [118].

4.2. Experimental setup and measurement protocol

On the contrary, deep inside the self-organised phase, the cavity fluctuations vanish and atomic behaviour becomes dominant, rendering particularly atom loss a key factor. A decrease in the atom number effectively increases $|\Delta_{\text{eff}}|$ when both Δ_c and U_0 are negative [cf. Eq. (4.6)], and it generally indicates that a higher pump strength E_p is required to achieve the same lattice depth [cf. Eq. (4.3)]. Therefore, all phase boundaries are shifted towards higher pump strength when atom loss occurs. Since a longer ramping time implies a larger atom loss and hence a larger shift in the boundary, a fast ramp with $T_r = 20$ ms is thus preferred for the measurement of the steady-state SSF–SMI boundary.

After understanding the dynamical effects on the boundaries, we first use the slow ramp $T_r = 40$ ms for the determination of the NP–SSF boundary. During the ramp, we record the transmitted photons leaking through one of the cavity mirrors using a single photon counting module (SPCM), and scale them with the detection efficiency to obtain the intracavity photon number N_{ph} . The threshold of corrected photon number $N_{\text{ph}} \approx 300$ is used for determining the NP–SSF boundary as shown in Fig. 4.2, which is later compared to the simulated one as a calibration.

We then use the fast ramp $T_r = 20$ ms to determine the SSF–SMI boundary, which is extracted from the momentum space density distribution $\tilde{\rho}(\mathbf{k})$ [RL8, 119, 144, 146, 149] using time-of-flight single-shot absorption measurement. Thereafter, we extract the width of the central peak from the distribution, and mark the SSF–SMI boundary at the pump strength where the width starts to increase. The measured SSF–SMI boundary is marked as the black line with circles in the phase diagram Fig. 4.2. With the fast ramping protocol $T_r = 20$ ms, the measured dynamical NP–SSF is indeed significantly shifted towards larger pump strengths due to retardation effects, but the cavity field and the induced potential converge to the steady-state values soon after the system dynamically enters the self-organised phase, as verified in Ref. [118]. This significantly reduces the retardation effect on the dynamical SSF–SMI boundary.

Caution needs to be taken when analysing the experimental measurements. The experimentally calibrated pump strength $E_{p,\text{exp}}$ is different from the pump strength E_p entering the Hamiltonian, because the experimental pump laser is not strictly monochromatic. These two pump strengths are related through a calibration factor

$$\gamma \equiv E_{p,\text{exp}}/E_p > 1 \quad (4.7)$$

which is not measurable through experiments without applying significant hardware changes to the system. To determine the factor γ , we need to compare the experimental and simulated phase diagrams, and require that they coincide

with each other. This comparison will be performed in Section 4.3.2 after obtaining the simulated NP-SSF boundary.

4.3 Simulation methodology

4.3.1 Numerical method

We use the approach Multiconfigurational Time-Dependent Hartree Method for Indistinguishable Particles (MCTDH-X) to simulate the steady state of the system and extract the observables of interest [RL6, 83–85, RL11, 157, 158], like the momentum space density distribution and the cavity field expectation value. Importantly for the current work, the number of orbitals used in a simulation depends on the nature of the quantum state of interest. For example, the formation of the cavity-induced potential and thereby the self-organisation of the atoms can well be observed in the mean-field limit with $M = 1$ orbital [RL8, RL9, 83]. In contrast, to correctly describe a Mott-insulator state, the number of orbitals should be at least as large as the number of lattice sites [RL8, 86, 87, 158, 171]. Since the required computational resources scale as $\binom{N-M+1}{M}$ [84], given the currently available processors, it is computationally unfeasible to simulate with MCTDH-X the full experimental cavity-BEC system. Therefore, we need to simplify the problem and reduce the number of orbitals and particles needed for the MCTDH-X simulations. We will now elaborate on the methodology for choosing this simplification.

4.3.2 Reduction of system dimensionality and rescaling of the contact interaction strength

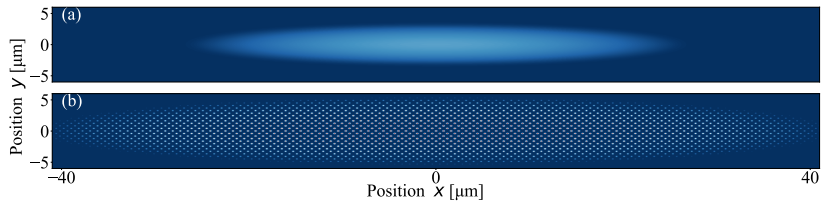


Figure 4.3: Real space density distributions $\rho(x)$ of (a) a normal BEC state and (b) a self-organised state of the full two-dimensional system simulated in the mean-field limit using MCTDH-X. The zooms of the two states around the centre of the harmonic trap are shown in Figs. 4.5(s) and 4.5(t), respectively.

The computational complexity can be significantly reduced by lowering the system dimensionality. We argue that the system can be well represented by

4.3. Simulation methodology

a two-dimensional model, and determine the effective atom-atom interaction strength in this model.

In experiments, the system is divided into two-dimensional slices by the deep external optical lattice. The hopping between two slices is strongly suppressed by the strong external lattice, and thus the slices are independent from each other on the atomic level [cf. Eq. (4.1)]. On the other hand, atoms from all slices collectively contribute to the cavity field, and therefore they are strongly coupled to each other through the cavity [cf. Eq. (4.2)]. In order to represent the full system by one two-dimensional slice, we propose to decouple the slices by simulating Eqs. (4.1) and (4.2) with N_{2D} atoms at $z = 0$, and using the scaling of parameters [161]

$$U_0 \mapsto \tilde{U}_0 = U_0 \frac{N_{3D}}{N_{2D}}, \quad \alpha \mapsto \alpha \sqrt{\frac{N_{2D}}{N_{3D}}}. \quad (4.8)$$

Under this scaling, the equations of motion for the cavity field [Eq. (4.2)] as well as the cavity-induced potential V_{opt} [Eq. (4.1)] remain invariant for a fixed atomic density profile. We thus expect that the atomic many-body wavefunction of the two-dimensional system obtained from Eq. (4.8) approximately reproduces the wavefunction of the original system at $z = 0$,

$$|\Psi_{2D}(x, y)\rangle \approx |\Psi_{3D}(x, y, z = 0)\rangle. \quad (4.9)$$

This approach requires a knowledge of the effective contact interaction in the two-dimensional slice, which is crucial for the formation of Mott insulation. The strength g_{2D} is estimated according to the harmonic trapping frequencies and the corresponding Thomas-Fermi radii [172],

$$N_{2D}g_{2D} = \frac{\pi m_{\text{Rb}}}{4} \frac{r_x^4 \omega_x^3}{\omega_y}, \quad (4.10)$$

which yields $g_{2D} \approx 0.34\hbar^2/m_{\text{Rb}}$ for $N_{2D} = 6,900$.

With the effective single slice, we can simulate the physics of the realistic experimental system using MCTDH-X at different pump lattice depths E_p and effective detunings Δ_{eff} in simulations, and as the first observable we choose the cavity field strength. The self-organisation and the accompanying macroscopic activation of the cavity field can already be captured with sufficient precision by using $M = 1$ orbital in the mean-field limit. Exemplary real space density distributions of a normal BEC state with a Thomas-Fermi profile and a self-organised state with a chequerboard lattice are shown in Fig. 4.3. Along with the density distributions, these mean-field simulations also yield the cavity field expectation values $\alpha_{\text{MF}}(E_p, \Delta_{\text{eff}})$. The NP-SSF boundary can then be

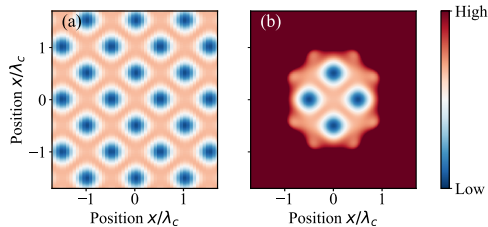


Figure 4.4: A comparison between (a) the cavity-induced lattice potential $V_{\text{opt}}(z=0)$ [Eq. (4.1)] and (b) the four-well potential $V_{4\text{well}}$ [Eq. (4.12)]. Each of the four wells faithfully reproduces the lattice sites of the lattice.

drawn at $|\alpha_{\text{MF}}|^2 \approx 0.1$. Although this choice of threshold is different from the experimental one, it does not induce substantial difference due to the rapid increase of photon number across the boundary. Both criteria are chosen based on the analytically expected boundary and the respective limitations in experiments and simulations.

With the simulation results, the calibration factor γ [cf. Eq. (4.7)] for the experimental pump strength can now be calculated to be $\gamma = 1.36$. This is determined by requiring that the measured NP–SSF boundary and the simulated one, which are fitted as $\Delta_{\text{eff}}/2\pi = (-8.536E_{p,\text{exp}}/E_{\text{rec}} + 6.305)$ kHz and $\Delta_{\text{eff}}/2\pi = (-11.616E_p/E_{\text{rec}} + 5.834)$ kHz respectively, have the same slope as functions of pump strengths. For the fitting of the experimental boundary, only the data measured between cavity detunings $-2\pi \times 5$ kHz and $-2\pi \times 20$ kHz are taken into account, because atom loss already slightly shifts the boundary at more negative detunings. The experimental and simulated NP–SSF boundaries indeed collapse upon each other when this calibration factor is taken into account (cf. Fig. 4.2). The effective contact interaction strength $g_{2\text{D}}$ and the calibration factor γ are the last two system parameters to be determined for the comparison to the experimental system.

4.3.3 Four-well model

We now proceed to simulate the SSF–SMI transition. A proper description of this transition requires at least one orbital for each lattice site. Given the large number of atoms and lattice sites, it is impractical to simulate the quantum state of the full two-dimensional system, and thus further simplification of the model is needed. Since the SSF–SMI transition is mainly driven by the competition between on-site interaction and hopping between nearest-neighbouring sites, the loss of superfluidity of the whole system should already be quantitatively captured by a local representation. A minimal choice for such

4.3. Simulation methodology

a local representation is a unit cell consisting of four lattice sites in the centre of the harmonic trap, which is shown in Fig. 4.4(b).

This four-well potential can be described by the Hamiltonian

$$\mathcal{H}_{4\text{well}} = \int dx dy \Psi^\dagger \left(-\frac{\hbar^2 \nabla^2}{2m_{\text{Rb}}} + V_{4\text{well}} \right) \Psi + \frac{g_{2\text{D}}}{2} \int dx dy \Psi^\dagger \Psi^\dagger \Psi \Psi, \quad (4.11)$$

where a tight non-harmonic confining potential is applied on top of the optical lattice

$$V_{4\text{well}} = \tilde{V}_{\text{opt}} + V_{\text{conf}}. \quad (4.12a)$$

The ideal confining potential should be relatively flat in the centre of the system $x^2 + y^2 < \lambda_c^2$, but form a rapidly increasing wall surrounding the four wells at $x^2 + y^2 > \lambda_c^2$. This can be achieved by using an algebraic function of $x^2 + y^2$ with high power. For example, the following confining potential is chosen for our simulation:

$$V_{\text{conf}}(x, y) = 13E_{\text{rec}}(x^2 + y^2)^4 / \lambda_c^8. \quad (4.12b)$$

We note that this is not the unique choice for the confining potential, and simulated SSF-SMI boundary should not be sensitive to the choice.

However, a straightforward implementation of the tight confining potential can easily distort the underlying optical lattice, because the equations of motion [Eqs. (4.1), (4.2)] are solved self-consistently and the solution can be very sensitive to slight changes of parameters, especially near the self-organisation boundary. We thus make use of the previously simulated expectation value of the cavity field $\alpha_{\text{MF}}(E_p, \Delta_{\text{eff}})$ to determine the depths of the cavity-induced potential, i.e., $U_0 |\alpha_{\text{MF}}|^2$ and $2\sqrt{\hbar E_p U_0} \text{Re}(\alpha_{\text{MF}})$, which is equivalent to using

$$\tilde{V}_{\text{opt}}(x, y) = V_{\text{opt}}(x, y, z = 0, \alpha = \alpha_{\text{MF, odd}}). \quad (4.12c)$$

The \mathbb{Z}_2 symmetry of the cavity-BEC system corresponds to two energetically degenerate states, which are distinguishable by a π phase shift of the intracavity field $\alpha_{\text{MF, even}} = -\alpha_{\text{MF, odd}}$. Here we explicitly choose the one corresponding to the odd configuration, whose lattice sites are located at the desired positions $(0, \pm\lambda_c/2)$ and $(\pm\lambda_c/2, 0)$. The four-well potential is compared to the original lattice in Fig. 4.4. Indeed, the shape of each of the four wells precisely recreates the shape of the each lattice site of the original optical lattice.

With four sites in total and each containing $\nu \approx 25$ atoms, we perform the simulations with $\tilde{N} = 100$ atoms and $\tilde{M} = 4$ orbitals subject to one-body potential $V_{4\text{well}}$ and contact interaction with strength $g_{2\text{D}} = 0.34\hbar^2/m_{\text{Rb}}$. MCTDH-X generates a numerically highly accurate many-body wavefunction for the four-well system. In terms of the quantities related to the SSF-SMI transition, for

example the momentum space density distribution and the one-body correlation function between neighbouring sites, the four-well model Eq. (4.12) should produce the same result as the full three-dimensional experimental setup from Eqs. (4.1) and (4.2). A summary of the simulation approaches and parameters is given in Table 4.1.

The representation of the full effective optical lattice by our four-well model is a crucial non-trivial simplification. The complexity of the minimal model is mainly determined by the symmetry of the full system and the filling factor ν . The symmetry of the checkerboard lattice contributes significantly to the simplicity of the minimal representative four-well model. In contrast, for a system with weaker symmetry, the number of lattice sites in a unit cell N_{site} increases. This will significantly increase the computational workload, which scales as $\binom{N_{\text{site}}(\nu-1)+1}{N_{\text{site}}}$.

Moreover, the validity of this simplification is based on the nature of the SSF-SMI phase transition and the geometry of the system. The finite size effect of this minimal representation for the full lattice system still provides the main source of systematic errors in the simplification scheme. More specifically, the transition point of a Bose-Hubbard model is subject to finite size effect, and is increased by tens of percent in terms of the ratio t/U compared to the thermodynamic limit [163, 164]. However, in a cavity-BEC system, the ratio t/U decreases exponentially as the pump strength E_p increases [RL8]. As a result, the shift of the SSF-SMI boundary due to finite size effect in terms of E_p is negligible. The simulated boundaries show a systematic variance of roughly $0.5E_{\text{rec}}$, and the result has indeed already converged with the four-well model.

4.3. Simulation methodology

Table 4.1: Summary of the experimental and computational methods and parameters. Here a_B is the Bohr radius.

	Experiments	Simulation Step 1 “Full two-dimensional model”	Simulation Step 2 “Four-well model”
Methods			
Hamiltonians and/or Equations of Motion	Eqs. (4.1), (4.2)	Eqs. (4.1), (4.2) with $z = 0$	Eq. (4.11)
Solved state	Evolving state	Steady state	Ground state
Extracted quantities	$N_{\text{ph}}, \tilde{\rho}(\mathbf{k})$	α_{MF}	$\tilde{\rho}(\mathbf{k}), \rho(\mathbf{x})$
General setup parameters			
Particle number	$N_{3\text{D}} = 5.5 \times 10^4$	$N_{2\text{D}} = 6,900$	$\tilde{N} = 100$
Orbital number	—	$M = 1$	$\tilde{M} = 4$
Particle mass		$m_{\text{Rb}} = 1.44 \times 10^{-25}$ kg	
Dimensions	3	2	2
Interaction strength	$g \approx 98 \times 4\pi\hbar^2 a_B / m_{\text{Rb}}$ [173]	$g_{2\text{D}} = 0.34\hbar^2 / m_{\text{Rb}}$	$g_{2\text{D}} = 0.34\hbar^2 / m_{\text{Rb}}$
Trap	Harmonic with $(\omega_x, \omega_y, \omega_z) = 2\pi \times (25.2, 202.2, 215.6)$ Hz	Harmonic with $(\omega_x, \omega_y) = 2\pi \times (25.2, 202.2)$ Hz	Octic with form Eq. (4.12b)
Parameters related to optical lattice potentials			
Wave length		$\lambda_c = 803$ nm	
Recoil energy		$E_{\text{rec}} = \hbar \times 2\pi \times 3.55$ kHz	
Pump strength	$E_{p,\text{exp}} = 0$ to $14.5E_{\text{rec}}$	$E_p = 0$ to $11E_{\text{rec}}$	—
Single photon shift	$U_0 = -2\pi \times 0.36$ kHz	$\tilde{U}_0 = -2\pi \times 2.87$ kHz	—
Effective detunings	$\Delta_{\text{eff}} = 0$ to $-2\pi \times 40$ kHz	$\Delta_{\text{eff}} = 0$ to $-2\pi \times 40$ kHz	—
Cavity decay rate	$\kappa = 2\pi \times 4.45$ kHz	$\kappa = 2\pi \times 4.45$ kHz	—
Other input parameters	—	—	α_{MF} obtained from Step 1

4.4 Results

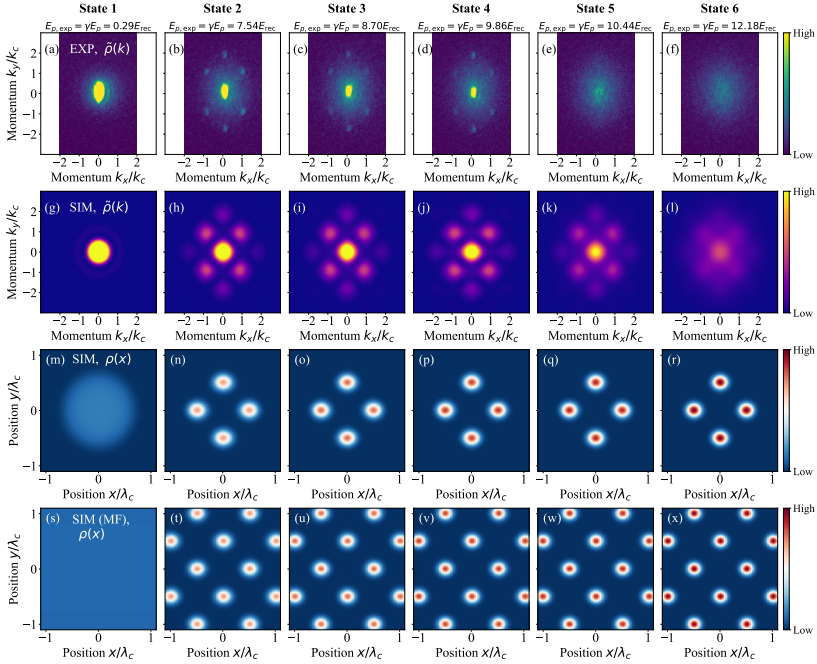


Figure 4.5: (a-f) Experimentally measured and (g-l) simulated momentum space density distributions $\tilde{\rho}(k_x, k_y)$, as well as simulated real space density distributions $\rho(x, y)$ of the *four-well model* for six different parameter sets. The chosen states range from normal BEC state to SSF states to SMI states. (s-x) For comparison, $\rho(x, y)$ of the *full two-dimensional model* [cf. Eq. (4.9)] simulated in the mean-field limit. To facilitate the comparison with panels (m-r), we zoom around the trap centre and choose only the odd configurations. These states are simulated or measured at $\Delta_{\text{eff}} = -2\pi \times 30$ kHz and at different pump strengths E_p , which correspond respectively to the points 1 to 6 indicated in Fig. 4.6(b). In panel (m) the BEC is highly localised at the trap centre due to the tight trap [Eq. (4.12b)], whereas in panel (s), the BEC has an almost uniform non-zero distribution in the centre of the trap due to the relatively loose harmonic trap.

4.4.1 The Mott transition

The momentum space density distribution $\tilde{\rho}(\mathbf{k})$ measured from experiments and calculated from simulations can be used to extract the SSF-SMI phase boundary. The obtained phase diagram of the cavity-BEC system against

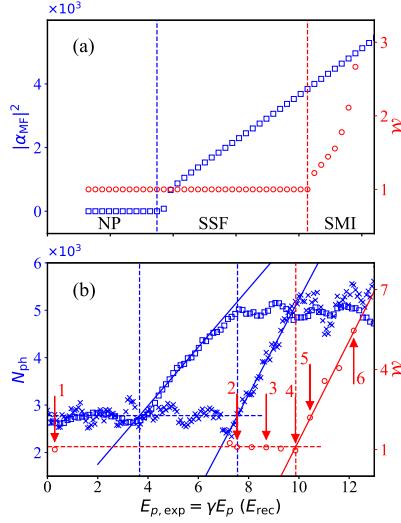


Figure 4.6: Cavity field magnitude $|\alpha_{\text{MF}}|^2$, intracavity photon number N_{ph} , and the relative width of the central Bragg peak \mathcal{W} as functions of pump strength $E_{p,\text{exp}} = \gamma E_p$ at fixed detuning $\Delta_{\text{eff}} = -2\pi \times 30$ kHz. The relative width of the central Bragg peak for the BEC is set to be $\mathcal{W} = 1$. As the pump strength increases, the system transitions through all three phases, i.e., NP, SSF, and SMI. Panel (a) shows simulated steady-state results for $|\alpha_{\text{MF}}|^2$ (blue squares) obtained from the mean-field $M = 1$ simulations, and \mathcal{W} (red circles) obtained from the beyond-mean-field $M = 4$ simulations. Panel (b) shows experimentally measured N_{ph} for the $T_r = 40$ ms ramping protocol (blue squares), as well as N_{ph} (blue crosses) and \mathcal{W} (red circles) for the $T_r = 20$ ms ramping protocol. A background radiation of $N_{\text{ph}} \approx 2.7 \times 10^3$ originating from diffuse light forming the external lattice potential. This background count offset can be safely subtracted for the determination of the NP–SSF boundary. The numbers indicate the representative points whose simulated and measured density distributions are shown in Fig. 4.5.

pump strength E_p and effective detuning Δ_{eff} is shown in Fig. 4.2. It serves as a map to identify the three different phases of matter, NP, SSF, and SMI, which are realised in both experiments and simulations. To illustrate the system behaviour in the three different phases, we choose a series of states at $\Delta_{\text{eff}} = -2\pi \times 30$ kHz, and show their simulated and experimentally measured density distributions in Fig. 4.5. The numbering (1 to 6) of the quantum states in Fig. 4.5 refers to the different pump strengths indicated in Fig. 4.6(b).

In the normal phase, the real space density distribution of the BEC has a Thomas-Fermi profile [Fig. 4.5(m)], whereas the momentum space density dis-

tribution has correspondingly a single blob [Fig. 4.5(a,g)]. This can be observed both in experiments and simulations. The momentum space distribution has an elliptical shape in experiments but a circular shape in simulation. This is because the harmonic trap is anisotropic in the experimental setup $\omega_x \neq \omega_y$, while the confining potential in simulations [Eq. (4.12b)] is isotropic in the x and y directions.

As the cavity is switched on, the momentum space density distributions $\tilde{\rho}(\mathbf{k})$ behave similarly in experiments [Fig. 4.5(a-f)] and simulations Fig. 4.5(g-l)], except for the thermal background in experiments which is due to heating of the sample and cannot be captured by our model. In both experiments and simulations, $\tilde{\rho}(\mathbf{k})$ in the SSF and SMI phases are completely different. It provides a way to determine the phase boundary. A typical SSF state is represented by “State 2”, whose measured and simulated momentum space densities are shown in Figs. 4.5(b) and 4.5(h), respectively. In the SSF phase, the central Bragg peak at $(k_x, k_y) = (0, 0)$ is high and narrow and the satellite peaks are clearly visible. The four Bragg peaks at $(k_x, k_y) = (\pm k_c, \pm k_c)$ are the next dominant peaks and they indicate a strong coherence between atoms in the immediately neighbouring sites of the checkerboard lattice, which are $(\pm \lambda_c/2, \pm \lambda_c/2)$ apart from each other in the real space. On top of these strong peaks, small peaks are seen at $(k_x, k_y) = (0, \pm 2k_c)$ and barely visible at $(k_x, k_y) = (\pm 2k_c, 0)$, which correspond to the optical pump lattice and the intra-cavity lattice, respectively. In contrast, “State 6” is a good representative of the SMI phase, whose measured and simulated momentum space densities are shown in Figs. 4.5(f) and 4.5(l), respectively. In the SMI phase, the central peak becomes broad and low, and the satellite peaks become diffuse. They indicate the strong localisation of the atoms in the individual lattice sites and the lack of coherence between the atoms [RL2, RL8, 87, 91, 92, 119, 144–146, 165–167]. The localisation and loss of coherence of the atoms accompanying the increasing pump strength does not trigger qualitative change in the real space density distributions $\rho(\mathbf{x})$ [Fig. 4.5(m-r)], despite their significant impact in the momentum space. These images are not available from our experimental setup because the resolution of the absorption imaging system in the experiment is not good enough to resolve the individual lattice sites. Nevertheless, as a sanity check, we confirm that the four-well model and the full two-dimensional mean-field model [Fig. 4.5(s-x)] produce the same real space density distributions locally at the centre of the harmonic trap.

For different pump strengths at the fixed detuning $\Delta_{\text{eff}} = -2\pi \times 30$ kHz, we summarise the simulated cavity field magnitude $|\alpha_{\text{MF}}|^2$, the measured intra-cavity photon number N_{ph} , as well as the simulated and measured relative widths \mathcal{W} of the central Bragg peak in Fig. 4.6. In both simulations [Fig. 4.6(a)] and experiments [Fig. 4.6(b)], the NP–SSF boundary is defined as where $|\alpha_{\text{MF}}|^2$

4.4. Results

or N_{ph} starts to increase, whereas the SSF–SMI boundary is defined as where \mathcal{W} starts to increase. Specifically for the experimental SSF–SMI boundary, we fit a line, shown as the red solid line in Fig. 4.6(b), using the first five data points after \mathcal{W} starts to increase. The crossing with the initial width, i.e., the horizontal red dashed line, marks the SSF to SMI phase boundary.

We further discuss the discrepancies between the experimental and simulation results. The retardation effect discussed in Section 4.2.2 clearly manifests itself in N_{ph} for the fast ramp. This dynamical effect, however, cannot be reproduced numerically because it requires prohibitively large amount of computational resources. To better appreciate the retardation effect, we perform a fit on the respective N_{ph} for both ramps, shown as blue solid lines in Fig. 4.6(b). These two fitted lines have different slopes, and when they cross with each other, the retarded cavity field is expected to reach its steady-state value. Compared to the simulation results, a plateau is further seen in N_{ph} for large pump strengths in experiments [Fig. 4.6(b)] for both fast and slow ramps as a result of atom loss. For the fast ramp, this plateau occurs slightly later than the increase in \mathcal{W} , thus contributes negligibly to the position of the SSF–SMI boundary. However, it contributes to one of the two factors why the increase behaviour of \mathcal{W} is also different between experiments and simulations in the SMI phase. The other factor is the different shapes of the initial BEC cloud in experiments and simulations due to the different confining potentials. The above analysis for $\Delta_{\text{eff}} = -2\pi \times 30$ kHz helps us comprehend the trade-off we encountered when choosing the ramping time. Even with a fast ramp $T_r = 20$ ms, the estimated position of the SSF–SMI boundary still suffers non-negligible systematic errors from the retardation effect. However, the heating and atom loss are anticipated to immediately set in and introduce further systematic errors for a slightly slower ramp.

The experimental and simulated SSF–SMI boundaries for all detunings are obtained in a similar manner, and shown in Fig. 4.2 as black and blue lines, respectively. Here we briefly discuss the effects of the retardation and atom loss for different detunings. The retardation effects are dominating for less negative detunings and are secondary for more negative detunings. In particular, for the least negative detunings, the steady-state SSF–SMI boundary could take place earlier than the dynamical NP–SSF boundary for the fast ramp. On the contrary, the atom loss has a larger impact for more negative detunings, where a larger pump strength is required for the self-organisation and Mott insulation. We thus generally expect that the experimentally measured SSF–SMI boundary takes place at a slightly larger pump strength than the steady-state boundary. With all the experimental and simulation systematic error under consideration, our results show that the experimental and simulation results are generally in good agreement for more negative detunings.

4.4.2 Comparison to Wannier-based Bose-Hubbard approaches

The quantitative determination of the SSF–SMI boundary can also be achieved by other existing approaches besides our MCTDH-X-based approach proposed above. We describe here an alternative approach which is based on the mapping to the Bose-Hubbard model. Given the effective optical lattice potential, the Wannier functions can be estimated by different numerical methods, many of which are available for quantum optical systems [174–177]. The Wannier functions then allow the extraction of the Bose-Hubbard parameters t and U [cf. Eq. (4.4)], which can be further used to determine the superfluid–Mott-insulator boundary. The last step can be performed by utilizing an empirical formula [168]. For the prediction of the Mott boundary, the criterion based on the Bose-Hubbard ratio U/t has been shown to be compatible with the criterion based on the behaviours of the central Bragg peak [165]. This approach no longer suffers from the finite size effect in comparison to our proposed simplification scheme. Nevertheless, when calculating the Wannier functions the broadening of Wannier function induced by on-site interaction is generally not taken into account [178, 179]. This could result in an underestimation in the Bose-Hubbard ratio t/U , and give rise to a different kind of systematic errors in comparison to our proposed MCTDH-X scheme.

We compare here the MCTDH-X predictions of the SSF–SMI boundary with the maximally localised generalised Wannier states (MLGWS) package [176] used for optical lattice potentials. We consider the optical lattice potential \tilde{V}_{opt} obtained in Eq. (4.12c) for different pump strengths E_p at fixed detuning $\Delta_{\text{eff}} = -2\pi \times 30$ kHz. Using the MLGWS method, we obtain the ratio of the Bose-Hubbard parameters $U/g_{2D}t$ in units of m_{Rb}/\hbar^2 as shown in Fig. 4.7(a). The SSF–SMI boundary of the two-dimensional system can then be determined using the empirical formula presented in Ref. [168]:

$$(U/t)_c = 2\nu(5.80 + 2.66\nu^{-2.19}). \quad (4.13)$$

For the experimentally appropriate filling factor of $\nu = 25$, the SSF-SMI boundary is estimated to be $(U/t)_c \approx 290$. This threshold is indicated as red squares in Fig. 4.7(a) for different values of g_{2D} . We emphasise that the MLGWS method does not take into account the broadening effects of the Wannier functions due to the finite contact interaction g_{2D} . Consequently, the curve $U/g_{2D}t$ remains unchanged for different values of g_{2D} . The method can significantly underestimate the hopping strength t and thus predicts that the SSF–SMI transition takes place at a much smaller pump strength.

The MCTDH-X predictions are obtained from the width \mathcal{W} of the central peak in the momentum space density for different values of contact interaction g_{2D} . These simulations are performed at different pump strengths E_p at fixed detuning $\Delta_{\text{eff}} = -2\pi \times 30$ kHz. Fig. 4.7(b-h) presents a comparison of the

4.4. Results

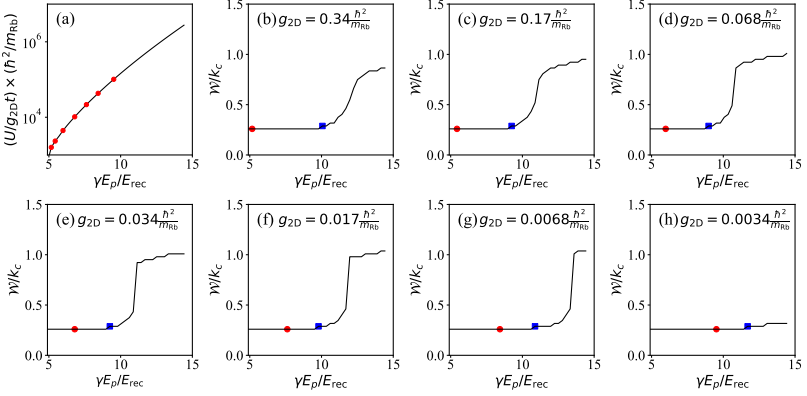


Figure 4.7: (a) The ratio of the Bose-Hubbard parameters $U/g_{2D}t$ as a function of the pump strength E_p calculated using the MLGWS package [176]. The red squares indicate the predicted Mott transition point $(U/t)_c \approx 290$ [cf. Eq. (4.13)] for different values of contact interaction strength: (from left to right) $g_{2D}m_{\text{Rb}}/\hbar^2 = 0.34, 0.17, 0.068, 0.034, 0.017, 0.0068, 0.0034$. (b-h) The width \mathcal{W} of the central peak in the momentum space as a function of pump strength E_p for different values of contact interactions g_{2D} simulated using MCTDH-X. The Mott transition is determined by the onset of the increase in \mathcal{W} , and is indicated in the figures by the blue squares. The Mott transition points predicted in panel (a) are also shown in the corresponding panels (b-h) as red squares.

SSF-SMI boundaries obtained using both methods. For the large, experimentally relevant value $g_{2D} = 0.34\hbar^2/m_{\text{Rb}}$ [Fig. 4.7(b)], the MCTDH-X boundary occurs at a much larger pump strength than that predicted by MLGWS. This difference can be attributed to the realistic width of the local atomic clouds at each individual lattice site. As g_{2D} decreases, the boundaries predicted by the two methods approach each other. Nonetheless, a difference remains for example at $g_{2D} = 0.0034\hbar^2/m_{\text{Rb}}$, we encounter a difference of $\gamma\Delta E_p \approx 2E_{\text{rec}}$ at [Fig. 4.7(h)]. A potential source of this discord is the non-trivial effects induced by the trapping potential, which is not considered by the MLGWS package.

Interestingly, the position of the boundary predicted by MCTDH-X does not move monotonically as g_{2D} decreases. In particular, when g_{2D} decreases from $0.34\hbar^2/m_{\text{Rb}}$ to $0.068\hbar^2/m_{\text{Rb}}$, we observe that the MCTDH-X boundary moves slightly towards shallower optical lattice potential depths, which is contradictory to straightforward expectation. This indicates that, as the contact interaction g_{2D} decreases, the increase in the hopping strength t due to atomic cloud expansion dominates over the decrease in the on-site interaction U in this

regime. This result is in consistent with the findings of Ref. [178], where t has been observed to increase more significantly with g_{2D} for a larger value of νg_{2D} .

We have thereby confirmed the consistency between the MLGWS package and the MCTDH-X scheme at weak contact interaction. More importantly, we have confirmed that the MCTDH-X scheme can cooperate higher order effects induced by a strong contact interaction.

4.5 Conclusions

We have used MCTDH-X to quantitatively determine the SSF–SMI boundary of a recoil resolved cavity-BEC system. This is the first time that MCTDH-X simulation results are directly compared quantitatively to experimental results for a cavity-BEC system, and the comparison is non-trivial due to limitation in computational resources. In contrast to the significant dynamical effects at play and a relatively large size of lattice, our two-dimensional simulations are limited to steady states and a small number of lattice sites. These computational difficulties can be judiciously circumvented by choosing different ramping rates for the measurement of different quantities on the experimental side, as well as simplifying the full lattice to a minimal four-well representation in the simulation. The systematic errors of our proposed approach mainly stem from the small size of the lattice system used in simulations, and are small when expressed in terms of the pump rate. We have thereby established MCTDH-X a feasible numerical method for the quantitative calculation of the superfluid–Mott-insulator boundary in an ultracold atomic system which forms a lattice with a large number of atoms per site.

PART II

Driven-dissipative cavity-boson systems with inherent system-bath rotation

INTRIGUINGLY, the straightforward picture of drive and dissipation introduced in Part I proves to be inaccurate and incomplete. Driven-dissipative systems are shown to manifest entirely different quantum features and collective dynamics in comparison to static systems which share the same effective Hamiltonian. In this Part, we discuss how this distinction is induced by driving, and then controlled by dissipation.

This requires a conjunction of the Floquet formalism with the Keldysh formalism, where the latter captures dissipation systematically by modelling it as the coupling of the system to a thermal bath. The Floquet-Keldysh formalism is to Lindblad formalism, as quantum field theory is to Hamiltonian formalism. It provides access to, for instance, two-point correlation functions, which allows us to harness a more profound understanding of a variety of physical behaviours. As a specific example, inspired by the discussion in Ref. [82], we provide an intuitive physical picture and qualitative arguments for explaining the different mechanisms of driven-dissipative (in)stabilities, particularly those seen in the cavity-boson systems. We also allude at a more rigorous comparison elucidating the consistency between the Keldysh and Lindblad formalisms, which is worthy of future investigations in detail.

The last three Chapters of this Part are dedicated to the wide range of consequences due to the driven-dissipative stabilities and instabilities. Specifically, we explore a few examples in cavity-boson systems, and discuss how phases unconventional to static systems, like limit cycles and multistable states, are achieved by drive and dissipation, and how they lead to the direct visualisation of non-Hermitian dynamics in experimental realisations.

5 | Keldysh formalism

Originality declaration: This Chapter is a review of established results in literature on the Keldysh formalism [81, 82, 180], with a focus on the description of the Lindbladian in such a formalism [82]. In Section 5.2, I highlight the essential differences induced by the relative rotation between the system and the environment due to the inherently driven nature, which lays the foundation for the discussion in Chapter 6.

5.1 The Keldysh formalism

The Keldysh formalism is suited for capturing dissipative systems at zero and finite temperatures. Generally, a quantum state is mixed in a dissipative system, and thus described by a density matrix rather than a wavefunction. In contrast to a pure state, the dynamical evolution of a density matrix $\rho = \sum_i p_i |\phi_i\rangle\langle\phi_i|$ requires two unitary operators, each acting forward on the kets $|\phi_i\rangle$ and backward on the bras $\langle\phi_i|$, respectively. Such bidirectional evolution motivates the introduction of the Keldysh contour consisting of two branches, a forward propagating one (+) and a backward propagating one (−), as sketched in Fig. 5.1.

The dissipative quantum system can be fully represented by its two-time correlation functions, where the two time points can be located on either branch of the Keldysh contour. A different kind of Green function is then chosen correspondingly. When both time points lie on the forward (backward) propagating branch, the retarded (advanced) Green function G^R (G^A) is needed, which is consistent with the standard quantum many-body field theory. Meanwhile, the correlation between the two branches is described by the Keldysh component of the Green function G^K . This is summarised in the table on the right.

t_1	t_2	G
<	<	G^A
>	>	G^R
<	>	0
>	<	G^K

For completeness of the formalism, we note that a complete Keldysh contour actually consists an additional temperature branch. Nevertheless, this temperature branch is found to be decoupled from the forward and backward propagating branches, and can thus be effectively neglected. In Keldysh formalism,

5.1. The Keldysh formalism

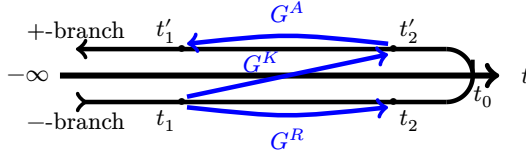


Figure 5.1: Schematics of the Keldysh contour and the retarded, advanced and Keldysh Green functions.

the temperature can be fully captured by the thermal distribution.

The retarded, advanced, and Keldysh Green functions in Keldysh formalism can be integrated into a 2×2 matrix in the basis of $(\psi_+, \psi_-)^T$, where $\psi_{\pm} = (\psi_{1,\pm}, \psi_{2,\pm}, \dots, \psi_{n,\pm})$ are the wavefunctions propagating forwards (+) and backwards (-),

$$\mathcal{G} = \begin{pmatrix} G^R & G^K \\ 0 & G^A \end{pmatrix} \quad (5.1)$$

$$\begin{aligned} \mathcal{G}^{-1} &= \begin{pmatrix} (G^R)^{-1} & (G^{-1})^K \\ 0 & (G^A)^{-1} \end{pmatrix} \\ &= \underbrace{\begin{pmatrix} (G_0^R)^{-1} & (G_0^{-1})^K \\ 0 & (G_0^A)^{-1} \end{pmatrix}}_{\text{system}} + \underbrace{\begin{pmatrix} i\Sigma & 2i\rho\Sigma \\ 0 & -i\Sigma \end{pmatrix}}_{\text{bath}} \end{aligned} \quad (5.2)$$

It is worth immediately emphasising that the retarded/advanced components of the inverted Green function can be straightforwardly given by the retarded/advanced Green function, but there is a priori no similar relation between the Keldysh component of the inverted Green function and the Keldysh Green function,

$$(G^{-1})^{R/A} = (G^{R/A})^{-1}, \quad (G^{-1})^K \neq (G^K)^{-1}. \quad (5.3)$$

Later, particularly in the presence of driving, the complex relation between $(G^{-1})^K$ and $(G^K)^{-1}$ will be shown to induce significant physical consequences.

Moreover, the total Green function in the Keldysh formalism consists of two major contributions. It can be modelled as a static, non-dissipative (closed) system

$$(G_0^{-1})^{R/A} = H \pm i\eta^+, \quad (G_0^{-1})^K = 2i\rho\eta^+, \quad (5.4)$$

where η^+ is infinitesimally positive, is coupled to a bath. The bath can be treated as a large ensemble of harmonic oscillators. The coupling is weak and

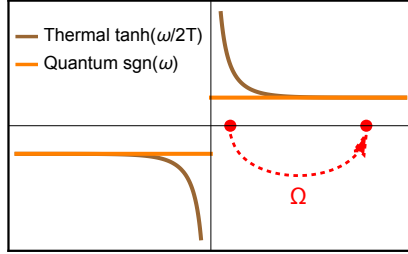


Figure 5.2: Relation between the pole and the thermal distribution $\rho(\omega)$ compared between quantum phase transition, thermal phase transition, and driven-dissipative phase transition.

the scale of the bath is much larger than the system, such that any change in the system should not have influence on the bath. The bath is characterised by its thermal distribution $\rho(\omega)$ and its spectral function $\Sigma(\omega)$. The former is determined by its quantum statistical behaviours,

$$\rho(\omega) = 1 \pm 2n(\omega) = \begin{cases} \coth(\omega/2T), & \text{bosons} \\ \tanh(\omega/2T), & \text{fermions} \end{cases}, \quad (5.5)$$

with $n(\omega)$ the Bose-Einstein or Fermi-Dirac distribution, and the + and – sign for bosons and fermions, respectively. The spectral function of the bath Σ in the Green function is a result of integration over the bath degree of freedom. It can admit different forms, e.g., Markovian, Ohmic, super- or sub-Ohmic, and fully characterises the bath from the point of view of the system. A more detailed treatment for the bath will be discussed in Section 10.2.1. In this thesis, we do not focus on the effects induced from the choice of these different spectral functions (which is by itself also very interesting), and assume all baths are Markovian, $\Sigma(\omega) = \Sigma$.

A comparison between the Green function and its inverse in Keldysh formalism yields the fluctuation-dissipation relation

$$G^K = G^R(G^{-1})^K G^A \quad (5.6)$$

$$= \rho(G^R - G^A), \quad (5.7)$$

where we have used the identity $\rho[(G^R)^{-1} - (G^A)^{-1}] = 2i(G^{-1})^K$ in the second step. The importance of this relation cannot be over-emphasised, as it relates the spectral features ($G^{R/A}$) and the thermal features (G^K) of the excitations. To relate, the Keldysh Green function G^K corresponds to the time-ordered Green function G^T in the framework of quantum field theory for closed systems. The Keldysh Green function contains useful information regarding to

5.2. Combining Keldysh and Floquet formalisms in bosonic Nambu space

the excitations. This includes the stability of the state (see Appendix B.7 for details) and the thermal occupation of the excitations. The latter can be used to quantify the quantum fluctuations on top of a mean-field steady state, and is given by

$$\langle a_n^\dagger a_n \rangle = \frac{1}{2} \left(i \int \frac{d\omega}{2\pi} (G^K)_{n,n} - 1 \right), \quad (5.8)$$

where the subscript n, n indicates a projection of the Green function onto the corresponding basis. As a teaser to the discussion in the following Sections, we remark that the thermal distribution ρ of the bath is the core reason why quantum and thermal phase transitions have different critical exponents. Take bosons as an example. As the system approaches critical points and the energy of the lowest excitations E vanishes, the fluctuations diverge as $n \sim \rho(\omega = E)G(\omega = E) \sim \rho(\omega = E)/E$. For thermal (quantum) phase transition at finite (zero) temperature, the thermal distribution diverges as $\rho(\omega) \sim 1/\omega$ (remains constant $\rho(\omega) = \text{sgn}(\omega)$), as illustrated in Fig. 5.2. As a result, we obtain different critical behaviours $n \sim 1/E^2$ and $n \sim 1/E$ for thermal and quantum phase transitions, respectively.

5.2 Combining Keldysh and Floquet formalisms in bosonic Nambu space

The interplay between quantum optical driving and coupling between bosonic particle-like and hole-like excitations can potentially lead to unusual stability and instability mechanisms unique to driven-dissipative systems, as to be further discussed in Chapter 6. We first discuss the static-dissipative system. To preserve the commutation relation of the bosons, the bosonic Green functions in Nambu space are constructed as [82, 181, 182],

$$(G_{\text{static}}^R)^{-1} = \begin{pmatrix} \omega + i\Sigma - H & K \\ K & -\omega - i\Sigma - H \end{pmatrix} \quad (5.9)$$

$$(G_{\text{static}}^{-1})^K = \tau_z \begin{pmatrix} 2i\rho(\omega)\Sigma & 0 \\ 0 & 2i\rho(\omega)\Sigma \end{pmatrix}. \quad (5.10)$$

In the absence of particle-hole coupling $K = 0$, the hole system is an exact replica of the particle system, and the two systems have their excitations at exactly the opposite energies. The flipping of the sign $+i\Sigma \mapsto -i\Sigma$ stems from the consistency of causality in both systems, and ensures that the stability of the system remain exactly the same when viewing it as particles or holes. Note that particles and holes experience the same thermal distribution $\rho(\omega)$, without a change of sign in frequency.

The structure of the bosonic Nambu space also requires that the corresponding Green functions be diagonalised under symplectic transformation. In order to simplify this procedure, we can introduce (see Appendix B.6)

$$\tilde{G}^R = G^R \tau_z, \quad \tilde{G}^A = \tau_z G^A, \quad (5.11)$$

where τ_z is the Pauli matrix in the Nambu space, such that \tilde{G} can be diagonalised under unitary transformation. In the presence of $K \neq 0$, this effectively introduces non-Hermiticity in the system,

$$(\tilde{G}_{\text{static}}^R)^{-1} = \begin{pmatrix} \omega + i\Sigma - H & K \\ -K & \omega + i\Sigma + H \end{pmatrix}, \quad (5.12)$$

which is crucial for a large variety of phenomena in cavity-boson systems. This includes, among others, the exceptional point instability in the Dicke model, see discussions in Section 6.

The effects of driving can be systematically captured by promoting the Green functions into the Floquet space, as introduced in Section 2.1. In the absence of bosonic particle-hole coupling, this combination of Floquet and Keldysh formalism is straightforward, where the most important ingredient is to implement the Floquet structure in the thermal distribution,

$$\rho_{m,n}^f = \delta_{m,n} \rho(\omega - m\Omega) = \delta_{m,n} \coth\left(\frac{\omega - m\Omega}{2T}\right). \quad (5.13)$$

Nevertheless, the particle-hole coupling brings in more complexity. We illustrate this by first considering the static-dissipative system with the full Floquet structure implemented. Most straightforwardly, in the $(0,0)$ -Floquet sector, we naturally have $(\mathbb{G}_{\text{static}}^{R/K})_{0,0}^{-1} = (G_{\text{static}}^{R/K})^{-1}$. However, in the $(1,1)$ -Floquet sector, the Floquet construction Eq. (2.4) dictates that the Hamiltonian is now effectively shifted by the driving frequency $H \mapsto H + \Omega$. This yields the retarded Green function as

$$(\mathbb{G}_{\text{static}}^R)_{1,1}^{-1} = \begin{pmatrix} \omega + i\Sigma - H - \Omega & K \\ K & -\omega - i\Sigma - H - \Omega \end{pmatrix}. \quad (5.14)$$

Remarkably, the accompanying picture that $\mathbb{G}_{1,1}(\omega + \Omega) = \mathbb{G}_{0,0}(\omega)$ becomes invalid. Instead, the frequency is shifted in opposite directions for particles and holes. From another point of view, the energies of the particle excitations and hole excitations are both shifted away from the zero energy in a symmetric way, and the particle-hole symmetry of the problem is preserved. Meanwhile, we expect the same arguments are also valid with respect to the thermal distribution ρ^f . Depending on the nature of particle or hole, the thermal

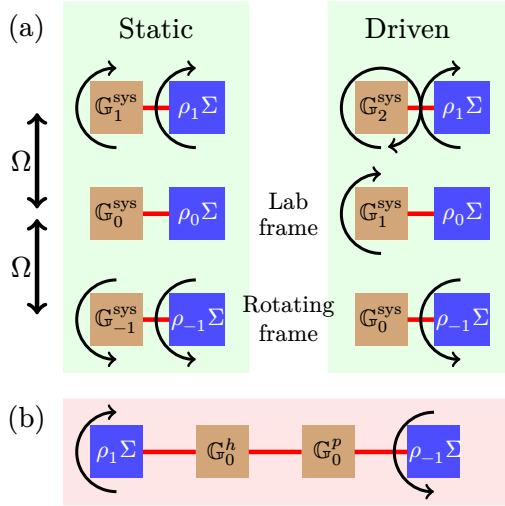


Figure 5.3: (a) Schematics illustrating the behaviours of (brown) the system and (blue) the bath in the -1 , 0 and $+1$ Floquet sectors in a static and a driven system. In the static system, the system and the bath have synchronised dynamics. They are either both static or both rotating at the same rate in each Floquet sector. In the driven system, there is always a relative rotation between them in all Floquet sectors. In the driven system, effectively the system is shifted one Floquet sector upwards, while the bath is kept unmoved. (b) In the presence of particle-hole coupling in the driven system, effectively the particle sector and the hole sector are coupled to baths rotating at opposite directions. This gives rise to the stability and instability mechanisms of driven-dissipative systems to be discussed in Chapter 6. Here ρ_m refers to $\rho(\omega - m\Omega)$.

distribution is also shifted in opposite directions, $\rho_{m,n}^f = \delta_{m,n} \coth\left(\frac{\omega \mp m\Omega}{2T}\right)$. This thus yields the Keldysh component of the inverse Green function as

$$(\mathbb{G}_{\text{static}}^{-1})_{1,1}^K = \tau_z \begin{pmatrix} 2i\rho(\omega - \Omega)\Sigma & 0 \\ 0 & 2i\rho(\omega + \Omega)\Sigma \end{pmatrix}. \quad (5.15)$$

The Green functions $(\mathbb{G}_{\text{static}}^{R/A})_{0,0}^{-1}$ and $(\mathbb{G}_{\text{static}}^{R/A})_{1,1}^{-1}$ are physically equivalent. As illustrated in Fig. 5.3(a), the Green functions in the $(1,1)$ -Floquet sector views both the system and bath in a rotating frame, but there should be no relative rotations between them.

After understanding the static-dissipative bosonic particle-hole coupled system in the Floquet-Keldysh formalism, we now proceed to consider the driven-dissipative counterpart. Relative rotations between the system and the bath

generally results in an incompatibility between the Green function \mathbb{G}^R (i.e. system) and the thermal distribution matrix ρ^f (i.e. bath), meaning that the distribution of particles becomes non-thermal from the perspective of the system [see illustration in Fig. 5.3(a)]. Generally, \mathbb{G}^R and ρ^f cannot be diagonalised simultaneously in the Floquet space, leading to driven effects which cannot be captured by the effective stroboscopic Hamiltonian. Anticipating a more general discussion in Chapter 10, for the moment we focus on the case of driven-dissipative quantum gaseous systems, where the system always experiences a rotation of $\mathbb{P} = \mathbb{F}_1$ relative to the bath, cf. Eq. (2.15), because the driving frequency dominates over the other energy scales of the system. This rotation keeps ρ^f diagonal in the Floquet space, but effectively shifts the thermal distribution by one Floquet sector. When the driving frequency is large in comparison to the temperature, effectively the thermal distribution appears uniform, $\rho = \coth(\omega/2T) \rightarrow \rho = \coth[(\omega - \Omega)/2T] \approx 1$, as illustrated in Fig. 5.2. This argument can be substantiated using the Keldysh formalism. In the rotating frame where the system is static and the bath has a relative rotation given by $\mathbb{P} = \mathbb{F}_{-1}$, the retarded and Keldysh Green functions for both the system and the bath are given respectively by

$$\begin{aligned} (\mathbb{G}_{\text{driven}}^R)^{-1} &= (\mathbb{G}_{\text{system}}^R)^{-1} + \mathbb{P}^\dagger (\mathbb{G}_{\text{bath}}^R)^{-1} \mathbb{P} = (\mathbb{G}_{\text{system}}^R)^{-1} + (\mathbb{G}_{\text{bath}}^R)^{-1} \\ (\mathbb{G}_{\text{driven}}^{-1})^K &= \mathbb{P}^\dagger (\mathbb{G}_{\text{bath}}^{-1})^K \mathbb{P} \Rightarrow (\mathbb{G}_{\text{driven}}^{-1})_{i,j}^K = (\mathbb{G}_{\text{static}}^{-1})_{i-1,j-1}^K. \end{aligned} \quad (5.16)$$

Since the bath is Markovian, i.e. its spectral function Σ is independent of frequency ω , the relative rotation between the system and the environment is not explicit in the retarded Green function. However, it becomes explicit in the Keldysh Green function, where the thermal distribution is frequency-dependent. We thus find in the $(0, 0)$ Floquet sector that

$$\begin{aligned} (\mathbb{G}_{\text{driven}}^R)_{0,0}^{-1} &= (\mathbb{G}_{\text{static}}^{-1})_{0,0}^K = \begin{pmatrix} \omega + i\Sigma - H & K \\ K & -\omega - i\Sigma - H \end{pmatrix} \\ (\mathbb{G}_{\text{driven}}^{-1})_{0,0}^K &= (\mathbb{G}_{\text{static}}^{-1})_{-1,-1}^K = \tau_z \begin{pmatrix} 2i \operatorname{sgn}(\omega + \Omega)\Sigma & 0 \\ 0 & 2i \operatorname{sgn}(\omega - \Omega)\Sigma \end{pmatrix} \\ &\stackrel{|\omega| \ll \Omega}{=} \tau_z \begin{pmatrix} 2i\Sigma & 0 \\ 0 & -2i\Sigma \end{pmatrix} = 2i\Sigma\tau_0, \end{aligned} \quad (5.17)$$

where we have assumed that the driving frequency Ω dominates over other energy scales of the system. To understand the unusual physical effects achieved by driving, we should focus on the results $\tau_z(2i\Sigma\tau_z)$. The first prefactor of τ_z is a standard construction of the bosonic Nambu space. The second τ_z indicates that the particles and holes are effectively experiencing opposite thermal distributions $\rho = \pm 1$, as they are rotating in opposite directions in comparison to the bath [see Fig. 5.3(b)]. Such intrinsic relative rotation

between particles and holes induces significant effects when the two sectors are coupled to each other, which will be discussed in details in Chapter 6.

5.3 From formalism to practical methodology: Hamiltonian and Lindbladian

Going through the full calculation based on the Keldysh Green function can be laborious and is avoided for quantum gaseous systems in this Part. To conclude this Chapter 5, we discuss the validity of several simplified representations of the Keldysh Green function, mainly including the Hamiltonian and the Lindbladian.

Static, non-dissipative systems – Hamiltonian

For a static, non-dissipative system, the Keldysh representation becomes redundant and the conventional quantum many-body theory is sufficient. In this case, the Hamiltonian already contains all information of the quantum system. As a result, it is possible to extract observables, for example quantum fluctuations and stability of the quantum state, by direct diagonalisation of the Hamiltonian.

Driven systems – Lindblad form

For quantum optical systems, one important tool for analysing the system dynamics is the Heisenberg equations of motion Eq. (2.20), which are derived from the Liouvillian master equation Eq. (2.19), and in turn equivalent to the driven-dissipative Green function Eq. (5.17) for the description of, e.g. equal-time observables, as shown in Ref. [82]. Indeed, the Markovian spectral function of the bath and the uniform thermal distribution together provide a simple form for taking dissipation into account in the driven system. In contrast, because of the non-trivial time-dependence corresponding to $\text{sgn}(\omega)$, a similarly simple form of equations of motion does not exist for static dissipative systems.

The Liouvillian equation of motion serves as a representation of the Keldysh Green function retaining many useful information of the quantum system. It can thus be used for investigating not only dynamics but also other properties of steady states of driven-dissipative systems, like quantum fluctuations, excitations and stability. This is usually solved using two different kinds of techniques. The first technique uses the stationarity of the steady states, and sets the time derivative of expectation values of corresponding quantum quantities in the Liouvillian evolution to be zero. The second technique called third quantisation [71, 72] uses exact diagonalisation to solve the excitation spectrum of a Liouvillian with quadratic Hamiltonian and linear jump operator. These two methods are complementary to each other and probe different aspects of

the system. A discussion relating and comparing the Keldysh formalism and the third quantisation technique can be found in Appendix B.7.

While dealing with the Liouvillian equation of motion and third quantisation, there is a caveat regarding to the non-dissipative limit. Specifically, the usual Heisenberg equation of motion for static, non-dissipative systems is recovered by setting $\kappa = 0$. This implies setting $\kappa = 0$ loses the information on whether the system is static or driven. This can be understood from two perspectives. From the general field theory perspective, it is always necessary to choose the contour when passing through a pole of the Green function. This corresponds to an infinitesimal dissipation rate $\kappa \rightarrow 0$. From the specific perspective of the Keldysh formalism, the information of uniform thermal distribution is encoded in $(G^{-1})^K = 2i\Sigma$, which in turn translates to the term $\sum_i \kappa_i L_i \rho L_i^\dagger$ in the Liouvillian. This has serious consequences in the validity of our later application of different methods for investigating the system stability and quantum fluctuations. As a general rule, the features of a driven, non-dissipative system should be considered in the limit $\kappa \rightarrow 0$ instead of taking exactly $\kappa = 0$, although in some scenarios, both approaches might yield the same results.

Static, dissipative system

We are now left with the final case of static, dissipative systems, whose treatment requires the full Keldysh formalism. Nevertheless, we understand from conventional arguments that dissipation always stabilises an eigenstate with lower energy in this scenario, and it will not be a focus of this thesis.

In conclusion, the formalism and its relation to the practical methodology are essential for our understanding of driven-dissipative stability and dynamics discussed below for a variety of cavity-boson systems.

6 | Mechanisms of driven-dissipative stabilities and instabilities

Originality declaration: This Chapter uses established results on the Dicke model [114] and Tavis-Cummings model [79, 80, 183] for elaborating the mechanisms of driven-dissipative stabilities and instabilities. The discussion and classification of these mechanisms are our new unpublished results. In Section 6.2, we use MCTDH-X to simulate the cavity fluctuations in the cavity-boson system and compare them to the prediction from the Dicke model. This is an improved result based on part of our published work [Phys. Rev. A 100, 013611 \(2019\) \[RL8\]](#).

Drive and dissipation together can stabilise completely different phases of matter from the static, non-dissipative system. In Chapter 5, we understood the significant driving impacts on the thermal distributions felt by the system. In this Chapter, we illustrate further driven-dissipative effects on two well-studied models, the Dicke model [114] and the Tavis-Cummings model [79, 80, 183], where direct comparison between closed and open systems are possible. This allows us to identify the different mechanisms through which the system destabilises, and more importantly, how these mechanisms are induced and impacted by drive and dissipation, respectively.

Specifically, we will investigate the quantum fluctuations in and the stability of the normal phase, and view them from the perspective of our narrative above. The analysis requires an effective Hamiltonian describing the fluctuations in the mean-field state, which can be obtained using a Holstein-Primakoff transformation [69]. In the normal phase where $\langle a \rangle = 0$, $\langle J_z \rangle = -N/2$, $\langle J_x \rangle = 0$, we can approximate

$$J_x \approx \sqrt{N}(b + b^\dagger), \quad J_z \approx -\frac{N}{2} + b^\dagger b, \quad (6.1)$$

where b is a bosonic field describing the atomic fluctuations. A schematic illustrating this transformation is shown in Fig. 6.1, and more details of the transformation can be found in Appendix B.3.

6.1. The Dicke model and the cavity-boson system

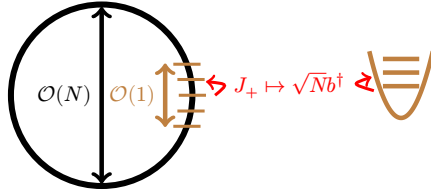


Figure 6.1: Schematics of Holstein-Primakoff transformation. The bosonic mode after transformation provides local information in the vicinity of the mean-field solution of the original collective spin system.

Holstein-Primakoff Hamiltonians can indicate the stability of the original state. A high occupation of the Holstein-Primakoff bosonic mode indicates a large deviation from the mean-field description. However, since the transformed Hamiltonian truncates the Hilbert space of the system in the vicinity of the mean-field solution to the order of $\mathcal{O}(1)$, any finite occupation of the Holstein-Primakoff bosonic mode indicates that the deviation has not reached the order of $\mathcal{O}(N)$. The mean-field description thus remains valid. In contrast, if there exists a mechanism activating an infinite occupation of the Holstein-Primakoff bosonic modes, it corresponds to a deviation in the order of $\mathcal{O}(N)$ in the full system, which invalidates the mean-field description. In the following, we discuss the different mechanisms leading to such infinite occupation.

6.1 The Dicke model and the cavity-boson system

6.1.1 Stability of the normal phase in the Dicke model – Exceptional point instability

The fluctuations in the normal phase of the Dicke model Eq. (3.1) are described by the Holstein-Primakoff Hamiltonian [114] (see Appendix B.3 for detailed calculations)

$$H = \omega_c a^\dagger a + \omega_0 b^\dagger b + \lambda(a + a^\dagger)(b + b^\dagger), \quad (6.2)$$

where a and b are the cavity and atomic harmonic oscillator modes, respectively. The coupling of these two modes indicates that the excitations described by this Hamiltonian are of polaritonic nature.

In the static, non-dissipative system, the validity of the fluctuation-dissipation relation Eq. (5.7) indicates that the Hamiltonian contains all the required information, which can be extracted by diagonalisation. However, the diagonalisation of the Hamiltonian in the Nambu space needs to respect the symplectic nature of bosonic Bogolyubov transformations. A systematic procedure to solve

these transformations is available through the following matrix written under the basis $(a, b, a^\dagger, b^\dagger)^T$ [184–186]

$$\tilde{H} = \tau_z H = \begin{pmatrix} \omega_c & 0 & \lambda & \lambda \\ 0 & -\omega_0 & \lambda & \lambda \\ -\lambda & -\lambda & -\omega_c & 0 \\ -\lambda & -\lambda & 0 & -\omega_0 \end{pmatrix}. \quad (6.3)$$

The matrix \tilde{H} is also referred to as the *dynamical matrix* and denoted by D in literatures. Its construction is essentially similar to the construction of $\tilde{G}^{R/A}$ in Eq. (5.11), and is discussed in more details in Appendix B.6. This matrix can be diagonalised using standard technique of similarity transformation. Both the real and imaginary parts of its spectrum are symmetric about zero energy by construction due to its particle-hole symmetry:

$$E = \pm E_\pm, \quad E_\pm = \pm \frac{1}{\sqrt{2}} \sqrt{\omega_c^2 + \omega_0^2 \pm \sqrt{(\omega_c^2 - \omega_0^2)^2 + 16\lambda^2 \omega_c \omega_0}}. \quad (6.4)$$

As the coupling strength becomes higher than the critical value λ_c given in Eq. (3.11), the spectrum E goes from real to imaginary, indicating instability.

$$E = \pm |E| \xrightarrow{\text{exceptional point}} E = \pm i |E|. \quad (6.5)$$

This is an exceptional point instability stemming from the symplectic structure of the bosonic Nambu space. It corresponds to an instability induced by spontaneous symmetry breaking, and its existence is thus completely insensitive to the driven-dissipative nature of the system.

Using the third quantisation technique [71, 72] for calculating the excitation spectrum of the driven-dissipation system, whose details are shown in Appendix B.4, we find

$$E_{\text{driven-dissipative}} \approx E_{\text{static,non-dissipative}} + \frac{i}{2} \kappa \quad (6.6)$$

as illustrated in Fig. 6.2, where $E_{\text{static,non-dissipative}}$ refers to the results in Eq. (6.4). Notice that we have chosen a convention of the third quantisation such that its real and imaginary parts are consistent with those obtained from the usual Hamiltonian analysis. The constant positive shift in the imaginary part is attributed to the dissipation, and makes the spectrum generally complex. It postpones but does not prevent the advent of a negative imaginary part of E due to exceptional point instability. Particularly, the instability is almost insensitive to the dissipation far from the critical point. We thus conclude that drive and dissipation only bring in relatively small quantitative changes to the stability of the normal state. We remark that the dissipative shifting of the phase boundary should intuitively not be seen in a static system at zero temperature.

6.1. The Dicke model and the cavity-boson system

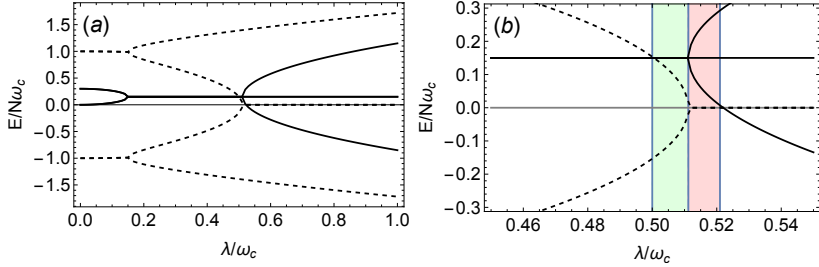


Figure 6.2: The excitation spectrum of the normal phase of the Dicke model. The solid lines indicate the stability of the state, with negative values indicating the state being unstable. The dashed lines indicate the energy of the excitation. Panel (b) is a zoom-in of panel (a) in the vicinity of the critical point. The green (red) region is where dissipation implicitly (explicitly) stabilises the exceptional point instability. Parameters are taken as $\omega_0 = \omega_c$, $\kappa = 0.3\omega_c$.

6.1.2 Cavity fluctuations in the normal phase of the Dicke model

We proceed to investigate the cavity fluctuations in the normal phase, where completely different techniques are used in static and driven systems. Particularly, the validity of different techniques reflects the validity of our arguments in Chapter 5 based on the Keldysh formalism, and sheds light on the important consequences from the change in the effective thermal distribution.

In the static system where the energy minimisation argument is obeyed, the particles (holes) are occupying the state with the lowest positive energy $+E_-$ (highest negative energy $-E_-$). We can thus find the cavity fluctuation by directly diagonalising the Holstein-Primakoff Hamiltonian and calculating the occupation of the state,

$$\begin{aligned} \langle a^\dagger a \rangle &\approx \frac{\omega_c(\omega_0^2 - \omega_c^2) - 4\lambda^2\omega_0 + \omega_c\sqrt{(\omega_c^2 - \omega_0^2)^2 + 16\lambda^2\omega_0\omega_c}}{\sqrt{2E_-}\sqrt{(\omega_c^2 - \omega_0^2)^2 + 16\lambda^2\omega_0\omega_c}} \\ &\sim \frac{1}{E_-} \sim \frac{1}{(\lambda_c - \lambda)^{1/2}}, \end{aligned} \quad (6.7)$$

where the critical value λ_c has been given in Eq. (3.11).

In the driven-dissipative system, similar energetic arguments are no longer valid, and the cavity fluctuations thus need be found by solving the equations of motion for the family of correlation operators, whose values are set to be 0 for the steady states [79, 104, 116, 187]. There are ten equations in total governing the expectation values of the correlation operators, as given by the

following equations and their complex conjugated counterparts

$$\begin{aligned}
 0 &= \partial_t \langle aa \rangle = -(2i\omega + 2\kappa) \langle aa \rangle - 2i\lambda (\langle ab \rangle + \langle a^\dagger b \rangle) \\
 0 &= \partial_t \langle a^\dagger a \rangle = i\lambda \langle (a - a^\dagger)(b + b^\dagger) \rangle - 2\kappa \langle a^\dagger a \rangle \\
 0 &= \partial_t \langle bb \rangle = -2i[\omega_0 \langle bb \rangle + \lambda (\langle ab \rangle + \langle a^\dagger b \rangle)] \\
 0 &= \partial_t \langle b^\dagger b \rangle = i\lambda \langle (b - b^\dagger)(a + a^\dagger) \rangle \\
 0 &= \partial_t \langle ab \rangle = -i(\omega_0 + \omega - i\kappa) \langle ab \rangle - i\lambda (\langle aa \rangle + \langle bb \rangle + \langle a^\dagger a \rangle + \langle b^\dagger b \rangle + 1) \\
 0 &= \partial_t \langle a^\dagger b \rangle = -i(\omega_0 - \omega - i\kappa) \langle a^\dagger b \rangle - i\lambda (\langle a^\dagger a^\dagger \rangle - \langle bb \rangle + \langle a^\dagger a \rangle - \langle b^\dagger b \rangle).
 \end{aligned} \tag{6.8}$$

The cavity fluctuation can thus be found as

$$\langle a^\dagger a \rangle = \frac{\lambda^2 (\omega_c^2 + \kappa^2)}{2\omega_0 (\omega_0 (\omega_c^2 + \kappa^2) - 4\lambda^2 \omega_c^2)} \sim \frac{1}{\lambda_c - \lambda}. \tag{6.9}$$

We now provide a qualitative estimation for the difference between static and driven systems from the structure of the Keldysh Green function. In a static system, the fluctuation-dissipation relation Eq. (5.7) clearly indicates that $G^K(\omega = E_-) \sim 1/E_-$, which is consistent with our results for the energy spectrum Eq. (6.4) and the fluctuations Eq. (6.7). In the driven system, however, the shifting of the thermal distribution together with the bosonic Nambu structure effectively changes the relation between the retarded/advanced Green function and the Keldysh component of the inverted Green function into $[(\mathbb{G}^R)_{0,0}^{-1} - (\mathbb{G}^A)_{0,0}^{-1}] = 2i\tau_z (\mathbb{G}^{-1})_{0,0}^K$, cf. Eq. (5.17), where an extra factor of τ_z in the Nambu space is required, and the effective thermal distribution $\rho(\omega) = 1$ is already taken into account. This further invalidates the simplification of Eq. (5.6) into the fluctuation-dissipation relation Eq. (5.7), indicating $G^K(\omega = E_-) \sim 1/E_-^2$ instead. This argument is valid even at zero temperature, and thus results in Eq. (6.9). Based on this consideration, we remark that the fact that the driven-dissipative phase transition and thermal phase transition sharing the same critical exponents is essentially a coincidence. Even though their mechanisms both are related to the thermal distribution $\rho(\omega)$ in a certain way, they are fundamentally different.

It should be noted that, upon setting $\kappa = 0$ in Eq. (6.8), the family of equations becomes under-determined with a two-dimensional null space, accommodating in principle both the solutions for the static and driven systems (Eq. (6.7) and Eq. (6.9)). The pathology of setting $\kappa = 0$ can only be observed in the calculation of quantum fluctuations, but not in the macroscopic behaviours like the dynamical evolution of the system in Eq. (3.10). Indeed, the fluctuations are intrinsically quantum and related to the Keldysh Green function, confirming our previous argument that taking $\kappa = 0$ is ill-defined, because it loses the information on how the poles of the Green function are approached.

6.1.3 Cavity fluctuations in a cavity-boson system with effective long-range interaction

For a comprehensive comparison between the cavity-boson system and the Dicke model, we use MCTDH-X to simulate the critical exponent of the cavity fluctuations for the driven-dissipative system, making use of the beyond-mean-field capability of MCTDH-X.

In order to reduce the computational cost to a feasible level, we simplify the equation of motion of the cavity-boson system by taking the bad-cavity limit, where the cavity dissipation is assumed to be much larger than the atomic energy scale $\kappa \gg \omega_0$, such that the cavity always follows the atomic configuration. This can be described by adiabatically eliminating the cavity field and setting $\partial_t a = 0$ in Eq. (3.7). It yields the following steady state relation between cavity and atomic operators [160]

$$a = \frac{\eta}{\Delta_c + i\kappa} \int dx \Psi^\dagger(x) \Psi(x) \cos(k_c x). \quad (6.10)$$

Substituting into the cavity-boson system Hamiltonian Eq. (3.6), we obtain (see Ref. [115] and Section 3.3 of Ref. [188])

$$H = \int dx \Psi^\dagger(x) \left\{ -\frac{\nabla^2}{2m} + V_{\text{trap}}(x) \right\} \Psi(x) + \frac{\eta^2}{\Delta_c^2 + \kappa^2} \int dx dx' \Psi^\dagger(x) \Psi(x) \Psi^\dagger(x') \Psi(x') \cos(k_c x) \cos(k_c x'), \quad (6.11)$$

where turn off the atom-atom contact interaction for emphasising the critical behaviours. For clarity we consider the one-dimensional version of the system by taking $z = 0$. This should not have an impact on the critical behaviours, because the transition is driven by an effective infinite-range two-body interaction, which leads to the Weiss mean-field scenario, minimising the effects of dimensionality. Under this treatment, the cavity fluctuation can be extracted from the atomic correlation functions as

$$\begin{aligned} \langle a^\dagger a \rangle &= \frac{\eta^2}{\Delta_c^2 + \kappa^2} [N(N-1)R + NB - N^2\theta^2] \\ R &= \int dx dx' \rho^{(2)}(x, x') \cos(k_c x) \cos(k_c x') \\ \theta &= \int dx d\rho(x) \cos(k_c x), \\ B &= \int dx \rho(x) \cos^2(k_c x), \end{aligned} \quad (6.12)$$

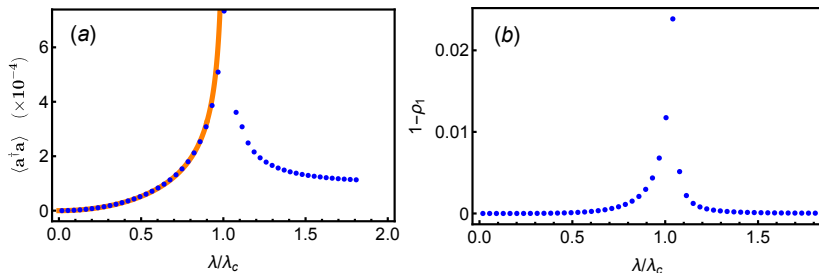


Figure 6.3: (a) The cavity fluctuations of (blue dots) the cavity-boson system simulated using MCTDH-X, which solves the many-body Schrödinger equation based on the effective infinite-range interaction Hamiltonian Eq. (6.11). It is consistent with (orange line) the analytical prediction from the closed system Eq. (6.7) in the normal phase, with the slight deviation close to the critical point stemming from convergence issue due to insufficient number of MCTDH-X orbitals. (b) The deviation of the simulation results from Gross-Pitaevskii mean-field limit, as characterised by the vacancy in the highest-occupying orbital $1 - \rho_1$. The system is perfectly described by mean-field limit when $1 - \rho_1 = 0$.

with $\rho^{(2)}(x, x') = \langle \Psi^\dagger(x) \Psi^\dagger(x') \Psi(x) \Psi(x') \rangle / N(N-1)$ the Glauber two-body correlation function and $\rho(x) = \langle \Psi^\dagger(x) \Psi(x) \rangle / N$ the one-body density distribution.

We investigate the implication of this limit for cavity fluctuations with the help of MCTDH-X. The cavity fluctuation is exactly consistent with the analytical results based on static system Eq. (6.7) in the normal phase, as compared in Fig. 6.3(a). Notice that quantum fluctuations are a many-body phenomenon, and can be captured in MCTDH-X only by activating at least a second orbital $M \geq 2$. This is confirmed in Fig. 6.3(b), which shows more and more orbitals are macroscopically occupied in the vicinity of the critical point.

With the effective infinite-range interaction yielded by adiabatic elimination, the openness of the system is no longer retained, and the dissipation indeed *merely* provides a renormalisation to the interaction strength. We emphasise that this is only partially because of the adiabatic elimination of the cavity field. Similar to putting $\kappa = 0$ in the calculation of quantum fluctuations above, adiabatic elimination of the cavity field only makes it ambiguous whether the system is static or driven. However, the system is then solved by MCTDH-X according to the many-body Schrödinger equation, where the system is fully treated as static. As a result, we are only able to extract critical exponents of static quantum phase transitions from MCTDH-X simulations. This exemplifies the potential failure of the adiabatic elimination for capturing important

6.2. The Tavis-Cummings model

features of driven-dissipative systems.

6.2 The Tavis-Cummings model

In the Dicke models, the driven-dissipative nature modifies the quantum fluctuations of the system, but does not have qualitative impact on the collective stability of the quantum state. In the following, we discuss the Tavis-Cummings model, where the stability of the normal phase is governed by mechanisms, unlike the exceptional point instability, are inherently related to the driven-dissipative nature of the system. The model is described by the Hamiltonian

$$H = \omega_c a^\dagger a + \sum_{i=1}^N \omega_0 |1_i\rangle\langle 1_i| + \frac{\lambda}{\sqrt{N}} (a^\dagger |0_i\rangle\langle 1_i| + a |1_i\rangle\langle 0_i|), \quad (6.13)$$

and has been investigated in details as the U(1) symmetry line of the interpolating Dicke–Tavis-Cummings model [79, 80, 183].

In the static system, energetic arguments predict that the Tavis-Cummings model has the same phase transition point λ_c [cf. Eq. (3.11)] as the Dicke model, above which the normal phase becomes unstable towards the superradiant phase. However, this transition is surprisingly not a result of spontaneous symmetry breaking, or more specifically by exceptional point instability, although the U(1) symmetry of the system is indeed broken in the ground state beyond the critical point. Instead, the Tavis-Cummings model is an integrable model [189–191] conserving a new quantity, $a^\dagger a + \sum_{i=1}^N |1_i\rangle\langle 1_i|$, in comparison to the Dicke model. As a result of this conservation, the system is not able to evolve ergodically in the whole Hilbert space, but only in the subspace corresponding to the given initial state. Particularly, the ground state at vanishing coupling strength, $\prod_{i=1}^N |0_i\rangle$, is completely decoupled from the rest of the Hilbert space. This analysis indicates that the superradiant transition of the Tavis-Cummings model is in essence a level crossing, and the system undergoes a Landau-Zener transition across it.

The unusual properties of the Tavis-Cummings model yield interesting consequences for the driven-dissipative system. We further investigate the Holstein-Primakoff Hamiltonian for its normal phase,

$$H = \omega_c a^\dagger a + \omega_0 b^\dagger b + \lambda (a^\dagger b + b^\dagger a). \quad (6.14)$$

This is a usual quadratic bosonic Hamiltonian which does not couple particle-like and hole-like excitations (cf. terms like $a^\dagger b^\dagger$), and the lack of such coupling has significant consequences in stability mechanisms as to be explained in details in Section 6.3. Upon diagonalisation, the spectrum of the system is

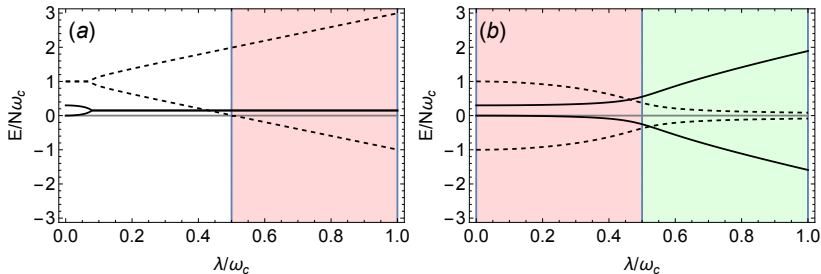


Figure 6.4: The excitation spectrum of the normal phase of (a) the Tavis-Cummings model and (b) the anti-Tavis-Cummings model. The solid lines indicate the stability of the state, with negative values indicating the state being unstable. The dashed lines indicate the energy of the excitation. In panel (a), the red region indicates where the driven nature stabilises the Landau-Zener transition. In panel (b), the red region indicates where the system is destabilised by dissipation, while the green region indicates where the system is destabilised by exceptional point instability. Parameters are taken as $\omega_0 = \omega_c$, $\kappa = 0.3\omega_c$.

found to be

$$E_{\pm} \approx \frac{\omega_c + \omega_0}{2} \pm \frac{\sqrt{(\omega_c - \omega_0)^2 + 4\lambda^2}}{2} + i\frac{\kappa}{2}, \quad (6.15)$$

which is shown in Fig. 6.4(a). Because of the absence of particle-hole symmetry, the Nambu space is no longer necessary and thus the real part of the spectrum is no longer symmetric about zero energy. In comparison to the excitation spectrum of the Dicke normal phase, this spectrum shows two main features: the absence of exceptional point, and the driven-dissipative stabilisation.

The spectrum remains completely real apart from the contribution directly from dissipation, as in fundamental contrast to the Dicke model. A level crossing instead of an exceptional point gap closure is clearly seen at the critical point: one of the excitation branch goes from positive to negative energy as λ exceeds the critical value λ_c . This is consistent with our previous arguments. In static system, this level crossing immediately indicates a phase transition to an energetically more favourable phase, but in the driven-dissipative system, the spectrum confirms that the normal phase is always stable. The significant contrast between these two systems can be explained using our Keldysh-based arguments developed in Section 5.2, which is schematically shown in Fig. 6.5. In the static system, the negative energy immediately corresponds to a negative thermal distribution $\rho = 1 \rightarrow -1$, which indicates a preference for the system absorbing energies from the bath, and implies an instability of the state towards lower-energy states. In contrast, in the driven system, the thermal distribution

6.3. Stabilisation and destabilisation mechanisms in driven-dissipative systems

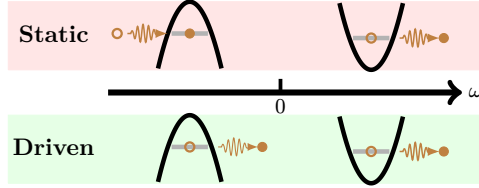


Figure 6.5: Cartoon illustrating stability of a dissipative particle-like state with positive and negative energies in static and driven systems. When the system energy is positive, the system always tends to dissipate energies to the bath. When the system energy is negative, the static system tends to absorb energies from the bath because of a change in thermal distribution $\rho(\omega)$, while the driven system tends to dissipate energies into the bath.

is insensitive to the change of excitation energy, indicating that the system keeps losing energies to the bath, and the normal state remains stable.

The north pole of the spin- $N/2$ Bloch sphere is another collective state worth investigating, which we call the inverted state because of its population inversion. It is also characterised by a vanishing macroscopic cavity field $\langle a \rangle = 0$, and the fluctuations in it are described by the Holstein-Primakoff Hamiltonian

$$H = \omega_c a^\dagger a + \omega_0 b^\dagger b + \lambda(a^\dagger b^\dagger + ab). \quad (6.16)$$

Naively, we expect that this Hamiltonian is exactly the same as Eq. (6.15) via the identification $b^\dagger \mapsto c$. This is, however, not true as indicated by the vastly different excitation spectrum shown in Fig. 6.4(b). The exceptional point is reinstated similar to the one from the Dicke model, while the driven-dissipative feature leads to an intriguing destabilisation mechanism unseen before.

The essential difference between these two cases comes from the fact that the number of bosonic excitations as described by a harmonic oscillator is bounded from below but not above. While the coupling $a^\dagger b + b^\dagger a$ [Eq. (6.15)] conserves the total number of excitations, the coupling $a^\dagger b^\dagger + ab$ [Eq. (6.16)] does not, providing a mechanism for creating a large number of excitations and destabilising the collective state.

6.3 Stabilisation and destabilisation mechanisms in driven-dissipative systems

After the case-by-case study of several scenarios, we summarise below and illustrate in Fig. 6.6 the three mechanisms leading to stabilities and instabilities of states in the driven-dissipative Dicke-like models. More specifically, we investigate the dissipative processes of two bosonic harmonic oscillators, one

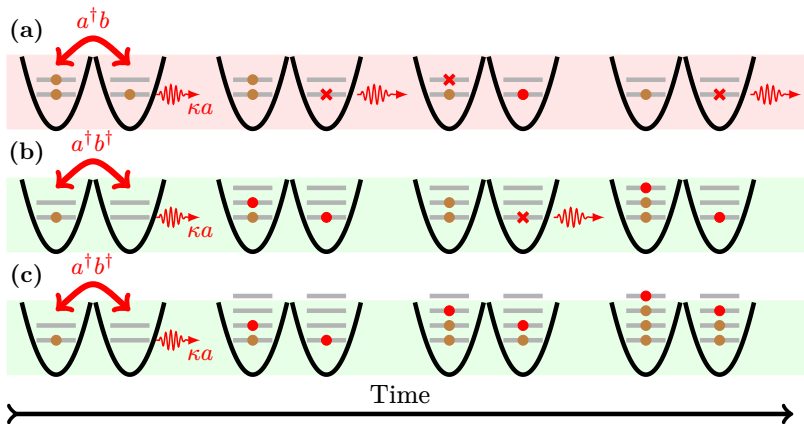


Figure 6.6: Cartoons illustrating and summarising different mechanisms stabilising and destabilising a collective state in a driven-dissipative Dicke model or Tavis-Cummings model. These mechanisms can all be described by two coupled Holstein-Primakoff harmonic oscillators, where one of them is dissipative. Here, the brown circles represent the existing excitations, the red circles the newly created excitations, whereas the red crosses the newly annihilated/dissipated excitations.

Description of processes: (a) Dissipation stabilises perturbations and fluctuations by decreasing the total number of excitations. (b) When coupling between particle-like and hole-like excitations exists, dissipation in one oscillator can destabilise the system by accumulating excitations in the non-dissipative oscillator. This is an intrinsically quantum process not reproducible in classical systems. (c) A destabilisation process through exceptional point instability, where an accumulation of excitations is energetically favourable.

dissipative and the other not, which are coupled either as $a^\dagger b$ [Fig. 6.6(a)] or $a^\dagger b^\dagger$ [Fig. 6.6(b,c)]

Figure 6.6(a,b) illustrates the first two mechanisms which are intrinsically related to the driven-dissipative nature. The coupling $a^\dagger b$ conserves the total number of bosonic excitations in the oscillators, which is only annihilated by dissipation. As a result, any perturbation from the state will eventually decay by dissipation, stabilising the underlying collective state. A characteristic of such driven-dissipative stabilisation mechanism is that its stability rate is largely independent of most parameters of the system, but only on the dissipation rate,

$$\text{Im } E_{\min} \approx \frac{\kappa}{2} > 0 \quad (6.17a)$$

where the subscript min denotes the branch of the excitation spectrum with

the smallest imaginary part, which determines the stability of the system.

In contrast, the coupling $a^\dagger b^\dagger$ creates and annihilates the bosonic excitations in pairs, with one in each oscillator. Unexpectedly, the excitation in one oscillator can decay due to dissipation, leaving the excitation in the other oscillator alone and decoupled from annihilation channel. As a result, dissipation in one oscillator can effectively accumulate excitations in the non-dissipative oscillator, making the state unstable. A characteristic of such driven-dissipative destabilisation mechanism is that its instability rate is controlled by not only the dissipation rate of the cavity field, but also the coupling strength as well,

$$\text{Im } E_{\min} \approx -\frac{4\lambda^2\kappa}{(\omega_c + \omega_0)^2} < 0. \quad (6.17b)$$

We finally discuss the exceptional point instability [Fig. 6.6(c)]. The coupling $a^\dagger b$ conserving the total number of excitations forbids a destabilisation channel for the state, while the coupling $a^\dagger b^\dagger$ favours excitations when the coupling strength overcomes the energy cost of introducing more excitations. The creation of a macroscopic number of excitations will eventually result in destabilisation of the collective state. Indeed, the Tavis-Cummings model still possesses a symmetry-breaking exceptional point instability at large coupling strength, but the normal state is insensitive to it only because of the integrability of the model and the resulting decoupling of the normal state from the rest of the system, particularly the cavity field. In other words, the normal state is a dark state of the system [192–194]. The presence of dissipation can suppress this process by partially removing the excitations similar to the first mechanism.

Remarkably, the dissipative destabilisation (the second mechanism) has unique features and unlike the other two mechanisms, (i) it requires at least two coupled oscillators, and (ii) it is intrinsically a quantum mechanism. The first feature can be understood straightforwardly by an investigation into the Kerr oscillators [195, 196], which consists of only one oscillator but manifests exceptional point instability as well as its partial dissipative stabilisation. The second feature means that this mechanism does not have a classical counterpart by mapping the quantum mechanical model Eq. (6.16) to a classical one by $a \mapsto \frac{1}{\sqrt{2}}(\sqrt{\omega_0}q + i\frac{1}{\sqrt{\omega_0}}p)$ (supposing $\omega_0 = \omega_c$). Such mapping yields a classical Hamiltonian

$$H = \frac{1}{2}(p_1^2 + p_2^2 + \omega_0^2 q_1^2 + \omega_0^2 q_2^2) + \frac{\lambda}{2} \left(\omega_0 q_1 q_2 - \frac{1}{\omega_0} p_1 p_2 \right), \quad (6.18a)$$

and correspondingly a classical Lagrangian upon Legendre transformation

$$L = \frac{1}{2(1 - \alpha^2)^2} \left[(1 - 3\alpha^2)(\dot{q}_1^2 + \dot{q}_2^2) - 4\alpha^3 \dot{q}_1 \dot{q}_2 - \frac{\omega_0^2}{2}(q_1^2 + q_2^2 + 2\alpha q_1 q_2) \right], \quad (6.18b)$$

with $\alpha = \lambda/2\omega_0$. Investigating the dynamics of this system using Euler-Lagrange equation, it can be shown that although traits of the exceptional point instability remain in this classical model, dissipation appearing as $\kappa\dot{q}_1$ always reduces rather than enhances perturbation. We thus confirm that the driven-dissipative destabilisation due to bosonic particle-hole coupling is inherently quantum mechanical.

6.4 Conclusions

With the investigation into the Dicke model and the Tavis-Cummings model, we have thus identified three driven-dissipative mechanisms determining the stability of the system in comparison to static systems in this Chapter: (i) partial stabilisation of the exceptional point instability by dissipation, (ii) stabilisation of negative energy particle-like excitations, and (iii) destabilisation of positive energy particle-like excitations via particle-hole coupling. These driven-dissipative mechanisms have substantial consequences. In a static system, we intuitively predict the stabilisation of classical and quantum states based on energy minimisation. A state with lower energy is always expected to be favoured by dissipation. However, this is no longer true in a driven system. In a driven system, the energy of an excitation becomes irrelevant to the stability of the state, and there is no intuitive picture describing which states are stabilised by dissipation in a driven system without going through calculations. Particularly, the naive picture that dissipation always tends to suppress the cavity field is incorrect. As a result, in driven systems, dissipation can in principle bring the system to any state regardless of the energy landscape. In hindsight, the discussion regarding to the energy landscape in Fig. 3.3 is thus no longer surprising. In fact, dissipation can in principle stabilise any dynamics, including any number (even including none and infinitely many) of quantum states as well as more exotic dynamics like limit cycles. These will be explored in the context of cavity-boson systems in the following Chapters 7, 8, and 9.

7 | Quasi-periodic dynamics and chaos in a cavity-boson system

As discussed in the last Chapter, the driven nature of quantum optical and gaseous systems potentially stabilises a large variety of dynamics. In this Chapter, we present the first example, where limit cycles and chaotic behaviours are predicted in the cavity-boson systems, and studied from both analytical and numerical perspectives. Alongside a series of works in the community, such as Refs. [126, 127, 143, 197], this work contributes to the eventual experimental realisation of the long-pursued topological pumps [131] and “discrete time crystals” [129] in cavity-boson systems. Apart from the dynamical aspects, this work also investigates new many-body phases in the system resulting from the dimerisation of the optical lattice.

Originality declaration: This Chapter is adapted from our published work *Phys. Rev. A* **101**, 061602(R) (2020) [RL2] under supervision of R. Chitra and in collaboration with Paolo Molignini and Axel Lode.

7.1 Introduction

The driven-dissipative nature of quantum optical and gaseous system potentially can destabilise the lowest-energy state, potentially resulting in a large variety of non-trivial dynamics in a quantum many-body system. One of the long-pursued goal of the community is the realisation of limit-cycle behaviours in such systems, where the system follows a periodic trajectory in the phase space in the long-time limit. In comparison to other commonly seen oscillations like Rabi oscillations, limit cycle has a time periodicity not trivially defined by the energies of the eigenstates, and its dynamics is strongly robust to perturbation during evolution. With the existence of limit cycles, it appears that the system has spontaneously broken the continuous or discrete time translational symmetry. As a result, they are also coined as “discrete time crystals” in literature, a phenomenon shown to be prohibited in static quantum systems [198, 199].

7.1. Introduction

Prior theoretical work highlighted the ability of blue-detuned cavity-atom system to stabilise limit cycles and chaos [126, 200]. Though the predicted limit cycles were not seen in the first experimental study of this regime, interesting dynamical instabilities were reported [201]. Motivated by this study, we go beyond Refs. [126, 200] and explore the atomic correlations and dynamical instabilities in a realistic harmonically trapped cavity-boson system [Fig. 7.1(a)], and map the rich phase diagram in Fig. 7.1(b). On the pathway to chaos, we reveal an unexpected hierarchical deformation of the optical lattice into a double-well lattice, which generates new correlated phases of the atoms. In the dynamically unstable regime, we also observe that quasi-periodicity dominates instead of strict periodicity, which is compatible with experiments. Our proposed phase diagram and methodology is relevant for different experimental realisations like in Refs. [102], [119], and [122]. In retrospect, our work indeed contributes to the eventual experimental realisation of both the topological pumps [131] and the “discrete time crystals” [129] in cavity-boson systems.

We consider a cavity-boson system with N bosonic atoms of mass m . From a computational perspective, since the physics of the system does not qualitatively depend on the dimensionality, we study a one-dimensional version of the model and later discuss the validity of the results obtained for the two-dimensional system. In the rotating frame of the pump laser, the system is described by the following coupled equations of motion for the cavity expectation value α and the atomic field operators $\Psi^{(\dagger)}(x)$ [160, 161]:

$$i\partial_t\Psi(x) = \left[-\frac{\partial_x^2}{2m} + g\Psi^\dagger(x)\Psi(x) + V_{\text{trap}}(x) \right. \\ \left. + U_0 \cos^2(k_c x)|\alpha|^2 + \eta \cos(k_c x)(\alpha + \alpha^*) \right] \Psi(x). \quad (7.1a)$$

$$\partial_t\alpha = (i\Delta_c - iNU_0B - \kappa)\alpha - i\eta N\theta. \quad (7.1b)$$

Here, k_c is the wave vector of the cavity field and corresponds to the recoil frequency $\omega_R \equiv k_c^2/2m$. g is the weak interatomic interaction, U_0 the atomic single photon light shift, η the effective pump rate, Δ_c the cavity detuning, and κ the cavity dissipation rate. The blue detuning of atoms and cavity is reflected in U_0 and Δ_c being positive, respectively. The atoms are confined by a harmonic trap $V_{\text{trap}}(x) = \frac{m}{2}\omega_x^2x^2$. Since we are interested in regimes far from the normal-superradiant boundary, the cavity is in a coherent state with negligible fluctuations [RL8, 78, 116, 117], and can thus be represented by a complex number α . The variables $\theta = \int dx\rho(x)\cos(k_c x)$ and $B = \int dx\rho(x)\cos^2(k_c x)$ in Eq.(7.1b) are the order parameters associated with superradiance, where $\rho(x) = \langle\Psi^\dagger(x)\Psi(x)\rangle/N$ is the position space density distribution. This equation of motion Eq. (7.1) is describing the same system as the Hamiltonian in Eqs. (3.6) and (4.1), but a different parameter regime is explored in this Chapter.

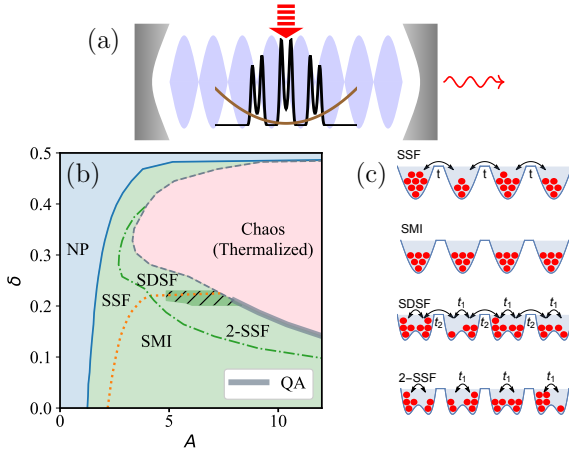


Figure 7.1: (a) Schematic setup of a cavity-BEC system with trapped bosons. (b) Phase diagram. For cavity detuning $0 < \delta < 1/2$, the system transitions from the normal phase to the dynamically unstable region via superradiance with increasing pump rate $A \propto \eta$. The strongly correlated phases are a self-organised superradiant (SSF), a self-organised Mott insulator (SMI), a self-organised dimerised superfluid (SDSF), and a self-organised second-order superfluid (2-SSF) phase. The orange line delineates superfluid phases and globally Mott insulating phases, while the green line marks the hierarchical self-organisation to dimerised phases. Pronounced sensitivity to the ramping protocol is seen in the hatched dark green region. At higher A , the system is dynamically unstable to the formation of quasiperiodic attractors (QA) followed by chaos. The QAs only exist in the region represented by the thick grey line, while the thin dashed section represents a direct transition to the chaos. The dimensionless detuning δ and the potential strength A are normalised with respect to NU_0 and $\sqrt{\omega_R}$, respectively [see Eq. (7.2)]. (c) Sketch of the SSF, SMI, SDSF, and 2-SSF phases.

This is essentially the same many-body system as presented in Eq. (3.6), but in the regime where the cavity is blue-detuned $\Delta_c > 0$, and the single-atom shift is positive $U_0 > 0$ in contrast to Chapter 4. In this case, self-organisation takes place in both a red-detuned cavity $\delta < 0$ and a blue-detuned cavity $0 < \delta < 1/2$ [102, 161, 202]. In the former case, the $\cos(k_c x)$ term dominates and the atoms are localised at the lattice sites $x_n = n\pi/k_c$ with all n either even or odd. However, in the latter case, the two terms in V_{cav} can be equally significant, forming a local double well at each site. This double-well lattice can realise the Su-Schrieffer-Heeger model in a cavity-fermion system [120]. This analysis provides the first glimpse of intrinsically different physics in the blue-detuned region.

The discussion of this system consists of two parts. In the first part, we apply an analytical point of view to investigate the non-trivial dynamics like limit cycle and chaos. For the illustration of these effects, it is enough to treat the system in one dimension and in the mean-field limit, including both the cavity and the atoms. In the second part, we apply the numerical tool MCTDH-X for investigating the beyond-mean-field aspects of the system. This mainly includes the different correlated phases due to dimerisation of the optical lattice in our system. Finally, MCTDH-X is also able to give us a guidance on the realisation of these dynamical and correlated phases in realistic two-dimensional experimental setups.

7.2 Mean-field features: Dynamical behaviours and dimerisation

The main characteristic features of the system are direct results of the cavity-induced potential. For our analytical considerations, we neglect the atomic interactions, atomic correlations, and the harmonic trap, and adiabatically eliminate the cavity field via setting $\partial_t \alpha = 0$. This makes the atoms effectively subject to the potential [161]

$$V_{\text{cav}}(x) = A^2 \omega_R [2(\delta - B)\theta \cos(k_c x) + \theta^2 \cos^2(k_c x)], \quad (7.2)$$

with $A = \eta N \sqrt{U_0} / \sqrt{[(\Delta_c - NU_0 B)^2 + \kappa^2] \omega_R}$ the dimensionless overall effective potential strength and $\delta = \Delta_c / NU_0$ the dimensionless cavity detuning. The cavity dynamically creates an optical lattice potential comprising two sinusoidal terms, $\cos^2(k_c x)$ and $\cos(k_c x)$, whose amplitudes are determined by the instantaneous atomic state via θ and B .

The blue-detuned cavity-boson system manifests a wide range of phases of matter and dynamical behaviours, including the atomic self-organisation, the double-well lattice, and the dynamical instabilities, most of which can be revealed by the evolution in the (B, θ) phase space in discretised time. The evolution can be found by noticing that the instantaneous potential Eq. (7.2) is controlled by the two order parameters from the past step, (B_t, θ_t) , and subsequently determines the quantum state and thus the parameters in the next step, (B_{t+1}, θ_{t+1}) . In order to obtain discretised evolution equations for these two parameters, we investigate the effective potential V_{cav} below while neglecting the atom-atom contact interaction $g = 0$.

When $B - \delta \geq |\theta|$, the minima of the effective potential lie at $x_n = 2n\pi/k_c$ [$x_n = (2n + 1)\pi/k_c$], $n \in \mathbb{N}$, for positive (negative) θ . In the vicinity of the minima, the effective potential can be expanded into a quadratic form

$$V_{\text{cav}}(x = x_n + \delta x) = \omega_R A^2 |\theta| (B - \delta - |\theta|) k_c^2 \delta x^2 \equiv \frac{m}{2} \Omega_1^2 \delta x^2. \quad (7.3)$$

The ground state of the effective potential can be approximated by a sum of Gaussians,

$$\rho(x; \theta, B) \propto \sum_n \exp \left[-\frac{m\Omega_1(\theta, B)(x - x_n)^2}{\hbar} \right]. \quad (7.4)$$

Suppose that at time t the density distribution of the atoms $\rho(x; \theta_t, B_t)$ is determined by the instantaneous θ_t and B_t . At the next time step, $\theta_{t+1} = \int_{-\infty}^{\infty} \cos(k_c x) \rho(x; \theta_t, B_t)$ and $B_{t+1} = \int_{-\infty}^{\infty} \cos^2(k_c x) \rho(x; \theta_t, B_t)$, respectively. According to the Gaussian ansatz of the density distribution, these are given explicitly by

$$\begin{aligned} \theta_{t+1} &= \text{sgn}(\theta_t) \exp \left(-\frac{k_c^2}{4m\Omega_1} \right) \\ &= \text{sgn}(\theta_t) \exp \left[-\frac{1}{4\sqrt{A^2|\theta_t|(B_t - \delta - |\theta_t|)/2}} \right] \end{aligned} \quad (7.5a)$$

$$\begin{aligned} B_{t+1} &= \frac{1}{2} + \frac{1}{2} \exp \left(-\frac{k_c^2}{m\Omega_1} \right) \\ &= \frac{1}{2} + \frac{1}{2} \exp \left[-\frac{1}{\sqrt{A^2|\theta_t|(B_t - \delta - |\theta_t|)/2}} \right] \end{aligned} \quad (7.5b)$$

The fixed points of the system (θ_{t+1}, B_{t+1}) are potentially the steady states of the system. This discretised time evolution can already predict the superradiant self-organisation phase boundary. Apart from the solution $(\theta = 0, B = 1/2)$ which is always satisfied, Eqs. (7.5) have another fixed point given by the solution to the following equation

$$\sqrt{|\theta|} \log |\theta| = -\frac{1}{2\sqrt{2}A\sqrt{\frac{1}{2} - \delta}} = -\frac{\sqrt{((\Delta_c - NU_0/2)^2 + \kappa^2)\omega_R}}{2\sqrt{2}\eta N\sqrt{NU_0/2 - \Delta_c}} \quad (7.6)$$

This is indeed the case when

$$\eta\sqrt{N} \geq \frac{e}{4\sqrt{2}} \frac{\sqrt{((\Delta_c - NU_0/2)^2 + \kappa^2)\omega_R}}{\sqrt{NU_0/2 - \Delta_c}}. \quad (7.7)$$

This result agrees reasonably well with the one obtained by a mapping to the Dicke model Eq. (3.11) $\eta\sqrt{N} \geq \frac{1}{2} \frac{\sqrt{((\Delta_c - NU_0/2)^2 + \kappa^2)\omega_R}}{\sqrt{NU_0/2 - \Delta_c}}$, by a difference of factor of $e/2\sqrt{2} \approx 0.96$. Nevertheless, the discretised time evolution predicts incorrectly a jump in the order parameter from $\theta = 0$ to $\theta = 1/e^2 \approx 0.14$ at the critical point. In the other limit where A is large, we notice that the superradiant fixed point of Eqs. (7.5) converges to $(|\theta| = 1, B = 1)$, which

7.2. Mean-field features: Dynamical behaviours and dimerisation

indicates that the condition $B - \delta \geq |\theta|$ is no longer satisfied. This signals that each lattice site dimerises into two sub-lattice-sites, and a different treatment is required.

When $|\theta| > B - \delta > 0$, the minima x_n of the effective potential satisfy

$$k^* = \frac{\pi k_c}{\arccos[(B - \delta)/|\theta|]}. \quad (7.8)$$

In the vicinity of the minima, the effective potential can be expanded as

$$V_{\text{cav}}(x = x_n + \delta x) = \omega_R A^2 k^2 [\theta^2 - (\delta - B)^2] k_c^2 \delta x^2 \equiv \frac{m}{2} \Omega_2^2 \delta x^2. \quad (7.9)$$

With the Gaussian ansatz of the ground state, the evolution of the parameters θ and B are given by

$$\begin{aligned} \theta_{t+1} &= \exp\left(-\frac{k_c^2}{4m\Omega_2}\right) \cos(k_c x_n) \\ &= \exp\left[-\frac{1}{4\sqrt{A^2[\theta_t^2 - (\delta - B_t)^2]/2}}\right] \frac{B_t - \delta}{\theta_t} \end{aligned} \quad (7.10a)$$

$$\begin{aligned} B_{t+1} &= \frac{1}{2} + \frac{1}{2} \exp\left(-\frac{k_c^2}{m\Omega_2}\right) (2 \cos^2 k_c x_n - 1) \\ &= \frac{1}{2} + \frac{1}{2} \exp\left[-\frac{1}{\sqrt{A^2[\theta_t^2 - (\delta - B_t)^2]/2}}\right] \left[2 \left(\frac{B_t - \delta}{\theta_t}\right)^2 - 1\right] \end{aligned} \quad (7.10b)$$

The dynamical evolution of the system following Eqs. (7.10) exhibits even more interesting feature, specifically a bifurcation, as A increases. This can be studied by linearisation in the vicinity of the fixed point, which is performed via the Jacobian

$$J = \begin{pmatrix} \frac{\partial \theta_{t+1}}{\partial \theta_t} & \frac{\partial \theta_{t+1}}{\partial B_t} \\ \frac{\partial B_{t+1}}{\partial \theta_t} & \frac{\partial B_{t+1}}{\partial B_t} \end{pmatrix}. \quad (7.11)$$

The eigenvalues of the Jacobian are denoted as λ_1 and λ_2 , which are complex conjugates $\lambda_1 = \lambda_2^*$ for the dimerised scenario Eqs. (7.10) with $\delta - B < |\theta|$. This corresponds to a spiral fixed point of the discretised-time system, which goes from stable to unstable as the moduli of its eigenvalue $|\lambda_1| = |\lambda_2|$ passes through 1 from below to above. This is called a Neimark-Sacker bifurcation [203, 204], whose counterpart in continuous time is the Hopf bifurcation [205, 206].

In comparison to the effective long-range interaction approach in Section 6.1.3, the self-consistency equation approach intrinsically eliminates the ambiguity of

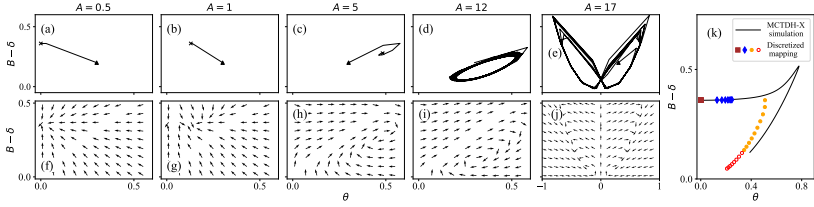


Figure 7.2: (a-e) The trajectory of the parameter pair (B, θ) on phase space evolving according to Eq. (7.12), with randomly chosen initial values marked by triangles and fixed points marked by crosses. (f-i) The corresponding flow vector plots, with normalised arrows showing only the flow directions. In all panels, we choose $\delta = 0.14$. As A increases, the system is in (a,f) a normal phase at $A = 0.5$, (b,g) a single-well lattice at $A = 1$, (c,h) a double-well lattice at $A = 5$, (d,i) an attractor phase at $A = 12$, and (e,j) chaos at $A = 17$. (k) The trajectory of the fixed points as A changes. The solid blue and orange points are stable fixed points for single-well and double-well lattices, respectively. The red empty points show the unstable fixed points. A blue line is superposed to show the trajectory in MCTDH-X simulation in dynamically stable phases.

whether the system is static or driven. This is because it is fundamentally a result of the Liouvillian equation of motion with a dissipation rate κ larger than other frequency scales of the system, particularly the ones related to the atomic motion. As a result, it can indeed capture the limit cycle, which only exists in a driven system but not in a static system as we discussed in Section 6.2.

To summarise the discussion above, with the mapping to the (θ, B) phase space, we can thus already capture the most important dynamics of the system for the parameter regime $0 < \delta < 1/2$ by the discretised time evolution

$$\theta_{t+1} = e^{-1/4\Omega_t} \chi_t, \quad B_{t+1} = \frac{1}{2} + \frac{1}{2} e^{-1/\Omega_t} (2\chi_t^2 - 1) \quad (7.12a)$$

with

$$\Omega_t = \begin{cases} A\sqrt{|\theta_t|(B_t - \delta - |\theta_t|)/2}, & B_t - \delta \geq |\theta_t| \\ A\sqrt{[\theta_t^2 - (\delta - B_t)^2]/2}, & B_t - \delta < |\theta_t| \end{cases} \quad (7.12b)$$

$$\chi_t = \begin{cases} \text{sgn}(\theta_t), & B_t - \delta \geq |\theta_t| \\ (B_t - \delta)/\theta_t, & B_t - \delta < |\theta_t|. \end{cases} \quad (7.12c)$$

As A increases from 0, the system transitions through 4 different phases, the normal phase with $(\theta = 0, B = 1/2)$, the self-organised phase with $|\theta| < B - \delta$, the dimerised self-organised phase with $|\theta| > B - \delta$, and finally the limit cycle phase. This series of dynamics is illustrated in Fig. 7.2(a-j).

7.2. Mean-field features: Dynamical behaviours and dimerisation

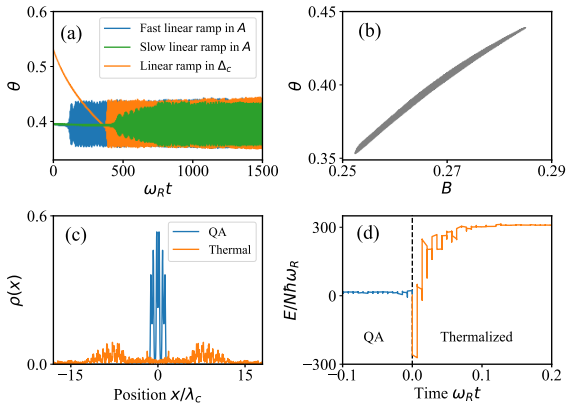


Figure 7.3: (a) The order parameter θ as a function of time for three different ramping protocols from the stable region into the quasiperiodic attractor (QA) phase ($\delta = 0.14$, $A = 11.8$). In the blue and green trajectories, the detuning is fixed at $\delta = 0.14$ and the pump rate $A \propto \eta$ is ramped up linearly at rates of (blue) $dA/dt = 4 \times 10^{-4} \omega_R$ and (green) $dA/dt = 8 \times 10^{-5} \omega_R$, respectively. In the orange trajectory, the pump rate is fixed at $A = 11.8$ and the detuning is ramped up linearly at a rate of $d\delta/dt = 1.5 \times 10^{-4} \omega_R$. (b) For all three cases, the system converges to the same attractor in the (B, θ) phase space. (c) Density distribution $\rho(x)$ of (blue) a QA state and (orange) a thermalised state. (d) Evolution of the system energy as the system becomes thermalised. The reference time $t = 0$ is set roughly when the thermalisation starts.

We further confirm this prediction by Gross-Pitaevskii mean-field evolution of the cavity-boson system using MCTDH-X in Fig. 7.2(k). A good agreement is seen between the Gross-Pitaevskii evolution and the discretised time evolution. In term of the steady states, the MCTDH-X simulations clearly show the transition from normal phase to self-organised lattice at a critical pump rate η_c roughly consistent with the mean-field prediction $A(\eta_c) = 1/\sqrt{1 - 2\delta}$ [161], as well as a dimerisation of the lattice sites. There are, however, obvious quantitative discrepancies between MCTDH-X simulations and discretised time evolution upon dimerisation. Qualitative agreement is also observed in the dynamical phases. When the discretised time evolution predicts a limit cycle without sign switching of θ (cf. Fig. 7.2(d,i)), the MCTDH-X simulations show quasi-periodic behaviours. Importantly, with arbitrary ramping protocols, the system converges to the same quasi-periodic attractors (QA) on the phase space, as shown in Fig. 7.3(a,b), confirming the stability to the limit cycle. Finally, when the discretised time evolution predicts a limit cycle with switching signs of θ in time [Fig. 7.2(e,j)], the cavity-boson system gradually thermalises because of the repeated transient vanishing of the optical lattice V_{cav} and

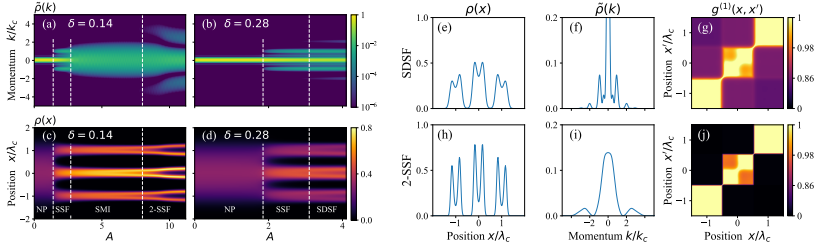


Figure 7.4: (a-d) The momentum and position space density distributions $\tilde{\rho}(k)$ and $\rho(x)$ as a function of pump rate $A \propto \eta$ at two detunings $\delta = 0.14$ and $\delta = 0.28$. At lower detuning, $\delta = 0.14$, the system starts from the normal phase and then enters the SSF phase at $A = 1.4$, the SMI phase at $A = 2.7$, and the 2-SSF phase sequentially. At higher detuning $\delta = 0.28$, the system starts from the normal phase and then enters the SSF phase at $A = 1.9$, and the SDSF phase sequentially. The dotted lines are guides to the eye. (e-j) The position and momentum space density distributions and the Glauber one-body correlation function of an SDSF state (first row) and a 2-SSF state (second row). In panels (g,j), the colour code follows the function $-\ln(1 - g^{(1)})$. The double-well splitting is seen in the central lattice site but not in the other two lattice sites, because only $M = 4$ orbitals are used in the numerical simulations.

the resulting activation of high momentum modes, see Fig. 7.3(c,d). All the differences between MCTDH-X simulations and the discretised time evolution indicate a more fluctuative behaviours in the continuum model as expected, and are mainly attributed to the truncation of higher-order modes in the discretised time evolution. The Gross-Pitaevskii mean-field simulation results from MCTDH-X is summarised in the phase diagram Fig. 7.1(a) using colour codes (blue, green, grey, pink).

7.3 Correlated many-body phases

Apart from the stability behaviours, our numerics also allow us to probe the many-body correlated phases inside the stable regime, which is another interesting aspect of our system. The many-body correlations are characterised by the position space density distribution $\rho(x)$, the momentum space density distribution $\tilde{\rho}(k) = \langle \Psi^\dagger(k)\Psi(k) \rangle / N$, and the Glauber one-body correlation function $g^{(1)}(x, x') = \langle \Psi^\dagger(x)\Psi(x') \rangle / \sqrt{N^2 \rho(x)\rho(x')}$ [90, 207], whose behaviours are summarised in Fig. 7.4. We thus simulate the many-body phases of the cavity-boson system using $M = 4$ orbitals, and observe four phases with different atomic correlations as captured by $\rho(x)$ and $\tilde{\rho}(k)$ and illustrated in the schematic representation Fig. 7.1(c).

7.3. Correlated many-body phases

The *self-organised superfluid* (SSF) phase is characterised by a continuous density distribution $\rho(x)$ with pronounced peaks at the sites of the emergent lattice with spacing $\lambda_c = 2\pi/k_c$. The corresponding $\tilde{\rho}(k)$ is characterised by a principal peak at the centre $k = 0$ straddled by two satellite peaks at $k = \pm k_c$ stemming from the superfluid correlations between the atoms at different lattice sites [RL8, 94, 119]. At lower detunings $\delta < 0.2$ and larger pump rate, the system transitions from the superfluid into a *self-organised Mott insulator* (SMI) phase. This phase is characterised by the disappearance of the peaks at $k = \pm k_c$ and the broadening of the central peak at $k = 0$ in $\tilde{\rho}(k)$ [Fig. 7.1(c)] [RL8, 119, 144, 146, 208]. The superfluid and Mott insulating phases are analogue to the ones in a standard Bose-Hubbard model [RL8]. In the (B, θ) phase space, these two phases with single-well lattices are characterised by stable fixed points with $B - \delta > |\theta|$ [Fig. 7.2(b,g)]. Such phases always appear first as A passes a critical value and the system leaves the normal phase ($B = 1/2, \theta = 0$) [Fig. 7.2(a,f)].

As the pump rate increases further, the fixed point in the phase space moves. As $B - \delta$ becomes smaller than $|\theta|$ [Fig. 7.2(c,h)], local double-well potentials are formed at lattice sites according to Eq. (7.2). This is unique to blue-detuned systems. Depending on the degree of correlations between the atoms at different sites, we obtain either a *self-organised dimerised superfluid* (SDSF) where global superfluid correlations persist across the double-well dimers, or a *self-organised second-order superfluid* (2-SSF) phase where superfluid correlations exist only within each double-well dimer. The signatures of these two states lie in the distributions $\rho(x)$ and $\tilde{\rho}(k)$ and the correlation function $g^{(1)}(x, x')$ as shown in Figs. 7.4(e)-(j). The double-well optical lattice is confirmed by the two-humped density distribution in $\rho(x)$ at each lattice site [Fig. 7.4(e,h)], and the concomitant reduction of the one-body correlation from unity within one lattice site [Fig. 7.4(g,j)]. Within each double-well dimer, local superfluidity exists and manifests itself as two peaks in $\tilde{\rho}(k)$ appearing at $k = \pm k^*$ [Fig. 7.4(f,i)], where

$$k^* = \frac{\pi k_c}{\arccos[(B - \delta)/|\theta|]} \quad (7.13)$$

corresponds to the distance between the minima of the double-well potential. As the pump rate increases, k^* approaches $2k_c$ from above and the peak height increases as the double well becomes deeper.

In the SDSF (2-SSF) phase, global superfluid correlations between different pairs of double wells is present (absent). This corresponds to the presence (absence) of the peaks at k_c in $\tilde{\rho}(k)$ [Fig. 7.4(f,i)], and a finite (vanishing) correlation in $g^{(1)}$ between different lattice sites [Fig. 7.4(g,j)]. In a 2-SSF state, superfluidity has a completely different length scale from the SSF and SDSF states, since coherence exists only locally within each double-well dimer. Although superfluidity usually refers to long-range coherence, it can also be used to describe coherence within a double well [209]. These two new phases realise

a variant of the Bose-Hubbard model with degenerate double-well lattices with Hamiltonian

$$\begin{aligned}
 H_{\text{BH}} = & - \sum_i (t_1 c_{i,L}^\dagger c_{i,R} + t_2 c_{i,R}^\dagger c_{i+1,L} + \text{H.c.}) \\
 & + \sum_{i,\sigma=L,R} \left[\frac{U}{2} (c_{i,\sigma}^\dagger c_{i,\sigma})^2 + \mu_i c_{i,\sigma}^\dagger c_{i,\sigma} \right],
 \end{aligned} \tag{7.14}$$

where L, R denote the dimer sub-sites [70].

7.4 Conclusions

We have thus shown the rich collection of correlated many-body phases and driven-dissipative dynamics in the blue-detuned regime of the cavity-boson system described by Eq. (7.1), which is unseen in the red-detuned regime as discussed in Chapter 4. Specifically, we observe correlated many-body phases associated to dimerisation of the optical lattice, and more importantly for our narrative, quasi-periodic and chaotic dynamics intrinsically associated to the driven-dissipative nature of the system. With the rich dynamics already seen in the standard cavity-boson setup, we continue to explore in the next two sections more intriguing, unexpected driven-dissipative phenomena in more complex cavity-boson systems.

8 | Dissipation-engineered family of nearly-dark many-body states in a cavity-boson system

We have already seen a few examples where the driven nature introduces new phases of matter, changing quantum and collective behaviours of the system. In this Chapter, we further study a many-body cavity-atom system where the atomic subspace has an enlarged symmetry, and unveil how the mechanisms discussed in Chapter 6 leads to dissipative stabilisation of excited states and thus the realisation of a continuous family of dark and nearly-dark steady states with intrinsic many-body correlations. This Chapter sets the theoretical building blocks for explaining the intriguing experimentally observed non-Hermitian dynamics to be discussed in Chapter 9.

Originality declaration: This Chapter is adapted from our published work *Phys. Rev. Lett.* **128**, 153601 (2022) [RL3] under supervision of R. Chitra and in collaboration with the experimental group R. Rosa-Medina, F. Ferri, F. Finger, K. Kroeger, T. Donner and T. Esslinger.

8.1 Introduction

Ultracold atomic gases in high-finesse optical cavities have emerged as a versatile platform to simulate hitherto unexplored strongly coupled light-matter phases [66, 102, 139]. A paradigmatic example is the realisation of the Dicke superradiant phase [105, 106, 108, 210] in a weakly interacting Bose-Einstein condensate (BEC) coupled to a cavity [102, 119]. The ubiquitous dissipation present in these systems can be exploited to obtain squeezing and entanglement [75], chiral states [211], as well as oscillatory and chaotic dynamics [RL2, 126, 127, 142, 143, 200, 201, 212–215]. Particularly, cavity dissipation is known to stabilise excited eigenstates as steady states in the interpolating Dicke–Tavis-Cummings model where two-level atoms are coupled to both quadratures of the cavity field [79, 196], which has recently been experimentally verified by

8.1. Introduction

coupling thermal atoms [216] or a spinor BEC [217] to an optical cavity. An exciting but relatively under-explored frontier in cavity-QED systems is many-body dark-state physics [218–220].

We consider N identical, effective V-shaped three-level atoms coupled to a dissipative cavity with resonance frequency ω and dissipation rate κ in the thermodynamic limit $N \rightarrow \infty$ [Fig. 8.1(a)]. The atoms have two distinct but degenerate levels $|1\rangle$ and $|2\rangle$ separated by an energy ω_0 from the lowest level $|0\rangle$. The transitions between the ground level and the excited levels are exclusively mediated by coherent couplings to the two orthogonal quadratures of the cavity fields with respective strengths λ_1 and λ_2 . In atomic gases, such an effective atomic spectrum can be designed by addressing motional degrees of freedom with external laser fields [RL4, 128, 130, 221], or by combining them with internal atomic levels [222].

The Hamiltonian governing this system is given by

$$H = \omega a^\dagger a + \omega_0(\Sigma_{11} + \Sigma_{22}) + \frac{i\lambda_1}{\sqrt{N}}(a - a^\dagger)(\Sigma_{01} + \Sigma_{10}) + \frac{i\lambda_2}{\sqrt{N}}(a + a^\dagger)(\Sigma_{02} - \Sigma_{20}), \quad (8.1)$$

from a theoretical perspective, where a is the cavity annihilation operator, and $\Sigma_{\mu\nu} = \sum_{j=1}^N |\mu\rangle_j \langle \nu|_j$ are the collective pseudo-spin operators with $|\mu\rangle_j$ denoting the μ -th level ($\mu \in \{0, 1, 2\}$) of the j -th atom. In the next Section 9, we will discuss the experimental motivation and consequences. A similar model has been considered in Ref. [222], which focused on the superradiant features in the low energy sectors.

The Hamiltonian possesses a $\mathbb{Z}_2 \times \mathbb{Z}_2$ parity symmetry $\Pi = \mathcal{T}_1 \circ \mathcal{T}_2$, where \mathcal{T}_1 and \mathcal{T}_2 are defined by $(a, \Sigma_{01}, \Sigma_{02}) \xrightarrow{\mathcal{T}_1} (-a^\dagger, \Sigma_{01}, -\Sigma_{02})$ and $(a, \Sigma_{01}, \Sigma_{02}) \xrightarrow{\mathcal{T}_2} (a^\dagger, -\Sigma_{01}, \Sigma_{02})$, and can be broken separately. When $\lambda_1 = \lambda_2$, this symmetry is enlarged to a U(1) symmetry with generator $\mathcal{G} = a^\dagger a - (\Sigma_{12} + \Sigma_{21})$. The levels $|1\rangle$ and $|2\rangle$ have completely equivalent roles in the Hamiltonian.

The closed system phase diagram can be found by minimisation of energy, and is summarised in Fig. 8.1(b). For small couplings $\lambda \equiv \max(\lambda_1, \lambda_2) < \lambda_c = \frac{1}{2}\sqrt{\omega\omega_0}$, the system stays in the normal phase with an empty cavity and atoms collectively populating the $|0\rangle$ level. When either coupling exceeds the threshold $\lambda > \lambda_c$, the system enters the superradiant phase where the cavity field is coherently populated as $|\langle a \rangle| = \frac{\lambda\sqrt{N}}{\omega} \sqrt{1 - (\frac{\omega_0\omega}{4\lambda^2})^2}$. For $\lambda_1 > \lambda_2$ ($\lambda_2 > \lambda_1$), the \mathcal{T}_1 (\mathcal{T}_2) symmetry is spontaneously broken, leading to a non-zero expectation value of the imaginary (real) quadrature of the cavity field and an occupation of the $|0\rangle$ and $|1\rangle$ ($|2\rangle$) levels. For $\lambda_1 = \lambda_2 > \lambda_c$, the broken U(1) symmetry results in a population of all three atomic levels. From the

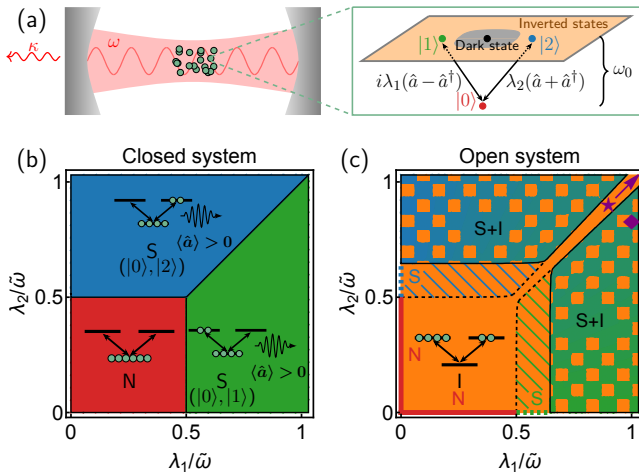


Figure 8.1: (a) System schematics illustrating an ensemble of three-level ($|0\rangle$, $|1\rangle$ and $|2\rangle$) atoms with energy splitting ω_0 coupled to an optical cavity a with resonance frequency ω and dissipation rate κ through coupling strengths $\lambda_{1,2}$. Also shown is a representation of the inverted states as mixed/superposition states of the levels $|1\rangle$ and $|2\rangle$, including the nearly dark (grey region) and the dark (black point) states. (b,c) Phase diagrams illustrating (b) the ground states for the closed system, and (c) the steady states for the open system. Pictorial representations of the normal (N), superradiant (S) and inverted (I) states are superimposed. In panel (c), the thick solid and dotted lines indicate that the normal and superradiant states are stable only for $\lambda_1 = 0$ or $\lambda_2 = 0$. Superradiant states stably coexist with the inverted states in the tiled regions, and are physical but unstable in the hatched regions. The purple star and diamond indicate the end points of the ramps in Fig. 8.5 and Fig. 8.6, respectively. System parameters are $\omega = 2\tilde{\omega}$, $\omega_0 = 0.5\tilde{\omega}$ and $\kappa = 0.1\tilde{\omega}$ with reference frequency $\tilde{\omega}$.

perspective of the closed system, our system behaves like a simple combination of two Dicke models.

8.2 The underlying SU(3) atomic system

The pseudo-spin operators $\Sigma_{\mu\nu}$ follow the commutation relation of the Gell-Mann matrices, and thus span an SU(3) symmetry space. In comparison, a spin-1 implementation with SU(2) symmetry [223] realises an equally spaced Ξ -shaped three-level system, where the middle level is equally coupled to the upper and lower ones. This is qualitatively different from our V-shaped system.

Mapping to the SU(3) Gell-Mann matrices

We now briefly discuss the underlying symmetry of the atomic operators. Our model Eq. (8.1) has an SU(3) atomic space. This can be revealed by the relation between the collective atomic operators $\Sigma_{\mu\nu}$ to the Gell-Mann matrices g_i with $i = 1, 2, \dots, 8$, which are the generators of the SU(3) symmetry spanning the $\mathfrak{su}(3)$ Lie algebra. Together with the identity matrix $g_0 = \mathbb{1}_{3 \times 3}$, these Gell-Mann matrices,

$$\begin{aligned}
 g_1 &= \begin{pmatrix} 0 & 1 & 0 \\ 1 & 0 & 0 \\ 0 & 0 & 0 \end{pmatrix}, & g_2 &= \begin{pmatrix} 0 & -i & 0 \\ i & 0 & 0 \\ 0 & 0 & 0 \end{pmatrix}, & g_3 &= \begin{pmatrix} 1 & 0 & 0 \\ 0 & -1 & 0 \\ 0 & 0 & 0 \end{pmatrix}, \\
 g_4 &= \begin{pmatrix} 0 & 0 & 1 \\ 0 & 0 & 0 \\ 1 & 0 & 0 \end{pmatrix}, & g_5 &= \begin{pmatrix} 0 & 0 & -i \\ 0 & 0 & 0 \\ i & 0 & 0 \end{pmatrix}, & g_6 &= \begin{pmatrix} 0 & 0 & 0 \\ 0 & 0 & 1 \\ 0 & 1 & 0 \end{pmatrix}, & (8.2) \\
 g_7 &= \begin{pmatrix} 0 & 0 & 0 \\ 0 & 0 & -i \\ 0 & i & 0 \end{pmatrix}, & g_8 &= \frac{1}{\sqrt{3}} \begin{pmatrix} 1 & 0 & 0 \\ 0 & 1 & 0 \\ 0 & 0 & -2 \end{pmatrix},
 \end{aligned}$$

form a complete basis for 3×3 matrices. Notably, within the $\mathfrak{su}(3)$ algebra, there are an infinite number of sets of Gell-Mann matrices constituting $\mathfrak{su}(2)$ subalgebra, examples being $\{g_1, g_2, g_3\}$, $\{g_4, g_5, g_3/2 + \sqrt{3}g_8/2\}$, $\{g_6, g_7, -g_3/2 + \sqrt{3}g_8/2\}$, etc. If the Hamiltonian only contains terms which are linear combinations of matrices from a chosen $\mathfrak{su}(2)$ subalgebra, the system symmetry is reduced to SU(2).

With our Hamiltonian Eq. (8.1), we can find a mapping from the atomic operators to the Gell-Mann matrices preserving the commutation relation between the operators:

$$\begin{aligned}
 \Sigma_{01} + \Sigma_{10} &\mapsto g_1, \\
 i(\Sigma_{02} - \Sigma_{20}) &\mapsto g_5, \\
 \Sigma_{11} &\mapsto -\frac{1}{2}g_3 + \frac{1}{2\sqrt{3}}g_8 + \frac{1}{3}g_0, \\
 \Sigma_{22} &\mapsto -\frac{1}{\sqrt{3}}g_8 + \frac{1}{3}g_0.
 \end{aligned} \tag{8.3}$$

It is impossible to write these four operators as linear combinations of Gell-Mann matrices from an $\mathfrak{su}(2)$ subalgebra, and we thus conclude that the atomic subspace has an underlying SU(3) symmetry. Nevertheless, in the Dicke limit where $\lambda_2 = 0$ and thus the g_5 term vanishes, the operators can be spanned under the basis $\{g_0, g_1, g_2, g_3, g_8\}$. Among these basis matrices, $\{g_1, g_2, g_3\}$

constitute an $\mathfrak{su}(2)$ subalgebra, and all three matrices commute with g_8 , which by itself can be treated as the generator of a $U(1)$ symmetry. As a result, the underlying symmetry of our system is reduced to $SU(2) \times U(1)$. The same argument also applies for the case $\lambda_1 = 0$.

8.2.1 Conserved quantities in the atomic systems

An $SU(3)$ system has three intrinsic conserved quantities guaranteed by the symmetry. The first quantity is the expectation value of g_0 , whose conservation is guaranteed by the tracelessness of the Gell-Mann matrices g_i , $i = 1, 2, \dots, 8$; whereas the other two quantities are the expectation values of the quadratic and cubic Casimirs C_1 and C_2 of the $SU(3)$ symmetry, which are defined by

$$C_1 = \sum_{i=1}^8 g_i g_i, \quad C_2 = \sum_{i,j,k=1}^8 d_{i,j,k} g_i g_j g_k, \quad (8.4)$$

respectively, where $d_{i,j,k} = \text{Tr}(g_i g_j g_k + g_j g_i g_k)$. In the atomic system, the condition of tracelessness implies the conservation of total particles in the system

$$N = \sum_{\mu=0}^2 \langle \Sigma_{\mu\mu} \rangle \quad (8.5)$$

whereas the other two conserved quantities are respectively

$$\begin{aligned} C_1 &= \sum_{\mu=0}^2 \langle \Sigma_{\mu\mu} \rangle^2 + \sum_{\{\mu,\nu\}} \left(3 |\langle \Sigma_{\mu\nu} \rangle|^2 - \langle \Sigma_{\mu\mu} \rangle \langle \Sigma_{\nu\nu} \rangle \right) = N^2 \\ C_2 &= \frac{9}{2} \sum_{\{\mu,\nu,\rho\}} |\langle \Sigma_{\mu\nu} \rangle|^2 \left(\langle \Sigma_{\mu\mu} \rangle + \langle \Sigma_{\nu\nu} \rangle - 2 \langle \Sigma_{\rho\rho} \rangle \right) \\ &\quad - \frac{1}{2} \prod_{\{\mu,\nu,\rho\}} \left(\langle \Sigma_{\mu\mu} \rangle + \langle \Sigma_{\nu\nu} \rangle - 2 \langle \Sigma_{\rho\rho} \rangle \right) + 27 \left| \langle \Sigma_{01} \rangle \langle \Sigma_{12} \rangle \langle \Sigma_{20} \rangle \right| = N^3. \end{aligned} \quad (8.6)$$

where the summation $\sum_{\{\mu,\nu\}}$ runs over the pairs $\{\mu,\nu\} = \{0,1\}, \{1,2\}, \{2,0\}$, while the summation $\sum_{\{\mu,\nu,\rho\}}$ and the product $\prod_{\{\mu,\nu,\rho\}}$ run over the triplets $\{\mu,\nu,\rho\} = \{0,1,2\}, \{1,2,0\}, \{2,0,1\}$.

8.2.2 Three-level $SU(2)$ spin-1 systems

In the main text we have claimed that our system is essentially different from a system with an $SU(2)$ three-level atomic structure, i.e. a spin-1 atomic

8.3. Open system phase diagram

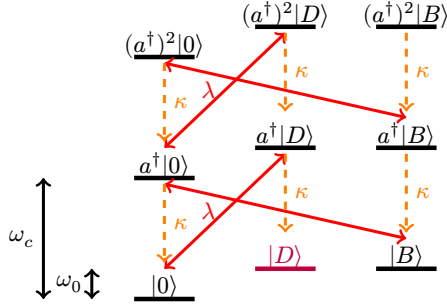


Figure 8.2: Schematics showing the structure of the energy levels of the system.

structure. Here we substantiate the claim by discussing the general form of the Hamiltonian of such a system, which reads [223]:

$$\begin{aligned}
 H = & \omega a^\dagger a + \omega_0 (\Sigma_{11} - \Sigma_{22}) \\
 & + \frac{1}{\sqrt{N}} (\lambda_1 a + \lambda_1^* a^\dagger) (\Sigma_{01} + \Sigma_{10} + \Sigma_{02} + \Sigma_{20}) \\
 & + \frac{1}{\sqrt{N}} (\lambda_2 a - \lambda_2^* a^\dagger) (\Sigma_{01} - \Sigma_{10} + \Sigma_{02} - \Sigma_{20}).
 \end{aligned} \tag{8.7}$$

This Hamiltonian describes a Ξ -shaped system with $|0\rangle$ level in the middle, and $|1\rangle$ and $|2\rangle$ levels separated from it with the same energy difference. Moreover, the couplings from the $|0\rangle$ level to the $|1\rangle$ and $|2\rangle$ levels always share the same strengths. The operators in the Hamiltonian can be mapped to the Gell-Mann matrices as

$$\begin{aligned}
 \Sigma_{11} - \Sigma_{22} & \mapsto g_3/2 + \sqrt{3}g_8/2 \\
 \Sigma_{01} + \Sigma_{10} + \Sigma_{02} + \Sigma_{20} & \mapsto g_1 + g_6 \\
 -i(\Sigma_{01} - \Sigma_{10} + \Sigma_{02} - \Sigma_{20}) & \mapsto g_2 + g_7
 \end{aligned} \tag{8.8}$$

These three operators obey the commutation relation of the $\mathfrak{su}(2)$ subalgebra, and thus span the basis for it. We can further identify these operators as the $SU(2)$ generators J_z , J_x , and J_y , respectively, which in a two-level system can be represented by the 2×2 Pauli matrices.

8.3 Open system phase diagram

8.3.1 Introduction to inverted states

After understanding the underlying atomic structure, we focus on one special family of states. In the high-energy sector, our model hosts a dark state

decoupled from the cavity field and thus stable, obeying $H|D\rangle = N\omega_0|D\rangle$ and $a|D\rangle = 0$ [192–194]:

$$|D\rangle = \prod_{j=1}^N \frac{\lambda_2|1\rangle_j + \lambda_1|2\rangle_j}{\sqrt{\lambda_1^2 + \lambda_2^2}}. \quad (8.9)$$

For an intuitive understanding of the dissipative process, we illustrate the relations between the states in Fig. 8.2. In the absence of dissipation, the dark state without photon $|D\rangle$ is completely decoupled from the rest of the system. Initialised in the normal BEC state $|0\rangle$, we are not able to reach $|D\rangle$ through any process. On the other hand, with dissipation, the state $|D\rangle$ can now be reached by losing a photon from the state $a^\dagger|D\rangle$, but there is no channel for the system leaving the state. As a result, the system is trapped in $|D\rangle$. This intuitive reasoning reveals the two contrasting dynamical behaviours in the presence and absence of dissipation.

The dark state $|D\rangle$ manifests a complete atomic population inversion with unoccupied $|0\rangle$ level. In fact, it is merely one element of a continuous family of states satisfying $\langle \Sigma_{0\nu} \rangle = 0$ and $\langle a \rangle = 0$ in $\mathcal{O}(N)$, which we term the *inverted states*. These states are uniquely defined by two parameters,

$$N_1 = \langle \Sigma_{11} \rangle, \quad \theta = \arg\langle \Sigma_{12} \rangle, \quad (8.10)$$

where $N_1 \in [0, N]$ is the occupation of the level $|1\rangle$, and $\theta \in (-\pi, \pi]$ is the relative phase between the levels $|1\rangle$ and $|2\rangle$. These quasi-degenerate inverted states have a much higher energy $E = N\omega_0$ compared to the polaritonic excitations, whose energy is in $\mathcal{O}(1)$. These states stem from the enlarged SU(3) symmetry and, in contrast to the dark state of Eq. (8.9), are characterised by non-trivial many-body correlations. Despite the inaccessibility of these inverted states with quasi-adiabatic protocols in the static system, they are inherently related to the dark state in the driven-dissipative system.

8.3.2 Excitation spectra and stabilities

The intuitive discussion above can be substantiated by solving the excitation spectrum using third quantisation on the Holstein-Primakoff transformed Hamiltonian. Notice that in this Chapter, an SU(3) version of the Holstein-Primakoff transformation is used [70]. The driven-dissipative nature induces dramatic consequences in the dynamical behaviours of the system, involving the normal, superradiant and inverted states. Nevertheless, our discussion will focus on the instability of the normal state towards the inverted states, which is the most relevant to the experiment to be discussed in Chapter 9. The driven-dissipative effects related to the superradiant phase will be briefly discussed in Section 8.5.

8.3. Open system phase diagram

The instability of the normal phase in the driven-dissipative system can be captured again using third quantisation technique on the Holstein-Primakoff Hamiltonian

$$H = \omega a^\dagger a + \omega_0(b_1^\dagger b_1 + b_2^\dagger b_2) + i\lambda_1(a - a^\dagger)(b_1 + b_1^\dagger) + i\lambda_2(a + a^\dagger)(b_2 - b_2^\dagger), \quad (8.11)$$

The resulting excitation spectrum is shown in Fig. 8.3(a,b). Once both couplings λ_1 and λ_2 are switched on, the normal state immediately becomes unstable ubiquitously, essentially because of the coupling to the dark mode. We argue that the instability mechanism is the same as the one from Eq. (6.16) and illustrated in Fig. 6.6(b). This argument can be easily confirmed in the case of $\lambda_1 = \lambda_2 = \lambda$, where we can clearly identify the coupling term as

$$-i\sqrt{2}\lambda a^\dagger(b_B + b_D^\dagger) + \text{H.c.} \quad (8.12)$$

with $b_{D/B} = (b_1 \pm b_2)/\sqrt{2}$. According to discussions in Section 6.2 and Fig. 6.6(a,b), a system with coupling $a^\dagger b_B$ corresponding to a level-crossing transition is stabilised by dissipation in a driven system, whereas a system with coupling $a^\dagger b_D^\dagger$ is de-stabilised. Nevertheless, these two processes take place in orthogonal channels and do not compete with each other. As a result, the system is always destabilised through the b_D channel, which is also valid for a general combination of λ_1 and λ_2 . Our argument is substantiated by the linear (quadratic) dependence of the instability on the dissipation rate (coupling strength), $\text{Im } E \propto \lambda_{1/2}^2 \kappa$, see Section 6.2.

For the inverted states with parameter N_1 and θ , the Holstein-Primakoff Hamiltonian is given by

$$H = \omega a^\dagger a - \omega_0 b_0^\dagger b_0 + i\eta_1(a - a^\dagger)(b_0^\dagger + b_0) + i\eta_2(a + a^\dagger)(e^{i\theta} b_0^\dagger - e^{-i\theta} b_0), \quad (8.13)$$

where b_0 is the Holstein-Primakoff mode corresponding to microscopic excitations in $|0\rangle$, $\eta_1 = \lambda_1 \sqrt{N_1/N}$, $\eta_2 = \lambda_2 \sqrt{1 - N_2/N}$. Note that there is effectively only one atomic excitation mode coupled to the cavity. The third quantisation technique yielding the excitation spectrum (Fig. 8.3(c,d)) predicts a large multistable region in the vicinity of the dark state $|D\rangle$, whose boundary is given by

$$\frac{\eta_1 \eta_2 \cos \theta}{\eta_1^2 + \eta_2^2} = \frac{\omega \omega_0}{\omega^2 + \omega_0^2 + \kappa^2} \equiv \Omega, \quad (8.14)$$

We emphasise that such a continuously multistable region cannot be realised using atoms with underlying SU(2) structure. In the following, we discuss the mechanism of this multistability by considering the simple scenario $\lambda_1 =$

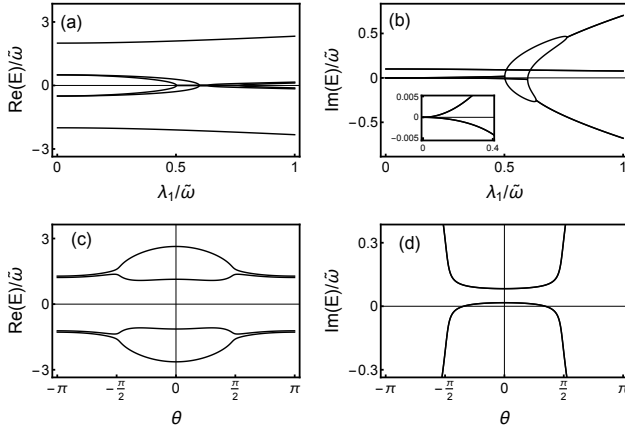


Figure 8.3: The excitation spectra of (a,b) the normal state and (c,d) the inverted states. The inset in panel (b) is a zoom-in of the spectrum in the vicinity of zero energy. The real part describes the excitation energy, whereas the imaginary part the stability, with negative values indicating instability. The parameters of the system are $\omega = 2\tilde{\omega}$, $\omega_0 = \tilde{\omega}/2$, $\kappa = 0.1\tilde{\omega}$. (a,b) For the normal state, we further choose $\lambda_2 = \lambda_1/1.2$ and tune λ_1 from 0 to $\tilde{\omega}$. (c,d) For the inverted state, we further fix $\lambda_1 = \lambda_2 = \tilde{\omega}$, $N_1 = N/2$, and tune θ from $-\pi$ to π .

$\lambda_2 = \lambda$. The results can be straightforwardly generalised for unequal coupling strengths.

When $\kappa \rightarrow \infty$, the driven-dissipative stability and instability [cf. Fig. 6.6(a,b) and Eq. (6.17)] dominate over other mechanisms like exceptional point instability. Corresponding to $\Omega \rightarrow 0$ [cf. Eq.(8.14)], the stable region reaches $|\theta| < \pi/2$, obtaining its largest possible area. The stability boundary in this limit exactly splits the inverted states into two equally large subsets, $|\theta| < \pi/2$ (stable) and $\pi/2 < |\theta| < \pi$ (unstable), whose driven-dissipative stabilities are dominated by the coupling of the cavity field to the dark and bright states, respectively.

When $\kappa \rightarrow 0$, the instability mechanism is now dominated by non-driven-dissipative mechanism, which is the exceptional point instability in the current system. When $\omega_c = \omega_0$ and thus $\Omega = 1/2$, only the dark state is stable; but when $\omega_c \neq \omega_0$ and thus $0 < \Omega < 1/2$, there is a continuous subset of stable states. These states are not de-stabilised by exceptional point instability.

As summarised in Fig. 8.4(a), we find three regions, (i) $\frac{\eta_1 \eta_2 \cos \theta}{\eta_1^2 + \eta_2^2} < \frac{\omega \omega_0}{\omega^2 + \omega_0^2}$, which is stable under both exceptional point instability and driven-dissipative stability; (ii) $\frac{\eta_1 \eta_2 \cos \theta}{\eta_1^2 + \eta_2^2} > \frac{\omega \omega_0}{\omega^2 + \omega_0^2}$ and $|\theta| < \pi/2$, which is de-stabilised by exceptional

8.3. Open system phase diagram

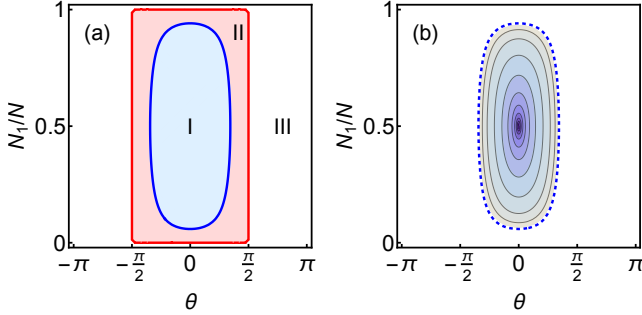


Figure 8.4: (a) Stability boundaries of the inverted state in the open system for different system parameters given by Eq. (8.14). The blue region (I) is stable in the limit $\kappa \rightarrow 0$, and is stable against exceptional point instability and driven-dissipative instability. The red region (II) is unstable because of exceptional point instability, but can be stabilised again by driven-dissipative stability at large enough dissipation. The white region (III) is always unstable as it experiences both kinds of instabilities. (b) Cavity field fluctuations $\langle \delta a^2 \rangle$ [cf. Eq. (8.15)] of different inverted states in the stable region, with system parameters taken as $\omega = 2\tilde{\omega}$, $\omega_0 = 0.5\tilde{\omega}$, $\kappa = 0.1\tilde{\omega}$, and $\lambda_1 = \lambda_2 = \tilde{\omega}$.

point instability, but is potentially stabilised by driven-dissipative stability; and (iii) $|\theta| > \pi/2$, which is unstable under both mechanisms.

The driven-dissipative stabilities of the normal and inverted phases discussed above are summarised in the open-system phase diagram 8.1(c). Indeed, there are substantial discrepancies between the phase diagram of the static (closed) system and the driven-dissipative (open) system, with the normal phase completely wiped out, giving way to the inverted states.

To distinguish between the inverted states, a direct measurement of the atomic observables N_1 and θ can be experimentally challenging. An alternative is to extract the cavity and atomic fluctuations as well as the excitation spectra harboured by the individual states. Particularly, the cavity fluctuations $\langle \delta a^2 \rangle \equiv \langle a^\dagger a \rangle - |\langle a \rangle|^2$ are found to be [see Fig. 8.4(b)]

$$\begin{aligned}
 \langle \delta a^2 \rangle &= A_1 / (2A_2 A_3) \\
 A_1 &= (\eta_1^4 + \eta_2^4 - 2\eta_1^2 \eta_2^2 \cos 2\theta)(\omega^2 + \kappa^2 + 4\eta_1 \eta_2 \cos \theta) \omega_0^2 \\
 A_2 &= 8\eta_1^2 \eta_2^2 (1 + \cos 2\theta) + 4(\eta_1^2 + \eta_2^2) \omega \omega_0 + (\omega^2 + \kappa^2) \omega_0^2 \\
 A_3 &= \eta_1 \eta_2 (\omega^2 + \omega_0^2 + \kappa^2) \cos \theta - (\eta_1^2 + \eta_2^2) \omega \omega_0,
 \end{aligned} \tag{8.15}$$

based on the Lindblad form. They vary over orders of magnitude within the stable region, diverging at the stability boundary and strongly suppressed

around $|D\rangle$. The vanishing cavity and atomic fluctuations at $|D\rangle$ corroborate its darkness and atomic coherence, whereas the states in its vicinity are mixed states with intrinsic many-body correlations and finite fluctuations. Moreover, the diverging cavity fluctuations at the stability boundary is consistent with the fact that the instability is driven by exceptional point. Measurements of the cavity fluctuations and the excitation spectra can uniquely determine the inverted state for unequal couplings $\lambda_1 \neq \lambda_2$, but only up to a closed contour in the N_1 - θ parameter space for equal couplings $\lambda_1 = \lambda_2$, as consistent with the $U(1)$ symmetry.

8.4 Dynamics: Cavity-mediated atomic transfer

The full Liouvillian dynamics of the system can be captured by numerically solving the coupled mean-field equations of motion for the cavity and atomic fields, using the normal state with a small cavity field as the initial state, and different time-dependent ramp protocols for the two couplings. These are seven coupled complex equations

$$\begin{aligned}
i\partial_t \langle a \rangle &= (\omega - i\kappa) \langle a \rangle - i \frac{\lambda_1}{\sqrt{N}} (\langle \Sigma_{01} \rangle + \langle \Sigma_{10} \rangle) + i \frac{\lambda_2}{\sqrt{N}} (\langle \Sigma_{02} \rangle - \langle \Sigma_{20} \rangle), \\
i\partial_t \langle \Sigma_{01} \rangle &= \omega_0 \langle \Sigma_{01} \rangle + i \frac{\lambda_1}{\sqrt{N}} (\langle a \rangle - \langle a^\dagger \rangle) (\langle \Sigma_{00} \rangle - \langle \Sigma_{11} \rangle) + i \frac{\lambda_2}{\sqrt{N}} (\langle a \rangle + \langle a^\dagger \rangle) \langle \Sigma_{21} \rangle, \\
i\partial_t \langle \Sigma_{02} \rangle &= \omega_0 \langle \Sigma_{02} \rangle - i \frac{\lambda_1}{\sqrt{N}} (\langle a \rangle - \langle a^\dagger \rangle) \langle \Sigma_{12} \rangle - i \frac{\lambda_2}{\sqrt{N}} (\langle a \rangle + \langle a^\dagger \rangle) (\langle \Sigma_{00} \rangle - \langle \Sigma_{22} \rangle), \\
i\partial_t \langle \Sigma_{00} \rangle &= i \frac{\lambda_1}{\sqrt{N}} (\langle a \rangle - \langle a^\dagger \rangle) (\langle \Sigma_{01} \rangle - \langle \Sigma_{10} \rangle) + i \frac{\lambda_2}{\sqrt{N}} (\langle a \rangle + \langle a^\dagger \rangle) (\langle \Sigma_{02} \rangle + \langle \Sigma_{20} \rangle), \\
i\partial_t \langle \Sigma_{11} \rangle &= -i \frac{\lambda_1}{\sqrt{N}} (\langle a \rangle - \langle a^\dagger \rangle) (\langle \Sigma_{01} \rangle - \langle \Sigma_{10} \rangle), \\
i\partial_t \langle \Sigma_{22} \rangle &= -i \frac{\lambda_2}{\sqrt{N}} (\langle a \rangle + \langle a^\dagger \rangle) (\langle \Sigma_{02} \rangle + \langle \Sigma_{20} \rangle), \\
i\partial_t \langle \Sigma_{12} \rangle &= -i \frac{\lambda_1}{\sqrt{N}} (\langle a \rangle - \langle a^\dagger \rangle) \langle \Sigma_{02} \rangle - i \frac{\lambda_2}{\sqrt{N}} (\langle a \rangle + \langle a^\dagger \rangle) \langle \Sigma_{10} \rangle.
\end{aligned} \tag{8.16}$$

As a representative case, the system parameters are chosen as $\omega = 2\tilde{\omega}$, $\omega_0 = 0.5\tilde{\omega}$ and $\kappa = 0.1\tilde{\omega}$ with reference frequency $\tilde{\omega}$.

We ramp up the couplings from $\lambda_1 = \lambda_2 = 0$ to $\lambda_1 = \lambda_2 = 2\tilde{\omega}$ using three different protocols as illustrated in Fig. 8.5(a,b), which differ in ramp rate and path in λ_1 - λ_2 parameter space. For a better visualisation, the ensuing Liouvillian trajectories are projected onto the Bloch sphere spanned by the axes $\text{Re}\langle \Sigma_{12} \rangle$, $\text{Im}\langle \Sigma_{12} \rangle$ and $\frac{1}{2}(\langle \Sigma_{22} \rangle - \langle \Sigma_{11} \rangle)$ [Fig. 8.5(c)]. Despite identical final couplings, the final converged state depends sensitively on both ramp rate and path, signalling the multistability of the inverted states. The nature of the dynamics is further elucidated by studying the cavity field evolution. As the atomic population inverts, correlations between atomic levels $\langle \Sigma_{01} \rangle$ and $\langle \Sigma_{02} \rangle$ are established. This automatically generates a non-zero $\langle a \rangle$ signifying a burst of photons [Fig. 8.5(d)]. We can best understand this in the bad-cavity limit $\kappa \gg \omega_0$, where the cavity field follows the atomic evolution adiabatically as

$$\langle a \rangle = \frac{i\lambda_1 \text{Re}\langle \Sigma_{01} \rangle + \lambda_2 \text{Im}\langle \Sigma_{02} \rangle}{\sqrt{N}(\omega + i\kappa)} \tag{8.17}$$

The quantitative consistency between cavity field dynamics and rapidities [Fig. 8.5(e,f)] confirms the consistency between the microscopic description of Holstein-Primakoff transformation and the collective description of the original

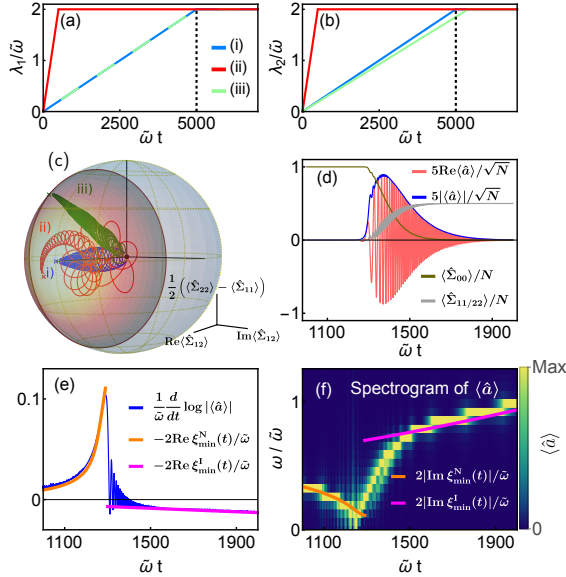


Figure 8.5: Dynamical evolution probing the multistability of the inverted states. (a,b) The time-dependence of (a) $\lambda_1(t)$ and (b) $\lambda_2(t)$ in the three protocols. (c) The trajectories of all three protocols projected on the Bloch sphere spanned by $|1\rangle$ and $|2\rangle$. The black dot indicates the starting point of the trajectories, i.e., the normal state, while the crosses indicate the final points. The stable region of the inverted states, appearing as the coloured spherical cap in this representation, corresponds to the one shown in Fig. 8.4(b). (d) Evolution of the cavity and atomic fields during the pulse in protocol (i), where (e,f) the simulated dynamics agrees quantitatively with the theoretically calculated rapidities ξ_{\min}^N for normal state and ξ_{\min}^I for inverted state with $(N_1, \theta) = (1/2, 0)$ evaluated with instantaneous coupling strengths. Particularly, (e) the time derivative of $|\langle \hat{a} \rangle|$ depicting the deviation/convergence rate agree quantitatively to $\text{Re} \xi_{\min}$, whereas (f) the spectrogram of $\langle \hat{a} \rangle$ depicting the oscillation frequency to $\text{Im} \xi_{\min}$.

Hamiltonian, and also confirms the dissipative nature of the instability driving the population inversion.

8.5 Instability in the superradiant phase

We finally briefly comment on the stability of the superradiant phase, whose stability is also sketched in the phase diagram Fig. 8.1(c). Similar to the interpolating Dicke–Tavis–Cummings model [79, 80], the U(1) symmetry broken

8.5. Instability in the superradiant phase

phase at $\lambda_1 = \lambda_2$ is eliminated and two superradiant boundaries separated by a sliver emerge symmetric about $\lambda_1 = \lambda_2$. Each superradiant boundary harbours both continuous and first order sections. In contrast to the interpolating Dicke–Tavis–Cummings model, the superradiant state is unstable in an intermediate region above the critical coupling of the closed system [hatched region in Fig. 8.1(c)].

The accessibility and stability of the superradiant steady states can be confirmed by simulating Liouvillian evolutions Eq. (8.16) using three ramp protocols satisfying $\lambda_1/\lambda_2 = 1.2$ [Fig. 8.6(a)]. They traverse the unstable superradiant region, and terminate in the region where both the superradiant state and the inverted states are stable [purple diamond in Fig. 8.1(c)]. We find a ramp-dependent dynamics mirroring the complex stability of the states, as shown in Fig. 8.6(b-d). For the slowest ramp [Fig. 8.6(b)], the dynamics is dominated by the instability of the normal state to the inverted state. For an intermediate ramp rate [Fig. 8.6(c)], the system first enters the unstable superradiant state before being driven by its instability to the inverted state. Finally, for a fast enough ramp [Fig. 8.6(d)], the system is quenched to the stable superradiant state before it can invert towards the nearly dark states.

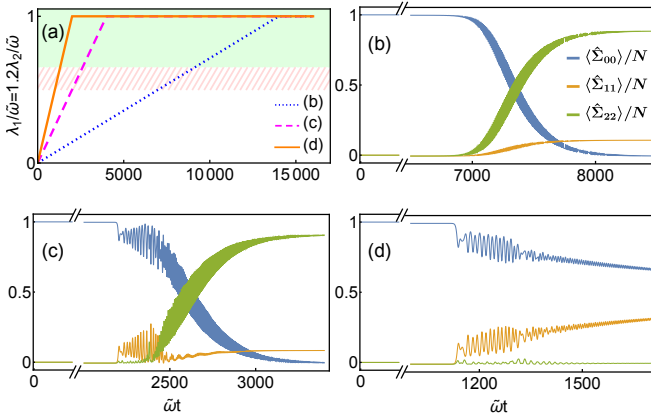


Figure 8.6: Dynamical evolution probing the accessibility of the superradiant states. (a) The ramp protocols of the coupling strengths. The regions in which the superradiant state is unstable, stable, and unphysical for the corresponding instantaneous coupling strengths are marked in green, hatched red, and white, respectively, cf. Fig. 8.1(c). (b-d) Qualitatively different evolutions of the atomic fields for the three protocols.

8.6 Conclusions

With the ensemble of V-shaped three-level atoms coupled to the cavity, we observe the overwhelming effects of driving and dissipation through the mechanisms discussed in Chapter 6. The dissipative stabilisation of a continuous family of excited many-body states as steady states establishes a new paradigm for preparing nearly dark states in cavity-atom systems. These salient features pave the way for a wide range of prospective applications. For instance, the large multistable region provides a potential platform for implementing fluctuation-driven phase transitions [224] and random walks like Lévy flight [225], which can be used for atom cooling [226–228].

9 | Uni-directional atomic current in a momentum lattice synthesised in a cavity-boson system

The model theoretically investigated in Chapter 8 has been motivated by an experimental setup, which will be presented and discussed in this Chapter. Surprisingly, the same driven-dissipative mechanism destabilising the low energy states of the three-level system eventually eliminates any potential steady state in the continuum model, through a cascade of cavity-mediated atomic transfers similar to those presented in Section 8.4. In this Chapter, we will investigate the continuum model mainly from the numerical perspective by performing Gross-Pitaevskii evolutions using MCTDH-X. Our simulations quantitatively capture not only the non-Hermitian dynamics in the momentum lattice, but also dephasing effects due to harmonic trap and contact interaction.

Originality declaration: This Chapter is adapted from our published work *Phys. Rev. Lett.* **128**, 143602 (2022) [RL4], where I, under supervision of R. Chitra, contributed as a theorist to the experimental work by R. Rosa-Medina, F. Ferri, F. Finger, N. Dogra, K. Kroeger, T. Donner and T. Esslinger. This Chapter puts an emphasis on the theory part of the work.

9.1 Introduction to the experimental setup

We first introduce the experimental realisation relevant to our V-shaped three-level atomic configuration presented in Chapter 8. It differs from the one described in Section 3.2 and later investigated in Chapters 4 and 7 in two aspects. First, the hyperfine structure of the BEC is now utilised, such that the spinor feature is exploited. The atoms are initialised in uniform distribution in $|F = 1, m_F = -1\rangle$ (denoted as $|\downarrow\rangle$ later), but $|F = 1, m_F = 0\rangle$ ($|\uparrow\rangle$) is also energetically relevant. Particularly, the hyperfine level $|F = 1, m_F = +1\rangle$ is irrelevant because its energy is shifted away by second-order Zeeman effects.

9.1. Introduction to the experimental setup

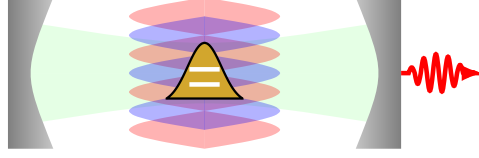


Figure 9.1: Schematics of the cavity-boson system used in experiments. Two laser pumps with orthogonally shifted phases is applied to a spinor BEC.

Second, two laser pumps are used, which are phase shifted by $\pi/2$ at the location of the BEC. This configuration exploits the orthogonal spatial modulations $\cos(k_c z)$ and $\sin(k_c z)$, which serve as the two degenerate higher-energy levels in Chapter 8.

The effective Hamiltonian of the cavity-boson system as sketched in Fig. 9.1 reads in two dimensions $\mathbf{x} = (x, y)$ and in the rotating frame as

$$\begin{aligned}
 H = \int d\mathbf{x} \Psi^\dagger(\mathbf{x}) \left\{ -\frac{\hbar^2 \nabla^2}{2m} + \frac{g}{2} \Psi^\dagger(\mathbf{x}) \Psi(\mathbf{x}) + V_{\text{trap}}(\mathbf{x}) + \hbar \delta_z \sigma_z \right\} \Psi(\mathbf{x}) \\
 + \frac{4\alpha_s}{\alpha_v} \int d\mathbf{x} \Psi^\dagger(\mathbf{x}) \Psi(\mathbf{x}) \\
 \left[\underbrace{\hbar \eta_r^2 / U_0}_{=E_r} \cos^2(k_c y) + \underbrace{\hbar \eta_b^2 / U_0}_{=E_b} \sin^2(k_c y) + \hbar U_0 a^\dagger a \cos^2(k_c x) \right] \\
 - \hbar \eta_r \int d\mathbf{x} \Psi^\dagger(\mathbf{x}) (a \sigma_- + a^\dagger \sigma_+) \Psi(\mathbf{x}) \cos(k_c x) \cos(k_c y) \\
 + \hbar \eta_b \int d\mathbf{x} \Psi^\dagger(\mathbf{x}) (a \sigma_+ + a^\dagger \sigma_-) \Psi(\mathbf{x}) \cos(k_c x) \sin(k_c y) \\
 - \hbar \Delta_c a^\dagger a.
 \end{aligned} \tag{9.1}$$

where $4\alpha_s/\alpha_v$ is the ratio between the atomic scalar and vector polarisabilities, $\Psi = (\Psi_\uparrow, \Psi_\downarrow)^T$ is the spinor encoding the hyperfine $|\downarrow\rangle$ and $|\uparrow\rangle$ states, and σ are the corresponding Pauli matrices. We now discuss the differences between this Hamiltonian and the one presented in Eq. (3.6). The two laser pumps provide phase shifted optical lattice potentials $\cos^2(k_c y)$ and $\sin^2(k_c y)$, whose depths E_r and E_b can in principal be tuned independently. Here the subscripts “red” and “blue” refer to the fact that the two optical lattices are technically achieved using slightly detuned laser pumps. Similar to the system in Eq. (3.6), the lattice depths E_r and E_b indirectly controls the coupling strengths η_r and η_b between the cavity field and the orthogonal atomic modes $\cos(k_c x) \cos(k_c y)$ and $\cos(k_c x) \sin(k_c y)$, respectively. In practice, balanced drive $E_r = E_b \gg NU_0$ is implemented to diminish the effects from the optical lattices (second line of the

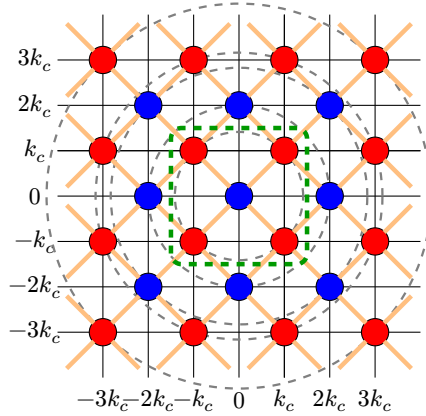


Figure 9.2: The tight-binding model Eq. (9.3) illustrated on the momentum lattice. The blue and red circles represent states in the $|\downarrow\rangle$ and $|\uparrow\rangle$ hyperfine sublevels, respectively. The orange lines indicate the couplings. The dashed circles represent the “chemical potential landscape” due to kinetic energy $\propto \omega_R$. The green dashed box in the centre highlights where the truncated model locally recovers the three-level model Eq. (8.1).

Hamiltonian). This requirement eventually imposes the limitation that only $\eta_r = \eta_b \equiv \eta$ can be achieved experimentally, corresponding to the U(1) line $\lambda_1 = \lambda_2$ of the model Eq. (8.1). The final crucial ingredient is the dissipation of the cavity, which as usual is captured by the Lindbladian as in Eq. (3.7).

$$i\hbar\partial_t a = i[H, a] - \hbar\kappa a \quad (9.2)$$

9.2 Mapping to Dicke-like model and uni-directional atomic current in the momentum lattice

The dominant dynamics of the system Eq. (9.1) with $\eta_r = \eta_b \equiv \sqrt{8N}\lambda$ can be captured by a mapping to a cavity-mediated tight-binding model as illustrated

9.2. Mapping to Dicke-like model and uni-directional atomic current in the momentum lattice

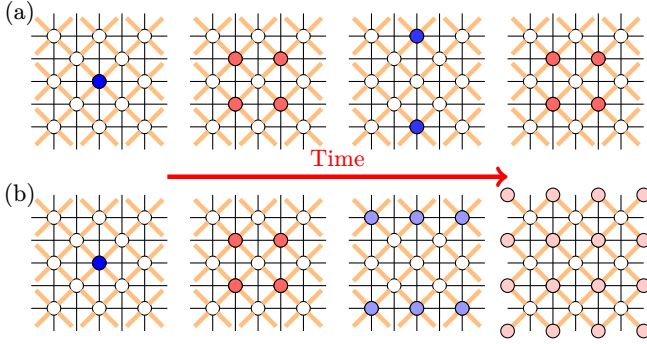


Figure 9.3: Atomic dynamics on the momentum lattice with (a) small coupling strength $\lambda < \omega_R$ and (b) large coupling strength $\lambda \gg \omega_R$. The colour brightness of the occupied sites represents their occupancy.

Fig. 9.2 with Hamiltonian

$$\begin{aligned}
 H = & \hbar\omega_c a^\dagger a \\
 & + \sum_{i=1}^N \sum_{\substack{\{j,k\} \in \mathbb{Z} \\ \sigma \in \{0,1\}}} \hbar\omega_{(2j+\sigma, 2k+\sigma), \sigma} |(2j+\sigma, 2k+\sigma), \sigma\rangle_i \langle (2j+\sigma, 2k+\sigma), \sigma|_i \\
 & - \frac{\hbar\lambda}{\sqrt{N}} \sum_{i=1}^N \sum_{\substack{\{j,k\} \in \mathbb{Z} \\ s_{1,2} = \pm 1}} a^\dagger \left[|(2j+s_1, 2k+s_2), \uparrow\rangle_i \langle (2j, 2k), \downarrow|_i \right. \\
 & \quad \left. - is_2 |(2j, 2k), \downarrow\rangle_i \langle (2j+s_1, 2k+s_2), \uparrow|_i + \text{h.c.} \right]
 \end{aligned} \tag{9.3}$$

where

$$|(l, m), \sigma\rangle = |l \times k_c, m \times k_c\rangle \otimes |\sigma\rangle = \frac{k_c}{2\pi} e^{ik_c(lx+mz)} \otimes |\sigma\rangle \tag{9.4}$$

The indices $l, m \in \mathbb{Z}$ and $\sigma \in \{0, 1\}$ label a discrete set of plane waves and the spin state associated to the Zeeman sublevels $|\downarrow\rangle$ and $|\uparrow\rangle$, respectively. The states are normalised within a unit cell $(x, y) \in [-\pi/k, \pi/k] \otimes [-\pi/k, \pi/k]$ in real space. The energies of these states are related to the recoil energy $\omega_R = \hbar k_c^2 / 2m = 2\pi \cdot 3.73$ kHz and the Zeeman splitting $\omega_0 \sim 2\pi \cdot 100$ kHz as

$$\omega_{(2j+\sigma, 2k+\sigma), \sigma} = [(2j+\sigma)^2 + (2k+\sigma)^2] \omega_R + \sigma \omega_0 \tag{9.5}$$

In fact, the cavity-boson system discussed in Chapter 3 can also be mapped to a similar tight-binding model in the momentum space. However, since the kinetic energy effectively provides a harmonic trapping potential in the momentum lattice [cf. Eq. (9.5)], it is possible to truncate the momentum modes and retain

the ones with the lowest energies. Such truncation was valid for the scenarios discussed in Chapter 3 because the Dicke model has low energy states, i.e. normal state and superradiant state, as its steady states. In contrast, if a similar truncation is used for the current model, the system with

$$\begin{aligned}
 |0\rangle &= |(0, 0), \downarrow\rangle \\
 |1\rangle &= \frac{1}{2} [|(+1, +1), \uparrow\rangle + |(+1, -1), \uparrow\rangle + |(-1, +1), \uparrow\rangle + |(-1, -1), \uparrow\rangle] \\
 |2\rangle &= \frac{i}{2} [|(+1, +1), \uparrow\rangle - |(+1, -1), \uparrow\rangle + |(-1, +1), \uparrow\rangle - |(-1, -1), \uparrow\rangle]
 \end{aligned} \tag{9.6}$$

yields the Hamiltonian Eq. (8.1). According to our theoretical results in Chapter 8, this model has states with high energy and high momentum as steady states. The coupling of these states with the rest of the momentum lattice should thus not be neglected.

We now discuss the dynamics of the system in this momentum lattice, which highly depends on the relative scale between the coupling strength λ and thus recoil energy ω_R providing the effective chemical potential in the lattice. In all cases, the initial state $|(0, 0), \downarrow\rangle$ is unstable towards $|(\pm 1, \pm 1), \uparrow\rangle$ because the Hamiltonian Eq. (8.1) is locally recovered, but the dynamics varies greatly after that.

When $\lambda \gg \omega_R$ [see Fig. 9.3(b)], the effective chemical potential becomes negligible, making the momentum lattice translationally invariant. Locally around $|(+1, +1), \uparrow\rangle$ (similarly for $|(\pm 1, \pm 1), \uparrow\rangle$), the Hamiltonian Eq. (8.1) is recovered, leading to a further hopping to $|(0, \pm 2), \downarrow\rangle$ and $|(\pm 2, \pm 2), \downarrow\rangle$. However, a hopping to $|(0, 0), \downarrow\rangle$ and $|(\pm 2, 0), \downarrow\rangle$ is prohibited by destructive interference, as the system is now in a (nearly-)dark state from the perspective of $|(0, 0), \downarrow\rangle$. Similar dynamics is repeated in a cascade manner, spreading the atoms to a wide range of momentum modes. This dynamics is non-Hermitian and uni-directional because of the non-Hermiticity brought by dissipation.

In contrast, when $\lambda < \omega_R$ [see Fig. 9.3(a)], the dynamics is very sensitive to the effective chemical potential. Locally around $|(\pm 1, \pm 1), \uparrow\rangle$, the Hamiltonian Eq. (8.1) is no longer recovered. Due to energetic reasons and destructive interference, the atoms can now only hop forth to $|(\pm 2, 0), \downarrow\rangle$ and back to $|(\pm 1, \pm 1), \uparrow\rangle$. Notably, an extra phase is gained during this forth-and-back hopping, switching the system from the dark state to the bright state from the perspective of $|(0, 0), \downarrow\rangle$, allowing a hopping back to $|(0, 0), \downarrow\rangle$. As a result, the system recovers its initial state, and will then repeat the same dynamics.

In both cases, the system will eventually dephase after a few hops due to the different time scales of the different hoppings. As a result of the dephasing, individual hoppings can no longer be clearly discerned from each other.

9.3 Gross-Pitaevskii simulations

The picture presented above can be confirmed by Gross-Pitaevskii equation simulations of the continuum model Eq. (9.1) using MCTDH-X [RL6, 83–85, 158]. Besides confirming the non-Hermitian dynamics, we elucidate the lifetime of the momentum lattice due to oscillatory dynamics in the harmonic trap. Although the corresponding experimental results are not fully discussed in this thesis, we confirm that our numerical simulations are consistent quantitatively with the experiments.

9.3.1 Equations of motion

We solve the time evolution of the two-component mean-field Hamiltonian

$$H = N \int \Phi^\dagger H^{(1)} \Phi dx dy + \frac{g}{2} N(N-1) \int |\phi_\downarrow + \phi_\uparrow|^4 dx dy \quad (9.7)$$

with $\Phi = (\phi_\downarrow, \phi_\uparrow)^T$, where $\phi_\downarrow(x, y)$ and $\phi_\uparrow(x, y)$ are the mean-field wavefunctions of the two spin levels $|\downarrow\rangle$ and $|\uparrow\rangle$ with normalisation $\int \Phi^\dagger \Phi dx dy = 1$. The second term describes contact interactions between the atoms, where we assume identical inter- and intra-spin coupling constants g_0 . This is a good approximation for ^{87}Rb atoms in the $F = 1$ manifold [229]. Moreover, the first term integrates over the single-particle Hamiltonian, which is given by

$$\begin{aligned} H^{(1)} = & \left[-\frac{\hbar^2 \nabla^2}{2m} + \frac{m}{2} (\omega_x^2 x^2 + \omega_y^2 y^2) \right] \mathbf{1} - \hbar \omega_0 \sigma_z \\ & + \hbar \eta (\alpha + \alpha^*) \cos(k_c x) \cos(k_c y) \sigma_y \\ & + i \hbar \eta (\alpha - \alpha^*) \cos(k_c x) \sin(k_c y) \sigma_x, \end{aligned} \quad (9.8)$$

where σ_j refer to the Pauli matrices, with $j \in \{x, y, z\}$. This Hamiltonian contains the same contributions as the one presented in Eq. (9.3), but sets explicitly $\eta_r = \eta_b = \eta$ and omits the cavity-field potential (last term in the second line). More specifically, the first line includes the kinetic term, the harmonic trap with typical experimental trapping frequencies $[\omega_x, \omega_y] = 2\pi \cdot [218, 172]$ Hz, and the total splitting between the two levels ($\propto \omega_0$). The second line describes the cavity-assisted Raman transitions between the two spin levels, and is essentially consistent with the last two lines of Eq. (9.3). The contact interaction strength $Ng = 1210\hbar^2/m$ is chosen such that the initial Thomas-Fermi radii coincide with the experimental values $[r_{\text{TF},x}, r_{\text{TF},z}] = [4.3, 5.5] \mu\text{m}$. The cavity field is treated as a coherent light field and represented by a complex number $\alpha = \langle a \rangle$, whose evolution follows

$$\begin{aligned} \partial_t \alpha &= [i\Delta_c - \kappa] \alpha - i\eta N \theta, \\ \theta &= \int \Phi^\dagger [\cos(k_c x) \cos(k_c y) \sigma_y + i \cos(k_c x) \sin(k_c y) \sigma_x] \Phi dx dy. \end{aligned} \quad (9.9)$$

9.3.2 Numerical solution of the dynamics

Using MCTDH-X, we employ a variational method and evolve the wavefunction $\Phi(x, y; t)$ to numerically solve the dynamics. The system is prepared in a slightly perturbed BEC state in a harmonic trap, where the perturbation represents the noise in the system, and is empirically set such that the first superradiant pulse occurs at a time comparable to the one observed in the experiment. We then activate the cavity field and evolve the system under two different sets of cavity parameters corresponding to those used in experiments, which also correspond to the two cases discussed in Fig. 9.3, respectively. The results presented below are quantitatively consistent with the experimental results [see Ref. [RL4]].

The first simulation is performed with $\Delta_c = -2\pi \cdot 0.7$ MHz and $\omega_0 = 2\pi \cdot 72.5$ kHz, while the coupling is increased to $\eta_{\max} = 2\pi \cdot 0.62$ kHz within $t_r = 1.5$ ms using an s-shaped ramp as in the experiment. The simulation results are presented in Fig. 9.4. The behaviour of the cavity field [Fig. 9.4(a)] and its spectrogram [Fig. 9.4(b)] reproduce the experimental results. Three strong photon pulses are observed, whose frequencies are determined by the atomic splitting and the recoil frequency according to Eq. (9.5). Accompanying each photon pulse, the energy of the atomic state $E = \langle H \rangle$ [Fig. 9.4(c)] and the atomic occupation of the $|\downarrow\rangle$ spin manifold [Fig. 9.4(d)] $N_\downarrow = N \int |\phi_\downarrow(x, y)|^2 dx dy$ change drastically. To better understand the atomic dynamics induced by the emerging cavity field, we look at four representative spin and density distributions taken between the photon bursts. The snap-shots of the real-space $\rho_{\downarrow/\uparrow}(x, y) = |\phi_{\downarrow/\uparrow}(x, y)|^2$ and momentum-space distributions $\rho_{\downarrow/\uparrow}(k_x, k_y) = |\phi_{\downarrow/\uparrow}(k_x, k_y)|^2$ at different points in time are shown in Fig. 9.4(e-t), where $\phi_{\downarrow/\uparrow}(k_x, k_y)$ are the Fourier transforms of $\phi_{\downarrow/\uparrow}(x, y)$, respectively. The atomic transfers in the momentum-space lattice are clearly visible, and the momentum space densities Fig. 9.4(g,h,k,l,o,p) qualitatively reproduce the experimental results and are consistent with the analysis in Fig. 9.3(a). Through the first and second bursts, the majority of the atoms undergo the transfer $|(0, 0), \downarrow\rangle \rightarrow |(\pm 1, \pm 1), \uparrow\rangle \rightarrow |(0, \pm 2), \downarrow\rangle$. This dynamics is also reflected in real space by the formation of the corresponding density waves. At long times $t > 1.83$ ms [Fig. 9.4(q-t)], the momentum distribution becomes washed out and starts to deviate from a tight-binding description. This is due to the combined effect of the harmonic trap and contact interactions, which induces complex dynamics in momentum space. In the next subsection, we characterise this effect in detail.

The second simulation is performed with $\Delta_c = -2\pi \cdot 1.26$ MHz and $\omega_0 = 2\pi \cdot 3.7$ kHz $\approx \omega_R$, while the coupling is increased up to $\eta_{\max} = 2\pi \cdot 0.50$ kHz within $t_r = 2$ ms using the experimental protocol. The simulations are shown in Fig. 9.5. Compared to the first simulation, here we observe a strong single photon burst lasting for a relatively long time [Fig. 9.5(a)], during which several

atomic transfers consistent with the analysis in Fig. 9.3(b) occurs. During this pulse, the spectrogram [Fig. 9.5(b)], system energy [Fig. 9.5(c)], and atomic occupation of the ϕ_{\downarrow} level [Fig. 9.5(c)] all show complex, rapidly changing behaviours. To better understand the system dynamics, we again choose four representative time points and show the corresponding density distributions in Fig. 9.5(e-t). From the momentum space densities in Fig. 9.5(g,h,k,l,o,p), we notice a “cascaded atomic transfer” taking place only between nearest neighbouring sites in the momentum lattice. Remarkably, the next tunnelling event starts before the previous one is fully completed. This is also evidenced in the population dynamics of $|\downarrow\rangle$ [Fig. 9.5(c)], which keeps decreasing as the mode $|(0, \pm 2), \downarrow\rangle$ gets populated. As the time elapses, the atoms gradually occupy modes with larger momentum within the same photon burst, giving rise to qualitatively different dynamics from the one presented in Fig. 9.4. We can thus understand this single pulse as a conjunction of several bursts, where due to the small energy difference between the two spin manifolds ($\omega_0 \approx \omega_R$), the succeeding pulse is stimulated by the preceding one and starts before the latter finishes. As a result, multiple sites in the momentum lattice can be occupied simultaneously as shown in Fig. 9.5(o,p). Moreover, in Fig. 9.5(o,p), we show that before oscillatory dynamics in the harmonic trap completely blurs the momentum lattice, the highest order momentum states occupied are $|(1, 3), \uparrow\rangle$, $|(1, -3), \uparrow\rangle$, $|(-1, 3), \uparrow\rangle$ and $|(-1, -3), \uparrow\rangle$. This is compatible to the experimental observations.

9.3.3 Dynamics due to harmonic confinement and contact interactions

Harmonically confined Bose-Einstein condensates exhibit oscillatory motion when prepared away from their equilibrium configuration [230, 231], for example through excited breathing modes [232]. As the states in the momentum lattice generally differ from the equilibrium Thomas-Fermi distribution, we expect them to oscillate in real space in the trap. This moves the momentum components out of the grid nodes, progressively rendering the tight-binding picture invalid. In particular, we observed in the simulations in Fig. 9.4, that the lifetime of the momentum lattice (~ 1 ms) is roughly on the same order as the inverse trap frequency. Since this time scale is on the same order of magnitude as the dynamics in the momentum lattice, it constitutes one of the main limitations of our scheme. Nevertheless, we observe in our simulations that contact interactions can increase this lifetime. To quantify this process, we perform Gross-Pitaevskii simulations for a spinless system, where we prepare an initial wavefunction

$$\phi(x, y) = \psi(x, y) \cos(k_c x) \cos(k_c y). \quad (9.10)$$

The envelop function ψ describes a Thomas-Fermi profile or a Gaussian profile, depending on whether contact interactions are considered or not. This state

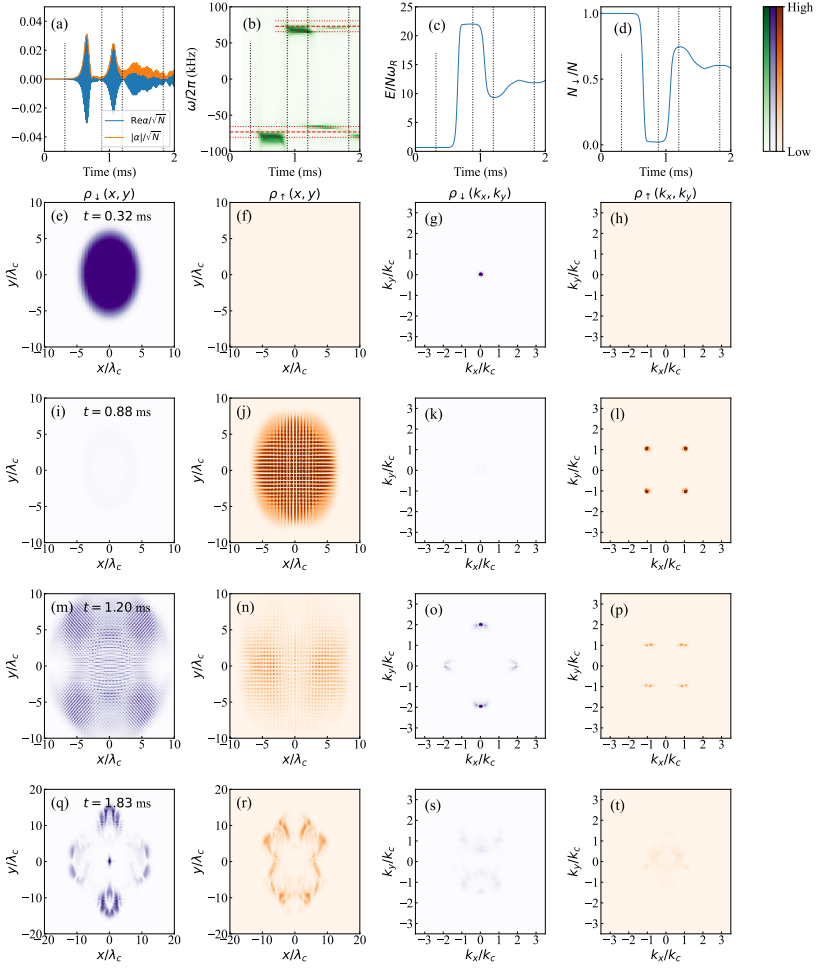


Figure 9.4: Simulations of Gross-Pitaevskii equations reproducing results from Fig. 3 in the main text. (a-d) Time evolution of the real part [(a), blue], magnitude [(a), orange] and spectrogram (b) of the cavity field, (c) system energy, and (d) occupation of the $|\downarrow\rangle$ mode. In panel (b), the thick dashed lines indicate $\omega = \pm\omega_0$, whereas the thin dotted lines indicate $\omega = \pm\omega_0 \pm 2\omega_R$. (e-t) The real space and momentum space density distributions are shown at four representative time points $t = \{0.32, 0.88, 1.20, 1.83\}$ ms for atoms in the spin states $|0\rangle$ (purple) and $|1\rangle$ (orange colour maps). These four time points are indicated as vertical dashed points in panels (a-d).

9.3. Gross-Pitaevskii simulations

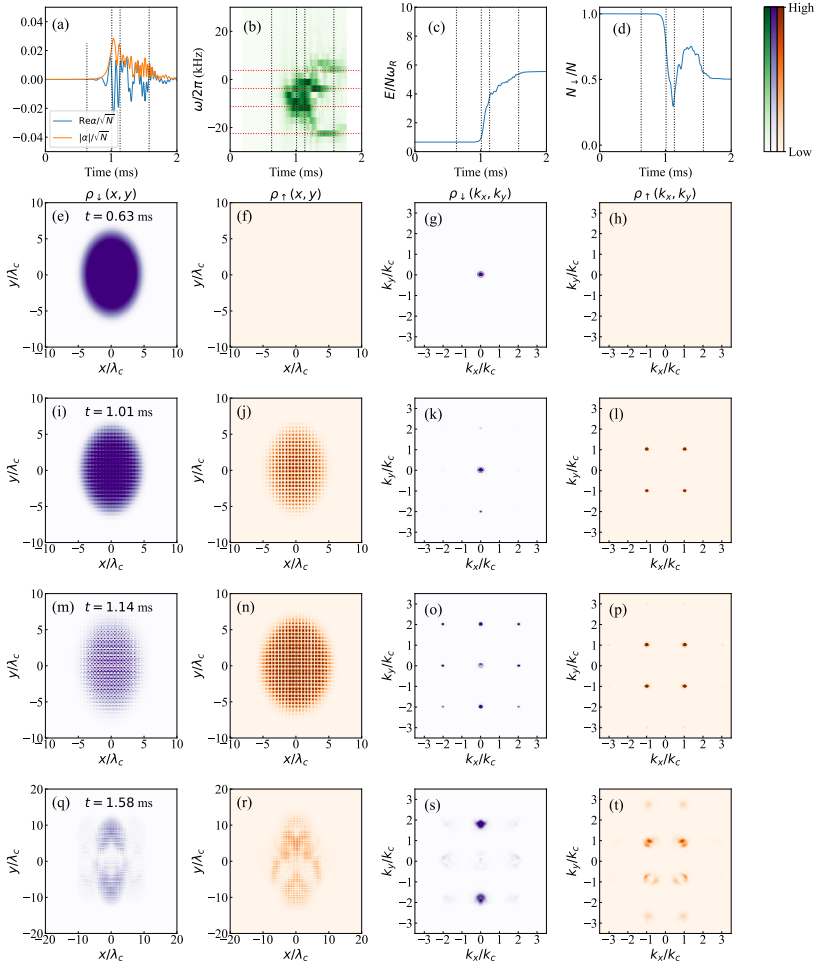


Figure 9.5: Simulations of Gross-Pitaevskii equations reproducing results from Fig. 4 in the main text. (a-d) The time evolution of the real part [(a), blue], magnitude [(a), orange] and spectrogram (b) of the cavity field, and (d) occupation of the ϕ_0 mode. In panel (b), the thick dashed lines indicate $\omega = \omega_R, -\omega_R, -3\omega_R$ and $-6\omega_R$, respectively. (e-t) The real space and momentum space density distributions at four representative time points $t = \{0.63, 1.01, 1.14, 1.58\}$ ms for atoms in the spin states $|0\rangle$ (purple) and $|1\rangle$ (orange colour maps). These four time points are indicated as vertical dashed points in panels (a-d).

resembles the atomic state after the first tunnelling event in the momentum lattice, i.e., $|(\pm 1, \pm 1)\rangle$ [cf. Figs. 9.4(j,l)]. We then propagate the state freely in the harmonic trap while deactivating the coupling to the cavity field. The same simulation is performed for both the experimentally relevant contact interaction strength $Ng = 1210 \hbar^2/m$ and for a smaller value $Ng = 121 \hbar^2/m$. During the simulation, we measure the overlap between the instantaneous wavefunction and the initial one

$$\begin{aligned} \zeta &= \left| \int dk_x dk_y \phi^*(k_x, k_y; t=0) \phi(k_x, k_y; t) \right| \\ &= \left| \int dx dy \phi^*(x, y; t=0) \phi(x, y; t) \right|, \end{aligned} \quad (9.11)$$

and show it in Fig. 9.6. For the experimentally relevant interaction strength, the lifetime is roughly 1 ms, which is approximately twice longer than for a system with weak contact interactions. The real and momentum space densities of the two simulations are also shown in Fig. 9.7. We observe that strong contact interactions effectively diffuse the lattice peaks in momentum space, which slows down the evolution of the atomic distribution away from the lattice sites in momentum space. We note that this lifetime is also consistent with the simulation results in Figs. 9.4 and 9.5, where oscillatory motion in the trap washes out the momentum lattice roughly 1 ms after the first photon pulse. In conclusion, these simulations of the Gross-Pitaevskii equations capture the dynamics observed in the experiment and validate the tight-binding description of the momentum lattice at sufficiently small times. In addition, they allow us to estimate the lifetime due to the dynamics in the harmonic trap in the presence of contact interactions.

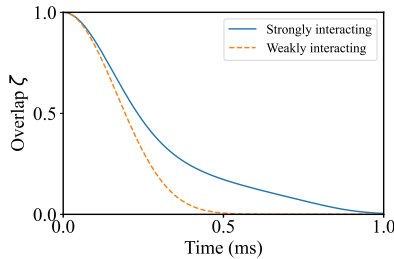


Figure 9.6: The overlap ζ [cf. Eq. (9.11)] as a function of time for the evolution of the state Eq. (9.10) in a harmonic trap with strong (blue solid line, $Ng = 1210\hbar^2/m$) and weak contact interactions (orange dashed line, $Ng = 121\hbar^2/m$).

9.3. Gross-Pitaevskii simulations

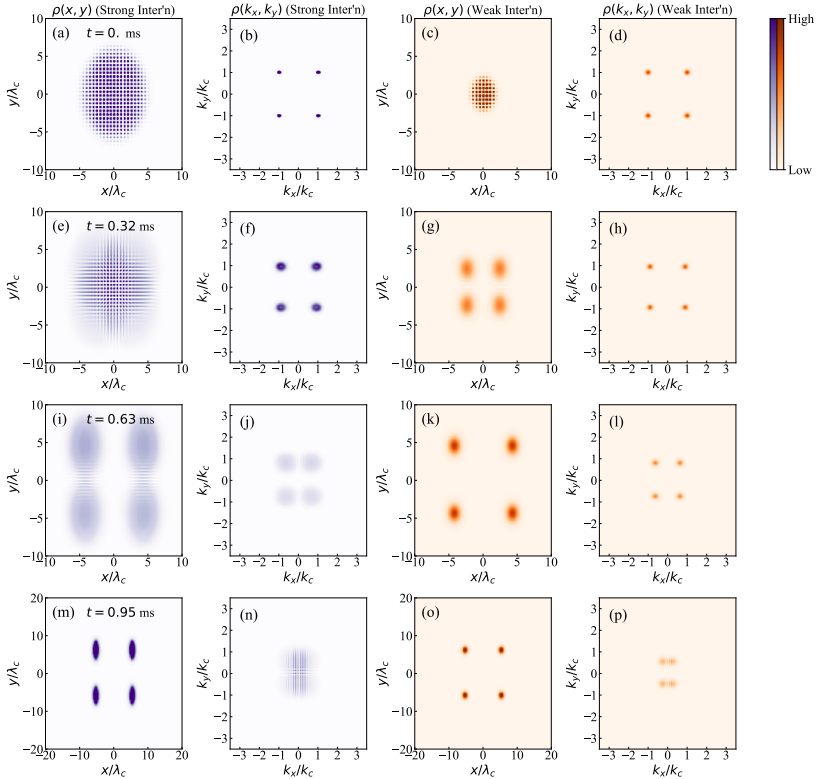


Figure 9.7: Representative snapshots of the evolution of the real and momentum space distributions for a 2D harmonically confined atomic cloud initialised in $\phi(x, y)$ with trap frequencies $[\omega_x, \omega_y] = 2\pi \cdot [218, 172]$ Hz [cf. Eq. (9.10)]. The purple (orange) colour map corresponds to the experimentally relevant (smaller) contact interactions, which are on the order of $Ng = 1210 \hbar^2/m$ ($Ng = 121 \hbar^2/m$).

9.4 Conclusions

The cavity-boson experimental setup implemented using two laser pumps and a spinor BEC realises a tight-binding model whose coupling between lattice sites is mediated by cavity field. The low-energy Hilbert space of this tight-binding model reproduces the three-level model investigated in Chapter 8, and indeed manifests an instability of the lowest-energy BEC mode due to the driven-dissipative instability mechanism from particle-hole coupling as introduced in Section 6.2. Depending on the parameter regime, this instability leads to a variety of non-Hermitian, uni-directional dynamics in the momentum lattice, as confirmed by Gross-Pitaevskii evolutions based on MCTDH-X. In realistic cavity-boson systems, such dynamics is eventually dephased by the harmonic trapping potential and the contact interaction.

This final work also concludes Part II. We have seen three different physical models, which gradually manifests more and more intriguing dynamics introduced by drive and dissipation. The theory work presented in the previous Chapters 5 and 6 based on a combination of Keldysh and Floquet formalism indeed clearly explains and discerns multiple novel mechanisms and instabilities, which arise in cavity-boson systems and lead to phenomenology which can be experimentally observed. The success of implementing and understanding driven-dissipative effects from a combination of Keldysh and Floquet formalism also inspires us to apply it beyond quantum gaseous systems, e.g. superconductors. This will be the focus of Part III.

PART III

Driven-dissipative enhancement of superconductivity

RECENTLY, Floquet engineering has been widely used in condensed matter systems, particularly on superconductors. Illuminating the superconducting electrons by laser and/or coupling it to an optical cavity enable us to manipulate novel many-body phases, including topological states [34, 37, 38, 233], odd-frequency superconducting pairs [234, 235], and Ampèrian superconducting pairs [236]. On the other hand, by driving either the electronic band structure or the interaction-mediating phonons, it is possible to enhance [237–241], and even induce [242–245] superconductivity. Furthermore, unconventional many-body effects can be achieved through driving, like η -pairing superconductivity [246–249], chiral superconductivity [250], and entropy-cooling mechanism [251]. Most of these Floquet engineering schemes depend on the effective stroboscopic picture the explanation of a large variety of driven phenomena. When seen in a rotating frame where the system appears to be static, the driving effectively creates new terms to and/or renormalises the coefficients of the Hamiltonian. For instance, the coupling to the electromagnetic field is typically captured by the minimal coupling $\mathbf{k} \rightarrow \mathbf{k} - e\mathbf{A}(t)$.

Based on our understanding of the driven-dissipative effects in quantum optical and ultracold gaseous systems, we anticipate that condensed matter systems such as superconductors should also be subject to similar effects. Analysis purely based on stroboscopic Hamiltonians fails, and we need to take the relative rotation between the system and the thermal environment into full account for an accurate description. Nevertheless, periodic drivings in condensed matter systems have vastly different features compared to those in quantum optical and gaseous systems: (i) The energy scales in the condensed matter systems are significantly larger than the ones in ultracold atom systems, and are thus closer to the driving frequency. As a result, the rotating wave approximation becomes less valid, and the drive thus takes the form of $\cos(\Omega t)$ rather than $e^{i\Omega t}$. (ii) Often electrons are driven in condensed matter systems. Their fermionic nature indicates that their Nambu space does not possess exotic symplectic

features as the bosonic one. This can potentially invalidate some of the driven-dissipative scenarios discussed in Part II, adding another layer of complexity to the treatment of the problem.

In this Part, we focus on the example of superconductors, where the well-established BCS theory for the static systems can facilitate our understanding of the corresponding driven-dissipative systems. Based on our results in Part II and Ref. [252], we further equip the self-consistency gap equation for superconductivity with Floquet and Keldysh structure. This helps us to systematically take the electronic thermal distribution into account, which appears as non-thermal when viewed from the superconductor. We discuss these effects upon the anomalous spectral and response functions, which eventually leads to the enhancement of superconductivity in the vicinity of, and beyond the critical temperature. As a proof of principle, we use flat-band superconductors as a main example due to the straightforward calculation. We emphasise again that this mechanism is essentially different from most of the schemes for Floquet-engineered superconductors.

Originality declaration: This Part, consisting of Chapters 10 and 11, is an integrated work in progress [RL5] under supervision of Aline Ramires and R. Chitra. The formalism we develop in Chapter 10 is based on the results in Ref. [252].

10 | Keldysh-Floquet formalism on superconductors

The goal of this Chapter is to derive the self-consistency equation for the superconducting order parameter, in the presence of driving and coupling to bath, based on the Keldysh-Floquet formalism and the Hubbard-Stratonovich transformation. The frame invariance of the equation will also be proven, which validates our later treatment in the lab frame. The equation obtained will be the basis for discussing our primary results in Chapter 11.

10.1 System description

We consider a periodically-driven superconductor coupled to a bath, which is schematically shown in Fig. 10.1, and described by the Hamiltonian

$$\mathcal{H}(t) = \sum_{\mathbf{k}} \Psi_{\mathbf{k}}^{\dagger} [H_{0,\mathbf{k}}^{\tau\sigma} + H_D^{\tau\sigma}(t)] \Psi_{\mathbf{k}} + \mathcal{H}_{\text{int}} \quad (10.1)$$

$$+ \sum_{\mathbf{k},\sigma=\{\uparrow,\downarrow\},q} (W_{\mathbf{k},q} c_{\mathbf{k},\sigma}^{\dagger} b_q + W_{\mathbf{k},q}^* b_q^{\dagger} c_{\mathbf{k},\sigma}) + \sum_q \xi_q b_q^{\dagger} b_q$$

$$\mathcal{H}_{\text{int}} = -g \sum_{\mathbf{k}_1,\mathbf{k}_2} c_{\mathbf{k}_1,\uparrow}^{\dagger} c_{-\mathbf{k}_1,\downarrow}^{\dagger} c_{\mathbf{k}_2,\uparrow} c_{-\mathbf{k}_2,\downarrow}. \quad (10.2)$$

The first part of \mathcal{H} describes a non-interacting electronic system, where

$$\Psi_{\mathbf{k}} = (c_{\mathbf{k},\uparrow}, c_{\mathbf{k},\downarrow}, c_{-\mathbf{k},\uparrow}^{\dagger}, c_{-\mathbf{k},\downarrow}^{\dagger})^{\text{T}} \quad (10.3)$$

is the Nambu spinor in Nambu (τ) and spin (σ) spaces, and $c_{\mathbf{k},\sigma}$ is the electronic annihilation operator. The non-interacting system consists of a term constant in time $H_0^{\tau\sigma}$ and a term driven periodically in time with $H_D^{\tau\sigma}(t) = \sum_{\ell \in \mathbb{Z} \setminus \{0\}} H_{\ell}^{\tau\sigma} e^{i\ell\Omega t}$, where τ_i and σ_i are Pauli matrices in the respective spaces, and the Hermiticity of the Hamiltonian is imposed by $H_{\ell}^{\tau\sigma\dagger} = H_{-\ell}^{\tau\sigma}$. In this Chapter, position and momentum independent drives are considered for the purpose of illustration. The third term describes the attractive interaction $g > 0$ of the superconductor, which could exist in different interaction channel.

10.2. The self-consistency equation for order parameter

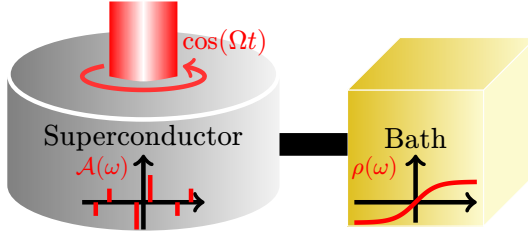


Figure 10.1: Schematics of the driven-dissipative superconductor. The superconductor characterized by its spectral function \mathcal{A} is coupled to a bath characterized by its thermal distribution ρ .

Without loss of generality, we consider the standard s -wave channel in $\tau_y \sigma_y$. Finally, the second line of \mathcal{H} is the dissipation channel described by a coupling of the superconductor to a fermionic bath b_q , with ξ_q the energy spectrum of the bath.

10.2 The self-consistency equation for order parameter

10.2.1 The coupling to the bath

We at first treat the coupling to the bath. For a clear presentation to emphasise the effects of the bath, we do not consider the interacting term for the moment, and suppress the momentum, spin and Nambu indices of the modes $c_{\mathbf{k},\sigma} \rightarrow \Psi$ since these modes are now decoupled and thus irrelevant to the current discussion. Each of these modes is coupled to a fermionic bath Φ_q , which can be thought as an electrode [81]. We always treat the system in the lab frame where there is no time dependence in either the bath or the coupling between the system and the bath. In other words, all time dependence lies in the Hamiltonian of the system H_D . This treatment will later be justified in Section 10.2.3.

The Floquet structure appears in the Keldysh partition function as [81]

$$Z_0 = \int D[\Psi_+^f, (\Psi_+^f)^\dagger, \Psi_-^f, (\Psi_-^f)^\dagger] \prod_q D[\Phi_{q,+}^f, (\Phi_{q,+}^f)^\dagger, \Phi_{q,-}^f, (\Phi_{q,-}^f)^\dagger] e^{iS_0^f} \quad (10.4)$$

$$S_0^f = S_{\text{sys}}^f + S_{\text{cp}}^f + S_{\text{bath}}^f, \quad (10.5)$$

where Ψ^f denote all Floquet components of the field Ψ ,

$$\Psi_\pm^f = (\dots, \Psi_{\pm, n=-2}, \Psi_{\pm, n=-1}, \Psi_{\pm, n=0}, \Psi_{\pm, n=1}, \Psi_{\pm, n=2}, \dots)^T, \quad (10.6)$$

with n the index of Floquet sectors.

Among the three terms in the action, only the action of the system intrinsically requires the Floquet structure since it contains the driving term $H^f = H_0^f + H_D^f$. It is given by

$$S_{\text{sys}}^f = \int d\omega \quad (10.7)$$

$$\left((\Psi_+^f)^\dagger \quad (\Psi_-^f)^\dagger \right) \begin{pmatrix} \omega_+ - H^f + \Omega N^f & 2i\rho^f(\omega)\eta^+ \\ 0 & \omega_- - H^f + \Omega N^f \end{pmatrix} \begin{pmatrix} \Psi_+^f \\ \Psi_-^f \end{pmatrix},$$

where $\omega_\pm = \omega \pm i\eta^+$ and η^+ is a positive infinitesimal. The matrix N^f has been defined in Eq. (2.5) (denoted as \mathbb{N}), and the thermal distribution ρ^f has been defined in Eq. (5.13). Meanwhile, the Floquet sectors in S_{cp}^f and S_{bath}^f are decoupled from each other because they are not subject to driving. This allows us to integrate out the bath field as usual by completion of squares. For example, in the $(0, 0)$ -Floquet sector where S_{cp} and S_{bath} are given respectively by [81]

$$S_{\text{cp}} = \sum_q \int d\omega \quad (10.8)$$

$$(W_q \Psi_+^* \Phi_{q,+} + W_q^* \Phi_{q,+}^* \Psi_+ + W_q \Psi_-^* \Phi_{q,-} + W_q^* \Phi_{q,-}^* \Psi_-)$$

$$S_{\text{bath}} = \sum_q \int d\omega \quad (10.9)$$

$$\begin{pmatrix} \Phi_{q,+}^* & \Phi_{q,-}^* \end{pmatrix} \begin{pmatrix} \omega + i\eta^+ - \xi_q + \Omega & 2i\rho(\omega)\eta^+ \\ 0 & \omega - i\eta^+ - \xi_q + \Omega \end{pmatrix} \begin{pmatrix} \Phi_{q,+} \\ \Phi_{q,-} \end{pmatrix},$$

which can be rewritten upon a transformation $\tilde{\Phi}_q = \Phi_q + W_q^* \Psi$ as

$$S_{\text{bath}} + S_{\text{cp}} \quad (10.10)$$

$$= \sum_q \int d\omega \begin{pmatrix} \tilde{\Phi}_{q,+}^* & \tilde{\Phi}_{q,-}^* \end{pmatrix} \begin{pmatrix} \omega + i\eta^+ - \xi_q + \Omega & 2i\rho(\omega)\eta^+ \\ 0 & \omega - i\eta^+ - \xi_q + \Omega \end{pmatrix} \begin{pmatrix} \tilde{\Phi}_{q,+} \\ \tilde{\Phi}_{q,-} \end{pmatrix}$$

$$- \sum_q \int d\omega \begin{pmatrix} \Psi_+^* & \Psi_-^* \end{pmatrix} \begin{pmatrix} \Sigma_q(\omega) & 2\rho(\omega)\Sigma_q(\omega) \\ 0 & -\Sigma_q(\omega) \end{pmatrix} \begin{pmatrix} \Psi_+ \\ \Psi_- \end{pmatrix},$$

10.2. The self-consistency equation for order parameter

with ¹

$$\Sigma_q(\omega) = \frac{|W_q|^2}{\omega - \xi_q + i\eta^+} \quad (10.11)$$

$$\Rightarrow \sum_q \text{Im} \Sigma_q(\omega) = -\pi \sum_q |W_q|^2 \delta(\omega - \xi_q) \equiv -\Sigma(\omega). \quad (10.12)$$

We only consider the contribution from the imaginary part, because the real part can be effectively absorbed into the chemical potential. A similar procedure can be repeated in other Floquet sectors, with a frequency shift $\omega \rightarrow \omega - n\Omega$. We can finally integrate out the bath field $\tilde{\Phi}_q$, and obtain an effective Green function for the system

$$S_{0,\text{eff}}^f = \int d\omega \left((\Psi_+^f)^\dagger \quad (\Psi_-^f)^\dagger \right) (G_{0,\text{eff}}^{-1})^{\kappa f} \begin{pmatrix} \Psi_+^f \\ \Psi_-^f \end{pmatrix} \quad (10.13)$$

$$(G_{0,\text{eff}}^{-1})^{\kappa f} = \begin{pmatrix} \omega + i\Sigma^f(\omega) - H^f + \Omega N^f & 2i\rho^f(\omega)\Sigma^f(\omega) \\ 0 & \omega - i\Sigma^f(\omega) - H^f + \Omega N^f \end{pmatrix}. \quad (10.14)$$

The infinitesimal positive number η^+ indicating the retarded/advanced Green function of the system is omitted because it is dominated by Σ .

Before moving on to include the interaction, we make a few remarks on the result. In $G^{\kappa f}$, the Hamiltonian H^f , the bath spectral function Σ^f , and the thermal distribution ρ^f are generally not simultaneously diagonalisable in the Floquet space. This means that generally there is no a frame where both the system and the bath appear static, and reflects the relative rotation between them. In the rest of this Chapter, we focus on the simple case of a Markovian bath $\Sigma^f(\omega) = \Sigma$, which is invariant as a function of ω in all rotating frames. Nevertheless, the frequency dependence in $\rho^f(\omega)$ is intrinsic and, in our case, defined in the lab frame. We remind ourselves that with these results we have also developed the formalism used for quantum optical systems in Section 5.2.

10.2.2 Hubbard-Stratonovich transformation

We now consider the interaction term on top of the single-particle terms, and reinstate the indices on Nambu space τ , spin space σ and momentum \mathbf{k} . Specifically, the electronic field Ψ is now a Nambu spinor

$$\Psi_{\pm,\mathbf{k}} = (\psi_{\pm,\mathbf{k},\uparrow}, \psi_{\pm,\mathbf{k},\downarrow}, \psi_{\pm,-\mathbf{k},\uparrow}^*, \psi_{\pm,-\mathbf{k},\downarrow}^*)^T. \quad (10.15)$$

¹We have used the Dirac identity

$$\frac{1}{x + i\eta^+} = \mathcal{P} \left(\frac{1}{x} \right) - i\pi\delta(x).$$

We also do not assume for the moment any specific form of time dependence of the single-particle Hamiltonian, it can in principle even be aperiodic in time. The interaction enters the action as

$$S_{\text{int}} = g \sum_{\mathbf{k}, \mathbf{k}'} \left[\int_{C_+} dt \psi_{+, \mathbf{k}, \uparrow}^* \psi_{+, -\mathbf{k}, \downarrow}^* \psi_{+, \mathbf{k}', \uparrow} \psi_{+, -\mathbf{k}', \downarrow} + \int_{C_-} dt \psi_{-, \mathbf{k}, \uparrow}^* \psi_{-, -\mathbf{k}, \downarrow}^* \psi_{-, \mathbf{k}', \uparrow} \psi_{-, -\mathbf{k}', \downarrow} \right], \quad (10.16)$$

where C_+ and C_- refer to the two branches of the Keldysh contour, respectively, see Fig. 5.1. A common strategy to solve this action is to perform a mean-field decoupling by introducing the auxiliary Hubbard-Stratonovich field Δ ,

$$1 = \int D[\Delta_+, \Delta_+, \Delta_-, \Delta_-] \quad (10.17)$$

$$\exp \left[i \frac{-1}{g} \left(\int_{C_+} dt |\tilde{\Delta}_+|^2 + \int_{C_-} dt |\tilde{\Delta}_-|^2 \right) \right] \\ \tilde{\Delta}_{\pm} = \Delta_{\pm} + g \sum_{\mathbf{k}} \psi_{\pm, \mathbf{k}, \uparrow} \psi_{\pm, -\mathbf{k}, \downarrow}, \quad (10.18)$$

giving

$$e^{iS_{\text{int}}} = \int D[\Delta_+, \Delta_+, \Delta_-, \Delta_-] e^{iS_{\Delta}} \quad (10.19)$$

$$S_{\Delta} = \int_{C_+} dt \frac{-1}{g} |\Delta_+|^2 - \left(\Delta_+^* \sum_{\mathbf{k}} \psi_{+, \mathbf{k}, \uparrow} \psi_{+, -\mathbf{k}, \downarrow} + \text{c.c.} \right) \\ + \int_{C_-} dt \frac{-1}{g} |\Delta_-|^2 - \left(\Delta_-^* \sum_{\mathbf{k}} \psi_{-, \mathbf{k}, \uparrow} \psi_{-, -\mathbf{k}, \downarrow} + \text{c.c.} \right). \quad (10.20)$$

We will next integrate out the electronic field, which can be straightforwardly performed in the ‘‘classical-quantum’’ representation after Keldysh rotation,

$$\Delta_c = \frac{1}{\sqrt{2}}(\Delta_+ + \Delta_-), \quad \Delta_q = \frac{1}{\sqrt{2}}(\Delta_+ - \Delta_-) \quad (10.21a)$$

$$\Psi_c = \frac{1}{\sqrt{2}}(\Psi_+ + \Psi_-), \quad \Psi_q = \frac{1}{\sqrt{2}}(\Psi_+ - \Psi_-) \quad (10.21b)$$

$$(\Psi_+^* \quad \Psi_-^*) G^{\kappa} \begin{pmatrix} \Psi_+ \\ \Psi_- \end{pmatrix} \mapsto (\Psi_c^* \quad \Psi_q^*) \underline{G}^{\kappa} \begin{pmatrix} \Psi_c \\ \Psi_q \end{pmatrix} \quad (10.21c)$$

$$\underline{G}^{\kappa} = \begin{pmatrix} 0 & G^R \\ G^A & G^K \end{pmatrix}, \quad (\underline{G}^{-1})^{\kappa} = \begin{pmatrix} (G^{-1})^K & (G^A)^{-1} \\ (G^R)^{-1} & 0 \end{pmatrix}. \quad (10.21d)$$

10.2. The self-consistency equation for order parameter

This representation is preferred because it automatically takes into account the integration direction along the Keldysh contour

$$\int_c dt \rightarrow \int dt. \quad (10.22)$$

It also provides direct physical interpretation. The classical field Δ_c corresponds to the macroscopic observable of the mean-field theory.

In the new representation, we can integrate out the electronic field using the Gaussian integral for Grassman number, after collecting S_{int} to the single-particle action. This yields the total partition function as

$$Z = \int D[\Delta_c, \Delta_c^*, \Delta_q, \Delta_q^*] e^{iS} \quad (10.23)$$

$$S = \int dt \frac{-1}{g} (\Delta_q^* \Delta_c + \Delta_c^* \Delta_q) - i \sum_k \text{Tr}_{\kappa\tau\sigma} \ln(\underline{G}_{\Delta,k}^{-1})^{\kappa\tau\sigma} \quad (10.24)$$

$$\begin{aligned} (\underline{G}_{\Delta,k}^{-1})^{\kappa\tau\sigma} &= (\underline{G}_{0,k}^{-1})^{\kappa\tau\sigma} - \frac{i}{\sqrt{2}} \sigma_y [\kappa_0 (\Delta_q^* \tau_+ - \Delta_q \tau_-) + \kappa_x (\Delta_c^* \tau_+ - \Delta_c \tau_-)] \\ &= (\underline{G}_{0,k}^{-1})^{\kappa\tau\sigma} - \frac{1}{\sqrt{2}} \begin{pmatrix} 0 & \Delta_q^* \sigma_y & 0 & \Delta_c^* \sigma_y \\ -\Delta_q \sigma_y & 0 & -\Delta_c \sigma_y & 0 \\ 0 & \Delta_c^* \sigma_y & 0 & \Delta_q^* \sigma_y \\ -\Delta_c \sigma_y & 0 & -\Delta_q \sigma_y & 0 \end{pmatrix}^{\kappa\tau}, \end{aligned} \quad (10.25)$$

where \underline{G}_0 is the Green function of the single-particle system, e.g. Eq. (10.14), in the classical-quantum representation, and the trace is normalised with respect to the dimension $\text{Tr} \mathbf{1} = 1$.

The classical field Δ_c can now be found by minimising the action [253]

$$\left. \frac{\delta S}{\delta \Delta_q^*} \right|_{\Delta_q = \Delta_q^* = 0} = 0, \quad (10.26)$$

which gives

$$\frac{\Delta_c(t)}{\sqrt{2}} = \frac{ig}{2} \sum_k \text{Tr}_{\kappa\tau\sigma} [(\underline{G}_{\Delta,k})^{\kappa\tau\sigma}(t, t) \sigma_y i\tau_+]_{\Delta_q = \Delta_q^* = 0} \quad (10.27)$$

$$= \frac{ig}{2} \sum_k \text{Tr}_{\tau\sigma} [(G_{\Delta,k}^K)^{\tau\sigma}(t, t) \sigma_y i\tau_+]_{\Delta_q = \Delta_q^* = 0}. \quad (10.28)$$

In the end, the information we obtain by introducing the Keldysh space is condensed into the Keldysh Green function, which indeed describes the thermal occupation as we discussed in Chapter 5. Another feature of this self-consistency equation is that the quantum field Δ_q vanishes by definition. In

the following, we identify the order parameter as the corresponding classical field

$$\Delta(t) = \frac{1}{\sqrt{2}} \Delta_c(t). \quad (10.29)$$

This self-consistency equation is valid in principle for Hamiltonians with any time dependence, but it is not solvable practically. By implementing the continuous or discrete translational symmetry in time, tractable equations for the Fourier components of the order parameter can be obtained. This constraint would be a constant $\Delta(t) = \Delta$ for a non-driven system, and for our system with periodic driving, it oscillates at frequencies which are multiples of the driving frequency

$$\Delta(t) = \sum_{n=-\infty}^{\infty} \Delta_n e^{in\Omega t}. \quad (10.30)$$

We emphasise that this construction inherently neglects potential non-trivial driven-dissipative dynamics like period doubling or limit cycles.

We thus promote the Fourier components of $\Delta(t)$ into the Floquet space by introducing

$$\Delta^f = \sum_n \Delta_n F_n^f, \quad (10.31)$$

which follows the self-consistency equation

$$\Delta^f = \frac{ig}{2} \sum_k \int \frac{d\omega}{2\pi} \text{Tr}_{\tau\sigma} [(G_{\Delta,k}^K)^{\tau\sigma f} \sigma_y i\tau_+], \quad (10.32)$$

where the Keldysh Green function G_{Δ}^K is related to the retarded/advanced Green function (already assuming a coupling to a Markovian bath in the lab frame)

$$((G_{\Delta,k}^{R/A})^{-1})^{f\tau\sigma} = (\omega \pm i\Sigma) \mathbf{1}^{f\tau\sigma} - H^{f\tau\sigma} - i\sigma_y [\Delta^f \tau_+ - (\Delta^f)^\dagger \tau_-], \quad (10.33)$$

by the generalised fluctuation-dissipation theorem in anti-Hermitised form [cf. Eq. (5.7) for static systems]

$$(G_{\Delta,k}^K)^{f\tau\sigma} = (G_{\Delta,k}^R)^{f\tau\sigma} \rho^f - \rho^f (G_{\Delta,k}^A)^{f\tau\sigma}. \quad (10.34)$$

Here, the fermionic thermal distribution in Floquet space ρ^f is defined as [cf. Eq. (5.13)]

$$\rho_{m,n}^f = \delta_{m,n} \tanh\left(\frac{\omega - m\Omega}{2T}\right). \quad (10.35)$$

In comparison to Ref. [252], we implement the thermal distribution ρ^f in the lab frame. The methodology used in Ref. [254] is also a special scenario of this formalism applied specifically on Rabi drive.

10.2.3 Invariance of order parameter in different frames

The self-consistency equation manifests invariance in different rotating frames as described by the rotating operator $P^{f\tau\sigma}$. This can be seen more clearly by rewriting the equation as

$$\Delta_n = \frac{ig}{2} \sum_{\mathbf{k}} \int \frac{d\omega}{2\pi} \text{Tr}_{f\tau\sigma} [(G_{\Delta,\mathbf{k}}^K)^{f\tau\sigma} \sigma_y i\tau_+ F_{-n}^f]. \quad (10.36)$$

A rotation $P^{f\tau\sigma}$ acts on all parts of the system (single-particle term and interaction) as well as the bath,

$$\begin{aligned} H^{f\tau\sigma} &\mapsto (P^{f\tau\sigma})^\dagger H^{f\tau\sigma} P^{f\tau\sigma} \\ \sigma_y \tau_+ &\mapsto (P^{f\tau\sigma})^\dagger \sigma_y \tau_+ P^{f\tau\sigma}, \\ \rho^f &\mapsto (P^{f\tau\sigma})^\dagger \rho^f P^{f\tau\sigma} \end{aligned} \quad (10.37)$$

resulting in

$$(G_{\Delta,\mathbf{k}}^K)^{f\tau\sigma} \mapsto (P^{f\tau\sigma})^\dagger (G_{\Delta,\mathbf{k}}^K)^{f\tau\sigma} P^{f\tau\sigma}, \quad (10.38)$$

and thus the self-consistency equation becomes

$$\Delta_n = \frac{ig}{2} \sum_{\mathbf{k}} \int \frac{d\omega}{2\pi} \text{Tr}_{f\tau\sigma} [(P^{f\tau\sigma})^\dagger (G_{\Delta,\mathbf{k}}^K)^{f\tau\sigma} \sigma_y i\tau_+ P^{f\tau\sigma} F_{-n}^f] \quad (10.39)$$

in the rotating frame. Since the rotation operators are functions of F_n^f , which commute with each other [cf. Appendix A.3], we finally obtain

$$\begin{aligned} \Delta_n &= \frac{ig}{2} \sum_{\mathbf{k}} \int \frac{d\omega}{2\pi} \text{Tr}_{f\tau\sigma} [(P^{f\tau\sigma})^\dagger (G_{\Delta,\mathbf{k}}^K)^{f\tau\sigma} \sigma_y i\tau_+ F_{-n}^f P^{f\tau\sigma}] \\ &\quad \frac{ig}{2} \sum_{\mathbf{k}} \int \frac{d\omega}{2\pi} \text{Tr}_{f\tau\sigma} [(G_{\Delta,\mathbf{k}}^K)^{f\tau\sigma} \sigma_y i\tau_+ F_{-n}^f], \end{aligned} \quad (10.40)$$

where we used the cyclic property of the trace and recover the same equation as in the original frame. We have thereby shown that the self-consistency equation, and thus its solution Δ_n , are independent from the frame. This ensures that we can securely work in the lab frame, where the thermal distribution ρ^f is defined in a simple form as in Eq. (5.13) and helps simplify calculations.

11 | Non-thermal driven effects in superconductors

With the formalism developed in Chapter 10, we discuss the consequences of the self-consistency equation, Eq. (10.32), for driven-dissipative superconductors in this Chapter. We first focus on the spectral functions and response functions describing the particle and hole excitations both close to and far from the Fermi surface. In particular, we focus on how the commutativity between the drive and the interaction channel determines some crucial aspects of the spectra. Based on this understanding, we discuss how to enhance superconductivity at finite temperatures using driving and dissipation. We demonstrate how superconductivity is stabilised at higher temperatures using the examples of a flat-band superconductor and a dispersive superconductor.

11.1 Spectral and response functions

We now discuss the effects induced by the relative rotation between the superconductor and the bath as captured by Eq. (10.32). To this end, we implement a weak, high frequency drive with only one principal frequency upon the static superconductor without spin-orbit coupling,

$$H_{0,\mathbf{k}}^{\tau\sigma} = \epsilon_{\mathbf{k}}\tau_z\sigma_0, \quad H_1^{\tau\sigma} = (H_{-1}^{\tau\sigma})^\dagger = \frac{a}{2}A^{\tau\sigma}, \quad H_{|\ell|\geq 2}^{\tau\sigma} = 0. \quad (11.1)$$

Specifically, the drive $A^{\tau\sigma}$ can in principle lie in τ_0 or τ_z Nambu sectors and any spin sector, and is sinusoidal $A^{\tau\sigma\dagger}A^{\tau\sigma} = \mathbf{1}^{\tau\sigma}$ with frequency Ω dominating over other energy scales. It can originate from, for example, a minimal coupling of the electrons to the magnetic field of an electromagnetic wave [34, 235]. We proceed to solve the system in the lab frame, and assume a priori that the oscillatory behaviours of the order parameter are negligible compared to its averaged value in time $|\Delta_{|\ell|\geq 1}| \ll |\Delta_0|$, and without loss of generality $\Delta_0 \geq 0$,

$$i\sigma_y(\Delta^f\tau_+ - (\Delta^f)^\dagger\tau_-) \approx \Delta_0\tau_y\sigma_y F_0^f. \quad (11.2)$$

11.1. Spectral and response functions

This facilitates us to write down the Dyson equation for the Green function in the Floquet space

$$G_{\mathbf{k}}^{R,\tau\sigma f} = \tilde{G}_{\mathbf{k}}^{R,\tau\sigma f} \sum_{n=0}^{\infty} \left[\frac{a}{2} (A^{\tau\sigma} F_1^f + A^{\tau\sigma\dagger} F_{-1}^f) \tilde{G}_{\mathbf{k}}^{R,f\tau\sigma} \right]^n, \quad (11.3)$$

where $\tilde{G}_{\mathbf{k}}^{R,\tau\sigma f} \equiv G_{\mathbf{k}}^{R,\tau\sigma f}(a = 0)$ describes the non-driven system and can be solved as

$$(\tilde{G}_{\mathbf{k}}^{R,\tau\sigma})_{\ell}^f(\omega) = \delta_{\ell,0} \tilde{G}_{\mathbf{k}}^{R,\tau\sigma}(\omega) = \frac{\omega_+ \tau_0 \sigma_0 + \epsilon_{\mathbf{k}} \tau_z \sigma_0 + \Delta_0 \tau_y \sigma_y}{\omega_+^2 - E_{\mathbf{k}}^2} \delta_{\ell,0}, \quad (11.4)$$

with $E_{\mathbf{k}} = \sqrt{\epsilon_{\mathbf{k}}^2 + \Delta_0^2}$ and $\omega_+ = \omega + i\Sigma$. Here the subscript ℓ refers to the ℓ -th Wigner component of the Shirley-Floquet Green function as introduced in Eq. (2.6), and the subscript Δ of the Green function is suppressed in comparison to the formulae in Chapter 10.

By substituting the obtained Green function Eq. (11.3) into the self-consistency equation Eq. (10.32), we observe that the ℓ -th Fourier component of the gap Δ_{ℓ} is determined by the ℓ -th Wigner component of the Green function $(G_{\mathbf{k}}^{R,\tau\sigma})_{\ell}^f$. This determination is direct for $\ell \neq 0$, and self-consistent for $\ell = 0$. Generally, the dominant contribution to $(G_{\mathbf{k}}^{R,\tau\sigma})_{\ell}^f$ and Δ_{ℓ} scale as

$$\begin{aligned} (G_{\mathbf{k}}^{R,\tau\sigma})_{\ell}^f &\sim \left(\frac{a}{2}\right)^{|\ell|} \tilde{G}_{\mathbf{k}}^{R,\tau\sigma}(\omega) \prod_{k=1}^{\ell} [A^{\tau\sigma(\dagger)} \tilde{G}_{\mathbf{k}}^{R,\tau\sigma}(\omega \pm k\Omega)] \\ \Delta_{\ell} &\sim \left(\frac{a}{\Omega}\right)^{|\ell|} \Delta_0, \end{aligned} \quad (11.5)$$

where we have used $\tilde{G}_{\mathbf{k}}^{R,\tau\sigma}(E_{\mathbf{k}} - k\Omega) \sim 1/\Omega$ for $k \neq 0$ due to the dominance of Ω . This result validates the a priori assumption Eq. (11.2), allowing us to focus on the constant component of the order parameter Δ_0 as determined self-consistently via the $\ell = 0$ Wigner component of Green function,

$$\Delta_0 = \frac{ig}{2} \sum_{\mathbf{k}} \int \frac{d\omega}{2\pi} \text{Tr}_{\tau\sigma} [(G_{\mathbf{k}}^{R,\tau\sigma})_{\ell=0}^f \sigma_y i\tau_+]. \quad (11.6)$$

The structure of $(G_{\mathbf{k}}^{R,\tau\sigma})_{\ell=0}^f$ thus reveals the behaviours of excitations, which can be characterised by the electron-hole spectral function \mathcal{A}_{eh} , the anomalous spectral function \mathcal{A}_{an} , and the (anomalous) response function \mathcal{R}_{an} . These are defined respectively as

$$\begin{aligned} \mathcal{A}_{\text{eh}}(\omega) &= -\text{Im} \text{Tr}_{\tau\sigma} [(G_{\mathbf{k}}^{R,\tau\sigma})_{\ell=0}^f] \\ \mathcal{A}_{\text{an}}(\omega) &= -\text{Im} \text{Tr}_{\tau\sigma} [i\tau_+ \sigma_y (G_{\mathbf{k}}^{R,\tau\sigma})_{\ell=0}^f] \\ \mathcal{R}_{\text{an}}(\omega) &= -\text{Im} \text{Tr}_{\tau\sigma} [i\tau_+ \sigma_y (G_{\mathbf{k}}^{K,\tau\sigma})_{\ell=0}^f]. \end{aligned} \quad (11.7)$$

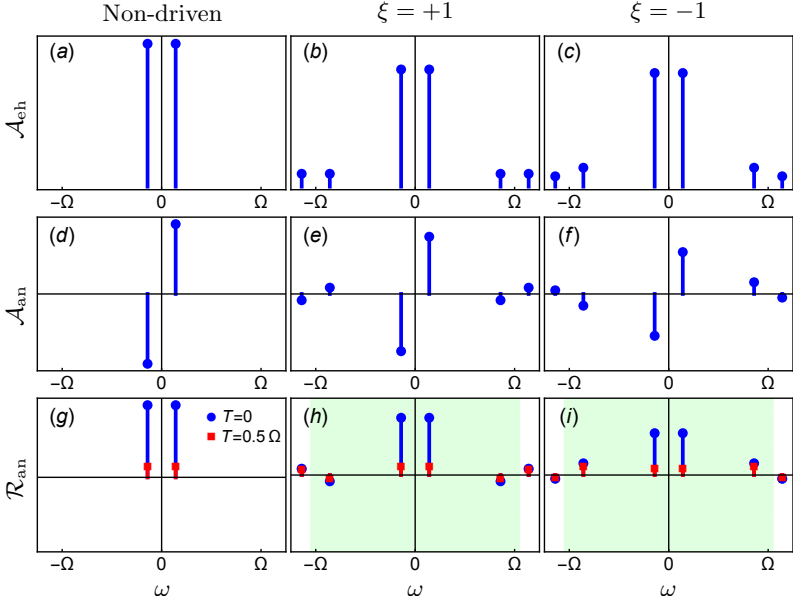


Figure 11.1: (a-c) The electron-hole spectral functions \mathcal{A}_{eh} , (d-f) the anomalous spectral functions \mathcal{A}_{an} , and (g-i) the anomalous response functions \mathcal{R}_{an} of the non-driven, commuting ($\xi = +1$), and anti-commuting ($\xi = -1$) superconductors in the first three temporal Brillouin zones $\omega \in (-3\Omega/2, 3\Omega/2]$. (g-j) For the response functions, results for (blue dots) zero-temperature and (red squares) high temperature are shown. The poles close to $\omega = 0$ are much more susceptible to temperature than the poles close to $\omega = \pm\Omega$. The green background indicates the region below the cutoff frequency.

We now contrast the spectral functions for the non-driven and driven superconductors. For the non-driven system, $(\tilde{G}_{\mathbf{k}}^{R,\tau\sigma})_{\ell=0}^f$ has two equivalent poles at $\omega_{\pm} = \pm E_{\mathbf{k}}$ reflecting the particle-hole symmetry, and its corresponding spectral functions are

$$\begin{aligned}\tilde{\mathcal{A}}_{\text{eh}}(\omega) &= \frac{1}{2} [L_{\Sigma}(\omega - E_{\mathbf{k}}) + L_{\Sigma}(\omega + E_{\mathbf{k}})] \\ \tilde{\mathcal{A}}_{\text{an}}(\omega) &= \frac{\Delta_0}{2E_{\mathbf{k}}} [L_{\Sigma}(\omega - E_{\mathbf{k}}) - L_{\Sigma}(\omega + E_{\mathbf{k}})],\end{aligned}\quad (11.8)$$

where L_{Σ} denotes a Lorentzian distribution $L_{\Sigma}(\omega) = 2\Sigma/(\omega^2 + \Sigma^2)$, which recovers a Dirac delta distribution $\delta(\omega)$ in the limit $\Sigma \rightarrow \eta^+$.

In comparison, the driven system $(G_{\mathbf{k}}^{R,\tau\sigma})_{\ell=0}^f$ has infinitely many shifted poles

11.1. Spectral and response functions

at $\omega_{\pm} = \pm E_{\mathbf{k}} + n\Omega$ with $n \in \mathbb{Z}$. Each electron-hole pair of these shifted poles lies in a different temporal Brillouin zone $\omega \in (n\Omega - \Omega/2, n\Omega + \Omega/2]$, $n \in \mathbb{Z}$. Specifically, the dominant contribution to \mathcal{A}_{eh} in the n -th temporal Brillouin zone is given by the term

$$(G_{\mathbf{k}}^{R,\tau\sigma})_{\ell=0}^f(\omega) \quad (11.9)$$

$$\approx \frac{a^{2|n|}}{2^{2|n|}} \tilde{G}_{\mathbf{k}}^{R,\tau\sigma}(\omega) \prod_{k=1}^n [A^{\tau\sigma\dagger} \tilde{G}_{\mathbf{k}}^{R,\tau\sigma}(\omega - k\Omega)] \prod_{k=n-1}^0 [A^{\tau\sigma} \tilde{G}_{\mathbf{k}}^{R,\tau\sigma}(\omega - k\Omega)],$$

further yielding

$$\mathcal{A}_{\text{eh}}(\omega) \approx \sum_{n=-\infty}^{\infty} \frac{a^{2|n|}}{\Omega^{2|n|}} \tilde{\mathcal{A}}_{\text{eh}}(\omega - n\Omega). \quad (11.10)$$

As shown in Fig. 11.1(a-c), it decays algebraically as functions of a/Ω , corroborating the Floquet picture that the driving imposes a coupling of strength a between replicas of the system with energies shifted by the driving frequency Ω , as illustrated in Fig. 2.1. More intriguing features can be revealed by the anomalous spectral function, which can be approximated by

$$\mathcal{A}_{\text{an}}(\omega) \approx \sum_{n=-\infty}^{\infty} \frac{a^{2|n|}}{\Omega^{2|n|}} \tilde{\mathcal{A}}_{\text{an}}(\omega - n\Omega) \text{Tr}_{\tau\sigma} [i\tau_{+}\sigma_y (A^{\tau\sigma\dagger})^n \tau_y \sigma_y (A^{\tau\sigma})^n]. \quad (11.11)$$

It depends explicitly on the commutation relation between the rotation operator $A^{\tau\sigma}$ and the interaction channel $\tau_y \sigma_y$. Since we are working in the product space of Nambu and spin, these two matrices can either commute ($\xi = 1$, e.g. $A^{\tau\sigma} = \tau_0 \sigma_0$) or anti-commute ($\xi = -1$, e.g. $A^{\tau\sigma} = \tau_z \sigma_y$),

$$[A^{\tau\sigma}, \tau_y \sigma_y]_{-\xi} = 0, \quad (11.12)$$

yielding

$$\mathcal{A}_{\text{an}}(\omega) \approx \sum_{n=-\infty}^{\infty} \xi^n \frac{a^{2|n|}}{\Omega^{2|n|}} \tilde{\mathcal{A}}_{\text{an}}(\omega - n\Omega). \quad (11.13)$$

When the matrices commute [Fig. 11.1(e)], the electron-hole excitations contribute to the order parameter in the same manner in all temporal Brillouin zones. When the matrices anti-commute [Fig. 11.1(f)], the electron-hole excitations have alternating contributions in the even and odd temporal Brillouin zones. The rotation operation brings a phase of π in the order parameter $\Delta_0 \rightarrow -\Delta_0$ in the odd Brillouin zones through the anti-commutativity. We note that the approximations for the spectral functions focus on the dominant term in each temporal Brillouin zone, rather than an expansion of the full spectral function to a given order. For example, both the sub-dominant term in $n = 0$ Brillouin zone and the dominant term in $n = \pm 1$ Brillouin zones

is in the order of $\mathcal{O}(a^2/\Omega^2)$, but only the latter ones are captured by the approximation.

The spectral functions mainly capture the effects of the driving on the superconductor, but not the accompanying relative rotation between the superconductor and the bath, particularly when it is Markovian. To this end, we need to consider the Keldysh Green function and the response function which directly enters the self-consistency equation Eq. (10.32). The response function has a simple relation with the spectral function

$$\mathcal{R}_{\text{an}}(\omega) = \tanh\left(\frac{\omega}{2T}\right) \mathcal{A}_{\text{an}}(\omega), \quad (11.14)$$

because we are working in the lab frame. It is shown in Fig. 11.1(g-i) for the different cases.

Our discussions above can be substantiated by the simple driving of $H_1^{\tau\sigma} = \frac{a}{2}\tau_0\sigma_0$, which admits the analytically solvable Green function [see Appendix C.1 for detailed derivation]

$$(G_{\mathbf{k}}^{R,\tau\sigma})_{\ell}^f(\omega) = \sum_{\tilde{\ell}} \tilde{G}_{\mathbf{k}}^{\tilde{R},\tau\sigma}(\omega + \tilde{\ell}\Omega) J_{\tilde{\ell}+\ell/2}\left(\frac{a}{\Omega}\right) J_{\tilde{\ell}-\ell/2}\left(\frac{a}{\Omega}\right), \quad (11.15)$$

with $\tilde{\ell}$ being integers (half-integers) for even (odd) ℓ , and J_{ℓ} the Bessel functions of the first kind. It confirms the asymptotic analysis for $\mathcal{A}_{\text{eh}}(\omega)$, and verifies the essential equivalence in the retarded/advanced Green functions between the driven and non-driven cases [96],

$$\int_{-\infty}^{\infty} d\omega G_{\mathbf{k}}^{R,f\tau\sigma}(\omega) = \int_{-\infty}^{\infty} d\omega \tilde{G}_{\mathbf{k}}^{\tilde{R},f\tau\sigma}(\omega), \quad (11.16)$$

where we have noticed $\sum_{n=-\infty}^{\infty} J_n(x)J_{n+\ell}(x) = \delta_{0,\ell}$. Indeed, the driving can be rotated out by $P^{f\tau\sigma} = \exp[i(F_1^f - F_{-1}^f)\tau_0\sigma_0]$, which corresponds to $P^{\tau\sigma} = \exp[i\cos(\Omega t)\tau_0\sigma_0]$ in the usual time-explicit representation, if only the superconductor is considered. However, the same argument is not true for the Keldysh Green function and the response function, which explicitly take the bath into account via the thermal distribution. Any rotation $P^{f\tau\sigma}$ acts simultaneously on both the superconductor and the bath, leaving their relative rotation untouched. Upon an integration over all frequencies, it can be verified that

$$\int_{-\infty}^{\infty} d\omega \tilde{\mathcal{R}}_{\text{an}}(\omega) > \int_{-\infty}^{\infty} d\omega \mathcal{R}_{\text{an}}(\omega), \quad (11.17)$$

because of the inequality $2 \tanh(x) > \tanh(x+y) + \tanh(x-y)$, $\forall x, y > 0$. The symmetric shifting of the poles effectively heats up the superconductor due to the Fermi-Dirac distribution in this scenario, and thereby reduces superconductivity.

11.2 Enhancement of superconductivity at finite temperature

We proceed to show in this Section that the relative rotation between the superconductor and the bath is not always detrimental to superconductivity, and under a well-designed scheme can indeed be used for enhancing superconductivity at finite temperature. To this end, we draw attention to three important features of the response function \mathcal{R}_{an} [cf. Fig. 11.1(h,i)] playing a key role in our following discussion. (i) The shifted poles, particularly the ones at $\omega_{\pm} = \pm(\Omega - E_{\mathbf{k}})$, are much farther away from the Fermi energy than the original ones at $\omega_{\pm} = \pm E_{\mathbf{k}}$, and they are thus almost insensitive to a change in temperature due to the dominance of Ω . (ii) In the anti-commuting case $\xi = -1$, the four poles closest to $\omega = 0$ of \mathcal{R}_{an} at $\omega_{\pm} = \pm E_{\mathbf{k}}$, $\omega_{\pm} = \pm(\Omega - E_{\mathbf{k}})$ all have positive weights. (iii) Upon integration over frequency $\int_{-\infty}^{\infty} d\omega$, the shifted poles at $\omega = k\Omega \pm E_{\mathbf{k}}$ almost cancel out each other in pairs. These observations inspire our scheme for enhancing superconductivity at finite temperature, which consists of two essential ingredients (i) an anti-commuting drive $\xi = -1$, and (ii) a driving frequency in near resonance with the natural cutoff frequency Ω_c of the superconductor, which is, for instance, given by the Debye frequency for phonon-mediated superconductivity. In other words, we now impose that the detuning

$$\delta\Omega \equiv \Omega - \Omega_c \ll \Omega \quad (11.18)$$

is small $|\delta\Omega| < E_{\mathbf{k}}$. As illustrated in Fig. 11.1(i), the detuning ensures that the poles favourable (detrimental) for superconductivity at $\omega_{\pm} = \pm(\Omega - E_{\mathbf{k}})$ ($\omega_{\pm} = \pm(\Omega + E_{\mathbf{k}})$) are retained (dropped).

Our proposed scheme can be most clearly manifested by the simple scenario of a flat-band superconductor $\epsilon_{\mathbf{k}} = 0$, which implies $E_{\mathbf{k}} = \Delta_0$. To order of $\mathcal{O}(a^2/\Omega^2)$, we can approximate the retarded Green function according to Eq. (11.9) as

$$(G_{\mathbf{k}}^{R,\tau\sigma})_{\ell=0}^f(\omega) \approx \tilde{G}_{\mathbf{k}}^{R,\tau\sigma}(\omega) + \sum_{s=\pm 1} \tilde{G}_{\mathbf{k}}^{R,\tau\sigma}(\omega) H_s^{\tau\sigma} \tilde{G}_{\mathbf{k}}^{R,\tau\sigma}(\omega + s\Omega) H_{-s}^{\tau\sigma} \tilde{G}_{\mathbf{k}}^{R,\tau\sigma}(\omega), \quad (11.19)$$

which for anti-commuting driving $\xi = -1$ and large driving frequency $\Omega \gg \Delta_0$ leads to the anomalous response function

$$\begin{aligned} \mathcal{R}_{\text{an}}(\omega) / \tanh\left(\frac{\omega}{2T}\right) &\approx \left(1 - \frac{a^2}{2\Omega^2}\right) (L_{\Sigma}(\omega - \Delta_0) - L_{\Sigma}(\omega + \Delta_0)) \\ &\quad - \frac{a^2}{4\Omega^2} (L_{\Sigma}(\omega - \Omega - \Delta_0) - L_{\Sigma}(\omega + \Omega + \Delta_0)) \\ &\quad + \frac{a^2}{4\Omega^2} (L_{\Sigma}(\omega - \Omega + \Delta_0) - L_{\Sigma}(\omega + \Omega - \Delta_0)). \end{aligned} \quad (11.20)$$

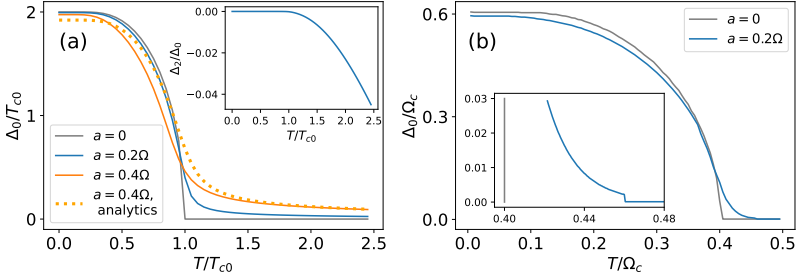


Figure 11.2: The order parameter Δ_0 as a function of temperature T for driven-dissipative (a) flat-band superconductors and (b) weakly-interacting dispersive superconductors. The self-consistency equation Eq. (10.32) is solved. In (a), the analytical approximation Eq. (11.21) is shown as dashed line, and the oscillating component Δ_2 (Δ_1 vanishing exactly) is compared to the constant component Δ_0 in the inset. In (b), the inset shows a zoom-in in the vicinity of the critical points T_{c0} and T_c of the un-driven and driven systems.

Taking the cutoff $\Omega_c \in (\Omega - \Delta_0, \Omega + \Delta_0)$ into account, the order parameter is now determined by the modified self-consistency equation in the weakly dissipative limit $\Sigma \rightarrow \eta^+$

$$\Delta_0 = 2T_{c0} \left[\left(1 - \frac{a^2}{2\Omega^2} \right) \tanh\left(\frac{\Delta_0}{2T}\right) + \frac{a^2}{4\Omega^2} \tanh\left(\frac{\Omega}{2T}\right) \right], \quad \forall \Delta_0 > \delta\Omega, \quad (11.21)$$

where T_{c0} is the critical temperature of the non-driven superconductor $a = 0$, and related to the density of states at the Fermi surface $N(\epsilon_F)$ as $T_{c0} = gN(\epsilon_F)/2$. We emphasise that this results is far beyond a conventional mean-field treatment, e.g. by directly investigating the Floquet stroboscopic Hamiltonian, or the time-dependent Heisenberg equation of the order parameter. This is particularly evidenced by the factor of $\tanh(\Omega/2T)$ in the second term. We also remark that a dissipation comparable to other energy scales will reduce the order parameter Δ_0 or even eliminate superconductivity [252], which is reminiscent of the dissipative stabilisation of normal phase in the Dicke model as discussed in Sections 3.3 and 6.1.

We proceed to discuss the intriguing features of the superconducting order parameter extracted from Eq. (11.21). At zero temperature, $\tanh(\Delta_0/2T) = \tanh(\Omega/2T) = 1$, the driving always reduces the order parameter Δ_0 due to the anti-commutativity between the drive and interacting channel. Such effect detrimental to superconductivity is similar to the one as discussed in Ref. [255] for static superconductors. At intermediate temperature $\Omega \ll T < T_c$, the

11.3. Conclusions

order parameter of the driven superconductor exhibits an asymptotic behaviour of

$$\Delta_0 \approx \frac{a^2}{8\Omega^2} \frac{T_{c0}}{T}, \quad (11.22)$$

with a first-order jump at the new superconducting transition temperature

$$T_c \approx \frac{a^2}{8\Omega^2} \frac{T_{c0}}{\delta\Omega}. \quad (11.23)$$

This indicates superconductivity can sustain at arbitrarily high temperature for a resonantly tuned driving frequency. The first-order behaviour at the transition temperature is reminiscent of the drive-induced re-entrance of superconductivity observed in Ref. [256, 257].

We confirm our analysis by numerical simulations of the original self-consistency equation Eq. (10.32) for the flat-band superconductor, as shown in Fig. 11.2(a). The numerical results according to Eq. (10.32) is consistent with the analytical results from Eq. (11.21), apart from deviations close to the critical point. This is due to higher order effects in $\mathcal{O}(a/\Omega)$. Through the simulation, we can also confirm our a priori assumption that the oscillating components Δ_2 (with $\Delta_1 = 0$, cf. Appendix C.2) is indeed negligible in comparison to the constant component.

It is worth emphasising that our scheme is not limited to flat-band superconductors, but can be easily generalised to dispersive superconductors. In the weakly interacting limit where the density of states is almost a constant in the vicinity of the Fermi surface of, e.g., an *s*-wave superconductor in three dimensions, the triple summation over momenta can be replaced by a simple summation over energy $\sum_{\mathbf{k}} \rightarrow N(\epsilon_F) \int_0^{\Omega_c} d\epsilon$. In this case, the critical temperature of the superconductor behaves as [see Appendix C.3 for detailed calculations]

$$\frac{T_c}{T_{c0}} \approx \left(\frac{3.57T_{c0}^6}{\Omega_c^5 \delta\Omega} \right)^{a^2/4\Omega^2}. \quad (11.24)$$

The corresponding simulated $\Delta_0(T)$ is shown in Fig. 11.2(b). Indeed, all mechanisms in our scheme related to enhancement of superconductivity beyond the critical point survive although being quantitatively weaker compared to the case of the flat-band superconductor.

11.3 Conclusions

In this Part we have presented our preliminary results on the driven-dissipative effects on superconductors, and proposed a scheme for increasing the critical

temperature of superconductors. Our investigation is currently still in progress. Our scheme relies on three essential ingredients, the relative rotation between the superconductor and the bath for creating a non-thermal distribution for the electrons and holes, the anti-commutativity between the rotation operator and the interaction channel creating a π -phase shift between replicas of the system in neighbouring temporal Brillouin zones, as well as a sharp cutoff from the interaction mediator (e.g. phonon) which is in close resonance with the driving frequency for suppressing counter-contributing excitations.

We comment on the essential differences between our scheme and two kinds of mechanisms for superconductivity enhancement developed recently. The first mechanism relies on parametric or non-linear driving on the phonons, where the driving dynamically squeezes the phonon and effectively increases the mediated electron-electron interaction strength [237, 238]. The second mechanism relies on coherent destruction of electronic hoppings induced by driving, and the accompanying reduction of electronic bandwidth. By increasing the ratio between the cutoff frequency and the bandwidth, it increases the effective density of states [239–241]. In the Floquet language, both mechanisms effectively renormalise the stroboscopic Hamiltonian, inducing an overall proportional enhancement of superconductivity at all temperatures. In comparison, our scheme uses a fundamentally different mechanism based on thermal distribution instead of stroboscopic Hamiltonian, and shows stark contrasts in its effects. Generally, our scheme manifests a reduction at low temperatures while an enhancement at high temperatures, and in principle can sustain superconductivity at arbitrarily high temperatures.

There are nevertheless a few potential limitations for our scheme. Similar to all other Floquet driven many-body systems, our system can also potentially thermalise due to quantum fluctuations, which is not captured by our mean-field treatment based on Hubbard-Stratonovich transformation. Moreover, our scheme requires a driving at frequency close to the cutoff frequency, which is typically the characteristic frequency of the mediating mechanism, e.g. phonons. We thus expect a full implementation should also take the driven effects on phonons into account. Finally, according to Eq. (11.24), a very precise resonance between the driving and the cutoff frequency needs to be achieved for usual BCS superconductors, where $T_{c0} \ll \Omega_c$, which is experimentally difficult. As a result, a superconductor with relatively high $T_{c0} \sim \Omega_c$ is preferred, where effects from Migdal-Eliashberg theory [258, 259] needs to be taken into account.

Summarising this Part III, we have applied the Keldysh-Floquet formalism inspired by our considerations of cavity-boson systems on superconductors. This formalism is able to capture the relative rotation between system and bath, which is beyond the stroboscopic Hamiltonian description of the driven system. With our formalism, we are able to engineer a scheme for achieving

11.3. Conclusions

and retaining superconductivity at relatively high temperatures.

Conclusions and Outlook

THIS doctoral thesis presented a collection of novel phenomena in quantum driven-dissipative many-body systems. At the core of these phenomena, which fundamentally have no static counterparts, lies the relative rotation between the driven system and the non-driven environment. This leads to a non-thermal distribution of particles from the point of view of the system. This simple feature has surprisingly a wide range of consequences for both microscopic and collective features observed in the context of engineered quantum optical systems (Part II) as well as condensed matter systems (Part III). These include limit cycles and chaos (Chapter 7), continuously multistable highly-excited steady states (Chapter 8), unidirectional atomic currents (Chapter 9), and the enhancement of superconductivity at finite temperatures (Chapter 11). In this thesis, I have endeavoured to deliver an overarching framework encompassing the various aspects of driven-dissipative effects in quantum many-body systems. Its generality is guaranteed by that of the Floquet and Keldysh formalisms, on which it is based. This framework is able to capture the subtleties among quantum systems of different characteristics, like bosonic and fermionic, high and intermediate driving frequencies, zero and finite temperatures.

We gradually developed in Chapters 2, 5, and 10 our formalisms mainly based on the Floquet formalism and the Keldysh formalism, and discussed their intrinsic relation to the Lindblad form commonly used for describing dissipative systems driven at high frequency. These formalisms were then used to tackle problems in the fields of quantum optics and condensed matter, which have distinct features. We first investigated through the lens of our formalism the cavity-boson systems, which were realised at hundreds of nanokelvins, and subject to drives at extremely high frequency of terahertz. These features guaranteed the robustness of the Lindblad form. Using the Lindblad form, we successfully predicted and explained in Chapter 6 the ubiquitous quantum dissipative instability seen in these systems, and pointed out the importance of the underlying symplectic bosonic structure. Unusual dynamics in cavity-boson systems resulting from these driven-dissipative processes were then discussed in different cases in Chapters 7, 8, and 9. Subsequently, we applied our formalism to the condensed matter system of superconductors, where the fermionic system typically functioned at a temperature of tens of kelvins, which become comparable to the driving frequency. More intriguingly, these features of the system prohibits the enormous simplifications yielding the Lindblad form, but also triggered more profound impact on driven-dissipative processes. As a representative example, we focused on the driven-dissipative enhancement of superconductivity at finite temperatures in Chapter 11.

Our results motivate a variety of topics for future study. For the interacting ultracold atomic gas, a necessary short-term goal is a direct and detailed comparison between the Keldysh formalism and the Lindblad form, where driven-dissipative effects on different observables like quantum fluctuations are calculated and compared quantitatively using these two methods. Such a comparison can potentially be based on existing techniques maturely developed for static systems like renormalisation group theory [260], and can further unveil the different aspects of driven-dissipative effects. As a specific example, a class of driven-dissipative systems following Kardar-Parisi-Zhang universality behaviours is currently receiving attention [261, 262], but comprehensive description and explanation are still under exploration. Ideally the formalism might eventually also lead to a functioning counterpart of energy minimisation for driven-dissipative systems, which can strategically improve the state-of-the-art circumstance where a case-by-case study is required for investigating the stability of driven-dissipative many-body states.

On top of this, our results can potentially motivate a variety of studies in the field of dissipative engineering in quantum optical systems, particularly when combined with techniques commonly used in quantum information processing. These include for instance quantum trajectory [263], which particularly captures the randomness of dissipation, and entanglement spectrum [264], which contains information on bipartite features and thermalisation. These techniques are still seldom used in the field of driven-dissipative Dicke-like models. These tools can potentially help investigations into the role of dissipation in the competition between long-range interaction induced by cavity and different correlated states of matter like spin-density-wave in a lattice model. With a thorough investigation in this direction, our understanding of driven-dissipative effects can eventually contribute to dissipation-based quantum many-body phase preparation and quantum information processing.

Furthermore, this thesis and most studies to-date predominantly focused on driven-dissipative effects in bosonic systems, where the underlying mechanisms of these driven-dissipative processes rely crucially on the symplectic structure of the bosonic Nambu space. In stark contrast, fermions are inherently subject to Pauli exclusions, as reflected by their positive definite density spectral functions [96]. As a result, the fermionic Nambu space follows the usual fermionic algebra. Therefore, a straightforward generalisation of the results to fermionic systems is not guaranteed, and deserves a thorough investigation. Importantly, this investigation is not only theoretically exciting but also experimentally relevant, as recently cavity-fermion setups have been built and studied in Lausanne [265–267] and Shanghai [268].

In the field of condensed matter, a more thorough and systematic investigation

into the driven-dissipative enhancement of superconductivity beyond our toy models is definitely a theme worth near-term efforts. Interesting effects can potentially arise by using different types of superconductors and drivings. For example, we expect our proposed enhancement of superconductivity could be significantly manifested in d -wave superconductors characterised by a gapless electron node, and strongly-interacting superconductors described by Migdal-Eliashberg theory. Moreover, an intermediate driving frequency close to the energy scale of the superconducting order parameter can induce significant excitation of higher harmonics, which potentially leads to more complex but more fascinating phenomena. Finally, driven-dissipative phenomena beyond mean-field description in superconductors are completely unexplored so far, including correlation functions, quantum fluctuations, Higgs excitations, and even many-body thermalisation. These quantities are potentially subject to qualitative changes as we learned from the driven-dissipative Dicke model of quantum optics.

The migration of the knowledge from quantum optics to condensed matter systems certainly goes beyond the regime of superconductivity. The ideas and formulae used in this thesis mainly involve spectral and response functions, which are universally used to characterise all kinds of quantum many-body systems, including but not limited to two-dimensional materials, strongly-correlated materials, and topological materials. The investigation into the intrinsic driven-dissipative effects in these regimes is thus expected to be far-reaching, leading to a new paradigm of dissipative engineering applicable to quantum many-body systems far beyond quantum optics.

In the end, our abundant results on driven-dissipative effects thus urge the development of a numerical method, which solves the many-body wavefunction far beyond the mean-field limit in a similar way as MCTDH-X, but also inherently and fully compatible to driven-dissipative systems as in quantum optics. Based on the current status of MCTDH-X, this leads to two potential directions, (i) an implementation of the full Keldysh formalism which should provide numerically exact results for observables of interest, like correlation functions and spectral functions, and (ii) a conjunction with methodology like quantum trajectory, which is computationally less demanding.

Appendices

A | Shirley-Floquet formalism

In Section 2.1, we have introduced the Shirley-Floquet formalism by claiming the structure of the Shirley-Floquet Hamiltonian, and the consequence of this structure like the quasi-energies and the Wigner families. However, a more detailed explanation and derivation of the formalism was lacking. In this Appendix, we complement our introduction in the main narrative by a derivation of the one-body Shirley-Floquet Hamiltonian [17], and a detailed solution for the well-studied Rabi driving based on the formalism.

A.1 Shirley-Floquet Hamiltonian

The Hamiltonian of a Floquet system, i.e., a system with time-periodic drives, can be represented by the Hamiltonian

$$H = \sum_{n \in \mathbb{Z}} H_n e^{in\Omega t}, \quad (\text{A.1})$$

where H_0 and H_n are possibly matrices. It can be rewritten in the Fourier representation

$$\mathbb{H}_{\text{Fourier}} = \sum_{n \in \mathbb{Z}} H_n \mathbb{F}_n e^{in\Omega t} \quad (\text{A.2})$$

by being duplicated under the basis

$$\left(\dots \quad |\Psi\rangle \quad |\Psi\rangle \quad |\Psi\rangle \quad |\Psi\rangle \quad |\Psi\rangle \quad \dots \right)^T, \quad (\text{A.3})$$

where each $|\Psi\rangle$ is a replica of the system. In the Hamiltonian, \mathbb{F}_n are infinite-dimensional matrices in the Floquet space

$$\mathbb{F}_n = \delta_{i,j-n} \quad (\text{A.4})$$

A.1. Shirley-Floquet Hamiltonian

also defined in the main text, including

$$\begin{aligned}
 \mathbb{F}_0 &= \begin{pmatrix} \dots & \dots & \dots & \dots & \dots & \dots \\ \dots & 1 & 0 & 0 & 0 & \dots \\ \dots & 0 & 1 & 0 & 0 & \dots \\ \dots & 0 & 0 & 1 & 0 & \dots \\ \dots & 0 & 0 & 0 & 1 & \dots \\ \dots & \dots & \dots & \dots & \dots & \dots \end{pmatrix} \\
 \mathbb{F}_1 &= \begin{pmatrix} \dots & \dots & \dots & \dots & \dots & \dots \\ \dots & 0 & 1 & 0 & 0 & \dots \\ \dots & 0 & 0 & 1 & 0 & \dots \\ \dots & 0 & 0 & 0 & 1 & \dots \\ \dots & 0 & 0 & 0 & 0 & \dots \\ \dots & \dots & \dots & \dots & \dots & \dots \end{pmatrix} \\
 \mathbb{F}_{-1} &= \begin{pmatrix} \dots & \dots & \dots & \dots & \dots & \dots \\ \dots & 0 & 0 & 0 & 0 & \dots \\ \dots & 1 & 0 & 0 & 0 & \dots \\ \dots & 0 & 1 & 0 & 0 & \dots \\ \dots & 0 & 0 & 1 & 0 & \dots \\ \dots & \dots & \dots & \dots & \dots & \dots \end{pmatrix}.
 \end{aligned} \tag{A.5}$$

Explicit time dependence has not yet been removed from the Hamiltonian, until a further transformation into the basis

$$\exp(i\Omega t\mathbb{N}) \begin{pmatrix} \dots \\ |\Psi\rangle \\ |\Psi\rangle \\ |\Psi\rangle \\ |\Psi\rangle \\ \dots \end{pmatrix} = \begin{pmatrix} \dots \\ e^{-2i\Omega t}|\Psi\rangle \\ e^{-i\Omega t}|\Psi\rangle \\ |\Psi\rangle \\ e^{i\Omega t}|\Psi\rangle \\ e^{2i\Omega t}|\Psi\rangle \\ \dots \end{pmatrix}, \tag{A.6}$$

which is also referred to as the Shirley-Floquet representation, through

$$\mathbb{H} = e^{i\Omega t\mathbb{N}} \mathbb{H}_{\text{Fourier}} e^{-i\Omega t\mathbb{N}} - ie^{i\Omega t\mathbb{N}} \partial_t e^{-i\Omega t\mathbb{N}}, \tag{A.7}$$

This transformation finally yields the Shirley-Floquet Hamiltonian

$$\mathbb{H} = \sum_{n \in \mathbb{Z}} H_n \mathbb{F}_n - \Omega \mathbb{N} \tag{A.8}$$

where

$$\mathbb{N} = j\delta_{j,j} = \begin{pmatrix} \dots & \dots & \dots & \dots & \dots & \dots & \dots \\ \dots & -2 & 0 & 0 & 0 & 0 & \dots \\ \dots & 0 & -1 & 0 & 0 & 0 & \dots \\ \dots & 0 & 0 & 0 & 0 & 0 & \dots \\ \dots & 0 & 0 & 0 & 1 & 0 & \dots \\ \dots & 0 & 0 & 0 & 0 & 2 & \dots \\ \dots & \dots & \dots & \dots & \dots & \dots & \dots \end{pmatrix}. \quad (\text{A.9})$$

A.2 Shirley-Floquet Green function

The two-time correlation function $G(t_1, t_2)$, also known as the Green function, is an alternative representation of a (time-periodic) Hamiltonian, which can provide direct access to important observables of the system like spectral functions. Despite the simple relation between Hamiltonian and Green function, which are inverse of each other, in the usual representation, this is not clear or guaranteed in the Shirley-Floquet formalism. In this Section of the Appendix, we show how the Green function can be obtained using the Shirley-Floquet formalism.

The relation between the Hamiltonian Eq. (A.1) and its corresponding Green function is

$$\left(i\partial_{t_1} - \sum_{n \in \mathbb{Z}} H_n e^{in\Omega t_1} \right) G(t_1, t_2) = \delta(t_2 - t_1). \quad (\text{A.10})$$

The time periodicity of the Hamiltonian is expected to be found also in the Green function

$$G(t_1, t_2) = G(t_1 + 2\pi/\Omega, t_2 + 2\pi/\Omega), \quad (\text{A.11})$$

which motivates us to use the representation of time difference δt and averaged time \bar{t} :

$$\delta t \equiv t_2 - t_1, \quad \bar{t} = (t_1 + t_2)/2, \quad (\text{A.12})$$

and rewrite the Green function in Fourier series,

$$G(t_1, t_2) = \sum_{n \in \mathbb{Z}} G_n(\delta t) e^{in\Omega \bar{t}}. \quad (\text{A.13})$$

A.2. Shirley-Floquet Green function

In the Fourier space where ω and $\bar{\Omega}$ respectively denote the frequencies of δt and \bar{t} , the identity Eq. (A.10) becomes ¹,

$$\begin{aligned} & \sum_{m \in \mathbb{Z}} \left(\omega - \frac{m}{2} \Omega \right) G_m(\omega) \delta(\bar{\Omega} - m\Omega) \\ & - \sum_{m, n \in \mathbb{Z}} H_n G_m \left(\omega + \frac{n}{2} \Omega \right) \delta(\bar{\Omega} - (m+n)\Omega) \\ & = \delta(\bar{\Omega}). \end{aligned} \quad (\text{A.14})$$

Consistent with the structure of the Shirley-Floquet matrices, we notice that this identity is continuous in ω but discretised in $\bar{\Omega}$. This structure motivates us to construct the following matrices of infinite dimensions,

$$\mathbb{H}'_{m,n} = H_{n-m} - m\bar{\Omega} \mathbf{1}_{m,n} \quad (\text{A.15})$$

$$\mathbb{G}'_{m,n}(\omega) = G_{n-m} \left(\omega + \frac{m+n}{2} \Omega \right). \quad (\text{A.16})$$

The relation between the Hamiltonian and the Green function as given by Eq. (A.10) can thus be translated to the following relation between these two matrices in Floquet space,

$$(\omega \mathbf{1} - \mathbb{H}') \mathbb{G}'(\omega) = \mathbf{1}. \quad (\text{A.17})$$

By noticing that the matrix \mathbb{H}' constructed above is exactly the Shirley-Floquet Hamiltonian introduced in Eq. (A.8), and the matrix \mathbb{G}' contains all information of the Green function $G(t_1, t_2)$, we can thus define the Shirley-Floquet Green function $\mathbb{G}(\omega)$ through the Shirley-Floquet Hamiltonian \mathbb{H} as

$$\mathbb{G}(\omega) = [\omega \mathbf{1} - \mathbb{H}]^{-1}. \quad (\text{A.18})$$

Specifically, its Wigner families

$$G_{k \equiv n-m}(\omega) = \mathbb{G}_{m,n} \left(\omega - \frac{m+n}{2} \Omega \right) \quad (\text{A.19})$$

are related to the two-time Green function in the Schrödinger (time-explicit) representation as

$$G(\omega, \bar{t}) = \sum_{n \in \mathbb{Z}} G_n(\omega) e^{in\bar{\Omega}\bar{t}}. \quad (\text{A.20})$$

¹We have used:

$$\partial_{t_1} = \frac{\partial \bar{t}}{\partial t_1} \Big|_{t_2} \partial_{\bar{t}} + \frac{\partial \delta t}{\partial t_1} \Big|_{t_2} \partial_{\delta t} = \frac{1}{2} \partial_{\bar{t}} - \partial_{\delta t}$$

A.3 Useful formulae for the Shirley-Floquet matrices

We provide several identities for the Shirley-Floquet matrices, which are useful for calculations later:

$$\begin{aligned}
 \mathbb{F}_m \mathbb{F}_n &= \mathbb{F}_{m+n} \\
 e^{\mathbb{F}_1} &= \sum_n \frac{1}{n!} \mathbb{F}_n \\
 [\mathbb{F}_n, \mathbb{N}] &= n \mathbb{F}_n \\
 e^{\alpha \mathbb{F}_n} \mathbb{N} e^{-\alpha \mathbb{F}_n} &= \mathbb{N} + \alpha n \mathbb{F}_n.
 \end{aligned} \tag{A.21}$$

The derivation of these identities follows directly from usual matrix and commutator algebra, and is omitted here.

We also remark on the straightforward correspondence between the Shirley-Floquet matrices and the operators in the Schrödinger (time-explicit) representation, as given below:

$$\begin{aligned}
 \mathbb{F}_n &\leftrightarrow e^{in\Omega t} \\
 \Omega \mathbb{N} &\leftrightarrow i\partial_t.
 \end{aligned} \tag{A.22}$$

A.4 Solution of Rabi driving in Shirley-Floquet formalism

The Rabi driving is commonly encountered in quantum optics, and in many of the time comes from a rotating-wave approximation for a dipolar driving. It can be formulated by the following Hamiltonian

$$H = a\sigma_z + be^{i\Omega t}\sigma_- + be^{-i\Omega t}\sigma_+, \tag{A.23}$$

with $\sigma_{\pm} = (\sigma_x \pm i\sigma_y)/2$, and has well-known results. In this Section, we demonstrate the Shirley-Floquet formalism by solving this driven Hamiltonian in two different ways. The goal is to calculate the effective stroboscopic Hamiltonian, which is equivalent to looking for a rotating frame where the Hamiltonian appears static.

A.4.1 Standard method

The Rabi driving is known to be solved by a rotation $P = \exp(-\frac{i}{2}\Omega t\sigma_z)$. As a demonstration, we first show how this solution can be expressed in the Shirley-Floquet formalism. One unusual feature is an artificial period-halving in the solution. The time periodicity of Ω is split into an addition of two $\Omega/2$ in the

A.4. Solution of Rabi driving in Shirley-Floquet formalism

two spin sectors. This can be captured by solving the problem in a Shirley-Floquet of frequency $\Omega/2$, where the Shirley-Floquet Hamiltonian of the Rabi driving is

$$\mathbb{H} = a\sigma_z\mathbb{F}_0 + b\sigma_-\mathbb{F}_2 + b\sigma_+\mathbb{F}_{-2} - \frac{\Omega}{2}\mathbb{N}. \quad (\text{A.24})$$

Since we already know that the rotation operator solving the Rabi driving is

$$P = \cos\left(\frac{\Omega}{2}t\right)\sigma_0 - i\sin\left(\frac{\Omega}{2}t\right)\sigma_z, \quad (\text{A.25})$$

we now straightforwardly use the correspondence Eq. (A.22) to write it down in the Shirley-Floquet representation as

$$\mathbb{P} = \frac{1}{2}\sigma_0(\mathbb{F}_1 + \mathbb{F}_{-1}) - \frac{1}{2}\sigma_z(\mathbb{F}_1 - \mathbb{F}_{-1}), \quad (\text{A.26})$$

which is indeed unitary $\mathbb{P}^\dagger\mathbb{P} = \sigma_0\mathbb{F}_0$, and diagonalises the Shirley-Floquet Hamiltonian as

$$\mathbb{H}' = \mathbb{P}^\dagger\mathbb{H}\mathbb{P} = \left(a - \frac{\Omega}{2}\right)\sigma_z\mathbb{F}_0 + b\sigma_x\mathbb{F}_0 - \frac{\Omega}{2}\mathbb{N}. \quad (\text{A.27})$$

We can thus extract the effective stroboscopic Hamiltonian

$$H' = \left(a - \frac{\Omega}{2}\right)\sigma_z + b\sigma_x. \quad (\text{A.28})$$

A.4.2 Alternative method

An alternative method for solving the stroboscopic Hamiltonian for the Rabi driving is available based on observation of the Shirley-Floquet structure, which is similar to the rotating wave approximation discussed in Section 2.1.2. This alternative method manifests the benefits of a good observation and interpretation of the Shirley-Floquet structure, since it would not be obviously obtained from a usual analysis in the time-dependent representation.

The Shirley-Floquet Hamiltonian of the Rabi driving is given by

$$\mathbb{H} = a\sigma_z\mathbb{F}_0 + b\sigma_-\mathbb{F}_1 + b\sigma_+\mathbb{F}_{-1} - \Omega\mathbb{N}, \quad (\text{A.29})$$

which is composed by small blocks of matrices spanning over neighbouring Floquet sectors, in a similar manner as in Eq. (2.12) of the main text. We thus

aim to diagonalise these block matrices, which can indeed be performed by the operator [cf. Eq. (A.21)]

$$\begin{aligned}
 \mathbb{P} &= \exp \left[\frac{1}{2} \arctan \left(\frac{b}{-\Omega/2 + a} \right) (\sigma_- \mathbb{F}_1 - \sigma_+ \mathbb{F}_{-1}) \right] \\
 &= \cos \left[\frac{1}{2} \arctan \left(\frac{b}{-\Omega/2 + a} \right) \right] \sigma_0 \mathbb{F}_0 \\
 &\quad + \sin \left[\frac{1}{2} \arctan \left(\frac{b}{-\Omega/2 + a} \right) \right] (\sigma_- \mathbb{F}_1 - \sigma_+ \mathbb{F}_{-1}).
 \end{aligned} \tag{A.30}$$

Denoting $\alpha = \frac{1}{2} \arctan \left(\frac{b}{-\Omega/2 + a} \right)$ and thereby noticing

$$[\mathbb{P}^\dagger, \mathbb{H}] = -\sin \alpha \{ (2a - \Omega) [\sigma_- \mathbb{F}_1 + \sigma_+ \mathbb{F}_{-1}] - 2b \sigma_z \mathbb{F}_0 \}, \tag{A.31}$$

we find

$$\begin{aligned}
 \mathbb{H}' &\equiv \mathbb{P}^\dagger \mathbb{H} \mathbb{P} = \mathbb{H} + [\mathbb{P}^\dagger, \mathbb{H}] \mathbb{P} \\
 &= \left(\frac{1}{2} \Omega + \sqrt{\left(a - \frac{\Omega}{2} \right)^2 + b^2} \right) \sigma_z \mathbb{F}_0 - \Omega \mathbb{N},
 \end{aligned} \tag{A.32}$$

where we have used $b - (2a - \Omega) \sin \alpha \cos \alpha - 2b \sin^2 \alpha = 0$ for simplifying the expression. We can thus confirm that \mathbb{P} is the rotation we are looking for.

This final expression allows us to extract the effective stroboscopic Hamiltonian

$$H' = \left(\frac{1}{2} \Omega + \sqrt{\left(a - \frac{\Omega}{2} \right)^2 + b^2} \right) \sigma_z. \tag{A.33}$$

To conclude the derivation, we remark that the rotation operator \mathbb{P} obtains the form of

$$P = \exp[\alpha(e^{-i\Omega t} \sigma_- - e^{i\Omega t} \sigma_+)] = \exp \left[\alpha \begin{pmatrix} 0 & -e^{i\Omega t} \\ e^{-i\Omega t} & 0 \end{pmatrix} \right] \tag{A.34}$$

in the Schrödinger (time-explicit) representation, which can be directly observed using the correspondence Eq. (A.22).

A.4.3 Geometric interpretation of the two transformations

The two methods above indeed yield consistent results, as the obtained stroboscopic Hamiltonians Eqs. (A.28) and (A.33) are directly related through a static unitary transformation. The relation between the two methods can be understood by a geometric interpretation of them, which is pictorially illustrated in Fig. A.1. The Rabi driving Eq. (A.23) can be considered as a system rotating periodically along a latitude of the Bloch sphere. In the first method, we choose a rotating frame with a fixed rotation axis (the z -axis), and a linearly increasing rotation angle, such that the rotation exactly follows the rotation of the system. In contrast, in the second method, the rotation axis is always chosen perpendicular to the plane spanned by both the z -axis and the system, whereas the rotation angle is also fixed. This rotation exactly shifts the system onto the z -axis.

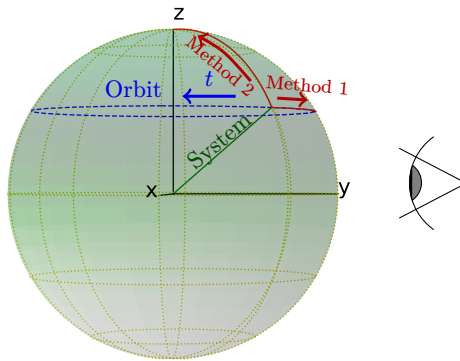


Figure A.1: Geometric illustration of the rotating frames used in the two methods for solving the Rabi driving. The eye represents the static lab frame.

B | Methodologies and techniques used in solving driven-dissipative quantum optical systems

In this Appendix, we collect and give a systematic review on different methods and techniques used in solving driven-dissipative quantum optical systems, by providing calculation examples based on the Dicke model [114]

$$H = \hbar\omega_c a^\dagger a + \frac{1}{2}\hbar\omega_0 J_z + \frac{\hbar\lambda}{\sqrt{N}}(a + a^\dagger)J_x \quad (\text{B.1})$$

where J_x and J_z are the collective spin- $N/2$ operators. All these methods and techniques have been introduced and used in Parts I and II of the main text, and are based on the Lindbladian in the Heisenberg picture

$$\begin{aligned} i\hbar\partial_t O &= i[H, O] - \hbar\kappa \left(a^\dagger O a - \frac{1}{2}a^\dagger a O - \frac{1}{2}O a^\dagger a \right) \\ &= \begin{cases} i[H, a] - \hbar\kappa a, & O = a \\ i[H, a], & O = J_{x,y,z} \end{cases} \end{aligned} \quad (\text{B.2})$$

B.1 Collective behaviours 1: Dynamical evolutions

The dynamics of the system can be described by the Liouvillian equation of motion of the cavity field and the atomic field in the Heisenberg picture. More specifically, because the atomic fields fundamentally lie in an $SU(2)$ space, its collective mean-field behaviours can be fully described by a decomposition into the J_x , J_y , and J_z collective spin sectors, allowing us to represent the collective behaviours of our system by four expectation values $\langle J_x \rangle$, $\langle J_y \rangle$, $\langle J_z \rangle$ and $\langle a \rangle$. After a mean-field decoupling between the cavity field and the atomic field, we

B.2. Collective behaviours 2: Steady state

obtain

$$\begin{aligned}
 i\partial_t \langle a \rangle &= (\omega_c - i\kappa) \langle a \rangle + \frac{\lambda}{\sqrt{N}} \langle J_x \rangle \\
 i\partial_t \langle J_x \rangle &= -\omega_0 \langle J_y \rangle \\
 i\partial_t \langle J_y \rangle &= \omega_0 \langle J_x \rangle - \frac{\lambda}{\sqrt{N}} (\langle a \rangle + \langle a \rangle^*) \langle J_z \rangle \\
 i\partial_t \langle J_z \rangle &= \frac{\lambda}{\sqrt{N}} (\langle a \rangle + \langle a \rangle^*) \langle J_y \rangle.
 \end{aligned} \tag{B.3}$$

An analytical solution of these differential equations is usually not accessible, and thus numerical solutions are usually solved instead.

As required by the underlying atomic structure, the dynamical evolution indeed preserves the total number of spins and the quadratic Casimir operator of the $\mathfrak{su}(2)$ algebra

$$\begin{aligned}
 \frac{N}{2} &= \langle \mathbf{1} \rangle \\
 \frac{N^2}{4} &= \langle J_x \rangle^2 + \langle J_y \rangle^2 + \langle J_z \rangle^2.
 \end{aligned} \tag{B.4}$$

While the first identity is trivial, we briefly comment on the second one. For an arbitrary representation of the $\mathfrak{su}(2)$ algebra, the Casimir defined as $\langle J_x^2 + J_y^2 + J_z^2 \rangle$ is a conserved quantity. This can be verified straightforwardly for any given representation, e.g., for spin-1/2 or spin-1. However, for a representation of high order $N \gg 1$, the variance $\langle J_i^2 \rangle - \langle J_i \rangle^2$ becomes negligible, which yields the approximated but more practical formula above. This identity is indeed always obeyed in our numerical simulations. For an algebra with more generators, e.g., $\mathfrak{su}(3)$ as introduced in Section 8.2, more Casimir operators are conserved.

B.2 Collective behaviours 2: Steady state

Collective dynamical evolutions of the Dicke system always converge to steady states. As discussed in the main text, particularly in Chapter 6, there is no systematic way to discriminate these states based on, e.g., energetic arguments. Therefore, we need to search for them using the dynamical evolutions obtained above based on a case-by-case study. Specifically, we set [79, 104, 116, 187]

$$\partial_t \langle a \rangle = \partial_t \langle J_x \rangle = \partial_t \langle J_y \rangle = \partial_t \langle J_z \rangle = 0, \tag{B.5}$$

which yields two kinds of solutions for the Dicke model. These include the normal solution for any λ

$$\langle a \rangle = \langle J_x \rangle = \langle J_y \rangle = 0, \quad \langle J_z \rangle = N/2, \tag{B.6}$$

and the superradiant solution for $\lambda > \lambda_c = \frac{1}{2} \sqrt{\omega_0(\omega_c^2 + \kappa^2)}/\omega_c$

$$\langle J_x \rangle = \pm \frac{N}{2} \sqrt{1 - \frac{\lambda_c^4}{\lambda^4}}, \langle J_y \rangle = 0, \langle J_z \rangle = \pm \frac{N \lambda_c^2}{2 \lambda^2}, \langle a \rangle = \frac{2\lambda}{\sqrt{N}(-\omega_c + i\kappa)} \langle J_x \rangle. \quad (\text{B.7})$$

These solutions are merely fixed points of the dynamical evolution. They are stationary but not necessarily stable. Their stability need to be tested not by a comparison of energy, but rather either by a linearisation of the dynamical evolution around the fixed points, or by an investigation into the excitation spectrum. Later using third quantisation, we will find that the normal (superradiant) solution is the steady state below (above) the critical coupling strength λ_c .

We remark that the consistency between these two techniques can so far be confirmed by a case-by-case study, and should not be regarded as trivial. As we discussed in Chapters 5 and 6, the stability of the states are of quantum nature as it depends significantly on the different behaviours of the quantum excitations due to the relative rotations between the system and the environment. Despite this, such stability can be correctly and completely captured by the collective dynamical evolution, which appears to be describing a classical system. This connection between a fully quantum system and a fully classical description would thus worth future investigation.

As a second remark, we would also emphasise the importance to solve the cavity field and atomic field simultaneously for obtaining the correct fixed-point solutions. Particularly, taking the bad-cavity limit and assuming that the cavity field approaches steady state faster than the atomic field can potentially lead to completely irrelevant results. In fact, this assumption completely misses all the driven-dissipative stability and instability mechanisms discussed in Chapter 6, and captures only the exceptional point instability. In the end, this treatment can only quantitatively correctly capture the dissipative stabilisation of exceptional point instability, which can be, at hindsight falsely, interpreted by the “mechanism” discussed by Fig. 3.3. This mistreatment would lead to, for example, the incorrect phase diagram obtained in Ref. [222], in contrast to our corrected results presented in Chapter 8.

B.3 Microscopic behaviours 1: Holstein-Primakoff transformation

To probe the fluctuative behaviours of the system in the vicinity of the collective mean-field solution obtained above, we can employ the Holstein-Primakoff

B.3. Microscopic behaviours 1: Holstein-Primakoff transformation

transformation [69, 70], which maps exactly the collective pseudo-spin operators $J_{x/y/z}$ into a harmonic oscillator mode b as

$$J_x = J_+ + J_-, \quad J_+ \mapsto b^\dagger \sqrt{N - b^\dagger b}, \quad J_- \mapsto \sqrt{N - b^\dagger b} b, \quad J_z \mapsto (b^\dagger b - N). \quad (\text{B.8})$$

Similar to the cavity mode a , the atomic harmonic oscillator mode b can also be seen as in a coherent state at the collective solution,

$$\langle b \rangle = \sqrt{\langle J_z \rangle + N}. \quad (\text{B.9})$$

As a result, in terms of the cavity and atomic harmonic oscillator modes, the mean-field solutions are given as

$$\alpha \equiv \langle a \rangle = 0, \quad \beta \equiv \langle b \rangle = 0 \quad (\text{B.10})$$

for the normal state, and

$$\alpha \equiv \langle a \rangle = \pm \frac{\lambda \sqrt{N}}{\omega_c - i\kappa} \sqrt{1 - \frac{\lambda_c^4}{\lambda^4}} \in \mathbb{C}, \quad \beta \equiv \langle b \rangle = \mp \sqrt{\frac{N}{2}} \sqrt{1 - \frac{\lambda_c^2}{\lambda^2}} \in \mathbb{R} \quad (\text{B.11})$$

for the superradiant state.

We can thus re-express a and b in the vicinity of the mean-field solution

$$a = \langle a \rangle + \tilde{a}, \quad b = \langle b \rangle + \tilde{b}, \quad (\text{B.12})$$

with operators \tilde{a} and \tilde{b} describing the fluctuations. Note that the Holstein-Primakoff transformed Hamiltonian is quadratic apart from the coupling term, which can be further split into three terms for our purpose

$$\begin{aligned} H_{\text{cp}} &= \frac{\hbar \lambda}{\sqrt{N}} (\tilde{a} + \tilde{a}^\dagger + 2 \text{Re } \alpha) (\tilde{b} + \tilde{b}^\dagger + 2\beta) \sqrt{N - \beta^2 - \beta(\tilde{b} + \tilde{b}^\dagger) - \tilde{b}^\dagger \tilde{b}} \\ &= \frac{\hbar \lambda}{\sqrt{N}} (\tilde{a} + \tilde{a}^\dagger) (\tilde{b} + \tilde{b}^\dagger) \sqrt{N - \beta^2 - \beta(\tilde{b} + \tilde{b}^\dagger) - \tilde{b}^\dagger \tilde{b}} \\ &\quad + \frac{2\hbar \lambda}{\sqrt{N}} [\text{Re } \alpha (\tilde{b} + \tilde{b}^\dagger) + \beta (\tilde{a} + \tilde{a}^\dagger)] \sqrt{N - \beta^2 - \beta(\tilde{b} + \tilde{b}^\dagger) - \tilde{b}^\dagger \tilde{b}} \\ &\quad + \frac{4\hbar \lambda \text{Re } \alpha \beta}{\sqrt{N}} \sqrt{N - \beta^2 - \beta(\tilde{b} + \tilde{b}^\dagger) - \tilde{b}^\dagger \tilde{b}}. \end{aligned} \quad (\text{B.13})$$

Our goal is to retain the terms up to an overall scaling of $\mathcal{O}(1)$ in N . To this end, we need to expand the square root up to different orders in $1/N$ for the two terms above. As both α and β scale as $\mathcal{O}(\sqrt{N})$, we need to retain the terms

up to $\mathcal{O}(\sqrt{N})$ for the first line, to $\mathcal{O}(1)$ for the second line, and $\mathcal{O}(1/\sqrt{N})$ for the third line.

$$\begin{aligned} & \sqrt{N - \beta^2 - \beta(\tilde{b} + \tilde{b}^\dagger) - \tilde{b}^\dagger \tilde{b}} \quad (\text{B.14}) \\ \approx & \underbrace{\sqrt{N - \beta^2}}_{\mathcal{O}(\sqrt{N})} - \underbrace{\frac{\beta}{2\sqrt{N - \beta^2}}(\tilde{b} + \tilde{b}^\dagger)}_{\mathcal{O}(1)} - \underbrace{\frac{1}{2\sqrt{N - \beta^2}}\tilde{b}^\dagger \tilde{b} - \frac{\beta^2}{8(N - \beta^2)^{3/2}}(\tilde{b} + \tilde{b}^\dagger)^2}_{\mathcal{O}(1/\sqrt{N})}. \end{aligned}$$

Collecting all the terms and denoting

$$\mu = \begin{cases} 1, & \text{normal} \\ \lambda_c^2/\lambda^2, & \text{superradiant} \end{cases} \quad (\text{B.15})$$

we obtain

$$H = E + H_{\text{linear}} + H_{\text{quadratic}}, \quad (\text{B.16})$$

where

$$E = -\frac{N\omega_c(1 - \mu)^2}{\omega_c^2 + \kappa^2} \quad (\text{B.17})$$

is the mean-field energy of the state in the order of $\mathcal{O}(N)$,

$$\begin{aligned} H_{\text{quadratic}} = & \omega_c \tilde{a}^\dagger \tilde{a} + \omega_0 \frac{1 + \mu}{2\mu} \tilde{b}^\dagger \tilde{b} + \omega_0 \frac{(1 - \mu)(3 + \mu)}{8\mu(1 + \mu)} (\tilde{b} + \tilde{b}^\dagger) \\ & + \lambda\mu \sqrt{\frac{2}{1 + \mu}} (\tilde{a} + \tilde{a}^\dagger) (\tilde{b} + \tilde{b}^\dagger) \end{aligned} \quad (\text{B.18})$$

is the quadratic Hamiltonian describing the fluctuations around the mean-field solution of the order $\mathcal{O}(1)$. It is the main subject in our following investigation and gives the excitation spectrum describing the energy and stability of the excitations. Finally, there is

$$H_{\text{linear}} = i\lambda\kappa\sqrt{N}\sqrt{1 - \mu^2} \left[\frac{1}{\omega_c + i\kappa} \tilde{a} - \frac{1}{\omega_c - i\kappa} \tilde{a}^\dagger \right] \quad (\text{B.19})$$

in the order of $\mathcal{O}(\sqrt{N})$. This linear term is non-vanishing only in the driven-dissipative system $\kappa > 0$ and around the superradiant state $\mu < 1$. It naturally arises because, due to the presence of the Lindbladian, the superradiant state is no longer a saddle point of the potential landscape as discussed in Fig. 3.3. Although it appears that this term does not contribute any essential effects to the fluctuations according to the literature to date, it might worth further investigating its role in the future.

B.4 Microscopic behaviours 2: Third quantisation

A systematic way to solve the spectrum of a bosonic/fermionic system with quadratic Hamiltonian and linear jump operator is the third quantisation [71, 72]. This method can be well applied to the Holstein-Primakoff transformed Hamiltonian obtained above for extracting information on the excitations, including its energy and stability, because of its quadratic form.

We start by describing the general formalism of the third quantisation for a bosonic system. We consider the system's quadratic Hamiltonian

$$H = \underline{a}^\dagger \mathbf{H} \underline{a} + \frac{1}{2} \underline{a} \mathbf{K} \underline{a} + \frac{1}{2} \underline{a}^\dagger \mathbf{K}^* \underline{a}^\dagger, \quad (\text{B.20})$$

as well as its linear jump operator

$$L = \underline{\ell}_1 \cdot \underline{a} + \underline{\ell}_2 \cdot \underline{a}^\dagger. \quad (\text{B.21})$$

under the basis

$$\underline{a} = (a_1, a_2, \dots, a_n)^T. \quad (\text{B.22})$$

The jump can be also represented by the following three matrices

$$\mathbf{M} = \underline{\ell}_1 \otimes \underline{\ell}_1^*, \quad \mathbf{N} = \underline{\ell}_2 \otimes \underline{\ell}_2^*, \quad \mathbf{L} = \underline{\ell}_1 \otimes \underline{\ell}_2^*. \quad (\text{B.23})$$

The excitation spectrum $\xi_i = \text{eig}(\mathcal{X})$ can be found by constructing and diagonalising the following matrix

$$\mathcal{X} = \begin{pmatrix} \mathbf{H} - i\mathbf{N} + i\mathbf{M}^* & \mathbf{K} - i\mathbf{L} + i\mathbf{L}^T \\ -\mathbf{K}^\dagger - i\mathbf{L}^* + i\mathbf{L}^\dagger & -\mathbf{H}^T - i\mathbf{N}^* + i\mathbf{M} \end{pmatrix}, \quad (\text{B.24})$$

where we have chosen a different convention in this thesis than the commonly-used one presented in Ref. [71, 72] for the consistency with similar spectrum analysis on Hamiltonians. In the convention chosen in this thesis, the real ($\text{Re } \xi_i$) and imaginary ($\text{Im } \xi_i$) parts of the eigenvalues represent the energy and stability of the Liouvillian system, respectively. Particularly, the system energy should be symmetric about zero energy ($\forall i \exists j \text{ Re } \xi_i = -\text{Re } \xi_j$) due to the Nambu structure of \mathcal{X} , while a negative imaginary part of the spectrum ($\text{Im } \xi_i < 0$) indicates instability. Under this convention, the excitation spectrum of the closed system can be obtained directly by setting $\kappa = 0$.

As an example, the fluctuations around the normal state of the Dicke model based on the Holstein-Primakoff Hamiltonian Eq. (6.2) and the corresponding

Lindbladian can be described by the matrix

$$\mathcal{X} = \begin{pmatrix} \omega_c + i\kappa & 0 & \lambda & \lambda \\ 0 & \omega_0 & \lambda & \lambda \\ -\lambda & -\lambda & -\omega_c + i\kappa & 0 \\ -\lambda & -\lambda & 0 & -\omega_0 \end{pmatrix}. \quad (\text{B.25})$$

In the limit $\kappa \rightarrow 0$, it recovers the Bogolyubov Hamiltonian for closed system, Eq. (6.3). The corresponding spectrum has been shown in Fig. 6.2.

B.5 Microscopic behaviours 3: Cavity fluctuations

The final observable in interest is the quantum fluctuations on top of the steady states, of which we take the cavity fluctuations as an example. Since the Holstein-Primakoff Hamiltonian fully describes the fluctuations around the corresponding steady states, it can be directly used to extract quantum fluctuations [79, 104, 116, 187]. The concrete method is similar to the one for solving the steady states, but is now concerning the bilinear operators like $a^\dagger a$ and aa . For the normal state of the Dicke model, these equations read

$$\begin{aligned} 0 &= \partial_t \langle aa \rangle = -(2i\omega + 2\kappa) \langle aa \rangle - 2i\lambda (\langle ab \rangle + \langle ab^\dagger \rangle) \\ 0 &= \partial_t \langle a^\dagger a \rangle = i\lambda \langle (a - a^\dagger)(b + b^\dagger) \rangle - 2\kappa \langle a^\dagger a \rangle \\ 0 &= \partial_t \langle bb \rangle = -2i[\omega_0 \langle bb \rangle + \lambda (\langle ab \rangle + \langle a^\dagger b \rangle)] \\ 0 &= \partial_t \langle b^\dagger b \rangle = i\lambda \langle (b - b^\dagger)(a + a^\dagger) \rangle \\ 0 &= \partial_t \langle ab \rangle = -i(\omega_0 + \omega - i\kappa) \langle ab \rangle - i\lambda (\langle aa \rangle + \langle bb \rangle + \langle a^\dagger a \rangle + \langle b^\dagger b \rangle + 1) \\ 0 &= \partial_t \langle a^\dagger b \rangle = -i(\omega_0 - \omega - i\kappa) \langle a^\dagger b \rangle - i\lambda (\langle a^\dagger a^\dagger \rangle - \langle bb \rangle + \langle a^\dagger a \rangle - \langle b^\dagger b \rangle). \end{aligned} \quad (\text{B.26})$$

The solution of these equations has been presented in Eq. (6.9). We emphasise again on the under-determination of these equations for non-dissipative systems $\kappa = 0$, where the equations cannot specify whether the system is driven or static (see Section 6.1.2).

B.6 Bosonic Bogolyubov transformation

In this thesis, a main common feature shared by different many-body systems is the coupling between particle and hole. This leads to many interesting phenomena, particularly for the bosonic systems. However, the Bogolyubov transformation, i.e., diagonalisation, of such a Hamiltonian is intrinsically more complicated than the commonly seen unitary transformation procedure [184,

B.6. Bosonic Bogolyubov transformation

185]. We thus provide here a brief derivation to the bosonic Bogolyubov transformation, and summarise the technical procedures [269, 270].

We seek to find the Bogolyubov transformation and diagonalise a bosonic Hamiltonian in the form of Eq. (B.20), which can be rewritten in the form of a $2n \times 2n$ matrix,

$$H = \frac{1}{2} \mathcal{A}^\dagger \mathcal{H} \mathcal{A}, \quad \mathcal{A} = \begin{pmatrix} \underline{a} \\ \underline{a}^* \end{pmatrix}, \quad \mathcal{H} = \begin{pmatrix} \mathbf{H} & \mathbf{K} \\ \mathbf{K}^\dagger & \mathbf{H}^\top \end{pmatrix}. \quad (\text{B.27})$$

The Bogolyubov transformation should be described by

$$\mathcal{A} = \mathcal{T} \mathcal{B}, \quad \mathcal{T} = \begin{pmatrix} U & V^* \\ V & U^* \end{pmatrix}, \quad \mathcal{B} = \begin{pmatrix} \underline{b} \\ \underline{b}^* \end{pmatrix} \quad (\text{B.28})$$

such that the Hamiltonian can now be written in the new basis \underline{b} as

$$H = \frac{1}{2} \mathcal{B}^\dagger \begin{pmatrix} \mathbf{E} & 0 \\ 0 & \mathbf{E} \end{pmatrix} \mathcal{B}, \quad (\text{B.29})$$

with $\mathbf{E} = \text{diag}(E_1, E_2, \dots, E_n)$ a diagonal matrix containing the energy spectrum $E_i \geq 0$ of the system. Alternatively, we can write

$$\mathcal{T}^\dagger \mathcal{H} \mathcal{T} = \begin{pmatrix} \mathbf{E} & 0 \\ 0 & \mathbf{E} \end{pmatrix}. \quad (\text{B.30})$$

In order to retain the bosonic commutation relation in the basis \underline{b} , $[b, b^\dagger] = 1$, $[b, b] = [b^\dagger, b^\dagger] = 0$, the transformation matrix $\mathcal{T} \in \text{Sp}(2n, \mathbb{C})$ needs to be symplectic,

$$U^\dagger U - V^\dagger V = \mathbf{1}_{n \times n}, \quad V^\dagger U^* - U^\dagger V^* = 0. \quad (\text{B.31})$$

Equivalently, the transformation leaves $\mathcal{I}_- = \tau_z \mathbf{1}_{n \times n}$ invariant,

$$\mathcal{T}^\dagger \mathcal{I}_- \mathcal{T} = \mathcal{I}_-, \quad \mathcal{I}_- = \begin{pmatrix} \mathbf{1} & 0 \\ 0 & -\mathbf{1} \end{pmatrix}. \quad (\text{B.32})$$

This immediately implies that \mathcal{T} is not unitary, $\mathcal{T}^\dagger \neq \mathcal{T}^{-1}$. Therefore, it is generically hard to solve for \mathcal{T} , because a solution by a similarity transformation is not available. Therefore, we need to exploit the properties of the symplectic group as a Lie group, specifically by constructing a new matrix

$$\mathcal{X} = \tau_z \mathcal{H} = \begin{pmatrix} \mathbf{H} & \mathbf{K} \\ -\mathbf{K}^\dagger & -\mathbf{H}^\top \end{pmatrix}. \quad (\text{B.33})$$

This matrix \mathcal{X} has been denoted as \tilde{H} in the main text, e.g. Eq. (6.3). It is a generator of the corresponding $\mathfrak{sp}(2n, \mathbb{C})$ algebra, $\mathcal{X} \in \mathfrak{sp}(2n, \mathbb{C})$, because it satisfies (\mathcal{J} being the symplectic bilinear form)

$$\mathcal{X}^T \mathcal{J} + \mathcal{J} \mathcal{X} = 0, \quad \mathcal{J} = \begin{pmatrix} 0 & \mathbf{1} \\ -\mathbf{1} & 0 \end{pmatrix}. \quad (\text{B.34})$$

With this observation, we can now use the adjoint representation of the Lie group, which states that an element of the Lie group (\mathcal{T}) can be viewed as an automorphism of the Lie algebra (\mathcal{X}). Specifically for us¹,

$$\mathcal{T}^{-1} \mathcal{X} \mathcal{T} = \begin{pmatrix} \mathbf{E} & 0 \\ 0 & -\mathbf{E} \end{pmatrix}. \quad (\text{B.35})$$

This relation allows us to diagonalise the matrix \mathcal{X} using similarity transformation, i.e., standard diagonalisation techniques. This can solve for both the energy spectrum \mathbf{E} as well as the transformation \mathcal{T} , and achieve the Bogolyubov transformation for the Hamiltonian \mathcal{H} . More specifically, we can construct \mathcal{T} using the eigenvectors v_i of \mathcal{X} ,

$$\mathcal{T} = (v_1 \quad v_2 \quad \dots \quad v_{2n}). \quad (\text{B.36})$$

We emphasise one technical detail. To respect the symplecticity Eq. (B.31), the eigenvectors $v_i = (v_{i,1}, v_{i,2}, \dots, v_{i,2n})$ need to be normalised in an uncommon way,

$$\sum_{j=1}^n |v_{ij}|^2 - \sum_{j=n+1}^{2n} |v_{ij}|^2 = 1. \quad (\text{B.37})$$

We provide an example for illustrating the calculation procedures. We consider the following Hamiltonian consisting of $n = 1$ bosonic mode,

$$H = 5a^\dagger a + 4(a^\dagger a^\dagger + aa), \quad \mathcal{X} = \begin{pmatrix} 5 & 4 \\ -4 & -5 \end{pmatrix}. \quad (\text{B.38})$$

The matrix \mathcal{X} can be diagonalised by

$$\mathcal{T} = \frac{1}{\sqrt{3}} \begin{pmatrix} 2 & -i \\ i & 2 \end{pmatrix} \quad (\text{B.39})$$

¹Strictly speaking, we have not proved that the transformation entering $\mathcal{T}_1^\dagger \mathcal{H} \mathcal{T}_1 = \tau_0 \mathbf{E}$ is the same as the one entering $\mathcal{T}_2^{-1} \mathcal{X} \mathcal{T}_2 = \tau_z \mathbf{E}$, i.e. $\mathcal{T}_1 = \mathcal{T}_2$. However, this can be verified straightforwardly.

B.7. Third quantisation from perspective of Keldysh formalism

as

$$\mathcal{T}^{-1}\mathcal{X}\mathcal{T} = \tilde{\mathcal{X}} = \begin{pmatrix} 3 & 0 \\ 0 & -3 \end{pmatrix}, \quad H = 3b^\dagger b, \quad (\text{B.40a})$$

or as

$$\mathcal{T}^\dagger\mathcal{H}\mathcal{T} = \tilde{\mathcal{H}} = \begin{pmatrix} 3 & 0 \\ 0 & 3 \end{pmatrix}, \quad H = 3b^\dagger b. \quad (\text{B.40b})$$

We can also confirm the bosonic commutation relation as

$$\begin{aligned} b^\dagger &= (2a - ia^\dagger)^\dagger = ia + 2a^\dagger, \\ [b, b] &= [2a - ia^\dagger, 2a - ia^\dagger] = 0, \\ [b, b^\dagger] &= [2a - ia^\dagger, ia + 2a^\dagger] = 1. \end{aligned} \quad (\text{B.41})$$

We conclude by a remark comparing bosons to fermions. For fermions, the anti-commutation relation requires that the transformation \mathcal{T} be unitary. As a result, the Bogolyubov Hamiltonian \mathcal{H} can be directly diagonalised using a similarity transformation. This is a common practice in the case of, e.g., superconductors.

B.7 Third quantisation from perspective of Keldysh formalism

To complement the narrative in Chapter 5, we discuss how to determine the stability of a state in Keldysh formalism, and its relation to the third quantisation technique. For this purpose, we first discuss a generic bosonic system whose partition function is given by

$$\begin{aligned} Z &= \int D[\psi_+^*, \psi_+, \psi_-^*, \psi_-] e^{iS} \\ S &= \int \frac{d\omega}{2\pi} \begin{pmatrix} \psi_+^* & \psi_-^* \end{pmatrix} \mathcal{G}^{-1} \begin{pmatrix} \psi_+ \\ \psi_- \end{pmatrix}, \\ \mathcal{G}^{-1} &= \begin{pmatrix} (G^R)^{-1} & (G^{-1})^K \\ 0 & (G^A)^{-1} \end{pmatrix}. \end{aligned} \quad (\text{B.42})$$

As discussed in Chapter 10, practical calculations and manipulations of the partition function requires a Keldysh rotation [cf. Eq. (10.21)] into the “classical-quantum” representation, which simplifies the treatment on the Keldysh con-

tour. This yields

$$\begin{aligned}
 Z &= \int D[\psi_c^*, \psi_c, \psi_q^*, \psi_q] e^{iS} \\
 S &= \int \frac{d\omega}{2\pi} \begin{pmatrix} \psi_c^* & \psi_q^* \end{pmatrix} \underline{\mathcal{G}}^{-1} \begin{pmatrix} \psi_c \\ \psi_q \end{pmatrix}, \\
 \underline{\mathcal{G}}^{-1} &= \begin{pmatrix} (G^{-1})^K & (G^A)^{-1} \\ (G^R)^{-1} & 0 \end{pmatrix}.
 \end{aligned} \tag{B.43}$$

In this formalism, the stability of the state is essentially captured by the convergence of the Gaussian integral in the partition function. A non-diverging partition function requires that $\text{Im } S \geq 0$, which in turn requires that, for all frequencies ω , all eigenvalues of $\underline{\mathcal{G}}^{-1}$ have non-negative imaginary parts. It turns out that it is more useful to implement this criterion on the Green function,

$$\underline{\mathcal{G}} = \begin{pmatrix} 0 & G^R \\ G^A & G^K \end{pmatrix}. \tag{B.44}$$

Because $G^R = (G^A)^\dagger$, any non-Hermiticity in $\underline{\mathcal{G}}$ related to the imaginary parts of the eigenvalues eventually should stem from the Keldysh Green function G^K . The stability of a state finally requires $\text{Im } G^K(\omega) \leq 0$ for all frequencies ω ². By defining the response function as [cf. Eq. (11.7)]

$$\mathcal{R}(\omega) = -\text{Im Tr } G^K(\omega), \tag{B.45}$$

we can thus determine the stability of the state by the non-negativity of $\mathcal{R}(\omega)$.

We further investigate the specific case of driven-dissipative systems as described by the Lindbladian, and first consider the system without particle-hole coupling. As usual, we consider the system from two perspectives, the retarded Green function and the thermal distribution. We diagonalise G^R and denote its eigenvalues as $E_n + i\kappa_n$ and its eigenstates as $|n\rangle$, where E_n and κ_n can be positive or negative. A crucial feature of driven-dissipative systems is that all their particle-like excitations are effectively experiencing the same thermal distribution $\rho = 1$. As a result, the thermal distribution is insensitive to any transformation of basis. In contrast, in a static system, each excitation mode is subject to a different ρ depending on, for example, $\text{sgn}(E_i)$. In the diagonalised basis, the quasi-particle excitations are thus subject to a complex relation to the thermal bath.

The insensitivity of the system-bath coupling to the change of basis in a driven-dissipative system thus allows us to work directly in the basis, where

²Note, $\text{Im } z > 0 \Leftrightarrow \text{Im}(1/z) < 0$, $z \in \mathbb{C}$.

B.7. Third quantisation from perspective of Keldysh formalism

the retarded Green function is diagonalised. In this case, the Keldysh Green function and the response function are respectively given by

$$G^K = -\sum_n \frac{2i\kappa_n}{(\omega - E_n)^2 + \kappa_n^2} |n\rangle\langle n|, \quad (\text{B.46})$$

$$\mathcal{R} = \sum_n \frac{2i\kappa_n}{(\omega - E_n)^2 + \kappa_n^2}. \quad (\text{B.47})$$

The stability of the system is thus determined by κ_i . If there exists any $\kappa_i < 0$, the system becomes unstable.

The presence of particle-hole coupling does not induce essential changes to the arguments above. In this case, the particles and holes are exactly experiencing opposite thermal distributions $\rho = \pm 1$, cf. Eq. (5.17). This can be rewritten as $\rho = \mathcal{I}_- = \tau_z \mathbf{1}$ using the Pauli matrix in Nambu space. However, this distinction between particles and holes is consistent with the bosonic Nambu space, as the thermal distribution remains invariant under symplectic transformations associated to bosonic Bogolyubov transformations, $\mathcal{T}^\dagger \mathcal{I}_- \mathcal{T} = \mathcal{I}_-$ [Eq. (B.32)]. For clarity, we reformulate our arguments also in the symplectic representation of the $\mathcal{X} = \tau_z \mathcal{H}$ matrix, also cf. Eq. (5.11). In this representation, the transformation matrix \mathcal{T} acts instead with a similarity transformation, which keeps the thermal distribution $\tilde{\rho} = \tau_z \mathcal{I}_- = \mathcal{I}_+ = \tau_0 \mathbf{1}$ invariant again, $\mathcal{T}^{-1} \mathcal{I}_+ \mathcal{T} = \mathcal{I}_+$. The validity of the aforementioned arguments in particle-hole coupled systems confirms the technical equivalence between the diagonalisation of \tilde{G}^R in Keldysh formalism with the third quantisation procedures.

C | Calculations pertaining to Part III

This Appendix provides details of calculations supplementary to the main narratives in Part III.

C.1 Retarded Green function for commuting drive

In this Section of the Appendix, we calculate the exact solution for the Green function when the drive commutes with the interacting channel $[A^{\tau\sigma}, \tau_x \sigma_x] = 0$, cf. Eq. (11.3), and derive the result Eq. (11.15). For this purpose, we look for the Shirley-Floquet Green function for the driven Hamiltonian

$$H^\tau = \epsilon\tau_z + \Delta\tau_x + a \cos(\Omega t)\tau_0, \quad (\text{C.1})$$

where for clarity of notation we have dropped the spin sector from the Hamiltonian $H = \epsilon\tau_z\sigma_0 + \Delta\tau_x\sigma_x + a \cos(\Omega t)\tau_0\sigma_0$ we originally intended to solve, as all commutation relations between the matrices $\tau_z\sigma_0 \mapsto \tau_z$, $\tau_x\sigma_x \mapsto \tau_x$, $\tau_0\sigma_0 \mapsto \tau_0$ are retained. Note that when the drive is switched off $a = 0$, the static Green function Eq. (11.4)

$$(\tilde{G}^{R,\tau})_\ell^f(\omega) = \delta_{\ell,0} \tilde{G}^{R,\tau}(\omega) = \frac{\omega_+ \tau_0 + \epsilon\tau_z + \Delta_0\tau_x}{\omega_+^2 - E^2} \delta_{\ell,0}, \quad (\text{C.2})$$

with $E = \sqrt{\epsilon^2 + \Delta^2}$ can be found.

In the Shirley-Floquet representation, the Hamiltonian of the driven system can be rewritten as

$$H^{f\tau} = (\epsilon\tau_z + \Delta\tau_x)F_0^f + \frac{a}{2}\tau_0(F_1^f + F_{-1}^f) - \Omega N^f. \quad (\text{C.3})$$

The commutativity of the drive with the rest of the Hamiltonian allows us to

C.1. Retarded Green function for commuting drive

diagonalise the Hamiltonian using ¹

$$\begin{aligned}
 P^f \tau &= \exp \left[-\frac{a}{2\Omega} \tau_0 (F_1^f - F_{-1}^f) \right] \\
 &= \sum_{m=0}^{\infty} \sum_{n=0}^{\infty} \frac{(-a/2\Omega)^m}{m!} \frac{(a/2\Omega)^n}{n!} \tau_0 F_m^f F_{-n}^f \\
 &= \tau_0 \sum_{n=-\infty}^{\infty} J_n \left(-\frac{a}{\Omega} \right) F_n^f
 \end{aligned} \tag{C.5}$$

as

$$H'^{f\tau} = P^{f\tau\dagger} H^{f\tau} P^{f\tau} = (\epsilon\tau_z + \Delta\tau_x) F_0^f - \Omega_0 N^f, \tag{C.6}$$

where we have used the identities in Eq. (A.21), and J_n are the Bessel functions of the first kind. This diagonalisation physically corresponds to looking for a rotating frame where the system behaves like a static system. We emphasise that the availability of a closed-form exact solution for $H'^{f\tau}$ relies on the commutativity $[A^\tau, \tau_x] = 0$ (or originally $[A^{\tau\sigma}, \tau_x \sigma_x] = 0$). Because the drive by definition lies in τ_0 or τ_z sector, its commutativity with the dispersive term $[A^\tau, \tau_z] = 0$ (or originally $[A^{\tau\sigma}, \tau_z \sigma_0] = 0$) is always satisfied.

It can be immediately recognised that the Hamiltonian in the rotating frame is exactly the same as the Hamiltonian without driving in the lab frame

$$H'^{f\tau} = \tilde{H}^{f\tau} \equiv H^{f\tau}(a=0). \tag{C.7}$$

Indeed, this is an evidence that the drive should not bring in physically observable effects to the system if it is not coupled to the environment. The Shirley-Floquet Green function of this effectively static Hamiltonian is given by Eq. (C.2) $G'^{R,f\tau} = \tilde{G}^{R,f\tau}$, which is related to the Green function of the system in the lab frame as

$$G^{R,f\tau} = P^{f\tau} G'^{R,f\tau} P^{f\tau\dagger}, \tag{C.8}$$

yielding

$$(G^{R,\tau})_\ell^f(\omega) = \sum_{\tilde{k} \in \mathbb{Z}} (-)^{\tilde{k}} \tilde{G}^{R,\tau} \left(\omega + \frac{2\tilde{k} - k}{2} \Omega \right) J_{\tilde{k}}(a/\Omega) J_{k-\tilde{k}}(a/\Omega). \tag{C.9}$$

This is equivalent to the expression shown in Eq. (11.15).

¹We have used the series expansion for the Bessel functions in the last step:

$$J_n(2x) = \sum_{k=0}^{\infty} \frac{(-1)^k}{k!(n+k)!} x^{n+2k}, \quad n \geq 0. \tag{C.4}$$

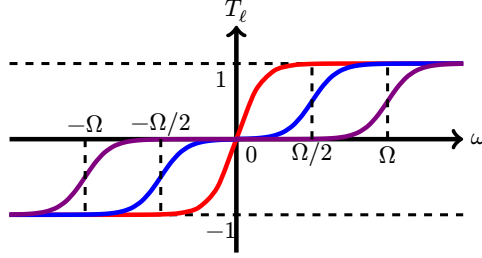


Figure C.1: Schematics of the functions T_ℓ at temperature $T = \Omega/3$, with (red) $\ell = 0$, (blue) $\ell = 1$, and (purple) $\ell = 2$.

C.2 Oscillating components of the order parameter

In this Section, we discuss the behaviours of the oscillating components of the order parameter. For clarity of the discussion, we focus only on the specific form of Hamiltonian Eq. (11.1) chosen in the main text, i.e.

$$H_{0,k}^{\tau\sigma} = \epsilon_k \tau_z \sigma_0, \quad H_1^{\tau\sigma} = (H_{-1}^{\tau\sigma})^\dagger = \frac{a}{2} A^{\tau\sigma}, \quad H_{|\ell| \geq 2}^{\tau\sigma} = 0, \quad (\text{C.10})$$

and construct the driving as discussed in details in Section 11.2.

The oscillating parts of the order parameter can be determined by

$$\Delta_\ell = \frac{ig}{2} \int_{-\Omega_c}^{\Omega_c} \frac{d\omega}{2\pi} T_\ell \left(\frac{\omega}{2T}, \Omega \right) \sum_{\mathbf{k}} \text{Tr}_{\tau\sigma} [(G_{\mathbf{k}}^{R,\tau\sigma})^f_{\tau_+ \sigma_x}] \quad (\text{C.11})$$

$$T_\ell \left(\frac{\omega}{2T}, \Omega \right) = \frac{1}{2} \tanh \left(\frac{\omega - \ell\Omega/2}{2T} \right) + \frac{1}{2} \tanh \left(\frac{\omega + \ell\Omega/2}{2T} \right), \quad (\text{C.12})$$

where we have combined the gap equation Eq. (10.32), the fluctuation-dissipation theorem Eq. (10.34), and taken the cutoff frequency $\Omega_c \approx \Omega$ into account explicitly.

We first briefly discuss the behaviours of T_ℓ as depicted in Fig. C.1. At zero temperature, it behaves like a sign function $\text{sgn}(\omega)$, except being zero $T_\ell(\omega) = 0$ in the interval $\omega \in (-\ell\Omega/2, \ell\Omega/2)$. This indicates that the poles of $(G_{\mathbf{k}}^{R,\tau\sigma})^f_\ell$ within this interval do not contribute to the order parameter Δ_ℓ . Considering also the fact that the drive is chosen to be in close resonance with the cutoff frequency $\Omega \approx \Omega_c$, it can be immediately recognised that $\Delta_{|\ell| \geq 3} = 0$ at zero temperature. At finite temperature, T_ℓ become smoothed in a similar way as the Fermi-Dirac distribution. This can activate an exponentially tiny contribution in $\Delta_{|\ell| \geq 3} \sim \exp \left[-\frac{(|\ell|/2 - 1)\Omega}{T} \right]$, which are still negligible in

C.2. Oscillating components of the order parameter

comparison to the lower harmonics $\Delta_{\pm 1, \pm 2} \sim 1$. We thus focus on $\Delta_{\pm 1}$ and $\Delta_{\pm 2}$ in the following discussions.

We first consider $\Delta_{\pm 1}$, which are related to the Green functions in the first Wigner families $(G_{\mathbf{k}}^R)_{\ell=\pm 1}$. To the order of $\mathcal{O}(a^2/\Omega^2)$, these Green's functions are approximated by [cf. Eq. (11.3)]

$$(G_{\mathbf{k}}^{R, \tau\sigma})_{\ell=\pm 1}^f(\omega) \approx a \tilde{G}_{\mathbf{k}}^{R, \tau\sigma}(\omega \mp \Omega/2) A^{\tau\sigma(\dagger)} \tilde{G}_{\mathbf{k}}^{R, \tau\sigma}(\omega \pm \Omega/2). \quad (\text{C.13})$$

With the choice Eq. (11.1), $\Delta_{\pm 1}$ vanishes unless the drive is in $\tau_0\sigma_0$ sector or the same sector as the dispersion, i.e. $\tau_z\sigma_0$. Otherwise, the trace vanishes $\text{Tr}_{\tau\sigma}[(G_{\mathbf{k}}^{R, \tau\sigma})_{\ell}^f \tau_+ \sigma_x] = 0$ as the drive rotates the order parameter into a sector orthogonal to the interaction channel. This argument in fact also applies to all odd Fourier components of the gap, Δ_{ℓ} , $\ell \in 2\mathbb{Z} + 1$. As a result of the vanishing $\Delta_{\pm 1}$, a frequency doubling in the order parameter is predicted.

We then consider $\Delta_{\pm 2}$ related to $(G_{\mathbf{k}}^{R, \tau\sigma})_{\ell=\pm 2}^f$. As a result of the cutoff Ω_c , the dominantly contributing poles of the Green function are the ones located at $\omega = \pm(\Omega - E_{\mathbf{k}})$. Using a similar argument based on Eq. (11.3), it can be shown that $\Delta_{\pm 2}$ generally do not vanish, but rather scale as a^2/Ω^2 , cf. Eq. (11.5). We finally should also consider the thermal distribution which behaves as $T_{\ell}(\omega) \approx \frac{1}{2}[1 - \tanh(E_{\mathbf{k}}/2T)]$ at $\omega = \pm(\Omega - E_{\mathbf{k}})$, yielding

$$\Delta_{\pm 2} \sim \frac{a^2}{\Omega^2} \left[1 - \tanh\left(\frac{E_{\mathbf{k}}}{2T}\right) \right]. \quad (\text{C.14})$$

At low temperature $T \ll E_{\mathbf{k}}$, $\Delta_{\pm 2}$ are thus suppressed exponentially. In this case, all oscillating components of the order parameter are either vanishing or exponentially negligible in comparison to the constant component. Our a priori assumption Eq. (11.2) is thus fully valid. At higher temperature $T \sim E_{\mathbf{k}}$, however, $\Delta_{\pm 2} \sim a^2/\Omega^2$ become sizeable corrections which are neglected in Eq. (11.2). Particularly, it is in the same order $\mathcal{O}(a^2/\Omega^2)$ as the enhancement of superconductivity discussed in Section 11.2. Nevertheless, this deviation only has quantitative consequences, and does not qualitatively invalidate our arguments in the main text.

Our arguments above is confirmed in the inset of Fig. 11.2(a) of the main text. At low temperature $T < T_{c0}$, $\Delta_{\pm 2}$ is vanishing, fully validating the a priori assumption Eq. (11.2). Notably, a deviation is seen between the two numerically exact results are compared to analytically approximated results Eq. (11.21). This deviation comes from the truncation of higher order correction in Eq. (11.21) in comparison to the complete expansion Eq. (11.3), instead of the a priori assumption. As the temperature increases to be comparable to the general energy scale of the problem $T > T_{c0}$, $\Delta_{\pm 2}$ becomes finite, obtaining a value in the order of $\frac{a^2}{\Omega^2} \Delta_0$, again consistent with our arguments above.

C.3 Dispersive superconductor in the weak coupling limit

In this Section of the Appendix, we complement our results for flat-band superconductors in Section 11.2 by more general calculations for dispersive superconductors. More specifically, we consider the weak coupling limit where the summation over momentum can be replaced by an integral over energy as

$$\sum_{\mathbf{k}} \rightarrow N(\epsilon_F) \int_{-\Omega_c}^{\Omega_c} d\epsilon. \quad (\text{C.15})$$

In the same spirit as Eq. (11.20), we evaluate the anomalous spectral and response functions up to the order of $\mathcal{O}(a^2/\Omega^2)$ but for a finite value of $\epsilon_{\mathbf{k}}$,

$$\mathcal{R}_{\text{an},\mathbf{k}}(\omega) = \tanh\left(\frac{\omega}{2T}\right) \mathcal{A}_{\text{an},\mathbf{k}}(\omega) \quad (\text{C.16a})$$

$$\mathcal{A}_{\text{an},\mathbf{k}}(\omega) \approx \left(\frac{\Delta_0}{E_{\mathbf{k}}} - \frac{a^2 \Delta_0}{\Omega^2} B_1\right) (L_{\Sigma}(\omega - E_{\mathbf{k}}) - L_{\Sigma}(\omega + E_{\mathbf{k}})) \quad (\text{C.16b})$$

$$\begin{aligned} & - \frac{a^2 \Delta_0}{\Omega^2} B_+ (L_{\Sigma}(\omega - \Omega - E_{\mathbf{k}}) - L_{\Sigma}(\omega + \Omega + E_{\mathbf{k}})) \\ & + \frac{a^2 \Delta_0}{\Omega^2} B_- (L_{\Sigma}(\omega - \Omega + E_{\mathbf{k}}) - L_{\Sigma}(\omega + \Omega - E_{\mathbf{k}})) \end{aligned}$$

$$B_1 = \frac{(16\epsilon_{\mathbf{k}}^2 E_{\mathbf{k}}^4 + 4(\Delta_0^2 - 4\epsilon_{\mathbf{k}}^2) E_{\mathbf{k}}^2 \Omega^2) + (3\epsilon_{\mathbf{k}}^2 + \Delta_0^2) \Omega^4}{2E_{\mathbf{k}}^3 (\Omega - 4E_{\mathbf{k}}^2)^2} \quad (\text{C.16c})$$

$$B_{\pm} = \frac{\Omega^2 - 4\epsilon_{\mathbf{k}}^2}{4E_{\mathbf{k}}(2E_{\mathbf{k}} \pm \Omega)^2} \quad (\text{C.16d})$$

$$E_{\mathbf{k}} = \sqrt{\epsilon_{\mathbf{k}}^2 + \Delta_0^2}. \quad (\text{C.16e})$$

Consistent with our requirement discussed in the main text, the poles at $\omega = \pm(\Omega - E_{\mathbf{k}})$ contributes positively to the response function when Ω dominates. This indicates that the enhancement of superconductivity at finite temperature can potentially also be observed in dispersive superconductor. In the following, we investigate the change in the critical temperature and the behaviours of Δ_0 in its vicinity. Under this approximation, the self-consistency equation for order

C.3. Dispersive superconductor in the weak coupling limit

parameter thus becomes

$$\frac{1}{gN(\epsilon_F)} = I_1 + \frac{a^2}{\Omega^2} I_2 \quad (\text{C.17a})$$

$$I_1 = \int_0^{\Omega - \delta\Omega} d\epsilon \frac{1}{E} \tanh\left(\frac{\epsilon}{2T_c}\right) \quad (\text{C.17b})$$

$$I_2 = \int_{\delta\Omega}^{2\Omega - \delta\Omega} d\epsilon B_- \tanh\left(\frac{\Omega - E}{2T_c}\right) - \int_0^{\Omega - \delta\Omega} d\epsilon B_1 \tanh\left(\frac{E}{2T_c}\right). \quad (\text{C.17c})$$

The critical temperature of the driven superconductor can be estimated by imposing $\Delta_0 = 0$, which yields the equation for T_c as

$$I_1(\Delta_0 = 0) \approx \ln\left(\frac{\Omega}{2T_c}\right) + \ln\left(\frac{4}{\pi}\right) + \gamma \quad (\text{C.18a})$$

$$I_2(\Delta_0 = 0) \approx \frac{1}{4} \left[\ln\left(\frac{\Omega}{\delta\Omega}\right) - 6 \ln\left(\frac{\Omega}{T_c}\right) + \ln\left(\frac{3^5 \pi^6}{2^{11}}\right) - 6\gamma \right], \quad (\text{C.18b})$$

where $\gamma \approx 0.577$ is Euler's constant. The new critical temperature T_c is thus approximately related to the non-driven critical point $T_{c0} = T_c(a = 0)$ as [cf. Eq. (11.24)]

$$\frac{T_c}{T_{c0}} \approx \left(\frac{3.573 T_{c0}^6}{\Omega^5 \delta\Omega} \right)^{\frac{a^2}{4\Omega^2}}. \quad (\text{C.19})$$

In comparison to the flat band superconductor [cf. Eq. (11.23)], our scheme has a much weaker effect on the dispersive superconductor. A much smaller detuning $\delta\Omega$ is required for achieving the same T_c , which is essentially due to a subset of negatively contributing excitations lying in the interval $\omega \in (\Omega_c, \Omega)$.

We now proceed on investigating the behaviours of $\Delta_0(T)$ close to the critical temperature, i.e., when Δ_0 is finite but small. To this end, we expand the two integrals I_1 and I_2 as functions of Δ_0 . Defining $\Delta I_j(T) = I_j(T, \Delta_0) -$

$I_j(T, \Delta_0 = 0)$ and $\Delta \tilde{I}_j(T) = I_j(T_c, \Delta_0 = 0) - I_j(T, \Delta_0 = 0)$, we evaluate

$$\begin{aligned}
 \Delta I_1(T) &\approx -\frac{7\zeta(3)\Delta_0^2}{8\pi^2 T^2} \\
 \Delta I_2(T) &\approx \frac{21\zeta(3)\Delta_0^2}{8\pi^2 T^2} + \frac{\pi\Delta_0}{2T} \\
 &\quad + \frac{1}{2} \left[\operatorname{artanh} \left(\frac{2\Omega/\Delta_0}{\sqrt{1+4\Omega^2/\Delta_0^2}} \right) - \operatorname{artanh} \left(\frac{\delta\Omega/\Delta_0}{\sqrt{1+\delta\Omega^2/\Delta_0^2}} \right) \right] \\
 &\approx \begin{cases} -\frac{1}{2} \ln \left(\frac{\Delta_0}{\delta\Omega} \right), & \Omega \gg \Delta_0 \gg \delta\Omega \\ \frac{\pi\Delta_0}{2T} + \frac{21\zeta(3)\Delta_0^2}{8\pi^2 T^2} - \frac{\Delta_0^2}{8\delta\Omega^2}, & \Omega \gg \delta\Omega \gg \Delta_0 \end{cases} \\
 \Delta \tilde{I}_1(T) &\approx -\left(1 - \frac{T}{T_c}\right) \\
 \Delta \tilde{I}_2(T) &\approx \frac{3}{2} \left(1 - \frac{T}{T_c}\right).
 \end{aligned} \tag{C.20}$$

The self-consistency equation for the order parameter can now be rewritten as

$$\Delta I_1(T) + \frac{a^2}{\Omega^2} \Delta I_2(T) = \Delta \tilde{I}_1(T) + \frac{a^2}{\Omega^2} \Delta \tilde{I}_2(T), \tag{C.21}$$

yielding the asymptotic behaviours of Δ_0 as function of $\Delta T = T_c - T$ as (given the choice $\frac{a}{\Omega} T_c \gg \delta\Omega$ and $\Omega \gg \delta\Omega$)

$$\Delta_0 \approx \begin{cases} \delta\Omega \exp \left[2 \left(1 - \frac{3a^2}{2\Omega^2} \right) \frac{\Delta T}{T_c} \right], & \Omega \gg \Delta_0 \gg \delta\Omega \\ \sqrt{\Delta T} \sqrt{\frac{8\pi^2 \delta\Omega^2 T_c \left(1 - \frac{3a^2}{2\Omega^2} \right)}{7\zeta(3)\delta\Omega^2 + \frac{a^2}{\Omega^2} \pi^2 T_c^2}}, & \delta\Omega \gg \Delta_0 \gg \frac{\delta\Omega^2}{T_c} \\ -\frac{2}{\pi} \left(1 - \frac{3a^2}{2\Omega^2} \right) \Delta T, & \frac{\delta\Omega^2}{T_c} \gg \Delta_0 \end{cases} \tag{C.22}$$

The order parameter behaves in an unusual manner. When the scale of the order parameter lies above the detuning, it decays exponentially as the temperature approaches the critical temperature. This is the dominant asymptotic behaviour seen above the static critical temperature $T > T_{c0}$ [cf. Fig. 11.2(b)].

C.3. Dispersive superconductor in the weak coupling limit

In a small temperature interval in the vicinity of the new critical temperature T_c , the order parameter recovers the usual quadratic behaviour seen in a static superconductor according to Ginzburg-Landau theorem. Nevertheless, the most intriguing behaviour of Δ_0 can be seen when it becomes the smallest energy scale of the problem. In this range, it increases linearly as temperature increases *above* T_c . This indicates a re-entrance of superconductivity and correspondingly a first-order phase transition. This behaviour is in essence the same as seen for the flat-band superconductor, where a jump in Δ_0 is seen at T_c [cf. Section 11.2]. Similar re-entrance and change of critical exponent are also seen in Ref. [257].

References

- [1] L. Euler, “De novo genere oscillationum”, *Commentarii academiae scientiarum imperialis Petropolitanae* **11**, 128 (1750).
- [2] L. Landau and E. Lifshitz, *Mechanics* (Butterworth-Heinemann, Oxford, 1976).
- [3] F. Melde, “Ueber die Erregung stehender Wellen eines fadenförmigen Körpers”, *Ann. Phys.* **187**, 513 (1860).
- [4] R. Lifshitz and M. C. Cross, “Nonlinear dynamics of nanomechanical and micromechanical resonators”, in *Reviews of nonlinear dynamics and complexity* (John Wiley & Sons, Ltd, 2008) Chap. 1, pp. 1–52.
- [5] M. Faraday, “On a peculiar class of acoustical figures; and on certain forms assumed by groups of particles upon vibrating elastic surfaces”, *Phil. Trans. R. Soc. Lond.* **3**, 49 (1837).
- [6] E. Mathieu, “Mémoire sur le mouvement vibratoire d’ une membrane de forme elliptique”, *J. math. pure appl.* **13**, 137 (1868).
- [7] Rayleigh, “On the maintenance of vibrations by forces of double frequency, and on the propagation of waves through a medium endowed with a periodic structure”, *The London, Edinburgh, and Dublin Philosophical Magazine and Journal of Science* **24**, 145 (1887).
- [8] P. L. Kapitza, “Маятник с вибрирующим подвесом (Pendulum with a vibrating suspension)”, *Phys. Uspekhi* **44**, 7 (1951).
- [9] W. W. Mumford, “Some notes on the history of parametric transducers”, *Proceedings of the IRE* **48**, 848 (1960).
- [10] D. Rugar and P. Grütter, “Mechanical parametric amplification and thermomechanical noise squeezing”, *Phys. Rev. Lett.* **67**, 699 (1991).
- [11] D. G. Figueroa and F. Torrentí, “Parametric resonance in the early universe—a fitting analysis”, *J. Cosmol. Astropart. Phys.* **2017**, 001 (2017).
- [12] J. A. Dror, K. Harigaya, and V. Narayan, “Parametric resonance production of ultralight vector dark matter”, *Phys. Rev. D* **99**, 035036 (2019).
- [13] G. Floquet, “Sur les équations différentielles linéaires à coefficients périodiques”, *Ann. Sci. Éc. Norm. Supér.* **12**, 47 (1883).
- [14] N. Goldman and J. Dalibard, “Periodically driven quantum systems: Effective Hamiltonians and engineered gauge fields”, *Phys. Rev. X* **4**, 031027 (2014).

References

- [15] M. Bukov, L. D'Alessio, and A. Polkovnikov, “Universal high-frequency behavior of periodically driven systems: from dynamical stabilization to Floquet engineering”, *Advances in Physics* **64**, 139 (2015).
- [16] J. H. Shirley, “Solution of the schrödinger equation with a hamiltonian periodic in time”, *Phys. Rev.* **138**, B979 (1965).
- [17] K. L. Ivanov, K. R. Mote, M. Ernst, A. Equebal, and P. K. Madhu, “Floquet theory in magnetic resonance: Formalism and applications”, *Progress in Nuclear Magnetic Resonance Spectroscopy* **126-127**, 17 (2021).
- [18] T. Ozawa and H. M. Price, “Topological quantum matter in synthetic dimensions”, *Nature Reviews Physics* **1**, 349 (2019).
- [19] H. M. Price, O. Zilberberg, T. Ozawa, I. Carusotto, and N. Goldman, “Four-dimensional quantum hall effect with ultracold atoms”, *Phys. Rev. Lett.* **115**, 195303 (2015).
- [20] M. Aidelsburger, M. Atala, S. Nascimbène, S. Trotzky, Y.-A. Chen, and I. Bloch, “Experimental realization of strong effective magnetic fields in an optical lattice”, *Phys. Rev. Lett.* **107**, 255301 (2011).
- [21] H. M. Price, T. Ozawa, and N. Goldman, “Synthetic dimensions for cold atoms from shaking a harmonic trap”, *Phys. Rev. A* **95**, 023607 (2017).
- [22] X. Wang, H.-R. Li, and F.-L. Li, “Generating synthetic magnetism via Floquet engineering auxiliary qubits in phonon-cavity-based lattice”, *New Journal of Physics* **22**, 033037 (2020).
- [23] I. Martin, G. Refael, and B. Halperin, “Topological frequency conversion in strongly driven quantum systems”, *Phys. Rev. X* **7**, 041008 (2017).
- [24] Y. Baum and G. Refael, “Setting boundaries with memory: Generation of topological boundary states in Floquet-induced synthetic crystals”, *Phys. Rev. Lett.* **120**, 106402 (2018).
- [25] Y. Peng and G. Refael, “Topological energy conversion through the bulk or the boundary of driven systems”, *Phys. Rev. B* **97**, 134303 (2018).
- [26] E. Lustig, S. Weimann, Y. Plotnik, Y. Lumer, M. A. Bandres, A. Szameit, and M. Segev, “Photonic topological insulator in synthetic dimensions”, *Nature* **567**, 356 (2019).
- [27] T. Ozawa, H. M. Price, N. Goldman, O. Zilberberg, and I. Carusotto, “Synthetic dimensions in integrated photonics: From optical isolation to four-dimensional quantum Hall physics”, *Phys. Rev. A* **93**, 043827 (2016).

- [28] E. S. Mananga and T. Charpentier, “Introduction of the Floquet-Magnus expansion in solid-state nuclear magnetic resonance spectroscopy”, *The Journal of Chemical Physics* **135**, 044109 (2011).
- [29] F. Grossmann, T. Dittrich, P. Jung, and P. Hänggi, “Coherent destruction of tunneling”, *Phys. Rev. Lett.* **67**, 516 (1991).
- [30] H. Lignier, C. Sias, D. Ciampini, Y. Singh, A. Zenesini, O. Morsch, and E. Arimondo, “Dynamical control of matter-wave tunneling in periodic potentials”, *Phys. Rev. Lett.* **99**, 220403 (2007).
- [31] M. Messer, K. Sandholzer, F. Görg, J. Minguzzi, R. Desbuquois, and T. Esslinger, “Floquet dynamics in driven Fermi-Hubbard systems”, *Phys. Rev. Lett.* **121**, 233603 (2018).
- [32] N. Tsuji, T. Oka, P. Werner, and H. Aoki, “Dynamical band flipping in fermionic lattice systems: An ac-field-driven change of the interaction from repulsive to attractive”, *Phys. Rev. Lett.* **106**, 236401 (2011).
- [33] Z. Zheng, C. Qu, X. Zou, and C. Zhang, “Floquet Fulde-Ferrell-Larkin-Ovchinnikov superfluids and Majorana fermions in a shaken fermionic optical lattice”, *Phys. Rev. A* **91**, 063626 (2015).
- [34] K. Takasan, A. Daido, N. Kawakami, and Y. Yanase, “Laser-induced topological superconductivity in cuprate thin films”, *Phys. Rev. B* **95**, 134508 (2017).
- [35] H. Chono, K. Takasan, and Y. Yanase, “Laser-induced topological s -wave superconductivity in bilayer transition metal dichalcogenides”, *Phys. Rev. B* **102**, 174508 (2020).
- [36] U. Kumar and S.-Z. Lin, “Inducing and controlling superconductivity in the Hubbard honeycomb model using an electromagnetic drive”, *Phys. Rev. B* **103**, 064508 (2021).
- [37] H. Deghani, M. Hafezi, and P. Ghaemi, “Light-induced topological superconductivity via Floquet interaction engineering”, *Phys. Rev. Res.* **3**, 023039 (2021).
- [38] S. Kitamura and H. Aoki, “Floquet topological superconductivity induced by chiral many-body interaction”, *Communications Physics* **5**, 174 (2022).
- [39] J.-i. Inoue and A. Tanaka, “Photoinduced transition between conventional and topological insulators in two-dimensional electronic systems”, *Phys. Rev. Lett.* **105**, 017401 (2010).
- [40] N. H. Lindner, G. Refael, and V. Galitski, “Floquet topological insulator in semiconductor quantum wells”, *Nature Physics* **7**, 490 (2011).
- [41] N. Fläschner, B. S. Rem, M. Tarnowski, D. Vogel, D.-S. Lühmann, K. Sengstock, and C. Weitenberg, “Experimental reconstruction of the Berry curvature in a Floquet Bloch band”, *Science* **352**, 1091 (2016).

References

- [42] J. W. McIver, B. Schulte, F. Stein, T. Matsuyama, G. Jotzu, G. Meier, and A. Cavalleri, “Light-induced anomalous hall effect in graphene”, *Nature Physics* **16**, 38 (2020).
- [43] M. H. Kolodrubetz, F. Nathan, S. Gazit, T. Morimoto, and J. E. Moore, “Topological Floquet-Thouless energy pump”, *Phys. Rev. Lett.* **120**, 150601 (2018).
- [44] J. Minguzzi, Z. Zhu, K. Sandholzer, A.-S. Walter, K. Viebahn, and T. Esslinger, “Topological pumping in a Floquet-Bloch band”, *Phys. Rev. Lett.* **129**, 053201 (2022).
- [45] M. Ueda, “Quantum equilibration, thermalization and prethermalization in ultracold atoms”, *Nature Reviews Physics* **2**, 669 (2020).
- [46] C. Fleckenstein and M. Bukov, “Prethermalization and thermalization in periodically driven many-body systems away from the high-frequency limit”, *Phys. Rev. B* **103**, L140302 (2021).
- [47] A. Rajak, R. Citro, and E. G. D. Torre, “Stability and prethermalization in chains of classical kicked rotors”, *J. Phys. A* **51**, 465001 (2018).
- [48] L. D’Alessio and M. Rigol, “Long-time behavior of isolated periodically driven interacting lattice systems”, *Phys. Rev. X* **4**, 041048 (2014).
- [49] A. Lazarides, A. Das, and R. Moessner, “Periodic thermodynamics of isolated quantum systems”, *Phys. Rev. Lett.* **112**, 150401 (2014).
- [50] J. M. Deutsch, “Eigenstate thermalization hypothesis”, *Reports on Progress in Physics* **81**, 082001 (2018).
- [51] B. Buča, *Unified theory of local quantum many-body dynamics: Eigenoperator thermalization theorems*, 2023, [arXiv:2301.07091](https://arxiv.org/abs/2301.07091).
- [52] K. Singh, C. J. Fujiwara, Z. A. Geiger, E. Q. Simmons, M. Lipatov, A. Cao, P. Dotti, S. V. Rajagopal, R. Senaratne, T. Shimasaki, M. Heyl, A. Eckardt, and D. M. Weld, “Quantifying and controlling prethermal nonergodicity in interacting Floquet matter”, *Phys. Rev. X* **9**, 041021 (2019).
- [53] T. Ishii, T. Kuwahara, T. Mori, and N. Hatano, “Heating in integrable time-periodic systems”, *Phys. Rev. Lett.* **120**, 220602 (2018).
- [54] A. Haldar, R. Moessner, and A. Das, “Onset of floquet thermalization”, *Phys. Rev. B* **97**, 245122 (2018).
- [55] R. Nandkishore and D. A. Huse, “Many-body localization and thermalization in quantum statistical mechanics”, *Annual Review of Condensed Matter Physics* **6**, 15 (2015).
- [56] D. A. Abanin, E. Altman, I. Bloch, and M. Serbyn, “Colloquium: Many-body localization, thermalization, and entanglement”, *Rev. Mod. Phys.* **91**, 021001 (2019).

- [57] M. Serbyn, Z. Papić, and D. A. Abanin, “Local conservation laws and the structure of the many-body localized states”, *Phys. Rev. Lett.* **111**, 127201 (2013).
- [58] D. A. Huse, R. Nandkishore, and V. Oganesyan, “Phenomenology of fully many-body-localized systems”, *Phys. Rev. B* **90**, 174202 (2014).
- [59] C. J. Turner, A. A. Michailidis, D. A. Abanin, M. Serbyn, and Z. Papić, “Weak ergodicity breaking from quantum many-body scars”, *Nature Physics* **14**, 745 (2018).
- [60] Q. Chen, S. A. Chen, and Z. Zhu, *Weak ergodicity breaking in non-Hermitian many-body systems*, 2022, [arXiv:2202.08638](https://arxiv.org/abs/2202.08638).
- [61] G. Lindblad, “On the generators of quantum dynamical semigroups”, *Communications in Mathematical Physics* **48**, 119 (1976).
- [62] H.-P. Breuer and F. Petruccione, *The theory of open quantum systems* (Oxford University Press, 2002).
- [63] D. Manzano, “A short introduction to the Lindblad master equation”, *AIP Advances* **10**, 025106 (2020).
- [64] A. Eckardt, “Colloquium: Atomic quantum gases in periodically driven optical lattices”, *Rev. Mod. Phys.* **89**, 011004 (2017).
- [65] T. Byrnes and E. O. Ilo-Okeke, *Quantum atom optics: theory and applications to quantum technology* (Cambridge University Press, 2021).
- [66] F. Mivehvar, F. Piazza, T. Donner, and H. Ritsch, “Cavity QED with quantum gases: new paradigms in many-body physics”, *Advances in Physics* **70**, 1 (2021).
- [67] X. Wu, X. Liang, Y. Tian, F. Yang, C. Chen, Y.-C. Liu, M. K. Tey, and L. You, “A concise review of Rydberg atom based quantum computation and quantum simulation”, *Chinese Physics B* **30**, 020305 (2021).
- [68] Ş. K. Özdemir, S. Rotter, F. Nori, and L. Yang, “Parity–time symmetry and exceptional points in photonics”, *Nature Materials* **18**, 783 (2019).
- [69] T. Holstein and H. Primakoff, “Field dependence of the intrinsic domain magnetization of a ferromagnet”, *Phys. Rev.* **58**, 1098 (1940).
- [70] A. Wagner, A. Nunnenkamp, and C. Bruder, “Mean-field analysis of spinor bosons in optical superlattices”, *Phys. Rev. A* **86**, 023624 (2012).
- [71] T. Prosen, “Third quantization: a general method to solve master equations for quadratic open Fermi systems”, *New Journal of Physics* **10**, 043026 (2008).
- [72] T. Prosen and T. H. Seligman, “Quantization over boson operator spaces”, *Journal of Physics A: Mathematical and Theoretical* **43**, 392004 (2010).

- [73] R. Tsekov, “Dissipation in quantum systems”, *Journal of Physics A: Mathematical and General* **28**, L557 (1995).
- [74] B. Buča, C. Booker, and D. Jaksch, “Algebraic theory of quantum synchronization and limit cycles under dissipation”, *SciPost Phys.* **12**, 097 (2022).
- [75] B. Buča and D. Jaksch, “Dissipation induced nonstationarity in a quantum gas”, *Phys. Rev. Lett.* **123**, 260401 (2019).
- [76] J. Tindall, C. Sánchez Muñoz, B. Buča, and D. Jaksch, “Quantum synchronisation enabled by dynamical symmetries and dissipation”, *New Journal of Physics* **22**, 013026 (2020).
- [77] C. Sánchez Muñoz, B. Buča, J. Tindall, A. González-Tudela, D. Jaksch, and D. Porras, “Symmetries and conservation laws in quantum trajectories: Dissipative freezing”, *Phys. Rev. A* **100**, 042113 (2019).
- [78] D. Nagy, G. Szirmai, and P. Domokos, “Critical exponent of a quantum-noise-driven phase transition: the open-system Dicke model”, *Phys. Rev. A* **84**, 043637 (2011).
- [79] M. Soriente, T. Donner, R. Chitra, and O. Zeitler, “Dissipation-induced anomalous multicritical phenomena”, *Phys. Rev. Lett.* **120**, 183603 (2018).
- [80] M. Soriente, R. Chitra, and O. Zeitler, “Distinguishing phases using the dynamical response of driven-dissipative light-matter systems”, *Phys. Rev. A* **101**, 023823 (2020).
- [81] H. Aoki, N. Tsuji, M. Eckstein, M. Kollar, T. Oka, and P. Werner, “Nonequilibrium dynamical mean-field theory and its applications”, *Rev. Mod. Phys.* **86**, 779 (2014).
- [82] L. M. Sieberer, M. Buchhold, and S. Diehl, “Keldysh field theory for driven open quantum systems”, *Reports on Progress in Physics* **79**, 096001 (2016).
- [83] A. U. J. Lode, “Multiconfigurational time-dependent Hartree method for bosons with internal degrees of freedom: Theory and composite fragmentation of multicomponent Bose-Einstein condensates”, *Phys. Rev. A* **93**, 063601 (2016).
- [84] O. E. Alon, A. I. Streltsov, and L. S. Cederbaum, “Multiconfigurational time-dependent Hartree method for bosons: Many-body dynamics of bosonic systems”, *Phys. Rev. A* **77**, 033613 (2008).
- [85] E. Fasshauer and A. U. J. Lode, “Multiconfigurational time-dependent Hartree method for fermions: Implementation, exactness, and few-fermion tunneling to open space”, *Phys. Rev. A* **93**, 033635 (2016).
- [86] A. U. J. Lode, K. Sakmann, O. E. Alon, L. S. Cederbaum, and A. I. Streltsov, “Numerically exact quantum dynamics of bosons with time-

- dependent interactions of harmonic type”, *Phys. Rev. A* **86**, 063606 (2012).
- [87] A. U. J. Lode and C. Bruder, “Dynamics of Hubbard Hamiltonians with the multiconfigurational time-dependent Hartree method for indistinguishable particles”, *Phys. Rev. A* **94**, 013616 (2016).
- [88] M. Hughes, A. U. J. Lode, D. Jaksch, and P. Mognini, “Accuracy of quantum simulators with ultracold dipolar molecules: a quantitative comparison between continuum and lattice descriptions”, *Phys. Rev. A* **107**, 033323 (2023).
- [89] C. Lévêque, F. Diorico, J. Schmiedmayer, and A. U. J. Lode, *Many-body density and coherence of trapped cold bosons*, 2020, [arXiv:2006.10755](https://arxiv.org/abs/2006.10755).
- [90] R. J. Glauber, “The quantum theory of optical coherence”, *Phys. Rev.* **130**, 2529 (1963).
- [91] B. Chatterjee and A. U. J. Lode, “Order parameter and detection for a finite ensemble of crystallized one-dimensional dipolar bosons in optical lattices”, *Phys. Rev. A* **98**, 053624 (2018).
- [92] B. Chatterjee, C. Lévêque, J. Schmiedmayer, and A. U. J. Lode, “Detecting one-dimensional dipolar bosonic crystal orders via full distribution functions”, *Phys. Rev. Lett.* **125**, 093602 (2020).
- [93] K. Sakmann and M. Kasevich, “Single-shot simulations of dynamic quantum many-body systems”, *Nature Physics* **12**, 451 (2016).
- [94] A. U. J. Lode and C. Bruder, “Fragmented superradiance of a Bose-Einstein condensate in an optical cavity”, *Phys. Rev. Lett.* **118**, 013603 (2017).
- [95] E. Wigner, “On the quantum correction for thermodynamic equilibrium”, *Phys. Rev.* **40**, 749 (1932).
- [96] G. S. Uhrig, M. H. Kalthoff, and J. K. Freericks, “Positivity of the spectral densities of retarded Floquet Green functions”, *Phys. Rev. Lett.* **122**, 130604 (2019).
- [97] J. H. Van Vleck, “On σ -type doubling and electron spin in the spectra of diatomic molecules”, *Phys. Rev.* **33**, 467 (1929).
- [98] H. Primas, “Eine verallgemeinerte Störungstheorie für quantenmechanische Mehrteilchenprobleme”, *Helvetica Physica Acta* **34**, 331 (1961).
- [99] H. Primas, “Generalized perturbation theory in operator form”, *Rev. Mod. Phys.* **35**, 710 (1963).
- [100] T. Shirai, J. Thingna, T. Mori, S. Denisov, P. Hänggi, and S. Miyashita, “Effective Floquet – Gibbs states for dissipative quantum systems”, *New Journal of Physics* **18**, 053008 (2016).
- [101] T. Becker, L.-N. Wu, and A. Eckardt, “Lindbladian approximation beyond ultraweak coupling”, *Phys. Rev. E* **104**, 014110 (2021).

References

- [102] K. Baumann, C. Guerlin, F. Brennecke, and T. Esslinger, “Dicke quantum phase transition with a superfluid gas in an optical cavity”, *Nature* **464**, 1301 (2010).
- [103] H. Keßler, J. Klinder, M. Wolke, and A. Hemmerich, “Steering matter wave superradiance with an ultranarrow-band optical cavity”, *Phys. Rev. Lett.* **113**, 070404 (2014).
- [104] F. Dimer, B. Estienne, A. S. Parkins, and H. J. Carmichael, “Proposed realization of the Dicke-model quantum phase transition in an optical cavity QED system”, *Phys. Rev. A* **75**, 013804 (2007).
- [105] R. H. Dicke, “Coherence in spontaneous radiation processes”, *Phys. Rev.* **93**, 99 (1954).
- [106] K. Hepp and E. H. Lieb, “On the superradiant phase transition for molecules in a quantized radiation field: the dicke maser model”, *Annals of Physics* **76**, 360 (1973).
- [107] Y. K. Wang and F. T. Hioe, “Phase transition in the Dicke model of superradiance”, *Phys. Rev. A* **7**, 831 (1973).
- [108] H. Carmichael, C. Gardiner, and D. Walls, “Higher order corrections to the Dicke superradiant phase transition”, *Physics Letters A* **46**, 47 (1973).
- [109] P. Nataf and C. Ciuti, “No-go theorem for superradiant quantum phase transitions in cavity QED and counter-example in circuit QED”, *Nature Communications* **1**, 72 (2010).
- [110] K. Baumann, “Experimental realization of the Dicke quantum phase transition”, <https://www.research-collection.ethz.ch/handle/20.500.11850/44725>, PhD thesis (ETH Zürich, 2011).
- [111] N. Dogra, “Interaction- and dissipation-induced phenomena in a quantum gas coupled to a cavity”, <https://www.research-collection.ethz.ch/handle/20.500.11850/383084>, PhD thesis (ETH Zürich, 2019).
- [112] X. Li, “Emergent structures and dynamics in a quantum gas with cavity-mediated long-range interactions”, <https://www.research-collection.ethz.ch/handle/20.500.11850/518042>, PhD thesis (ETH Zürich, 2021).
- [113] K. Baumann, R. Mottl, F. Brennecke, and T. Esslinger, “Exploring symmetry breaking at the Dicke quantum phase transition”, *Phys. Rev. Lett.* **107**, 140402 (2011).
- [114] C. Emary and T. Brandes, “Chaos and the quantum phase transition in the Dicke model”, *Phys. Rev. E* **67**, 066203 (2003).
- [115] R. Mottl, F. Brennecke, K. Baumann, R. Landig, T. Donner, and T. Esslinger, “Roton-type mode softening in a quantum gas with cavity-mediated long-range interactions”, *Science* **336**, 1570 (2012).

- [116] D. Nagy, G. Kónya, G. Szirmai, and P. Domokos, “Dicke-model phase transition in the quantum motion of a Bose-Einstein condensate in an optical cavity”, *Phys. Rev. Lett.* **104**, 130401 (2010).
- [117] F. Brennecke, R. Mottl, K. Baumann, R. Landig, T. Donner, and T. Esslinger, “Real-time observation of fluctuations at the driven-dissipative Dicke phase transition”, *Proceedings of the National Academy of Sciences* **110**, 11763 (2013).
- [118] J. Klinder, H. Keßler, M. Wolke, L. Mathey, and A. Hemmerich, “Dynamical phase transition in the open Dicke model”, *Proceedings of the National Academy of Sciences* **112**, 3290 (2015).
- [119] J. Klinder, H. Keßler, M. R. Bakhtiari, M. Thorwart, and A. Hemmerich, “Observation of a superradiant Mott insulator in the Dicke-Hubbard model”, *Phys. Rev. Lett.* **115**, 230403 (2015).
- [120] F. Mivehvar, H. Ritsch, and F. Piazza, “Superradiant topological peierls insulator inside an optical cavity”, *Phys. Rev. Lett.* **118**, 073602 (2017).
- [121] M. Landini, N. Dogra, K. Kroeger, L. Hruby, T. Donner, and T. Esslinger, “Formation of a spin texture in a quantum gas coupled to a cavity”, *Phys. Rev. Lett.* **120**, 223602 (2018).
- [122] R. M. Kroeze, Y. Guo, V. D. Vaidya, J. Keeling, and B. L. Lev, “Spinor self-ordering of a quantum gas in a cavity”, *Phys. Rev. Lett.* **121**, 163601 (2018).
- [123] S. Ostermann, H.-W. Lau, H. Ritsch, and F. Mivehvar, “Cavity-induced emergent topological spin textures in a bose – einstein condensate”, *New Journal of Physics* **21**, 013029 (2019).
- [124] S. Ostermann, H. Ritsch, and F. Mivehvar, “Many-body phases of a planar Bose-Einstein condensate with cavity-induced spin-orbit coupling”, *Phys. Rev. A* **103**, 023302 (2021).
- [125] N. Masalaeva, W. Niedenzu, F. Mivehvar, and H. Ritsch, “Spin and density self-ordering in dynamic polarization gradients fields”, *Phys. Rev. Res.* **3**, 013173 (2021).
- [126] F. Piazza and H. Ritsch, “Self-ordered limit cycles, chaos, and phase slippage with a superfluid inside an optical resonator”, *Phys. Rev. Lett.* **115**, 163601 (2015).
- [127] H. Keßler, P. Kongkhambut, C. Georges, L. Mathey, J. G. Cosme, and A. Hemmerich, “Observation of a dissipative time crystal”, *Phys. Rev. Lett.* **127**, 043602 (2021).
- [128] P. Kongkhambut, H. Keßler, J. Skulte, L. Mathey, J. G. Cosme, and A. Hemmerich, “Realization of a periodically driven open three-level Dicke model”, *Phys. Rev. Lett.* **127**, 253601 (2021).

References

- [129] P. Kongkhambut, J. Skulte, L. Mathey, J. G. Cosme, A. Hemmerich, and H. Keßler, “Observation of a continuous time crystal”, *Science* **377**, 670 (2022).
- [130] X. Li, D. Dreon, P. Zupancic, A. Baumgärtner, A. Morales, W. Zheng, N. R. Cooper, T. Donner, and T. Esslinger, “First order phase transition between two centro-symmetric superradiant crystals”, *Phys. Rev. Research* **3**, L012024 (2021).
- [131] D. Dreon, A. Baumgärtner, X. Li, S. Hertlein, T. Esslinger, and T. Donner, “Self-oscillating pump in a topological dissipative atom-cavity system”, *Nature* **608**, 494 (2022).
- [132] E. Colella, F. Mivehvar, F. Piazza, and H. Ritsch, “Hofstadter butterfly in a cavity-induced dynamic synthetic magnetic field”, *Phys. Rev. B* **100**, 224306 (2019).
- [133] A. Kosior, H. Ritsch, and F. Mivehvar, *Nonequilibrium phases of ultracold bosons with cavity-induced dynamic gauge fields*, 2022, [arXiv:2208.04602](https://arxiv.org/abs/2208.04602).
- [134] M. J. Bhaseen, J. Mayoh, B. D. Simons, and J. Keeling, “Dynamics of nonequilibrium Dicke models”, *Phys. Rev. A* **85**, 013817 (2012).
- [135] A. Frisk Kockum, A. Miranowicz, S. De Liberato, S. Savasta, and F. Nori, “Ultrastrong coupling between light and matter”, *Nature Reviews Physics* **1**, 19 (2019).
- [136] I. Bloch, “Ultracold quantum gases in optical lattices”, *Nature Physics* **1**, 23 (2005).
- [137] I. Bloch, J. Dalibard, and S. Nascimbène, “Quantum simulations with ultracold quantum gases”, *Nature Physics* **8**, 267 (2012).
- [138] C. Gross and I. Bloch, “Quantum simulations with ultracold atoms in optical lattices”, *Science* **357**, 995 (2017).
- [139] H. Ritsch, P. Domokos, F. Brennecke, and T. Esslinger, “Cold atoms in cavity-generated dynamical optical potentials”, *Reviews of Modern Physics* **85**, 553 (2013).
- [140] M. Aspelmeyer, T. Kippenberg, and F. Marquardt, “Cavity optomechanics”, *Reviews of Modern Physics* **86**, 1391 (2014).
- [141] L. Hruby, N. Dogra, M. Landini, T. Donner, and T. Esslinger, “Metastability and avalanche dynamics in strongly correlated gases with long-range interactions”, *Proceedings of the National Academy of Sciences* **115**, 3279 (2018).
- [142] P. Mognini, L. Papariello, A. U. J. Lode, and R. Chitra, “Superlattice switching from parametric instabilities in a driven-dissipative Bose-Einstein condensate in a cavity”, *Phys. Rev. A* **98**, 053620 (2018).
- [143] H. Keßler, J. G. Cosme, C. Georges, L. Mathey, and A. Hemmerich, “From a continuous to a discrete time crystal in a dissipative atom-cavity system”, *New Journal of Physics* **22**, 085002 (2020).

- [144] M. Greiner, O. Mandel, T. Esslinger, T. W. Hänsch, and I. Bloch, “Quantum phase transition from a superfluid to a Mott insulator in a gas of ultracold atoms”, *Nature* **415**, 39 (2002).
- [145] I. B. Spielman, W. D. Phillips, and J. V. Porto, “Mott-insulator transition in a two-dimensional atomic Bose gas”, *Phys. Rev. Lett.* **98**, 080404 (2007).
- [146] Y. Kato, Q. Zhou, N. Kawashima, and N. Trivedi, “Sharp peaks in the momentum distribution of bosons in optical lattices in the normal state”, *Nature Phys.* **4**, 617 (2008).
- [147] R. Landig, L. Hruby, N. Dogra, M. Landini, R. Mottl, T. Donner, and T. Esslinger, “Quantum phases from competing short- and long-range interactions in an optical lattice”, *Nature* **532**, 476 (2016).
- [148] Y. Li, L. He, and W. Hofstetter, “Lattice-supersolid phase of strongly correlated bosons in an optical cavity”, *Phys. Rev. A* **87**, 051604 (2013).
- [149] M. R. Bakhtiari, A. Hemmerich, H. Ritsch, and M. Thorwart, “Nonequilibrium phase transition of interacting bosons in an intracavity optical lattice”, *Phys. Rev. Lett.* **114**, 123601 (2015).
- [150] E. P. L. van Nieuwenburg, Y.-H. Liu, and S. D. Huber, “Learning phase transitions by confusion”, *Nature Physics* **13**, 435 (2017).
- [151] F. Schäfer and N. Lörch, “Vector field divergence of predictive model output as indication of phase transitions”, *Phys. Rev. E* **99**, 062107 (2019).
- [152] J. Arnold, F. Schäfer, M. Žonda, and A. U. J. Lode, “Interpretable and unsupervised phase classification”, *Phys. Rev. Research* **3**, 033052 (2021).
- [153] F. D’Angelo and L. Böttcher, “Learning the Ising model with generative neural networks”, *Phys. Rev. Research* **2**, 023266 (2020).
- [154] S. Ahmed, C. Sánchez Muñoz, F. Nori, and A. F. Kockum, “Classification and reconstruction of optical quantum states with deep neural networks”, *Phys. Rev. Res.* **3**, 033278 (2021).
- [155] B. S. Rem, N. Kämring, M. Tarnowski, L. Asteria, N. Fläschner, C. Becker, K. Sengstock, and C. Weitenberg, “Identifying quantum phase transitions using artificial neural networks on experimental data”, *Nature Physics* **15**, 917 (2019).
- [156] A. Valenti, G. Jin, J. Léonard, S. D. Huber, and E. Greplova, “Scalable Hamiltonian learning for large-scale out-of-equilibrium quantum dynamics”, *Phys. Rev. A* **105**, 023302 (2022).
- [157] L. S. Cederbaum, A. I. Streltsov, and O. E. Alon, “Fragmented metastable states exist in an attractive Bose-Einstein condensate for atom numbers well above the critical number of the Gross-Pitaevskii theory”, *Phys. Rev. Lett.* **100**, 040402 (2008).

References

- [158] A. U. J. Lode, C. Lévêque, L. B. Madsen, A. I. Streltsov, and O. E. Alon, “Colloquium: Multiconfigurational time-dependent Hartree approaches for indistinguishable particles”, *Rev. Mod. Phys.* **92**, 011001 (2020).
- [159] J. Klinder, H. Keßler, C. Georges, J. Vargas, and A. Hemmerich, “Bose – Einstein condensates in an optical cavity with sub-recoil bandwidth”, *Applied Physics B* **122**, 299 (2016).
- [160] C. Maschler, I. B. Mekhov, and H. Ritsch, “Ultracold atoms in optical lattices generated by quantized light fields”, *The European Physical Journal D* **46**, 545 (2008).
- [161] D. Nagy, G. Szirmai, and P. Domokos, “Self-organization of a Bose-Einstein condensate in an optical cavity”, *The European Physical Journal D* **48**, 127 (2008).
- [162] I. B. Mekhov, C. Maschler, and H. Ritsch, “Probing quantum phases of ultracold atoms in optical lattices by transmission spectra in cavity quantum electrodynamics”, *Nature Physics* **3**, 319 (2007).
- [163] M. Łącki, B. Damski, and J. Zakrzewski, “Locating the quantum critical point of the Bose-Hubbard model through singularities of simple observables”, *Scientific Reports* **6**, 38340 (2016).
- [164] O. A. Prośniak, M. Łącki, and B. Damski, “Critical points of the three-dimensional Bose-Hubbard model from on-site atom number fluctuations”, *Scientific Reports* **9**, 8687 (2019).
- [165] I. B. Spielman, W. D. Phillips, and J. V. Porto, “Condensate fraction in a 2D Bose gas measured across the Mott-insulator transition”, *Phys. Rev. Lett.* **100**, 120402 (2008).
- [166] S. E. Weiner, M. C. Tsatsos, L. S. Cederbaum, and A. U. J. Lode, “Phantom vortices: hidden angular momentum in ultracold dilute Bose-Einstein condensates”, *Scientific Reports* **7**, 40122 EP (2017).
- [167] P. B. Blakie and C. W. Clark, “Wannier states and Bose – Hubbard parameters for 2D optical lattices”, *Journal of Physics B: Atomic, Molecular and Optical Physics* **37**, 1391 (2004).
- [168] I. Danshita and A. Polkovnikov, “Superfluid-to-Mott-insulator transition in the one-dimensional Bose-Hubbard model for arbitrary integer filling factors”, *Phys. Rev. A* **84**, 063637 (2011).
- [169] N. Teichmann, D. Hinrichs, M. Holthaus, and A. Eckardt, “Bose-Hubbard phase diagram with arbitrary integer filling”, *Phys. Rev. B* **79**, 100503 (2009).
- [170] K. V. Krutitsky, “Ultracold bosons with short-range interaction in regular optical lattices”, *Physics Reports* **607**, 1 (2016).
- [171] C. Lévêque and L. B. Madsen, “Time-dependent restricted-active-space self-consistent-field theory for bosonic many-body systems”, *New Journal of Physics* **19**, 043007 (2017).

- [172] N. March, “The Thomas-Fermi approximation in quantum mechanics”, [Advances in Physics](#) **6**, 1 (1957).
- [173] M. Egorov, B. Opanchuk, P. Drummond, B. V. Hall, P. Hannaford, and A. I. Sidorov, “Measurement of s -wave scattering lengths in a two-component Bose-Einstein condensate”, [Phys. Rev. A](#) **87**, 053614 (2013).
- [174] N. Marzari and D. Vanderbilt, “Maximally localized generalized wannier functions for composite energy bands”, [Phys. Rev. B](#) **56**, 12847 (1997).
- [175] B. Wu, Y. Xu, L. Dong, and J.-R. Shi, “Self-consistent approach for mapping interacting systems in continuous space to lattice models”, [Chinese Physics Letters](#) **29**, 083701 (2012).
- [176] R. Walters, G. Cotugno, T. H. Johnson, S. R. Clark, and D. Jaksch, “Ab initio derivation of Hubbard models for cold atoms in optical lattices”, [Phys. Rev. A](#) **87**, 043613 (2013).
- [177] S. Paul and E. Tiesinga, “Wannier functions using a discrete variable representation for optical lattices”, [Phys. Rev. A](#) **94**, 033606 (2016).
- [178] S. Zhu and B. Wu, “Interaction effects on Wannier functions for bosons in an optical lattice”, [Phys. Rev. A](#) **92**, 063637 (2015).
- [179] M. Kremer, R. Sachdeva, A. Benseny, and T. Busch, “Interaction-induced effects on Bose-Hubbard parameters”, [Phys. Rev. A](#) **96**, 063611 (2017).
- [180] L. V. Keldysh, “Диаграммная техника для неравновесных процессов (Diagram technique for nonequilibrium processes)”, [Zh. Eksp. Teor. Fiz.](#) **47**, 1515 (1964).
- [181] M. Buchhold and S. Diehl, “Kinetic theory for interacting Luttinger liquids”, [The European Physical Journal D](#) **69**, 224 (2015).
- [182] N. Okuma, “Boundary-dependent dynamical instability of bosonic green’s function: Dissipative Bogoliubov–de Gennes Hamiltonian and its application to non-Hermitian skin effect”, [Phys. Rev. B](#) **105**, 224301 (2022).
- [183] A. Baksic and C. Ciuti, “Controlling discrete and continuous symmetries in “superradiant” phase transitions with circuit qed systems”, [Phys. Rev. Lett.](#) **112**, 173601 (2014).
- [184] M.-w. Xiao, *Theory of transformation for the diagonalization of quadratic Hamiltonians*, 2009, [arXiv:0908.0787](#).
- [185] P. T. Nam, *Bogoliubov theory and bosonic atoms*, 2011, [arXiv:1109.2875](#).
- [186] A. Ferraro, S. Olivares, and M. G. A. Paris, *Gaussian states in continuous variable quantum information*, 2005, [arXiv:quant-ph/0503237](#).
- [187] B. Öztop, M. Bordyuh, Ö. E. Müstecaplıoğlu, and H. E. Türeci, “Excitations of optically driven atomic condensate in a cavity: theory

- of photodetection measurements”, *New Journal of Physics* **14**, 085011 (2012).
- [188] R. Mottl, “Roton-type mode softening in a dissipative quantum many-body system with cavity-mediated long-range interactions”, <https://www.research-collection.ethz.ch/handle/20.500.11850/93725>, PhD thesis (ETH Zürich, 2014).
- [189] N. A. Sinitsyn and F. Li, “Solvable multistate model of Landau-Zener transitions in cavity QED”, *Phys. Rev. A* **93**, 063859 (2016).
- [190] C. Sun and N. A. Sinitsyn, “Landau-Zener extension of the Tavis-Cummings model: Structure of the solution”, *Phys. Rev. A* **94**, 033808 (2016).
- [191] R. K. Malla, V. Y. Chernyak, C. Sun, and N. A. Sinitsyn, “Coherent reaction between molecular and atomic Bose-Einstein condensates: integrable model”, *Phys. Rev. Lett.* **129**, 033201 (2022).
- [192] B. Kraus, H. P. Büchler, S. Diehl, A. Kantian, A. Micheli, and P. Zoller, “Preparation of entangled states by quantum Markov processes”, *Phys. Rev. A* **78**, 042307 (2008).
- [193] S. Diehl, A. Micheli, A. Kantian, B. Kraus, H. P. Büchler, and P. Zoller, “Quantum states and phases in driven open quantum systems with cold atoms”, *Nature Physics* **4**, 878 (2008).
- [194] D. Finkelstein-Shapiro, S. Felicetti, T. Hansen, T. Pullerits, and A. Keller, “Classification of dark states in multilevel dissipative systems”, *Phys. Rev. A* **99**, 053829 (2019).
- [195] T. L. Heugel, M. Oscity, A. Eichler, O. Zilberberg, and R. Chitra, “Classical many-body time crystals”, *Phys. Rev. Lett.* **123**, 124301 (2019).
- [196] M. Soriente, T. L. Heugel, K. Arimitsu, R. Chitra, and O. Zilberberg, “Distinctive class of dissipation-induced phase transitions and their universal characteristics”, *Phys. Rev. Research* **3**, 023100 (2021).
- [197] N. Dogra, M. Landini, K. Kroeger, L. Hruby, T. Donner, and T. Esslinger, “Dissipation-induced structural instability and chiral dynamics in a quantum gas”, *Science* **366**, 1496 (2019).
- [198] H. Watanabe and M. Oshikawa, “Absence of quantum time crystals”, *Phys. Rev. Lett.* **114**, 251603 (2015).
- [199] N. Y. Yao, A. C. Potter, I.-D. Potirniche, and A. Vishwanath, “Discrete time crystals: rigidity, criticality, and realizations”, *Phys. Rev. Lett.* **118**, 030401 (2017).
- [200] H. Keßler, J. G. Cosme, M. Hemmerling, L. Mathey, and A. Hemmerich, “Emergent limit cycles and time crystal dynamics in an atom-cavity system”, *Phys. Rev. A* **99**, 053605 (2019).
- [201] P. Zupancic, D. Dreon, X. Li, A. Baumgärtner, A. Morales, W. Zheng, N. R. Cooper, T. Esslinger, and T. Donner, “*P*-band induced self-

- organization and dynamics with repulsively driven ultracold atoms in an optical cavity”, *Phys. Rev. Lett.* **123**, 233601 (2019).
- [202] F. Piazza, P. Strack, and W. Zwerger, “Bose – Einstein condensation versus Dicke – Hepp – Lieb transition in an optical cavity”, *Annals of Physics* **339**, 135 (2013).
- [203] J. I. Neimark, “On some cases of periodic motions depending on parameters”, *Dokl. Akad. Nauk SSSR* **129**, 736 (1959).
- [204] R. J. Sacker, *On invariant surfaces and bifurcation of periodic solutions of ordinary differential equations*, 1964.
- [205] S. H. Strogatz, *Nonlinear dynamics and chaos* (Perseus Books, Cambridge, MA, 1994).
- [206] A. A. Andronov, E. A. Leontovich, I. J. Gordon, and A. G. Maier, *Theory of bifurcations of dynamical systems on a plane* (Israel Program Sci. Transl., 1971).
- [207] K. Sakmann, A. I. Streltsov, O. E. Alon, and L. S. Cederbaum, “Reduced density matrices and coherence of trapped interacting bosons”, *Phys. Rev. A* **78**, 023615 (2008).
- [208] S. Wessel, F. Alet, M. Troyer, and G. G. Batrouni, “Quantum Monte Carlo simulations of confined bosonic atoms in optical lattices”, *Phys. Rev. A* **70**, 053615 (2004).
- [209] M. Jääskeläinen and P. Meystre, “Dynamics of Bose-Einstein condensates in double-well potentials”, *Phys. Rev. A* **71**, 043603 (2005).
- [210] H. Wang and M. Thoss, “From coherent motion to localization: dynamics of the spin-boson model at zero temperature”, *New Journal of Physics* **10**, 115005 (2008).
- [211] N. Dogra, M. Landini, K. Kroeger, L. Hruby, T. Donner, and T. Esslinger, “Dissipation-induced structural instability and chiral dynamics in a quantum gas”, *Science* **366**, 1496 (2019).
- [212] F. Iemini, A. Russomanno, J. Keeling, M. Schirò, M. Dalmonte, and R. Fazio, “Boundary time crystals”, *Phys. Rev. Lett.* **121**, 035301 (2018).
- [213] E. I. R. Chiacchio and A. Nunnenkamp, “Dissipation-induced instabilities of a spinor Bose-Einstein condensate inside an optical cavity”, *Phys. Rev. Lett.* **122**, 193605 (2019).
- [214] K. C. Stitely, A. Giraldo, B. Krauskopf, and S. Parkins, “Nonlinear semiclassical dynamics of the unbalanced, open Dicke model”, *Phys. Rev. Research* **2**, 033131 (2020).
- [215] L. F. d. Prazeres, L. d. S. Souza, and F. Iemini, “Boundary time crystals in collective d -level systems”, *Phys. Rev. B* **103**, 184308 (2021).
- [216] Z. Zhang, C. H. Lee, R. Kumar, K. J. Arnold, S. J. Masson, A. L. Grimsmo, A. S. Parkins, and M. D. Barrett, “Dicke-model simula-

- tion via cavity-assisted Raman transitions”, *Phys. Rev. A* **97**, 043858 (2018).
- [217] F. Ferri, R. Rosa-Medina, F. Finger, N. Dogra, M. Soriente, O. Zilberberg, T. Donner, and T. Esslinger, “Emerging dissipative phases in a superradiant quantum gas with tunable decay”, *Phys. Rev. X* **11**, 041046 (2021).
- [218] M. Hayn, C. Emary, and T. Brandes, “Phase transitions and dark-state physics in two-color superradiance”, *Phys. Rev. A* **84**, 053856 (2011).
- [219] C. Emary, “Dark-states in multi-mode multi-atom Jaynes – Cummings systems”, *Journal of Physics B: Atomic, Molecular and Optical Physics* **46**, 224008 (2013).
- [220] E. G. D. Torre, S. Diehl, M. D. Lukin, S. Sachdev, and P. Strack, “Keldysh approach for nonequilibrium phase transitions in quantum optics: Beyond the Dicke model in optical cavities”, *Phys. Rev. A* **87**, 023831 (2013).
- [221] J. Skulte, P. Kongkhambut, H. Keßler, A. Hemmerich, L. Mathey, and J. G. Cosme, “Parametrically driven dissipative three-level Dicke model”, *Phys. Rev. A* **104**, 063705 (2021).
- [222] J. Fan, G. Chen, and S. Jia, “Atomic self-organization emerging from tunable quadrature coupling”, *Phys. Rev. A* **101**, 063627 (2020).
- [223] Z. Zhiqiang, C. H. Lee, R. Kumar, K. J. Arnold, S. J. Masson, A. S. Parkins, and M. D. Barrett, “Nonequilibrium phase transition in a spin-1 Dicke model”, *Optica* **4**, 424 (2017).
- [224] S. Diehl, A. Tomadin, A. Micheli, R. Fazio, and P. Zoller, “Dynamical phase transitions and instabilities in open atomic many-body systems”, *Phys. Rev. Lett.* **105**, 015702 (2010).
- [225] P. Lévy, *Théorie de l'addition des variables aléatoires* (Gauthier – Villars, 1954).
- [226] E. Bertin and F. Bardou, “From laser cooling to aging: a unified Lévy flight description”, *American Journal of Physics* **76**, 630 (2008).
- [227] F. Bardou, J.-P. Bouchaud, A. Aspect, and C. Cohen-Tannoudji, *Lévy statistics and laser cooling: how rare events bring atoms to rest* (Cambridge University Press, 2001).
- [228] E. G. Rocha, E. P. Santos, B. J. dos Santos, S. S. de Albuquerque, P. I. R. Pincheira, C. Argolo, and A. L. Moura, “Lévy flights for light in ordered lasers”, *Phys. Rev. A* **101**, 023820 (2020).
- [229] D. M. Stamper-Kurn and M. Ueda, “Spinor Bose gases: Symmetries, magnetism, and quantum dynamics”, *Rev. Mod. Phys.* **85**, 1191 (2013).
- [230] M.-O. Mewes, M. R. Andrews, N. J. van Druten, D. M. Kurn, D. S. Durfee, C. G. Townsend, and W. Ketterle, “Collective excitations of

- a Bose-Einstein condensate in a magnetic trap”, *Phys. Rev. Lett.* **77**, 988 (1996).
- [231] F. Dalfovo, S. Giorgini, L. P. Pitaevskii, and S. Stringari, “Theory of Bose-Einstein condensation in trapped gases”, *Rev. Mod. Phys.* **71**, 463 (1999).
- [232] F. Chevy, V. Bretin, P. Rosenbusch, K. W. Madison, and J. Dalibard, “Transverse breathing mode of an elongated Bose-Einstein condensate”, *Phys. Rev. Lett.* **88**, 250402 (2002).
- [233] R.-X. Zhang and S. Das Sarma, “Anomalous Floquet chiral topological superconductivity in a topological insulator sandwich structure”, *Phys. Rev. Lett.* **127**, 067001 (2021).
- [234] C. Triola and A. V. Balatsky, “Odd-frequency superconductivity in driven systems”, *Phys. Rev. B* **94**, 094518 (2016).
- [235] J. Cayao, C. Triola, and A. M. Black-Schaffer, “Floquet engineering bulk odd-frequency superconducting pairs”, *Phys. Rev. B* **103**, 104505 (2021).
- [236] F. Schlawin, A. Cavalleri, and D. Jaksch, “Cavity-mediated electron-photon superconductivity”, *Phys. Rev. Lett.* **122**, 133602 (2019).
- [237] A. Komnik and M. Thorwart, “BCS theory of driven superconductivity”, *The European Physical Journal B* **89**, 244 (2016).
- [238] M. Knap, M. Babadi, G. Refael, I. Martin, and E. Demler, “Dynamical Cooper pairing in nonequilibrium electron-phonon systems”, *Phys. Rev. B* **94**, 214504 (2016).
- [239] M. A. Sentef, A. F. Kemper, A. Georges, and C. Kollath, “Theory of light-enhanced phonon-mediated superconductivity”, *Phys. Rev. B* **93**, 144506 (2016).
- [240] J. R. Coulthard, S. R. Clark, S. Al-Assam, A. Cavalleri, and D. Jaksch, “Enhancement of superexchange pairing in the periodically driven Hubbard model”, *Phys. Rev. B* **96**, 085104 (2017).
- [241] K. Ido, T. Ohgoe, and M. Imada, “Correlation-induced superconductivity dynamically stabilized and enhanced by laser irradiation”, *Science Advances* **3**, e1700718 (2017).
- [242] M. Mitrano, A. Cantaluppi, D. Nicoletti, S. Kaiser, A. Perucchi, S. Lupi, P. Di Pietro, D. Pontiroli, M. Riccò, S. R. Clark, D. Jaksch, and A. Cavalleri, “Possible light-induced superconductivity in K_3C_{60} at high temperature”, *Nature* **530**, 461 (2016).
- [243] D. M. Kennes, M. Claassen, M. A. Sentef, and C. Karrasch, “Light-induced d -wave superconductivity through Floquet-engineered Fermi surfaces in cuprates”, *Phys. Rev. B* **100**, 075115 (2019).
- [244] M. Buzzi, D. Nicoletti, M. Fechner, N. Tancogne-Dejean, M. A. Sentef, A. Georges, T. Biesner, E. Uykur, M. Dressel, A. Henderson, T. Siegrist, J. A. Schlueter, K. Miyagawa, K. Kanoda, M.-S. Nam,

- A. Ardavan, J. Coulthard, J. Tindall, F. Schlawin, D. Jaksch, and A. Cavalleri, “Photomolecular high-temperature superconductivity”, *Phys. Rev. X* **10**, 031028 (2020).
- [245] M. Budden, T. Gebert, M. Buzzi, G. Jotzu, E. Wang, T. Matsuyama, G. Meier, Y. Laplace, D. Pontiroli, M. Riccò, F. Schlawin, D. Jaksch, and A. Cavalleri, “Evidence for metastable photo-induced superconductivity in K_3C_{60} ”, *Nature Physics* **17**, 611 (2021).
- [246] T. Kaneko, T. Shirakawa, S. Sorella, and S. Yunoki, “Photoinduced η pairing in the Hubbard model”, *Phys. Rev. Lett.* **122**, 077002 (2019).
- [247] J. Tindall, B. Buča, J. R. Coulthard, and D. Jaksch, “Heating-induced long-range η pairing in the Hubbard model”, *Phys. Rev. Lett.* **123**, 030603 (2019).
- [248] S. Ejima, T. Kaneko, F. Lange, S. Yunoki, and H. Fehske, “Photoinduced η -pairing at finite temperatures”, *Phys. Rev. Res.* **2**, 032008(R) (2020).
- [249] Y. Murakami, S. Takayoshi, T. Kaneko, Z. Sun, D. Golež, A. J. Millis, and P. Werner, “Exploring nonequilibrium phases of photo-doped Mott insulators with generalized Gibbs ensembles”, *Communications Physics* **5**, 23 (2022).
- [250] J. Li, M. Müller, A. J. Kim, A. M. Läuchli, and P. Werner, “Twisted chiral superconductivity in photodoped frustrated Mott insulators”, *Phys. Rev. B* **107**, 205115 (2023).
- [251] P. Werner, J. Li, D. Golež, and M. Eckstein, “Entropy-cooled nonequilibrium states of the Hubbard model”, *Phys. Rev. B* **100**, 155130 (2019).
- [252] Q. Yang, Z. Yang, and D. E. Liu, “Intrinsic dissipative Floquet superconductors beyond mean-field theory”, *Phys. Rev. B* **104**, 014512 (2021).
- [253] A. Altland and B. D. Simons, *Condensed matter field theory*, 2nd ed. (Cambridge University Press, 2010).
- [254] O. Hart, G. Goldstein, C. Chamon, and C. Castelnovo, “Steady-state superconductivity in electronic materials with repulsive interactions”, *Phys. Rev. B* **100**, 060508(R) (2019).
- [255] A. Ramires and M. Sgrist, “Identifying detrimental effects for multi-orbital superconductivity: application to Sr_2RuO_4 ”, *Phys. Rev. B* **94**, 104501 (2016).
- [256] G. M. Eliashberg, “Неупругие столкновения электронов и неравновесные стационарные состояния в сверхпроводниках (Inelastic electron collisions and nonequilibrium stationary states in superconductors)”, *Zh. Eksp. Teor. Fiz.* **61**, 1254 (1971).

- [257] B. I. Ivlev, S. G. Lisitsyn, and G. M. Eliashberg, “Nonequilibrium excitations in superconductors in high-frequency fields”, *Journal of Low Temperature Physics* **10**, 449 (1973).
- [258] A. V. Chubukov, A. Abanov, I. Esterlis, and S. A. Kivelson, “Eliashberg theory of phonon-mediated superconductivity — When it is valid and how it breaks down”, *Annals of Physics* **417**, 168190 (2020).
- [259] F. Marsiglio, “Eliashberg theory: a short review”, *Annals of Physics* **417**, 168102 (2020).
- [260] S. Mathey and S. Diehl, “Dynamic renormalization group theory for open Floquet systems”, *Phys. Rev. B* **102**, 134307 (2020).
- [261] A. Zamora, L. M. Sieberer, K. Dunnett, S. Diehl, and M. H. Szymańska, “Tuning across universalities with a driven open condensate”, *Phys. Rev. X* **7**, 041006 (2017).
- [262] Q. Fontaine, D. Squizzato, F. Baboux, I. Amelio, A. Lemaître, M. Morassi, I. Sagnes, L. Le Gratiet, A. Harouri, M. Wouters, I. Carusotto, A. Amo, M. Richard, A. Minguzzi, L. Canet, S. Ravets, and J. Bloch, “Kardar–Parisi–Zhang universality in a one-dimensional polariton condensate”, *Nature* **608**, 687 (2022).
- [263] A. J. Daley, “Quantum trajectories and open many-body quantum systems”, *Advances in Physics* **63**, 77 (2014).
- [264] N. Lafforencie, “Quantum entanglement in condensed matter systems”, *Physics Reports* **646**, 1 (2016).
- [265] K. Roux, H. Konishi, V. Helsen, and J.-P. Brantut, “Strongly correlated Fermions strongly coupled to light”, *Nature Communications* **11**, 2974 (2020).
- [266] H. Konishi, K. Roux, V. Helsen, and J.-P. Brantut, “Universal pair polaritons in a strongly interacting Fermi gas”, *Nature* **596**, 509 (2021).
- [267] V. Helsen, T. Zwettler, F. Mivehvar, E. Colella, K. Roux, H. Konishi, H. Ritsch, and J.-P. Brantut, “Density-wave ordering in a unitary Fermi gas with photon-mediated interactions”, *Nature*, [10 . 1038 / s41586-023-06018-3](https://doi.org/10.1038/s41586-023-06018-3) (2023).
- [268] X. Zhang, Y. Chen, Z. Wu, J. Wang, J. Fan, S. Deng, and H. Wu, “Observation of a superradiant quantum phase transition in an intracavity degenerate Fermi gas”, *Science* **373**, 1359 (2021).
- [269] *Bose Bogoliubov transformations*, (2017) http://people.physics.illinois.edu/stone/bose_bogoliubov.pdf.
- [270] J. Dereziński, “Bosonic quadratic Hamiltonians”, *J. Math. Phys.* **58**, 121101 (2017).

List of publications

Publications constituting Chapters in this thesis

- [RL1] **RL**, C. Georges, J. Klinder, P. Mognini, M. Büttner, A. U. J. Lode, R. Chitra, A. Hemmerich, and H. Keßler, “Mott transition in a cavity-boson system: A quantitative comparison between theory and experiment”, *SciPost Phys.* **11**, 030 (2021).
- [RL2] **RL**, P. Mognini, A. U. J. Lode, and R. Chitra, “Pathway to chaos through hierarchical superfluidity in blue-detuned cavity-BEC systems”, *Phys. Rev. A* **101**, 061602(R) (2020).
- [RL3] **RL**, R. Rosa-Medina, F. Ferri, F. Finger, K. Kroeger, T. Donner, T. Esslinger, and R. Chitra, “Dissipation-engineered family of nearly dark states in many-body cavity-atom systems”, *Phys. Rev. Lett.* **128**, 153601 (2022).
- [RL4] R. Rosa-Medina, F. Ferri, F. Finger, N. Dogra, K. Kroeger, **RL**, R. Chitra, T. Donner, and T. Esslinger, “Observing dynamical currents in a non-Hermitian momentum lattice”, *Phys. Rev. Lett.* **128**, 143602 (2022).
- [RL5] **RL**, A. Ramires, and R. Chitra, *Decoding the drive-bath interplay: A guideline to enhance superconductivity*, 2023, [arXiv:2306.02861](https://arxiv.org/abs/2306.02861).

Other publications

- [RL6] **RL**, P. Mognini, L. Papariello, M. C. Tsatsos, C. Lévêque, S. E. Weiner, E. Fasshauer, R. Chitra, and A. U. J. Lode, “MCTDH-X: The multiconfigurational time-dependent Hartree method for indistinguishable particles software”, *Quantum Sci. and Technol.* **5**, 024004 (2020).
- [RL7] A. U. J. Lode, **RL**, M. Büttner, L. Papariello, C. Lévêque, R. Chitra, M. C. Tsatsos, D. Jaksch, and P. Mognini, “Optimized observable readout from single-shot images of ultracold atoms via machine learning”, *Phys. Rev. A* **104**, L041301 (2021).
- [RL8] **RL**, L. Papariello, P. Mognini, R. Chitra, and A. U. J. Lode, “Superfluid–Mott-insulator transition of ultracold superradiant bosons in a cavity”, *Phys. Rev. A* **100**, 013611 (2019).
- [RL9] A. U. J. Lode, F. S. Diorico, R. Wu, P. Mognini, L. Papariello, **RL**, C. Lévêque, L. Exl, M. C. Tsatsos, R. Chitra, and N. J. Mauser, “Many-body physics in two-component Bose – Einstein condensates

in a cavity: fragmented superradiance and polarization”, *New J. of Phys.* **20**, 055006 (2018).

- [RL10] A. Scaramucci, H. Shinaoka, M. V. Mostovoy, **RL**, C. Mudry, and M. Müller, “Spiral order from orientationally correlated random bonds in classical *XY* models”, *Phys. Rev. Res.* **2**, 013273 (2020).

Repositories of Numerical Softwares and Toolkits

- [RL11] A. U. J. Lode, M. C. Tsatsos, E. Fasshauer, **RL**, L. Papariello, P. Mognini, C. Lévêque, S. E. Weiner, and M. Büttner, *MCTDH-X: The multiconfigurational time-dependent Hartree for indistinguishable particles software*, <https://gitlab.com/the-mctdh-x-repository/mctdh-x-releases>, 2022.
- [RL12] A. U. J. Lode, P. Mognini, **RL**, M. Büttner, P. Rembold, C. Lévêque, M. C. Tsatsos, and L. Papariello, *UNIQRN: Universal neural-network interface for quantum observable readout from *N*-body wavefunctions*, <https://gitlab.com/UNIQRN/uniqrn>, 2021.

Teaching duties

Courses as Teaching assistant

- Theorie der Wärme (FS 19, FS 21, FS 22), Elektrodynamik (FS 20), Quantenmechanik I (HS 20), Statistical Physics (HS 19, HS 21)

Semester projects as Co-supervisor

- **Justyna Stefaniak** Chaotic phase of driven ultracold atoms in an optical cavity (HS 20, with D. Dreon, R. Chitra, T. Esslinger)
- **Johannes Christmann** Quantum trajectories in Dicke-like models (FS 23, with R. Chitra)
- **Francesco Gargiulo** Interpolating Dicke–Tavis–Cummings model on a lattice with transverse field (FS 23, with R. Chitra)

Master theses as Co-supervisor

- **Andréas Roggo** Ultracold bosons in a periodically modulated optical lattice (HS 20, with R. Chitra)
- **Ruslan Mushkaev** Cavity-induced light-matter interactions (HS 21, with R. Chitra)
- **Zhuotao Jin** Floquet engineering of the Dicke model in a cavity-BEC system (FS 22, with R. Rosa-Medina, T. Esslinger, R. Chitra)
- **Daniel Ortuño** Cavity-fermion systems with imbalanced pump (FS 23, with J. Stefaniak, R. Chitra, T. Donner)

Curriculum vitae

Personal data

Name	Rui Lin 林睿
Date of birth	18 th May 1994
Nationality	China

Education

2019 – 2023	Doctoral studies in theoretical physics ETH Zürich, Switzerland
2016 – 2018	Master of Science in Physics ETH Zürich, Switzerland
2012 – 2016	Bachelor of Science in Physics Sun Yet-sen University (中山大学), Guangzhou, China
2009 – 2012	Secondary school Zhixin High School (执信中学), Guangzhou, China

Acronyms

General acronyms

BEC	Bose-Einstein condensate
QED	Quantum electrodynamics
BCS	Bardeen-Cooper-Schrieffer
SC	superconductor

Phases of matter in cavity-boson systems

SSF	self-organised superfluid
SMI	self-organised Mott insulator
2-SSF	self-organised second-order superfluid
SDSF	self-organised dimerised superfluid
QA	quasiperiodic attractor

Numerical methods

MCTDH-X	Multiconfigurational time-dependent Hartree method for indistinguishable particles
UNIQRN	Universal neural-network interface for quantum observable readout from N -body wavefunctions
MLGWS	Maximally localised generalised Wannier states

Institutions

ETH	Eidgenössische Technische Hochschule Zürich
UZH	Universität Zürich
PSI	Paul Scherrer Institut

Acknowledgments

I am very grateful to all people who encouraged and supported me during my doctoral study both personally and academically, and contributed to its success.

First and foremost, I would express my sincere gratitude to my thesis advisor, Dr. R. Chitra, for her support and guidance. Since our first discussion from master thesis, Chitra always supported me actively and patiently not only with her plentiful experience, profound insight, and inspiring guidance, but also as a mentor with skills in academic social life. I am also grateful to Prof. Manfred Sigrist, who genially welcomed me in his group and always conveyed to us his passion in physics.

I would also like to thank all my collaborators. Paolo Mognini has been one of my closest collaborators throughout the doctoral study. He gave me important guidance as a senior student, and exchanged with me plenty of helpful understandings of problems. I would also like to thank Dr. Axel U. J. Lode, who always eagerly shared with me his expertise in programming. Without him the existence and spread of the fascinating numerical tool of MCTDH-X would have never been possible. I also thank Dr. Hans Keßler, who patiently introduced me to his experimental setups and explained all the details necessary for understanding its physics, and Dr. Aline Ramires who shared with me her expertise in superconductivity. I would then express my thanks to Prof. Tilman Esslinger and Dr. Tobias Donner, and all the members of their group, including Dr. Davide Dreoni, Katrin Kröger, Rodrigo Rosa-Medina, Dr. Francesco Ferri, Fabian Finger, Justyna Stefaniak and Xiangliang Li (李相良). As the experimental colleagues across the street, they were always kind to explain to me the exciting physics taking place in their labs. I would also like to thank Miriam Büttner from Universität Freiburg for the enjoyable coding sessions.

My stay at the Institute for Theoretical Physics was really enjoyable because of the nice people I met. I would thus like to thank all the members of the condensed matter groups at ETH, UZH, and PSI. This in particular includes my former and current fellow PhD students: Yuto Shibata, Karin Sim, Bastian Zinkl, Tudor Pahomi, Lidia Stocker, Christian Carisch, Toni Heugel, Anina Leuch, Jan Košata, Yuhao Zhao(赵宇皓), Filippo Gaggioli, Valerio Peri, Matteo Sorriente, Antonio Štrkalj, Maximilian Holst, Tobias Wolf, Samuel Bird; the professors who I helped and learned a lot from as teaching assistant: Prof.

Acknowledgments

Gianni Blatter, Prof. Renato Renner, Prof. Gian Michele Graf; and all other colleagues: Dr. Andras Szabo, Dr. Mark Fischer, Prof. Wei Chen (陈伟) who shared office with me, Dr. Javier del Pino, Prof. Christopher Mudry, Dr. Markus Müller, and Prof. Wei Chen. The open and friendly atmosphere created by all these people was really enjoyable.

I am also grateful to my parents for their unconditional and everlasting supports, and Yaqi Zhao (赵桠琦) and her cats without whose mutual supports the hard times of Covid would have been even tougher. I would also like to thank all my friends I met in Zürich, including Minxiang Gao (郜敏祥), Tianjiao Yang (杨天娇), Dongqi Bao (鲍东琪), Yili Yang (杨易立), Ruocheng Han (韩若澄), Yang Bai (白曷), Weigutian Ou (欧韦古田), Zijin Lei (雷子瑾), and many others. We have spent great time exploring Switzerland via hiking, skiing, bouldering, and via-ferrata-ing.

Finally, I would acknowledge the financial support from the ETH Grant for my doctoral education and research.

Rui Lin
Zürich, 11th April 2023

林睿
癸卯年闰二月廿一于苏黎世

